THÈSE

En vue de l'obtention du

DOCTORAT DE L'UNIVERSITÉ DE TOULOUSE

Délivré par Institut National Polytechnique de Toulouse
Spécialité : *Énérgetique et transferts*

Présentée et soutenue par Michael BAUERHEIM

le 1er Décembre 2014

Theoretical and numerical study of symmetry breaking effects on azimuthal thermoacoustic modes in annular combustors

---

JURY

S. Candel	EM2C CNRS	Rapporteur
W. Polifke	TU Munich	Rapporteur
M.P. Juniper	Cambridge University	Examinateur
J.R. Dawson	NTNU	Examinateur
F. Nicoud	Montpellier 2	Examinateur
T. Poinsot	IMFT CNRS	Directeur de thèse
L. Gicquel	CERFACS	Co-directeur de thèse
M. Cazalens	CRT Safran	Encadrant Entreprise

École doctorale: Mécanique, Energétique, Génie Civil, Procédés (MEGeP)
Unité de recherche: CERFACS

Résumé

Une grande variété de phénomènes physiques, des molécules aux étoiles, contiennent des symétries de rotation et peuvent donc développer des modes azimutaux. Quand la symétrie est parfaite, ces modes sont dégénérés avec deux composantes de même fréquence. Cependant, si la symétrie est rompue, les deux composantes deviennent distinctes et leurs fréquences diffèrent. Cette brisure peut être alors accompagnée de la déstabilisation du système ou de comportements dynamiques chaotiques.

Il en va de même pour les chambres de combustion annulaires, sujettes aux instabilités thermo-acoustiques azimutales et aux brisures de symétries: ce théme constitue le sujet principal de cette thèse. En premier lieu, un outil analytique (ATACAMAC) est développé pour analyser les modes azimutaux dans une chambre annulaire connectée à des bruleurs. La symétrie de rotation est cassée en distribuant différents types de bruleurs le long de la chambre (brisure de type GS) ou en imposant une vitesse azimutale moyenne (type FS). L'expression analytique du taux d'accroissement révèle que la stabilité du système est contrôlée par trois paramètres: (1) une intensité de couplage, (2) le Mach azimutal moyen et (3) l'intensité de séparation associée à la brisure de symétrie. Cette théorie a été validée avec un solveur de Helmholtz 3D et montre un très bon accord. Ensuite, ATACAMAC est étendu à des configurations plus complexes où les 19 bruleurs sont alimentés par un plenum annulaire commun qui peut donc se coupler acoustiquement à la chambre. Cette configuration est étudiée en introduisant des incertitudes sur les 19 flammes, soit 38 paramètres $n - \tau$ incertains. L'approche Active Subspace est appliquée ici pour réduire cette dimension de 38 à 5 paramètres seulement. Une technique Monte-Carlo montre alors que le taux d'accroissement est extrêmement sensible aux incertitudes introduites qui brisent la symétrie du système.

Pour compléter cette théorie, des Simulations aux Grandes Echelles (SGE) de l'expérience annulaire de Cambridge ont été réalisées sur un cas mono-secteur. Les paramètres numériques et physiques ont été variés pour évaluer la robustesse des prédictions SGE, notamment des Fonctions de Transfert de Flammes (FTF). Ces FTFs sont ensuite introduites dans un solveur acoustique 3D pour déterminer la stabilité de la chambre annulaire. La stabilité est peu impactée par les paramêtres numériques, alors que remplacer le méthane par l'éthylène déstabilise la configuration. Enfin, la configuration annulaire complète (15 et 18 secteurs) est calculée. Les résultats numériques sont comparés à l'expérience. Notamment, un mode instable à 1800 Hz croît dans la simulation comme dans l'expérience. Néanmoins, à cause de son coût élevé, seules les premières phases ont pu être simulées, ce qui révèle le besoin crucial d'outils plus efficaces que la SGE pour la thermo-acoustique.

Une nouvelle approche, appelée AMT, est donc développée pour vérifier la qualité des prédictions linéaires obtenues par théorie ou simulations acoustiques en les injectant comme solution initiale à un solveur SGE. Cette méthodologie est validée sur des configurations longitudinales laminaires avec un champ de vitesse uniforme. Un cas test supplémentaire, turbulent, est présenté pour investiguer les effets de la turbulence sur l'acoustique. Les résultats indiquent que la turbulence génère des harmoniques alors que l'acoustique modifie la production de turbulence. Finalement, AMT est appliqué sur des chambres annulaires pour étudier les brisures de type FS et GS, notamment en distribuant des résonateurs de Helmholtz le long de la chambre. AMT capture correctement les brisures de type FS et GS mais est aussi utile pour estimer l'amortissement associé aux résonateurs. Cette approche permet également d'étudier la nature et la dynamique des modes azimutaux et révèle que briser les symétries fixe la structure du mode alors qu'elle est déterminée uniquement par la condition initiale dans des configurations symétriques.

Abstract

A large range of physical problems, from molecules to giant stars, exhibits rotational symmetry and can exhibit azimuthal waves or vibrations. When the rotational symmetry is perfect, these modes occur in a doubly-degenerate form with two orthogonal components at the same frequency. However, when symmetry is broken, the two identical pairs are split into two distinct modes with different frequencies, which can be accompanied by a destabilization of the system or by chaotic behaviors.

Symmetry breaking has become a new topic for annular gas turbines prone to azimuthal thermo-acoustic instabilities and constitutes the main topic of this PhD thesis. First, a theoretical tool (ATACAMAC) is developed to analyze azimuthal modes in an annular chamber connected to an arbitrary number of burners. Symmetry is broken by distributing different burner types along the annular chamber (GS breaking) or by imposing a mean azimuthal flow (FS breaking). The analytical expression of the growth rate reveals that the stability is controlled by three parameters: (1) a coupling strength, (2) the azimuthal Mach number and (3) a splitting strength associated to the symmetry breaking. This theoretical results are validated using a 3D Helmholtz solver on simplified annular configurations showing a very good agreement. Then, ATACAMAC is extended to more complex geometries where burners are fed by a common annular plenum, which can couple to the chamber. This type of configuration is studied where uncertainties is introduced on the 19 flames, leading to 38 uncertain parameters (n, τ). Therefore, the Active Subspace approach is presented to reduce this dimension from 38 to only 5 parameters, which then allows a Monte-Carlo technique to assess the growth rate sensitivity to FTF uncertainties. It shows that combustion instabilities are sensitive to subtle uncertainties on the 19 FTFs, which induce a symmetry breaking affecting the growth rate.

To complement theory, LES of the annular experiment of Worth & Dawson (2013*b*) is used. First, an analysis is performed on a single-sector, where numerical and physical parameters are varied to assess the robustness of numerical FTFs predictions. Then the stability of the 360° combustor is computed by a 3D Helmholtz solver, in which these FTFs are introduced. It shows that numerical models have only a minor impact on FTF and stability, while changing the fuel from methane to ethylene leads to azimuthal instabilities. The complete 360° configuration is then computed. Numerical results are compared to experimental data showing that LES captures correctly characteristic features of the annular rig. An unstable azimuthal mode at 1800 Hz grows in both the simulation and the experiment. Nevertheless, because of its extreme cost, only the start-up phase can be simulated, which reveals a crucial need for an efficient tool less expensive

than LES.

Thus, a novel approach called Acoustic Mode Triggering (AMT) is developed to verify the quality of linear predictions obtained by theory or Helmholtz simulations by using them as initial solutions of a LES or DNS solver. First, this methodology is validated on longitudinal laminar configurations with a uniform mean flow. An additional turbulent test case is presented to investigate effects of turbulence on acoustic modes. Results indicate that turbulence leads to harmonics generation, while acoustics can modify the turbulent production. Finally, AMT is applied on a simplified annular combustor to study effects of GS and FS breaking. In particular, GS breaking is investigated by distributing Helmholtz resonators in the chamber. It shows that AMT can capture GS and FS breaking, but is also useful to estimate the damping associated to particular mecanisms or devices. AMT also allows to study the azimuthal modes nature and dynamics and reveals that breaking symmetry fixes the mode structure, while for axisymmetric cases the mode structure is determined by the initial state.

Acknowledgements

I first want to thank SNECMA and SAFRAN group for having financed this PhD thesis (CIFRE), in particular Michel Cazalens who follows my research all long these three years. Computer resources from GENCI (Turing, Ada) have been also greatly appreciated and were indispensable for the work carried out here.

It is a real honor and pleasure to have in my jury Sebastian Candel, Wolfgang Polifke, James Dawson and Matthew Juniper. They are source of inspiration for young researchers and I always enjoyed my discussions with them at Stanford or the Symposium of San Francisco for instance.

A special thought is for Franck Nicoud, also in my jury, with who I enjoy to work and discuss acoustics all along these three years resulting in a fruitful collaboration with several publications.

Of course, this work would have not been possible without Thierry Poinsot and Laurent Gicquel, my PhD advisors, who have offered me this thesis opportunity at the first place and encourage me to work and be curious about all research topics studied at CERFACS or IMFT. I also really appreciate all their commitment and efforts to convey their knowledge as well as to correct my articles and this present thesis.

I also thank all other senior researchers at CERFACS, IMFT and Sherbrook University (B. Cuenot, O. Vermorel, E. Riber, A. Dauptain, F. Duchaine, L. Selle and S. Moreau) for their useful advices and kindness, with a special thought for G. Staffelbach, the Master of the computer science and resources at Cerfacs who has changed the HPC nightmare into a user-friendly approach. The heavy 360° simulation of more than millions CPu hours and 100 millions cells would have not been possible without him.

I also want to acknowledge all students, colleagues and now friends from CERFACS and IMFT who have generously shared their time, knowledge and friendship, with a special thought for Antho, Leader Furet, Dodo, Fuinette, le père Lapeyre, Raph, Lucas, Adrien, Manqi and Dimi for all the time spent together at coffee breaks, talking about black holes, doing sports and enjoying parties or during the numerous amazing Coinche games !

Finally, I really want to thank my family and friends from Orléans who have constantly supported me from more than twenty years now. They gave me everything and encourage me a lot in this work. And the last but not the least, I have a special thought for my beloved Déborah who has endured with me the good times and the hardest for more than two years now. "N'didi !"

I dedicate this thesis to my grandfather, who died during this PhD, who gave me so much and made me what I am now.

Contents

Chapter 1

Introduction

1.1 Overview of symmetry breaking in physics

A wide range of physical problems, from nano photonics crystal (Borisnika, 2006) (Fig. 1.1, a) and molecules (Creighton, 1982) to giant stars (Lavely, 1983) (Fig. 1.1, c), including annular combustion chambers (Fig. 1.1, d) which will be the focus of the present work, take place in tori or disks: they contain rotating symmetries and can therefore exhibit azimuthal/transverse oscillations such as electromagnetic waves (Pang *et al.*, 2007), acoustic waves (Krebs *et al.*, 2002; Noiray *et al.*, 2011; Parmentier *et al.*, 2012; Bauerheim *et al.*, 2014*d*), surface waves (Feng & Sethna, 1989; Simonelli & Gollub, 1989), magneto static spin-waves[1] (Hoffmann *et al.*, 2007; Guslienko *et al.*, 2008; Barman *et al.*, 2010; Kammerer *et al.*, 2011) or solid vibrations (Creighton, 1982; Perrin & Charnley, 1973; Lin & Parker, 2000*a*,*b*; Kumar & Krousgrill, 2012). When the rotating symmetry is perfect, these modes occur in doubly-degenerate pairs with two independent oscillations (a clockwise and a counter-clockwise waves) at the same frequency (a, in Fig. 1.2, left). However, when systems with rotational symmetry are modified either in their geometry or by spatially varying their properties or their boundary conditions, degenerate pairs can split into two distinct modes with different yet close frequencies (b, in Fig. 1.2, right). In some applications, the splitting frequency Δf can be fairly large and therefore cannot be ignored (e.g. $\Delta f = 0.25\ GHz$ for spin-wave modes in small ferromagnetic elements (Hoffmann *et al.*, 2007)).

In many applications, this splitting can lead to catastrophic effects, requiring studies to understand their underlying nature and methods to suppress them. For instance, photonics crystal (i.e. devices where several electromagnetical micro cavities are coupled with a specific pattern to form "photon molecules") with high quality-factor are essential for the development of the next generation of optoelectronic components, but undesired symmetry breaking and associated non-degenerate modes reduce their overall performances. To tackle this problem, Borisnika (2006) proposed arrangement patterns with enhanced symmetry characteristics, which reduce effects of non-degenerate modes and improve the quality factors of the devices: here, perfect axisymmetry is the objective.

[1] Spin waves are propagating disturbances in the ordering of magnetic materials.

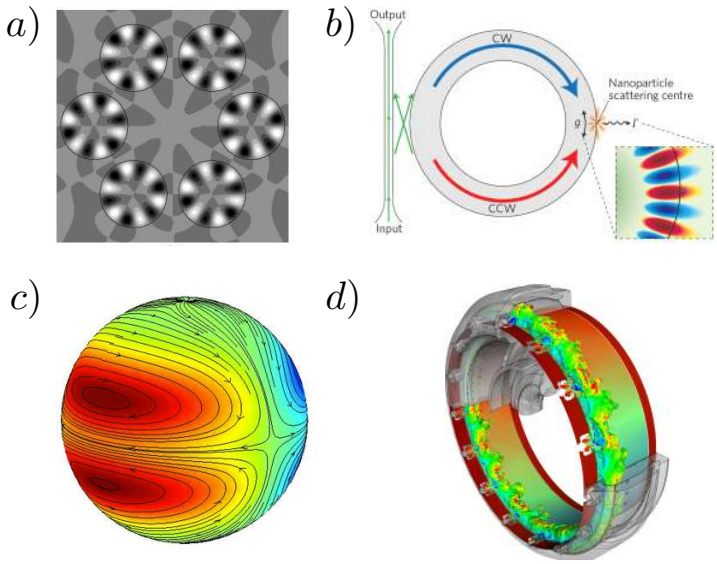

Figure 1.1: Several problems with rotation symmetry exhibiting azimuthal modes and symmetry breaking. a) Arrangement of photonics crystals b) Whispering gallery mode resonators (WGMs) where the symmetry is broken by particle. Theory and symmetry can be used together to approximate the particle size c) Azimuthal oscillations modes on a neutron star and d) Annular combustor exhibiting azimuthal combustion instabilities.

In applications based on magnetic disks which exhibit spin-waves (Hoffmann *et al.*, 2007; Guslienko *et al.*, 2008; Barman *et al.*, 2010; Kammerer *et al.*, 2011), theoretical models show that the splitting is a consequence of the interaction of the azimuthal mode with the vortex core gyrotropic motion. Both simulations and experiments have confirmed that removing the vortex core from the disk suppresses mode splitting (Hoffmann *et al.*, 2007). This suggests that theory, simulations or experiments can unveil the splitting origins and offer methods to suppress them.

In configurations where symmetry breaking is well described theoretically (Mazzei *et al.*, 2007), scientists can willingly introduce modifications, which alter symmetry, to analyze the phenomenon responsible for this splitting. For example, in ultra-high quality factor whispering gallery mode resonators (WGMs), a small imperfection (similar to the case b in Fig. 1.2) or a deposited particle (Fig. 1.1, b) can scatter light from one of the two cavity modes (counter-clockwise for instance) into free space as well as in the opposite direction (i.e. clockwise). Scientists can then exploit this splitting to accurately determine particle sizes (Mazzei *et al.*, 2007; Kippenberg, 2010). A similar methodology is used in helioseismology (Lavely, 1983; Kosovichev, 1999; Tripathy *et al.*, 2000), where the internal solar structure and dynamics can be inferred from observed frequencies, which can be split either by rotation, asphericity or the magnetic field of the star.

In the particular field of fluid mechanics, symmetry breaking phenomena are less studied due to complex geometries, high non-linear levels and complex physics. In simple configurations (square and quasi-square channels), such a splitting effect has been studied for surface waves (Feng & Sethna, 1989; Simonelli & Gollub, 1989). Results show that

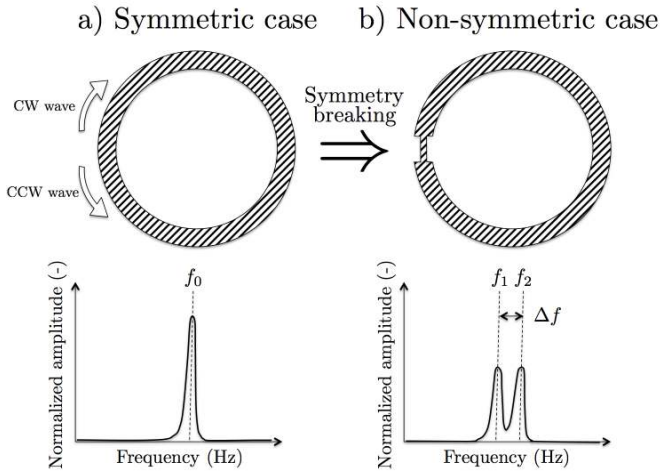

Figure 1.2: a) Sketch of a configuration with rotating symmetries (top) and its associated spectrum (bottom). Two waves (clockwise (CW) and counter-clockwise (CCW)) can exist and have the same frequency f_0: the mode is "degenerate". When the rotating symmetry is broken (b), the degenerate mode at f_0 is split into two distinct waves with different yet close frequencies f_1 and f_2 (bottom).

the symmetry of the configuration has dramatic effects on the dynamics. The degenerate case yields no time-dependent patterns. However, setups where the two components are separated in frequency, even by a small amount (about 1%), can lead to chaotic states (Simonelli & Gollub, 1989). Similarly Davey et al. (Davey & Salwen, 1994) investigate the linear stability of the first circumferential mode in both a circular and an elliptic pipe. They show analytically that the circular problem has a double degenerate eigenvalue f_0, while the ellipticity of the latter configuration splits the doublets into two distinct eigenvalues $f_0 \pm \Delta f/2$. The imaginary part of the splitting frequency Δf is non-zero and thus the ellipticity of the cross-sectional area always makes the flow less stable. This splitting mechanism induced by the symmetry reduction (from the axisymmetry group S^1 of the circular problem to the mirror symmetry group Z_2 associated to the elliptic cross-section) is briefly discussed in its fundamental mathematical aspects in (Guckenheimer & Mahalov, 1992) and applied to the instability of a vortex filament in a non-circular cylinder. Such a symmetry reduction also plays a crucial role on the oscillations of droplets due to a-sphericity (Cummings & Blackburn, 1991) and/or Coriolis forces if the droplet is rotating (Busse, 1984). Symmetry violation are also encountered in turbulent flows associated with helicity structures (Levich & Tsinober, 1983; Polifke, 1990).

In the field of combustion, symmetry breaking has recently become an interesting topic for annular gas turbines (Fig. 1.13, d) (Noiray *et al.*, 2011; Parmentier *et al.*, 2012; Bauerheim *et al.*, 2014*a*,*e*), which exhibit azimuthal acoustic waves produced by thermo-acoustic instabilities (O'Connor & T.Lieuwen, 2012*c*) (Fig. 1.3). This is the main topic of this PhD work, which is organized as follows: first an overview of combustion instabilities especially in annular chambers is given in Section 1.2. Then, tools and approaches used or developed in this thesis are briefly presented in Section 1.3, from analytical theory to the full 360° simulation of annular engines. Finally in Section 1.4, azimuthal modes and potential symmetry breaking encountered in annular gas turbines are described and

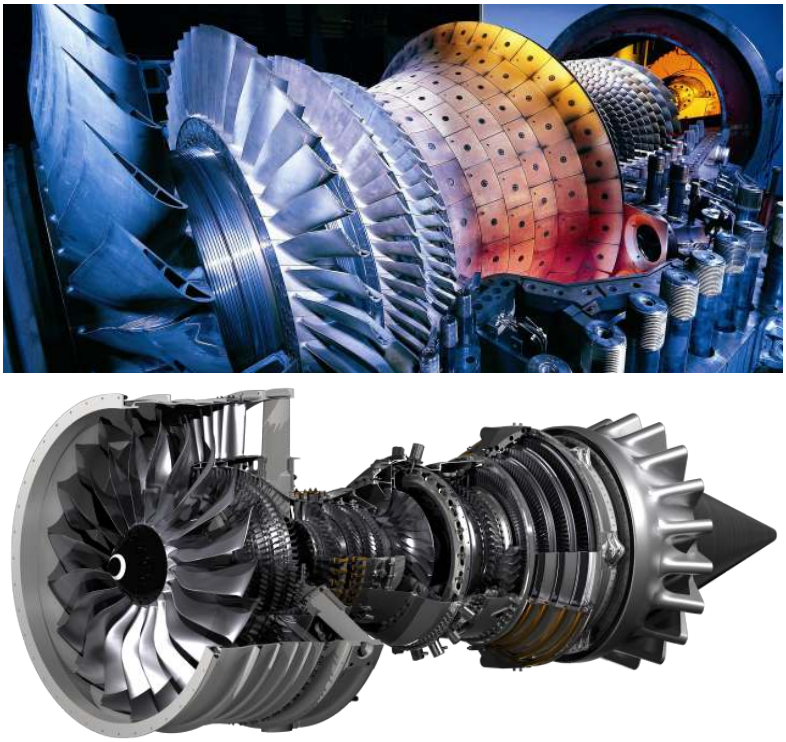

Figure 1.3: Example of gas turbines with annular combustion chambers for power generation (Siemens, top) and for aeropropulsion (Silvercrest Snecma, bottom).

constitute the main topic of this PhD (Section 1.5).

1.2 Combustion Instabilities overview

1.2.1 Instabilities: introduction and challenges

Large power densities in gas turbines can be accompanied by fluctuations leading to potential problems known as combustion instabilities (Culick & Kuentzmann, 2006; Lieuwen & Yang, 2005). They are due to a coupling effect between the flame and acoustics, creating high pressure and heat release oscillations in the chamber. These oscillations may destroy the propulsion system (Lynch, 2011; Poinsot & Veynante, 2011) as presented in Fig. 1.4 showing a five-burner combustion chamber before (left) and after (right) combustion instabilities highlighting damage provoked by such a phenomenon. Therefore, over the last sixty years, combustion instabilities have constantly been a key issue for aeronautics and space engines. A huge research effort (Candel, 2002; Culick & Kuentzmann, 2006; Lieuwen & Yang, 2005) has been dedicated to the investigation of coupling mechanisms and the control of unstable modes in high-performance engines (Harrje & Reardon, 1972; Culick, 1987; Yang & Anderson, 1995).

An underlying challenge in modeling combustion instabilities is the difficulty to perform full-scale experiments, or at least to carry out detailed measurements in the chamber

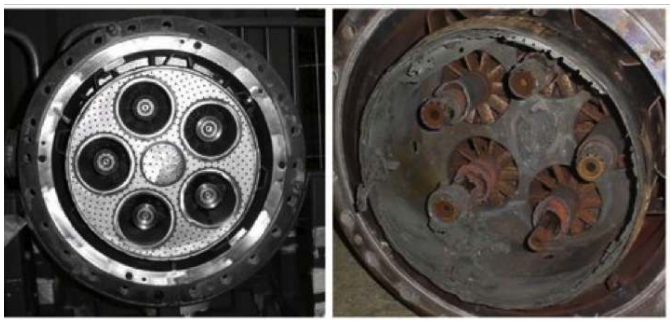

Figure 1.4: A five-burner combustion chamber before (left) and after (right) combustion instabilities.

due to the extreme conditions and the complex physics involved (Poinsot *et al.*, 1987; Lee & Santavicca, 2003; Lee & Anderson, 1999; Venkataraman *et al.*, 1999). Moreover, the necessity to perform experiments with inlet and outlet impedances matching real engine conditions make direct comparison of laboratory results and real engine data very difficult. Using simulation is therefore an attractive additional method: thanks to the increase of the computational power, numerical simulations on massively parallel computers are nowadays able to replicate the complex mechanisms involved in combustion instabilities in full-scale geometries (Wolf *et al.*, 2009; Staffelbach *et al.*, 2009; Wolf *et al.*, 2010). Low-order models and even theory on simple geometries (Dowling, 1995, 1997; Kopitz *et al.*, 2005; Evesque & Polifke, 2002) are also developed to guide LES and experiments. This is a crucial step to improve the understanding of these phenomena. Nevertheless, no industrial tool to date is able to predict instabilities at the design stage and key phenomena affecting the existence and the nature of modes are still under investigation.

1.2.2 Combustion instabilities mechanisms

Combustion instabilities are generally diagnosed when pressure oscillations (longitudinal, radial and azimuthal waves) lead to noise and potential damage (Lynch, 2011; Candel, 2002; McManus *et al.*, 1993). They may also be present in a gas turbine and have limited direct visibility even though they substantially affect the flame efficiency and the overall engine long term lifetime. These oscillations are due to a coupling effect between combustion (heat release) and acoustics (pressure or velocity field) (Brown *et al.*, 1986; Candel, 1992; Dowling & Stow, 2003).

In this coupled resonant loop, a first mechanism is the emission of sound by flames. Indeed, a fluctuation of the reaction rate of quasi-isobaric combustion acts as an unsteady local source of volume, which therefore generates sound (Strahle, 1972, 1985; Clavin & Siggia, 1991). The relation between the acoustic power P_a and the variation of volume flow rate (Searby, 2008) is (mechanism (1) in Fig. 1.5):

$$P_a = \frac{\rho_\infty}{4\pi c}\left(\frac{\rho_u}{\rho_b}-1\right)^2 < \left(\frac{d\dot{V}}{dt}\right)^2 > \quad \text{if } V \ll \lambda^3 \tag{1.1}$$

where ρ_u/ρ_b is the density ratio between cold and hot gases, c is the speed of sound and $\dot{V} = \Sigma S_f$ is the volume flow rate of the flame, which depends on the flame surface Σ

and flame speed S_f. This expression is valid only for compact sources, which assumes $V \ll \lambda^3$ where V is the volume of the source and λ is the acoustic wavelength. These heat release oscillations depend on many parameters such as geometrical features (Smith *et al.*, 2012, 2010), equivalence ratio fluctuations (Lieuwen & Zinn, 1998; Sattelmayer, 2003), flow rate modulation etc. Thus, even if methods and tools have been developed over the past few years, the understanding and prediction of such phenomena are still difficult regarding the complex physics involved.

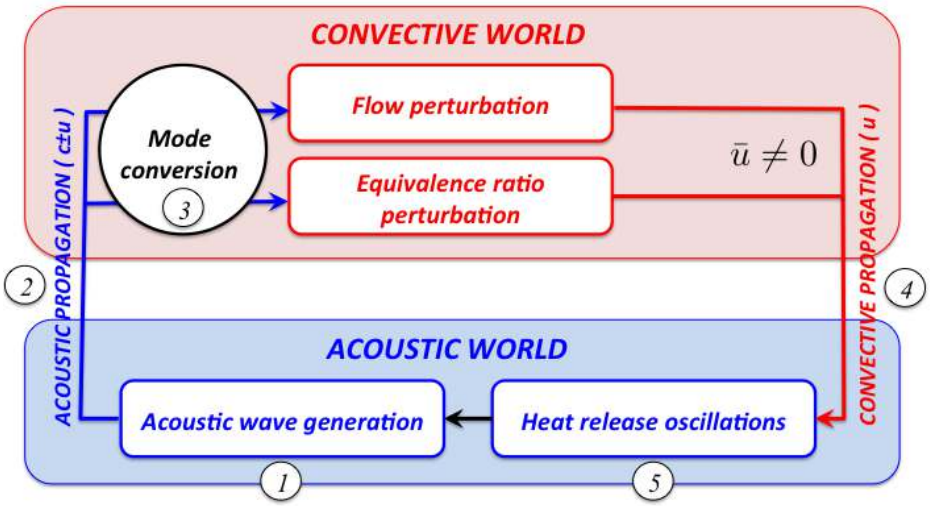

Figure 1.5: Schematic diagram of combustion instability: flow or equivalence ratio perturbations are convected by the mean flow ($\bar{u} \neq 0$), modify the flame surface and provoke heat release oscillations. The flame behaves like an acoustic monopole generating acoustic waves, which propagate at $u \pm c$. This acoustic energy propagating in the whole domain (upstream and downstream) may be converted, for example by a swirler, into a convective wave (equivalence ratio, vorticity, entropy) and a new cycle is starting.

The second mechanism involved in the generation of combustion instabilities is the sensitivity of flames to noise: as shown in Fig. 1.5, acoustic waves, generated by the unsteady combustion and propagating into the whole domain in subsonic flows (mechanism (2) in Fig. 1.5) may be converted into convective waves (vorticity, equivalence ratio or even entropy), for example by a swirler (mechanism (3) in Fig. 1.5). These waves are then convected by the mean flow ($\bar{u} \neq 0$, mechanism (4) in Fig. 1.5) and can perturb the flame and change the instantaneous rate of heat release (mechanism (5) in Fig. 1.5). The fluctuations of the heat release generating sound again, the acoustic wave might gain energy from interaction with the unsteady combustion as presented by Rayleigh et al. in 1894 (Rayleigh, 1894). If the gain is greater than the acoustic losses, the waves amplitude increases exponentially until a limit cycle controlled by non-linearities (Lieuwen & Neumeier, 2002; Krstic *et al.*, 1999) is reached or until the combustor explodes, quenches or is stopped by the operator.

The scenario of Fig 1.5 takes place in two different worlds (the convective and the acoustic worlds), where specific tools can be applied. While in the convective world, the mean flow is an essential feature (otherwise no convective propagation is possible and

reactants are frozen, which implies that no combustion may occur), it can be usually neglected in the acoustic world where the assumption $\bar{u} \pm c \simeq \pm c$ is sufficient to characterize acoustic wave propagation. In other words, while expensive DNS or LES has to be performed to capture mode conversion and flame responses in the convective world, simple tools such as Helmholtz solver or even theory can be applied to describe the acoustic world.

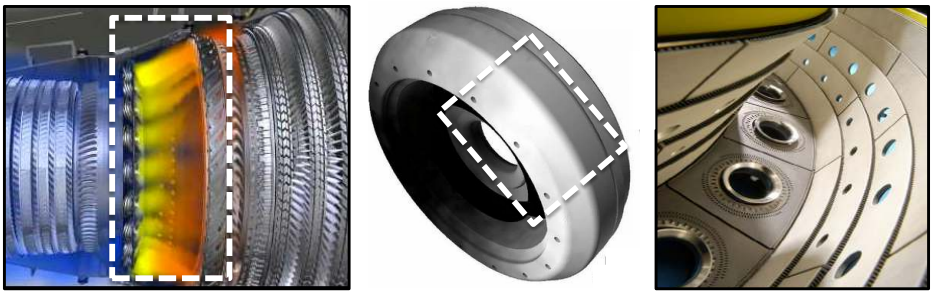

Figure 1.6: Photograph of a full engine of Pratt&Whitney (left), zoom on an annular combustion chamber from Turbomeca (middle) and details of some annular sectors of an annular combustion chamber from Rolls-Royce (right).

A very specific case where combustion instabilities raise multiple fundamental questions corresponds to the annular chambers of many gas turbines (Fig. 1.6): in these configurations, instabilities often take the form of azimuthal modes (Fig. 1.7) propagating along the azimuthal direction $\vec{e}_\theta$ and not only in the longitudinal direction $\vec{e}_z$ (Candel, 1992; Crighton *et al.*, 1992; Poinsot & Veynante, 2005; Lieuwen & Yang, 2005). Mechanisms leading to azimuthal instabilities are more complex than those encountered in longitudinal configurations. As presented in Fig. 1.8, which focuses on neighboring burners of an annular rig (Fig. 1.7, right), the azimuthal mode acts like a clock which modulates the axial mass flow rate in the burners (Fig. 1.8-a) but also creates a transverse excitation (Fig. 1.8-b), especially in burners located at a pressure node. These two mechanisms wrinkle the flame and affect its surface and position: they can promote flame-flame interaction (Fig. 1.8-c, also known as flame merging) but the effect of this interaction on thermo-acoustic instabilities is not yet fully understood (Lespinasse *et al.*, 2013; O'Connor & T.Lieuwen, 2012*c*,*b*). Note that the mechanisms presented in Fig. 1.8 assume that burners are compact with respect to the acoustic wavelength, an assumption which is usually valid for azimuthal modes in annular combustors: $\lambda \simeq 2L_c \gg a$ where λ is the azimuthal wavelength, $2L_c$ is the perimeter of the annular chamber and a is the burner diameter.

The structure of azimuthal modes has been a continuous topic of discussion since the work performed at Siemens (Krebs *et al.*, 2002), which proved that multiple modal structures could coexist in a real gas turbine: spinning, standing or even mixed, modes can appear successively and instabilities can switch from one structure to another (Schuermans *et al.*, 2006; Evesque *et al.*, 2003). Structures of spinning, standing and mixed modes are represented in Fig. 1.9. A first LES attempt to understand this peculiar phenomenon was carried out by Wolf *et al.* (2009), who showed that swirlers induce a mean azimuthal

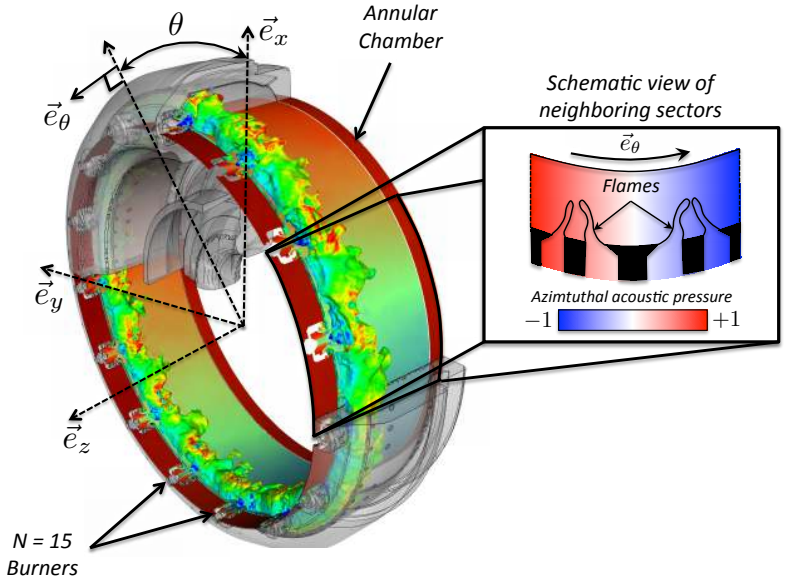

Figure 1.7: 3D view (left) and schematic view (right) of an azimuthal combustion instability (pressure fluctuations along the azimuthal direction $\vec{e}_\theta$) in an annular engine (left) and zoom on two neighboring burners (right).

velocity which can modify the flame-flame or flame-acoustic interactions and thus influence the spinning or standing modes occurrence as shown on the Dawson's experiment (Worth & Dawson, 2013*b*,*a*). Schuermans et al. have also argued in 2006 that at high pressure levels, only turning modes would survive because of non-linear effects (Schuermans *et al.*, 2006). Sensiau et al. (2008) and Noiray et al. (2011) have demonstrated that turning modes would appear only in purely axisymmetric cases, standing or mixed modes occurring otherwise (Noiray *et al.*, 2011; Sensiau, 2008; Sensiau *et al.*, 2009). However, the effect of the modes structure (standing, spinning) on the flame-acoustic interactions and therefore on instabilities is still an open question.

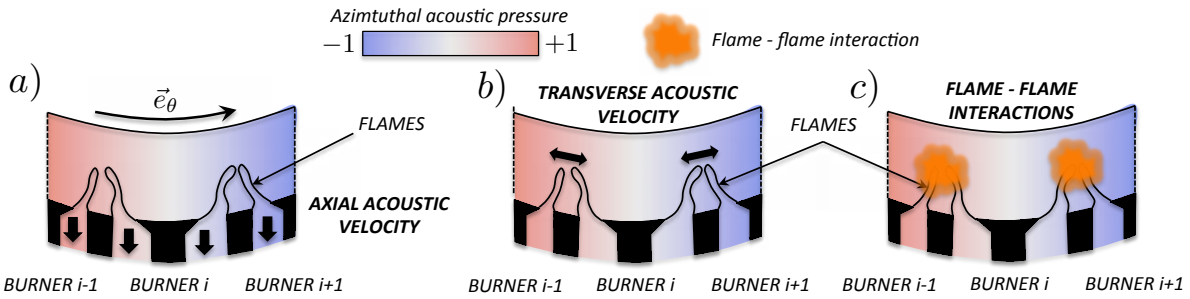

Figure 1.8: Azimuthal mechanisms driving combustion instabilities: the azimuthal mode acts like a clock modulating the axial mass flow rate in the burners (a) but also creates a transverse excitation (b). Both mechanisms can also generate flame-flame interaction (c) and its effect on thermo-acoustic instabilities is not yet understood.

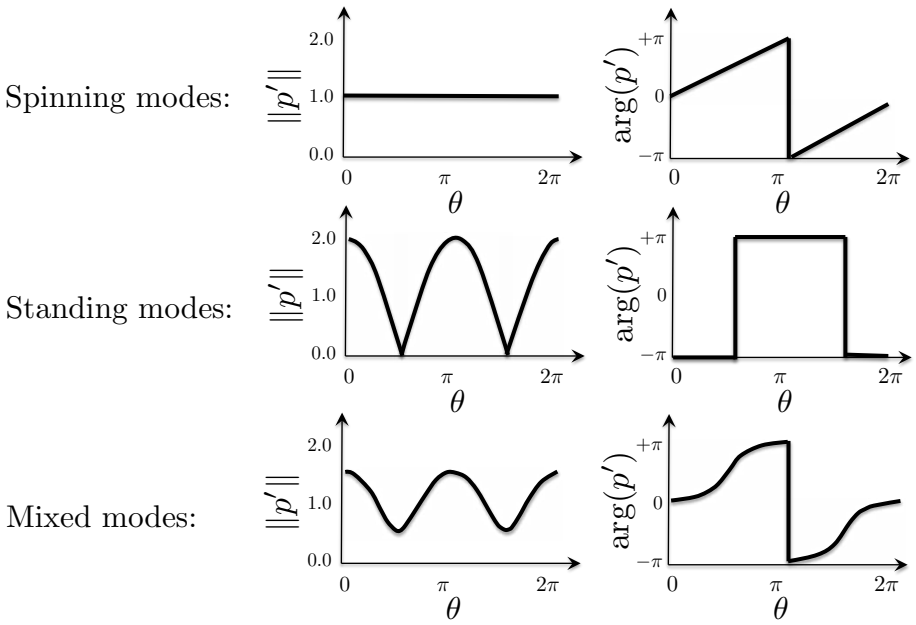

Figure 1.9: Structure of spinning (top), standing (middle) and mixed (bottom) modes (Poinsot & Veynante, 2005) determined by the modulus (left) and phase (right) of the complex pressure oscillations.

1.3 Approaches to study combustion instabilities

In order to study thermoacoustics of combustors in academic and real industrial configurations, several approaches may be found with pros and cons. This PhD thesis focuses mainly on modeling and simulations, from theoretical and analytical studies to full 360° detailed simulations on both academic (from Sections 6 to 8) and industrial configurations (not presented here for confidentiality purposes). Fig. 1.10 displays a simplified overview of methods used to predict combustion instabilities. In this thesis, all these tools will be used at different moments. Of course, experiments remain absolutely necessary but there has been only a few experimental studies in this field: the Sattelmayer group in Munich studied an annular chamber (Kopitz *et al.*, 2005) and very recently, the Cambridge (Worth & Dawson, 2013*b*,*a*) and the EM2C (Bourgouin *et al.*, 2013; Bourgouin, 2014) groups have developed new annular chambers, but the comparison between these chambers and prediction tools is only beginning. We will refer to these experiments every time this will be possible in this work.

1.3.1 Theoretical works on instabilities

On the left part of Fig. 1.10, theory is an essential element of combustion instabilities research. It is often neglected because developing theory in complex geometry systems is a challenge. Cerfacs objective was to insist on this aspect, which has been especially developed in this PhD thesis. Since the 50s, an important research effort has been performed on the underlying phenomena governing the feed-back loop and the flame-sound interaction leading to instabilities (Williams, 1985; Clavin & Joulin, 1983; Candel, 2002).

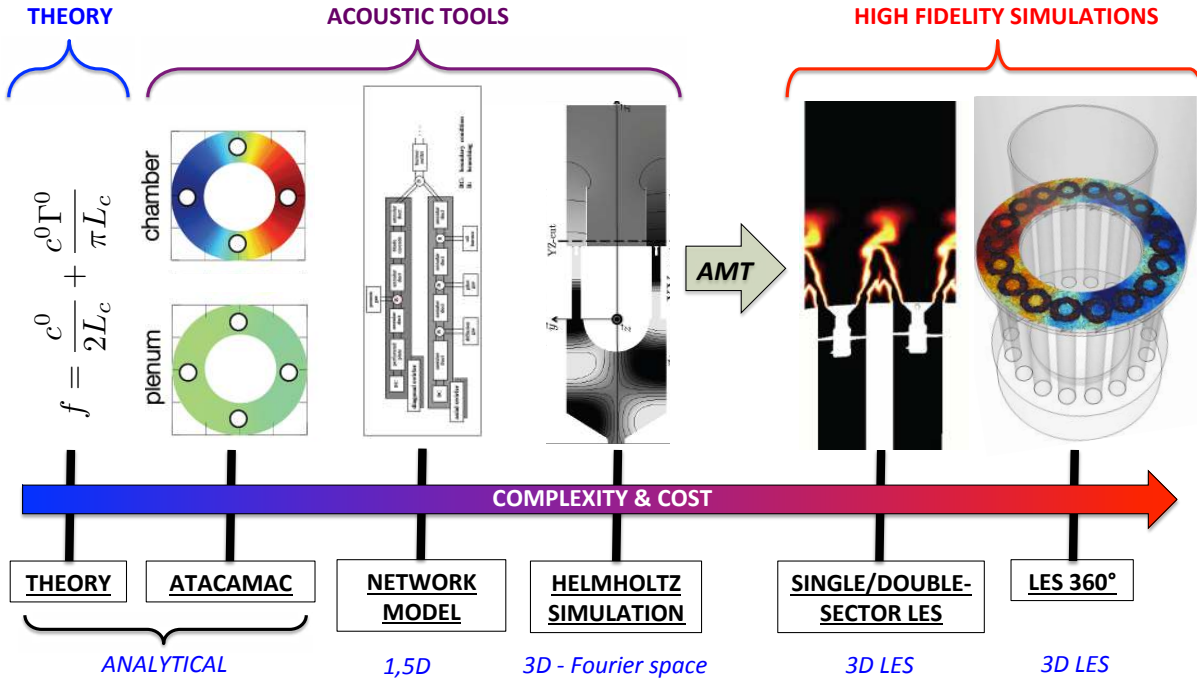

Figure 1.10: Overview of methods and tools used and/or developed in this PhD thesis to investigate and predict combustion instabilities, from cheap analytical theories to full 360° Large Eddy Simulations.

The first theoretical explanation and stability criterion for thermoacoustic combustion instabilities was provided very early by Lord Rayleigh (Rayleigh, 1894) based on the acoustic energy balance equation. Different forms of stability criteria may be obtained depending on which fluctuating energy definition is used (Chu, 1965; Nicoud & Poinsot, 2005; Brear *et al.*, 2012). In its incomplete form, at zero Mach number and for an energy based only on the acoustic pressure and velocity, the acoustic energy equation reads:

$$\frac{d\mathcal{E}}{dt} + \mathcal{F} = \mathcal{R} \tag{1.2}$$

$$\text{where } \mathcal{E} = \int_\Omega \left(\frac{1}{2}\rho_0 \langle \vec{u'^2} \rangle + \frac{1}{2}\frac{\langle p'^2 \rangle}{\rho_0 c_0^2} \right) d\Omega,\ \mathcal{F} = \int_A \langle p'\vec{u}' \rangle . \vec{n} dA \text{ and } \mathcal{R} = \int_\Omega \frac{\gamma - 1}{\gamma p_0} \langle p' \dot{\omega_T}' \rangle d\Omega$$

$\mathcal{E}$ being the acoustic energy in the domain Ω, $\mathcal{F}$ the acoustic flux through the boundary $\partial\Omega = A$ and $\mathcal{R}$ is a source term due to the fluctuating heat release produced by the flame $\dot{\omega_T}'$ coupled with the acoustic pressure field p'. $\langle . \rangle$ corresponds to the period-averaging operator. The energy $\mathcal{E}$ grows if the source term $\mathcal{R}$ dominates the acoustic flux $\mathcal{F}$, which leads to the Rayleigh criterion:

$$\int_\Omega \frac{\gamma - 1}{\gamma p_0} \langle p' \dot{\omega_T}' \rangle d\Omega > \int_A \langle p'\vec{u}' \rangle . \vec{n} dA \tag{1.3}$$

This criterion reveals that flame-acoustic interactions and acoustic damping included in the source $\mathcal{R}$ and flux $\mathcal{F}$ terms are crucial elements to understand and predict combustion instabilities:

- **Flame-acoustic interactions:** The source term $\mathcal{R}$ depends on the coupling between the pressure p' and the heat release $\dot{\omega_T}' = -(Q\dot{\omega_F})'$ produced by the flame. In flamelet theories, the unsteady reaction rate $\dot{\omega_F}'$ can be expressed as $\dot{\omega_F}' = \rho_0(s_c'\Sigma_0 + s_{c,0}\Sigma')$ where s_c is the consumption speed and Σ is the flame surface. Moreover, $Q' = \phi'\Delta H$ (in the lean regime, i.e. when $\bar{\phi} < 1$) where ϕ' is the equivalence ratio fluctuation and ΔH is the enthalpy at the stoichiometric condition. Therefore, acoustic waves can influence a flame through three effects:
  1. Modifications of the consumption speed s_c': this effect is mainly controlled by chemical kinetics, where pressure increases lead to density increases and therefore change the reaction rate (McIntosh, 1993; Jiménez *et al.*, 2012). However, this mechanism can dominate in spray flames where acoustics can affect the evaporation process and modulates the fuel flux at the flame front (Saito *et al.*, 1996; Clanet *et al.*, 1999).
  2. Modifications of the flame surface Σ', mostly because of large vortical structures wrinkling the flame front (Poinsot *et al.*, 1987; Candel *et al.*, 2014).
  3. Equivalence ratio fluctuations ϕ': this effect is mainly governed by the modulation of the air and fuel mass flow rates by acoustic waves leading to oscillations of the local equivalence ratio. Vortex shedding induced by acoustics could also modify mixing and therefore can affect the local air/fuel distribution.

  In real combustors (except in solid rocket boosters), the second effect is the most important and has been studied analytically for simple academic premixed planar, conical and V-flames by (Lieuwen, 2001; Schuller *et al.*, 2003) and more recently by (Cuquel *et al.*, 2011; Blumenthal *et al.*, 2013). For more complex configurations, flame-acoustic coupling is usually modeled using a Flame Transfer Function (FTF) based on the time-delay model (the so-called n-tau model) established by Crocco (1969) or its non-linear version called Flame Describing Function (FDF) proposed by Noiray *et al.* (2008). These transfer functions have to be characterized thanks to experiments or LES simulations because theoretical approaches cannot be used for most industrial cases equipped with swirlers. Indeed, Palies (2010); Palies *et al.* (2011) have shown that the unsteady flame dynamics and the swirl motion can interact constructively or destructively, leading to a different flame response to acoustics. Other swirl perturbations, such as helicoidal modes induced by a Precessing Vortex Core (PVC) can yield similar effects as shown by Moeck *et al.* (2012); Acharya & Lieuwen (2013) and reviewed by Candel *et al.* (2014). Nevertheless, these numerical flame models are available only for a few operating points, while the stability of engines has to be checked on all operating points. Analytical scaling methods (Kopitz *et al.*, 2005) can however provide the FTF for an operating point thanks to an already known FTF on an other operating point reducing the number of FTF needed for a complete study of industrial configuration stability. The work presented in this thesis focuses only on the linear regime, nevertheless a study of non-linear regimes using FDF's have been also explored using ATACAMAC and is briefly described in the Appendix C since it can lead to symmetry breaking as well (Ghirardo *et al.*, 2015).

- **Acoustic damping:** The flux term $\mathcal{F}$ in Eq. (1.2) is due to acoustic losses at boundaries. While simple impedances Z ($Z = 0$ corresponding to a pressure node or $Z = \infty$ for a velocity node) are usually a good first-order approximation of boundary conditions, they do not include acoustic damping (since $\langle p'\vec{u}'\rangle.\vec{n} = 0$ on the boundary) leading to approximate stability criterion. To correctly predict growth rates, much more precise conditions must be derived to provide acoustic reflection coefficients for subsonic and choked nozzles (Marble & Candel, 1977; Duran & Moreau, 2013). This requires taking into account the mean flow terms which make the formulation much more complex (Selle *et al.*, 2004*b*; Nicoud & Wieczorek, 2009; Motheau *et al.*, 2012). Specific efforts have also been applied on effusive plates, used for thermal cooling, that can generate efficient acoustic damping and act like passive control systems under certain conditions (Howe, 1979, 1997; Tran *et al.*, 2009; Mendez & Eldredge, 2009; Motheau *et al.*, 2012). However, more work on damping is needed to fully characterize combustion instabilities in real applications. This PhD thesis will propose in Section 9 a methodology to tackle this problem numerically.

Since flame-acoustic interactions and damping mechanisms depend on the acoustic pressure and velocity fields, theoretical approaches have also been developed to predict acoustic modes in simplified configurations and therefore to obtain the growth rates and stability of the system. Simple longitudinal configurations were intensively studied in both the linear (Schuller *et al.*, 2012; Mejia *et al.*, 2014) and non-linear regimes (Dowling, 1995; Stow & Dowling, 2004; Noiray *et al.*, 2008). Complex annular configurations were investigated analytically or quasi-analytically only recently, mainly based on acoustic network representations (Stow & Dowling, 2001; Evesque & Polifke, 2002; Moeck *et al.*, 2010).

The first part of this thesis will introduce an analytical theory based on the Annular Network Reduction (ANR) approach to compute analytically frequencies in a simplified annular combustor. This tool, called ATACAMAC (Analytical Tool to Analyze and Control Azimuthal Modes in Annular Combustors), allows to extract key parameters (effects of mean flow (Bauerheim *et al.*, 2014*a*), coupling between cavities (Bauerheim *et al.*, 2014*d*), input uncertainties (Bauerheim *et al.*, 2014*b*) as well as symmetry breaking (Bauerheim *et al.*, 2014*a*,*e*)) controlling instabilities in such a configuration. Being able to exhibit fully analytical expressions of the parameters controlling instabilities in an annular combustor is one of the main results of this PhD (Chapters 2 and 3).

1.3.2 Low-order modeling and Helmholtz solvers

A classical method to predict combustion instabilities is to use a network with acoustic elements leading to a simplified problem that can be solved analytically or numerically (Poinsot & Veynante, 2005; Stow & Dowling, 2001; Polifke *et al.*, 2001*a*; Krebs *et al.*, 2002; Krüger *et al.*, 2000, 1999; Lepers *et al.*, 2005). This approach makes predesign possible when only the first longitudinal or orthoradial modes are sought for. More recently, a semi-analytical approach using quasi-one dimensional network on annular configuration (one ring (Parmentier *et al.*, 2012)) has been extended to two rings configuration

or even 2D networks on the ATACAMAC tool (Analytical Tool to Analyse and Control Azimuthal Modes in Annular Chamber) (Bauerheim *et al.*, 2014*a*,*d*,*e*). This kind of tool is a first interesting step for pre-design industrial tools which capture azimuthal as well as longitudinal modes. Such an approach also provides key results on passive control techniques and mechanisms affecting the mode nature.

For more complex configurations, where 1D formulations do not hold, 3D Helmholtz tools can solve the Helmholtz equation at reduced cost in the frequency domain (Fig. 1.10, middle):

$$\nabla.\left(\frac{1}{\rho_0}\nabla\hat{p}\right) - \frac{\omega^2}{\gamma p_0}\hat{p} = j\omega\frac{\gamma-1}{\gamma p_0}\hat{q}(\mathbf{x}) \tag{1.4}$$

where ρ_0 and γ depend on the space variable $\mathbf{x}$ and the unknown quantities are the complex amplitude $\hat{p}(\mathbf{x})$ of the pressure oscillations and the complex frequency ω (Nicoud *et al.*, 2007). Acoustic flame coupling, acoustic damping (e.g. effusive plates), or realistic impedance effects on the mode structure and growth rate can therefore be numerically obtained. Rotating transverse modes were studied in a single-burner configuration using both LES and a Helmholtz solver by Selle *et al.* (2006). Evesque et al. applied a similar acoustic tool to study spinning and standing modes in a simplified multiple-burner annular combustor (Evesque & Polifke, 2002), which complement time-domain studies (Pankiewitz & Sattelmayer, 2003) where non-linear flame behaviors can be easily introduced, the difficulty being the description of complex impedances in a time-formulation. Combining non-linear Flame Describing Functions (FDF) and frequency-domain acoustic tool was proposed recently by Silva *et al.* (2013). Finally, Campa *et al.* (2011) applied a Helmholtz solver on a gas turbine with multiple annular cavities highlighting the strong effect of coupling between cavities on the results. Nevertheless, low-order modeling and acoustic tools suffer from multiple assumptions such as linearity, null mean flow or FTF depending only on the axial velocity fluctuations. A novel approach called AMT (Acoustic Mode Triggering) is therefore presented in Chapter 9 to relax these assumptions by combining both time and frequency domain computations. In AMT, a mode obtained by a Helmholtz solver is added to an LES solution to see how this mode really behaves when the assumption used in the Helmholtz solver are relaxed as can be done in LES or DNS.

1.3.3 LES approach for combustion instabilities

Low-order modeling techniques are fast and efficient to predict instabilities in real or simplified configurations if FTFs are known. However, the main convective and reacting phenomena are by-passed and hidden in the FTF. Thus network models or acoustic tools are not sufficient to understand and control the whole combustion instability process. An alternative solution is to go to more detailed simulations (Fig. 1.10, right), for instance using the Large Eddy Simulation approach (Chapter 6). LES is the main tool today to perform unsteady turbulent numerical computations. This computational method is based on the Kolmogorov's theory proposed in 1941 (Kolmogorov, 1941) and then widely improved for non-reactive flows (Smagorinsky, 1963; You & Moin, 2007*a*,*b*; Nicoud &

Ducros, 1999; Moin, 2002; Piomelli *et al.*, 1988) and in the last ten years for reacting flows (Jones & Whitelaw, 1982; Riber *et al.*, 2006; Pitsch, 2006; Poinsot & Veynante, 2011; Schmitt *et al.*, 2007; Janicka & Sadiki, 2004). By spatially low-pass filtering the Navier-Stokes equations, the LES approach models small scales of the solution and consequently reduces the computational cost of the simulations compared to full-scale simulations known as DNS (Direct Numerical Simulation). Multiple recent papers have demonstrated that LES is well-suited for the study of turbulent flames despite its high computational cost (Colin *et al.*, 1999; Pitsch, 2006; Riber *et al.*, 2006; Forkel & Janicka, 2000; Branley & Jones, 2001; Domingo *et al.*, 2002; Schmitt *et al.*, 2007).

Recently, this tool has been applied to azimuthal instabilities studies in a complex industrial annular chamber (Wolf *et al.*, 2009, 2010; Staffelbach *et al.*, 2009) using the compressible LES solver AVBP (Fig. 1.11) for a full ring computation of azimuthal instabilities in an helicopter engine. This important breakthrough showed that LES could capture self-excited azimuthal instabilities in annular chambers. Even though this was an exciting result, one of the main drawbacks of such an approach is obviously its extreme cost but also the heavy post-processing treatments. Indeed, LES simulations being highly turbulent, fluctuations quantities have both an acoustic and a turbulent part that might be difficult to discriminate. Mathematical methods based on POD (Proper Orthogonal Decomposition - firstly proposed by Lumley in 1967 (Lumley, 1967) and then used in CFD simulations at CERFACS (Wolf *et al.*, 2010; Roux *et al.*, 2007)) or CBF (Characteristic-Based filter) (J. Kopitz, 2005) have been applied successfully in order to extract the acoustic field from a turbulent unsteady field.

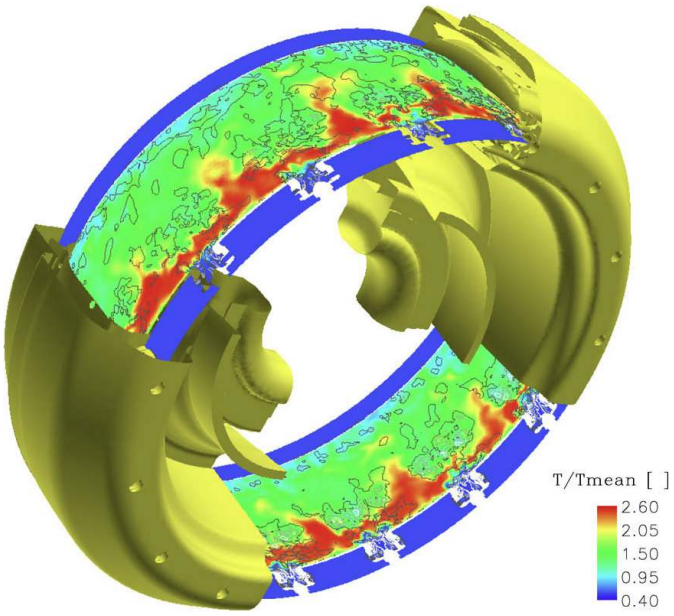

Figure 1.11: Full ring LES simulation performed by Wolf *et al.* (2012)

LES is therefore a promising tool to understand and control azimuthal modes in annular combustors. In this PhD work, this approach has been applied in this thesis on the academic annular experiment of Cambridge (Worth & Dawson, 2013*b*,*a*). First, forced

single-sector LES are combined with annular Helmholtz simulations to compute FTF and stability of the 360° system with respect to several parameters and models (Chapter 7). Comparison of these numerical results with experimental observations have proved that this hybrid method is able to predict the flame-acoustic interaction and stability of a real annular chamber despite its sensitivity to many features: mesh quality, description of boundary conditions making the acoustic waves treatment possible (Poinsot *et al.*, 1992), chemistry schemes and wall treatments and temperature (Tay-Wo-Chong & Polifke, 2012; Poinsot, 1987; Duchaine *et al.*, 2011; Mejia *et al.*, 2014; Bauerheim *et al.*, 2014*c*). From this analysis, a specific operating point is chosen to compute self-excited azimuthal modes in the complete 360° configuration (Chapter 8).

1.4 Azimuthal thermo-acoustic modes

1.4.1 Azimuthal vs. longitudinal modes

This overview on combustion instabilities and application to azimuthal modes reveals that important efforts on numerous topics have been developed since the early 50s but that azimuthal modes constitute a specific class of problem which has been less studied and raises new problems. For example, a simple comparison between longitudinal and azimuthal modes raises useful questions on the specificities of unstable modes encountered in annular configurations. To illustrate why instabilities in annular chambers need special investigations, this section briefly compares longitudinal modes in a straight duct (Fig. 1.12-a) and azimuthal modes in an annular combustor (Fig. 1.12-b). In the one-dimensional configuration of Fig. 1.12 (a, left), both propagating and standing waves can appear. Propagating waves ($q^{\pm} = p' \pm \bar{\rho}\bar{c}u'$) travel in opposite directions with phase variation along the longitudinal axis: $q^{\pm}(x + \Delta x) = q^{\pm}(x)e^{\pm jk\Delta x}$, where $k = \omega/\bar{c}$. With the boundary conditions of Fig. 1.12 (a, left), the local values of q^+ and q^- can be written:

$$\begin{cases} \begin{pmatrix} q^+ \\ q- \end{pmatrix}_{x=L} = \begin{bmatrix} e^{jkL} & 0 \\ 0 & e^{-jkL} \end{bmatrix} \begin{pmatrix} q^+ \\ q- \end{pmatrix}_{x=0} \\ q_0^+/q_0^- = -1 \quad \text{and} \quad q_L^+/q_L^- = +1 \end{cases} \tag{1.5}$$

Consequently, the key feature controlling the acoustic mode in a longitudinal configuration is the boundary conditions (here $u' = 0$ at $x = 0$ and $p' = 0$ at $x = L$). The system defined in Eq. (1.5) contains two boundary conditions which couple the first and second line of the matrix equation and thus impose both frequency and structure of all acoustic modes. The system becomes one-dimensional and only one solution per mode exists: for example, a quarter-wave standing mode ($\lambda = 4L$) at the frequency $f = c/4L$ for the first mode.

An annular configuration (Fig. 1.12-b) also features one-dimensional acoustic waves. However, in that case, the boundary condition is very different. As shown in Fig. 1.12-b, the condition does not fix a specific value of the ratio q^+/q^- but imposes axi-periodicity, i.e. $q^+(\theta_0^-) = q^+(\theta_0^+)$: the boundary does not couple q^+ and q^- as it does for longitudinal

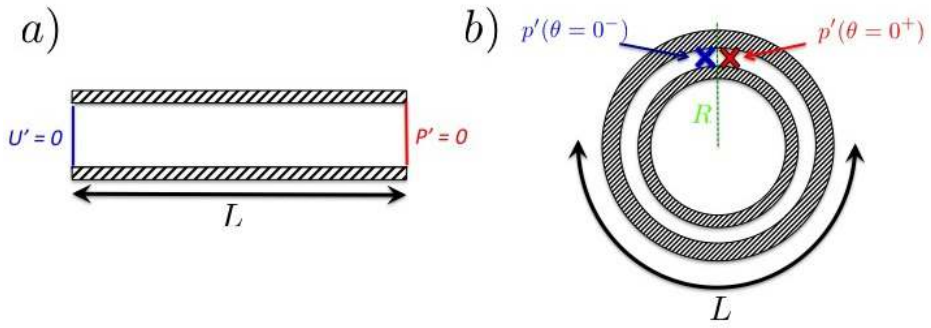

Figure 1.12: Typical longitudinal (a, left) and annular (b, right) configurations with boundary conditions ($u' = 0$ and $p' = 0$ or periodicity) and characteristic length scale L.

configurations. The formulation of the system is:

$$\begin{cases} \begin{pmatrix} q^+ \\ q- \end{pmatrix}_{\theta_0^-} = \begin{bmatrix} e^{jk^+L} & 0 \\ 0 & e^{-jk^-L} \end{bmatrix} \begin{pmatrix} q^+ \\ q- \end{pmatrix}_{\theta_0^+} \\ q^+_{0-} = q^+_{0+} \quad \text{and} \quad q^-_{0-} = q^-_{0+} \end{cases} \Rightarrow \underbrace{\begin{bmatrix} e^{jk^+L} - 1 & 0 \\ 0 & e^{-jk^-L} - 1 \end{bmatrix}}_{M} \begin{pmatrix} q^+ \\ q- \end{pmatrix} = \begin{pmatrix} 0 \\ 0 \end{pmatrix} \tag{1.6}$$

This formulation shows that periodicity conditions in perfect symmetric cases are weaker because only imposing the frequency but not the mode structure anymore: imposing $q^+_{0-} = q^+_{0+}$ is equivalent to $q^-_{0-} = q^-_{0+}$ in symmetric configuration since q^+ and q^- have a similar behavior. Thus, when the problem is **axi-symmetric**, the matrix of the system M is hermitian[2], i.e. $M = \begin{bmatrix} a & 0 \\ 0 & a^* \end{bmatrix}$ imposing here $k^+ = k^- = k$, and the clockwise q^+ and counter-clockwise q^- waves are both solutions of the problem with the same frequency: $f^\pm = \bar{c}/2L$. Since the problem is **linear**, any combination of these two waves is also a solution and therefore propagating, standing or mixed modes can be generated: the mode is degenerate. However, if axi-symmetry is broken leading for example to $k^\pm = k_0 \pm \delta k$, then the two equations of (1.6) are different, which yields two modes with different frequencies and a fixed structure: here two spinning modes at frequencies $f^\pm = \frac{\bar{c}}{2L} \pm \frac{\bar{c}\delta k}{2\pi}$.

In this PhD, two different symmetry breaking called geometrical (GS) and flow (FS) symmetry breaking are investigated, leading to different natures of the matrix M and therefore different mode structures:

- **FS breaking:** The clockwise and counter-clockwise waves are still decoupled but have different propagation properties ($k^+ \neq k^-$), leading to:

$$M = \begin{bmatrix} a & 0 \\ 0 & \mathbf{b}^* \end{bmatrix} \text{ with } a \neq b \tag{1.7}$$

[2]A matrix M is called hermitan if $(M^*)^t = M$ where $*$ is the conjugate operator and t the transpose operator.

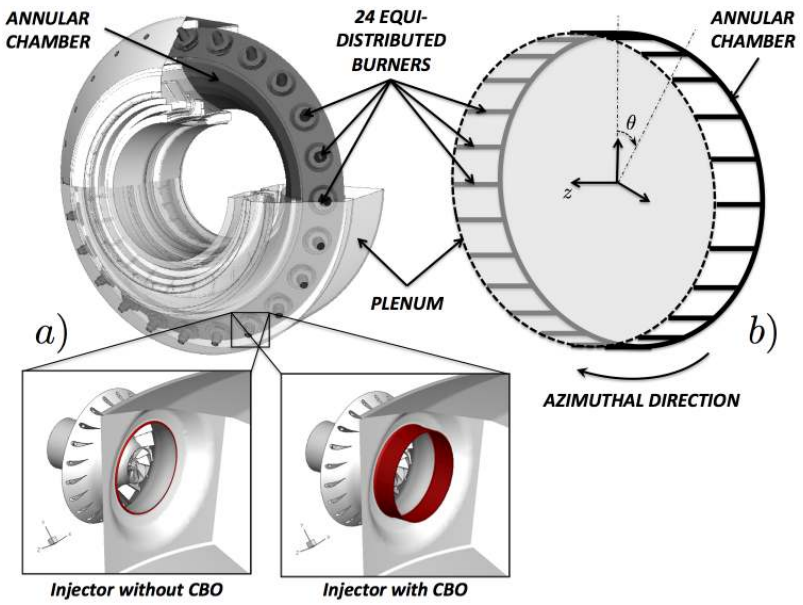

Figure 1.13: a) A typical 3D configuration of an industrial annular combustion chamber equipped with $N = 24$ burners with or without CBO and b) Network model of the annular chamber (——) with $N = 24$ burners. The annular plenum (- - -) is removed for the sake of simplicity.

where $*$ corresponds to the conjugate operator. FS breaking is obtained for example when a mean azimuthal flow exists, leading to different speed values $(\bar{u} \pm \bar{c})$ for the azimuthal waves.

- **GS breaking:** The clockwise and counter-clockwise waves are coupled through an interaction mechanism characterized by a parameter Γ (detailed in Chapter 2), leading to:

$$M = \begin{bmatrix} a & 0 \\ 0 & a^* \end{bmatrix} \begin{bmatrix} 1 & 0 \\ \Gamma & 1 \end{bmatrix} = \begin{bmatrix} a & 0 \\ \mathbf{\Gamma a}^* & a^* \end{bmatrix} \text{ with } \Gamma \neq 0 \tag{1.8}$$

GS breaking is obtained for example when the geometrical symmetry is broken by introducing baffles, Helmholtz resonators or different types of burners in the azimuthal direction.

As a conclusion, the mode structures observed in annular configurations are the results of two ingredients: the linearity of the system and its axi-periodicity. In other words, the mode structure is fixed by either non-linearities or by breaking the axi-periodicity of the configuration. Non-linear effects have already been studied by Noiray *et al.* (2011); Noiray & Schuermans (2013) and therefore this thesis will focus on both geometrical (GS) and flow (FS) symmetry breaking in annular combustors, a crucial element not yet explored in details for such a system.

1.4.2 Symmetry breaking in annular gas turbines

Recently, symmetry breaking has been investigated in complex annular gas turbines (figure 1.13) (Noiray *et al.*, 2011; Parmentier *et al.*, 2012) which exhibit azimuthal acoustic

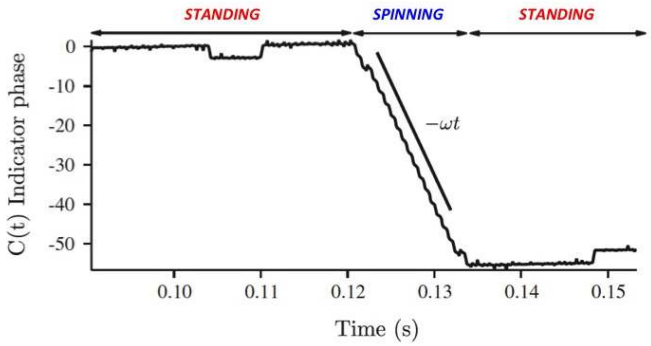

Figure 1.14: Nature of the azimuthal mode observed in (Wolf *et al.*, 2012). The nature is determined by the C-indicator phase (Appendix I): constant for a standing mode and proportional to ωt for a spinning mode.

waves produced by thermo-acoustic instabilities (O'Connor & T.Lieuwen, 2012*c*). In real engines, usually, identical burners (at least within manufacturing tolerances) are distributed regularly along the azimuthal direction (figure 1.13). Therefore, perfectly axisymmetric configurations have been intensively investigated using theoretical (Parmentier *et al.*, 2012; Bauerheim *et al.*, 2014*d*; Stow & Dowling, 2001; Pankiewitz & Sattelmayer, 2003; Stow & Dowling, 2003), acoustic and LES tools (Evesque & Polifke, 2002; Kopitz *et al.*, 2005; Staffelbach *et al.*, 2009; Wolf *et al.*, 2012) and more rarely experiments (Krebs *et al.*, 2002; Worth & Dawson, 2013*b*,*a*; Bourgouin *et al.*, 2013). Annular chambers exhibit specific azimuthal modes, which can be standing or spinning in the azimuthal direction (Fig. 1.9) (Evesque *et al.*, 2003; Sensiau *et al.*, 2009). Azimuthal modes are often "degenerate": two modes are found at the same frequency (two counter-rotating spinning modes for example). These two modes can combine and switch, leading to combustors which exhibit standing, spinning or mixed modes for various times, changing from one mode to another one at random instants as observed in LES (Fig. 1.14) (Wolf *et al.*, 2012), laboratory setups (Worth & Dawson, 2013*b*; Bourgouin *et al.*, 2013) and even in real gas turbines (Krebs *et al.*, 2002). Mode switching has been postulated to be due to random turbulent fluctuations (Noiray & Schuermans, 2013). However, azimuthal modes are not necessarily degenerate leading to a more complicated situation where the configuration is strongly affected by symmetry modifications, as shown by studies of sound produced by bells (Perrin & Charnley, 1973) where non-degenerate but very close azimuthal modes (also called "non-degenerate singlets") lead to "warble", an undesired low-frequency modulation due to the coupling of two modes with different but very close frequencies.

The effect of asymmetry on the eigenfrequencies and nature of azimuthal modes in annular chambers is still an open question and is the focus of this thesis. Earlier work has focused on symmetry breaking using baffles to prevent combustion instabilities in the F-1 rocket engines (reviewed by (Oefelein & Yang, 1993)). They suggested that asymmetry can be introduced to control unstable modes using passive techniques. Stow & Dowling (Stow & Dowling, 2003) applied azimuthal variations using Helmholtz resonators on an annular academical test bench. Similarly, (Berenbrink & Hoffmann, 2001) and

(Krüger *et al.*, 2000) (reviewed by (Culick & Kuentzmann, 2006)) broke the symmetry of an annular engine by using CBOs (Cylindrical Burner Outlet, figure 1.13-a, bottom) to modify the time-delay τ_i of some of the 24 flames and control instabilities in a $N = 24$ burners industrial combustor. They varied the number of CBOs installed among the 24 burners showing that adding CBOs improved stability. However, it was not clear wether the stabilization was due to the CBO devices rather than, as argued by the authors, to symmetry breaking in this particular case. Lately, Moeck *et al.* (2010); Gelbert *et al.* (2012) carried out an annular Rijke experiment with heating grids acting like flames. They introduced circumferential variations through asymmetric power distributions of the grids to modify azimuthal modes and noticed that the staging pattern can split degenerate azimuthal modes (doublets) into non-degenerate pairs (singlets) as suggested in (Perrin & Charnley, 1973) for bells.

A few theories consider the effect of asymmetry on the existence and nature of azimuthal modes (standing, spinning or mixed): Schuermans *et al.* (2006) suggest that standing modes are observed for low amplitudes but that, at higher amplitudes, one of the two rotating modes eventually dominates. However, Sensiau *et al.* (2009) have shown that even in the linear regime, any change in symmetry can lead to the appearance of one rotating mode dominating the other one: when the symmetry of the configuration is broken, the standing azimuthal mode is changed into two counter-rotating azimuthal modes with different growth rates so that one of them eventually dominates the other, at least in the linear phase. Noiray *et al.* (2011) have proved that the $2p^{th}$ Fourier coefficient of the heat release, temperature or even acoustic losses azimuthal distribution (where p is the order of the azimuthal mode considered) strongly impacts the frequency as well as the mode nature on an annular rig. Worth & Dawson (2013*b*,*a*) have also shown that the modes nature can result from the interaction with the mean flow by breaking symmetry thanks to clockwise/anti-clockwise swirlers: they observed a strong correlation between the bulk swirl direction and the direction of spin. They have then broken the rotating symmetry with baffles distributed along the azimuthal direction with a specific pattern. In that case, standing modes were dominant. Finally, two different classes of symmetry breaking have be studied, as mentioned in Eqs. 1.7 and 1.8:

- **Geometrical symmetry breaking:** The design of the annular combustor can be modified with a non-axisymmetric pattern of burners, for instance by using baffles or different flames, which can be done using a Cylindrical Burner Outlet (CBO) on some of the burners to modify the time-delay τ of the Flame Transfer Function. Experimentally, this kind of symmetry breaking seems to promote standing modes (Fig. 1.15) but the effect of the flame distribution and the asymmetry pattern on the mode structure as well as the stability of the configuration is still an open question. Geometrical symmetry breaking can also result from manufacturing tolerances, which lead to uncertainties and possible asymmetries in the system. For instance, Fig. 1.17 shows a DMD analysis of the heat release produced in an academic annular combustor installed at EM2C where three flames (black arrows) are out-of-phase (out of the sixteen burners of the combustor). This phenomenon clearly breaks the rotation symmetry of the configuration and might modify its stability.
- **Flow symmetry breaking:** Even if the geometry of the chamber is perfectly

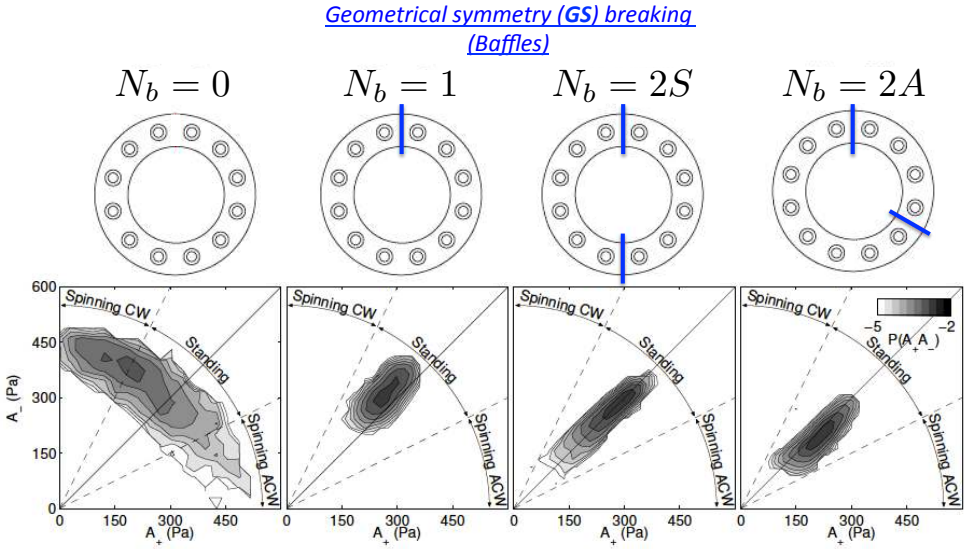

Figure 1.15: Geometrical symmetry (GS) breaking studied by Dawson & Worth (2014): the rotation symmetry is broken by N_b baffles distributed in the azimuthal direction with a specific pattern. Standing modes are promoted when GS breaking occurs. These diagrams present scatter plots of the two spinning mode amplitudes (clockwise and counter-clockwise, A^- and A^+ respectively).

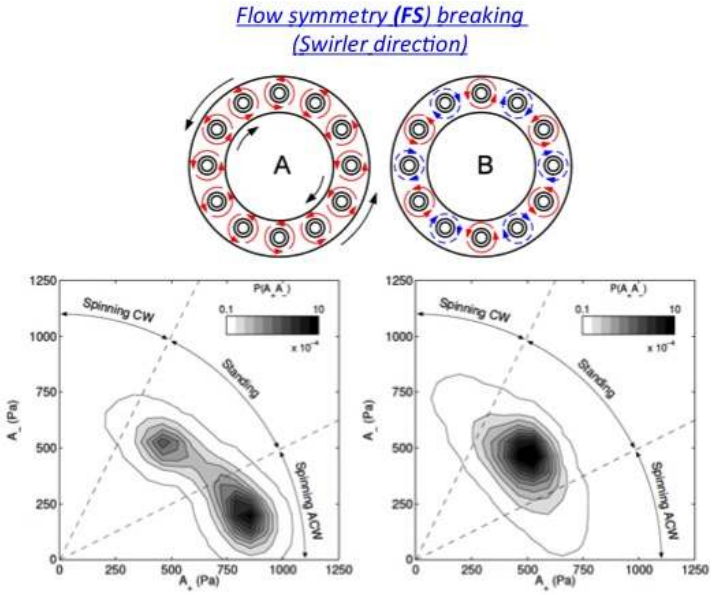

Figure 1.16: Flow symmetry (FS) breaking studied by Worth & Dawson (2013*b*): the rotation symmetry is broken by a mean azimuthal flow motion induced by swirlers (left, swirlers with the same direction). When swirlers directions are alternate (right), the mean azimuthal flow is absent leading to no symmetry breaking.

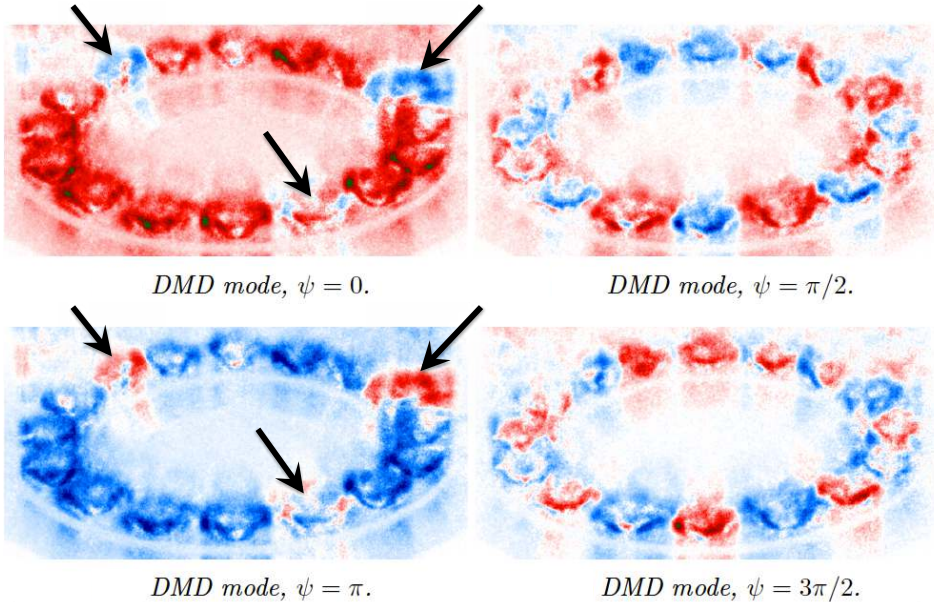

Figure 1.17: DMD analysis of the heat release produced by flames in an academic annular combustor (Bourgouin *et al.*, 2013). It shows that three of the flames (black arrows) are out-of-phase ($\psi = 0$ or π), which may denote an unwanted symmetry breaking.

axisymmetric, the mean flow itself can have a non-symmetric component which affects the azimuthal acoustic mode (via the sound speed for instance). This flow asymmetry can be generated by the compressor or diffuser outlet, swirlers or even effusive plates used in modern gas turbines to increase residential time and therefore improve mixing. Worth & Dawson (2013*a*) observed a strong correlation between the bulk swirl direction and the direction of spin of the azimuthal mode (Fig. 1.16). However, Worth & Dawson (2013*a*) have found that this correlation may depend on the number of burners introduced in the annular rig (i.e. the azimuthal confinement), which complexifies the situation. Until now, no theoretical background or numerical simulations can clarify this point and describe the effect of the mean azimuthal flow on the acoustic mode nature and growth rate.

1.5 PhD objectives and outline

The goal of this PhD thesis is to investigate the effects of symmetry breaking on the frequencies as well as the structures of azimuthal modes encountered in annular combustors. The two different methods to break symmetry (1 - Flow symmetry breaking (FS), when the flow itself breaks the rotation symmetry of the annular combustor and 2 - Geometrical symmetry (GS) breaking induced by the design, intended or not, of the combustion chamber) will be studied using a wide range of tools. These tools will be either existing codes (LES and Helmholtz solvers) or new approaches specifically developed for this PhD (ATACAMAC, AMT, Active Subspace), as shown in Fig. 1.19.

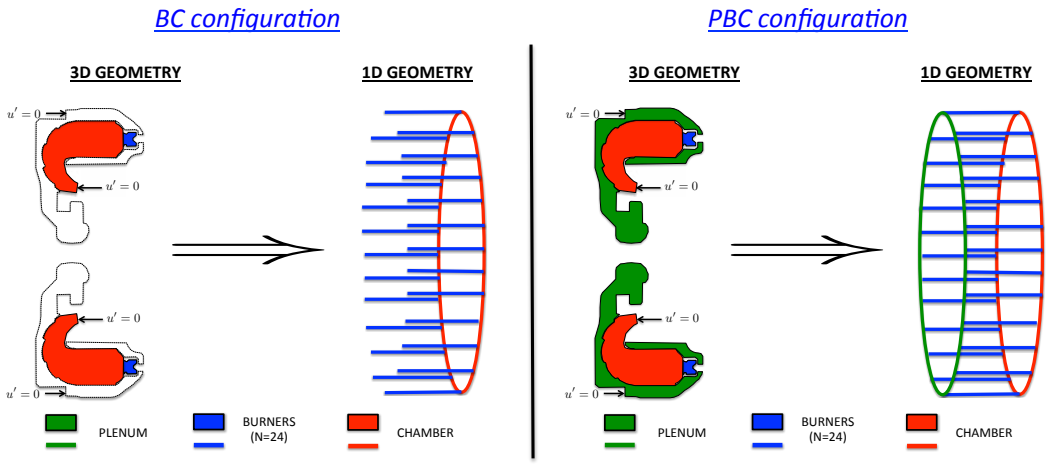

Figure 1.18: Transverse cut of an annular gas turbine and its associated network model. On the left, the configuration is reduced to an annular chamber connected to N burners, called BC configuration. On the right, the configuration is called PBC and the annular plenum is retained to study coupling mechanisms between the two annular cavities.

PART I - First, a theoretical framework is developed to produce analytical expressions for the nature and growth rate of modes in a BC (Burners+Chamber) configuration (Fig. 1.18, left) where an annular chamber connects N burners. Based on this framework, two mechanisms called GS (Chapter 2) and FS (Chapter 3) symmetry breaking are investigated. This analytical study is performed using the ATACAMAC tool (Analytical Tool to Analyze and Control Azimuthal Mode in Annular Chamber) and a reduced approach called ANR (Annular Network Reduction) introduced initially by Parmentier *et al.* (2012). It shows that both symmetry breaking methods split the degenerate mode into two distinct modes with different natures. Moreover, this splitting is always accompanied by the destabilization of the flames which can promote combustion instabilities. This analytical tool is then extended in Chapter 4 to more realistic configurations, called PBC (Plenum+Burners+Chamber), where the annular chamber is fed by N burners connected to an annular plenum (Fig. 1.18, right). This configuration corresponds more closely to real engines where burners are fed from the same annular plenum, adding one possible resonant cavity to the sitem compareed to BC cases. The coupling between the two annular cavities can modify the acoustic in the system and therefore its stability. A UQ (Uncertainty Quantification) approach is finally constructed in Chapter 5 on ATACAMAC to evaluate the effect of symmetry breaking in PBC configurations due to uncertainties on acoustic-flame interactions (i.e. in Flame Transfer Functions) showing that undesired symmetry breaking can result from manufacturing uncertainties and then affect the stability of a gas turbine: the control of uncertainties in a real gas turbines is required to predict stability with precision.

PART II - To complement the theoretical results of Part I, Large Eddy Simulations, presented in Chapter 6, are performed on the academic annular combustor of Cambridge (Worth & Dawson, 2013*b*,*a*). First, a sensitivity analysis based on single-sector computations (Chapter 7) shows which physical parameters affect the Flame Transfer

Function and therefore the growth of rate of the configuration, predicted by Helmholtz simulations of the whole annular combustor. This study also demonstrates that numerical models (SGS and combustion models) as well as the setup (grid refinement, single vs. double sector computation etc.) have almost no effect on FTF results which proves the accuracy of the LES approach chosen here. From this sensitivity study, a specific operating point is extracted to compute the full 360° configuration: the ethylene case with $N = 18$ burners is computed and compared to experimental results in Chapter 8. This study unveils a significant gap between the simple configuration studied theoretically in Part I and more realistic turbulent systems, which needs to be bridged.

PART III - Part I is developed using only theory (Fig. 1.19, top), while Part II focuses on heavy LES (Fig. 1.19, middle). Helmholtz solvers (Fig. 1.19, bottom) constitute an intermediate tool which is combined with LES in Part III: a new approach called AMT (Acoustic Mode Triggering) is developed in Chapter 9 and validated on longitudinal configurations. This tool is then applied on annular configurations in Chapter 10 to analyze fundamental aspects of combustion instabilities and both FS and GS symmetry breaking effects that theory fails to fully describe or that LES cannot solve because of its extreme cost. This methodology is based on injecting an acoustic mode (computed theoretically or with a Helmholtz solver) into a LES simulation. AMT allows to inject one single well-controlled mode into the LES. Therefore, it avoids the transient growth phase computation and directly leads to limit cycles. AMT also allows to investigate non-linear triggering by initializing LES with modes of arbitrary amplitudes (not detailed in this thesis) as well as to predict acoustic damping of real industrial systems (here damping due to Helmholtz resonators or baffles azimuthally distributed in the chamber), which can be computed by LES. It also provides a validation of certain theoretical results on symmetry breaking (Chapter 10) by post-processing the time-dependent simulations by a Dynamics Mode Decomposition (DMD) to extract the two azimuthal components: non-degenerate modes can be studied in details by analyzing their respective growth rates and structures.

Finally, this PhD thesis intends to provide general and fundamental rules on symmetry breaking effects on annular combustion instabilities, which can be then applied on real configurations such as the one currently developed at Snecma and Cerfacs called LEMCOTEC (not shown here for confidentiality purposes). Figure 1.19 summarizes the two symmetry breaking types (GS and FS) and tools (theory, UQ, AMT and LES) used in this thesis to investigate symmetry breaking effect on azimuthal thermoacoustic modes in annular combustors.

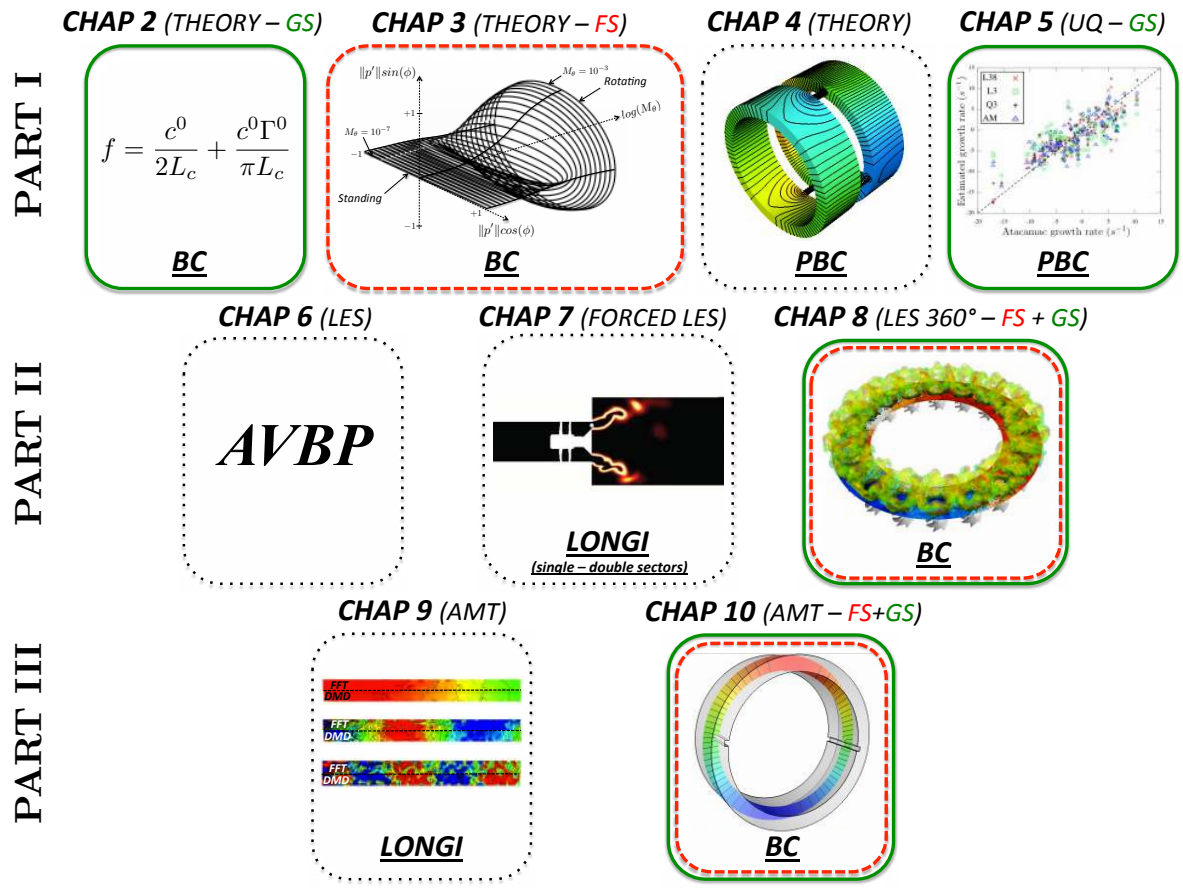

Figure 1.19: Summary of tools (Theory, Uncertainty Quantification, Large Eddy Simulation and Acoustic Mode Triggering) and symmetry breaking types (FS: - - - and GS: ———) studied in the different parts and chapters of this PhD thesis. Three classes of acoustic modes are studied: longitudinal mode in linear configurations for tools validations and azimuthal modes in BC (Fig. 1.18, left) and PBC (Fig. 1.18, right) annular systems.

Part I

Theoretical analysis of azimuthal modes

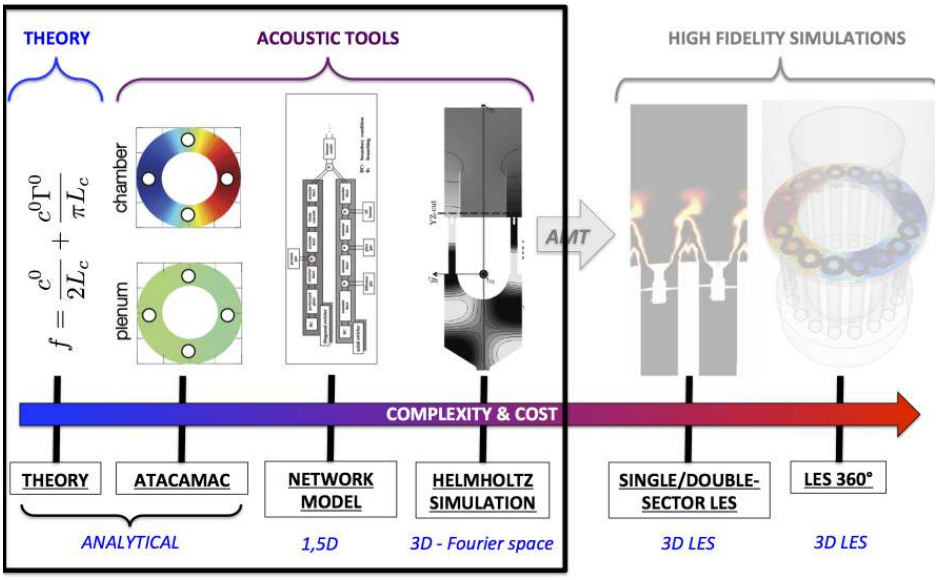

This part has lead to the following publications:

1) M. Bauerheim, J-F. Parmentier, P. Salas, F. Nicoud and T. Poinsot, 'An analytical model for azimuthal thermoacoustic modes in an annular chamber fed by an annular plenum' (2014) **Combustion and Flame** 161 (5), 1374-1389
2) M. Bauerheim, M. Cazalens and T. Poinsot, 'Theoretical study of mean azimuthal flow and asymmetry effects on thermo-acoustic modes in annular combustors' (2014) **Proceedings of the 35th Combustion Institute** (in press, DOI 10.1016/j.proci.2014.05.053)
3) M. Bauerheim, F. Nicoud and T. Poinsot, 'Theoretical analysis of the mass balance equation through a flame at zero and non-zero Mach numbers' (2014) **Combustion and Flame** (in press, DOI 10.1016/j.combustflame.2014.06.017)
4) M. Bauerheim, P. Salas, F. Nicoud and T. Poinsot, 'Symmetry breaking of azimuthal thermo-acoustic modes in annular cavities: a theoretical study' (2014) **Journal of Fluid Mechanics** (in press)
5) M. Bauerheim, A. Ndiaye, P. Constantine, G. Iaccarino, S. Moreau and F. Nicoud, 'Uncertainty quantification of thermo-acoustic instabilities in annular combustors' (2014) **Proceedings of the CTR Summer Program** (in press)
6) M. Juniper, L. Magri, M. Bauerheim and F. Nicoud, 'Applications of adjoint methods in thermoacoustics' (2014) **Proceedings of the CTR Summer Program** (in press)

Chapter 2

Theoretical analysis of azimuthal thermo-acoustic modes in an annular chamber fed by N burners

Contents

Annular combustion chambers found in many gas turbines can exhibit unstable acoustic modes which are due to a coupling between unsteady combustion and azimuthal acoustic waves propagating in the sectors of the chamber (usually 12 to 24). The acoustic structure of these modes is controlled by the design of the chamber. For a perfectly axisymmetric system with identical burners, degenerate acoustic modes are created: they can be standing, spinning or "mixed". The present work studies BC (Burners+Chamber) cases which are not perfectly axisymmetric, because different burners are installed along the azimuthal direction. Here two different types of burners are distributed in the chamber to break its azimuthal symmetry. These symmetry-breaking effects can be studied using a fully analytical method based on a network approach. The effects of symmetry breaking on the modes nature are studied in an idealized case where only 3 sectors are present in the chamber before considering a realistic case with 24 sectors. Similar results are obtained for both cases and show that the modes nature is controlled by a single factor called "splitting strength" which depends only on $\Gamma_1 - \Gamma_2$, where Γ_i characterizes the flame response to acoustic waves of burner i. The modes growth rates are determined by a second parameter called the "coupling strength" which is the sum of all Γ_i's. When 24 burners are used, the pattern used to distribute the two types of burners along the azimuthal direction also becomes a control parameter. To first-order however, the model suggests that when focusing on only one acoustic mode, the most stable configuration is obtained when using only one burner type corresponding to the most stable case and that mixing different burner types cannot improve the stability of the chamber independently of the burners distribution pattern. However, this strategy of mixing burners should be further investigated to stabilize multiple modes (for example the first and second azimuthal modes) or the same mode but at different operating conditions, by modifying the coupling strength while keeping the splitting strength as low as possible.

2.1 Introduction

The present chapter describes an analytical approach to investigate the effects of geometrical symmetry (GS) breaking on azimuthal modes in an annular chamber fed by N identical or non-identical burners. This configuration called BC (Burner+Chamber, Fig. 2.1) allows the investigation of asymmetry's effect on eigenfrequencies and nature of circumferential modes. The model is based on a network description (Fig. 1.13) of the combustion chamber where only plane acoustic waves travel and interact with flames (Parmentier *et al.*, 2012). It allows to take into account the effects of burners and of complex flame models (see the discussion in Section 2.3.2) while providing a solution which remains almost fully analytical. This analytical formulation reveals which parameters control the growth and the nature of the modes, something which would be impossible with a numerical approach. The work presented in this chapter focuses only on the linear regime, nevertheless a study of non-linear regimes using FDF's have been also explored using ATACAMAC and is briefly described in the Appendix C since it can lead

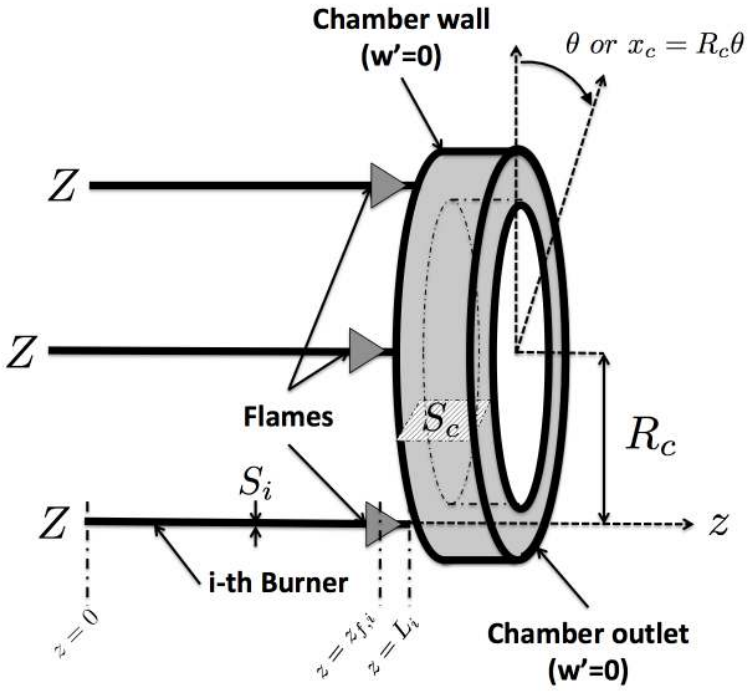

Figure 2.1: BC configuration to study unstable modes in annular chambers

to symmetry breaking as well (Ghirardo *et al.*, 2015).

This chapter is organized as follows: Section 4.2 briefly describes the principle of the acoustic network model called ATACAMAC ("Analytical Tool to Analyze and Control Azimuthal Modes in Annular Combustors") developed in this thesis and how an analytical dispersion relation can be obtained in such a configuration (Parmentier *et al.*, 2012). In Section 2.3, analytical calculations of eigenfrequencies are presented for both an "unperturbed" case (an annular cavity without flames) and for a general non-symmetric BC configuration (Fig. 2.1). Section 4.4 describes the test cases as well as the 3D Helmholtz solver used to validate the ATACAMAC results. Two application cases are presented : an academic chamber with $N = 3$ burners and a real configuration with $N = 24$ burners (Fig. 1.13). In Section 2.4.2, ATACAMAC is applied to a BC configuration with $N = 3$ identical burners (Section 2.4.2.a) and then $N = 3$ different burners (Section 2.4.2.b), highlighting the effect of circumferential patterns on eigenfrequencies and modes nature. ATACAMAC results are systematically compared to those provided by a 3D acoustic code solving the complete acoustic equations in three dimensions in the low Mach number case (Nicoud *et al.*, 2007; Silva *et al.*, 2013; Selle *et al.*, 2006; Sensiau *et al.*, 2009). Finally, Section 2.4.3 presents the effects of asymmetry on instabilities in a $N = 24$ burners configuration typical of real engines. Results are compared to observations made in real gas turbine engines (Berenbrink & Hoffmann, 2001; Krüger *et al.*, 2000), validating the choice of a theoretical approach to unveil symmetry breaking effect on azimuthal modes in this PhD thesis.

2.2 A network model for a BC (Burner+Chamber) non-symmetric configuration

2.2.1 Model description

This study focuses on a BC (Burners+Chamber) configuration where an annular chamber is fed by N burners (Fig. 2.1). An impedance Z is imposed at the upstream end of each burner. Mean density and sound speed are noted ρ^0 and c^0 in the annular chamber and ρ_u^0 and c_u^0 for the unburnt mixture in the N burners. The perimeter and the section of the annular chamber are noted $2L_c = 2\pi R_c$ and S_c respectively. The length and section of the i^{th} burner are L_i and S_i. The position along the annular cavity is given by the angle θ defining an abscissa $x_c = R_c\theta$. The location of the flames is similar in all burners and is given by the normalized abscissa $\alpha = z_{f,i}/L_i$ (Fig. 2.1)

This model corresponds to situations where pressure fluctuations in the combustion chamber depend on the angle θ (or the azimuthal position x) but not on the axial direction z in the chamber (they depend on the coordinate z only in the burners). This case can be observed in combustors terminated by choked nozzles which acoustically behave almost like a rigid wall (i.e. $u' = 0$ under the low upstream Mach number assumption (Marble & Candel, 1977)). Since the chamber inlet is also close to a velocity node, modes which have no variation along z can develop in the chamber, as shown by recent LES in real engines (Wolf *et al.*, 2009).

The model provides the analytical expression of eigenfrequencies for a general asymmetric case for any mode order p and any number of burners N as well as general rules on stability for annular combustors. Results on structure and nature of azimuthal modes (spinning, standing or mixed) will be derived using this analytical study to show how asymmetry can promote specific modes and control instabilities (Worth & Dawson, 2013*b*,*a*; Moeck *et al.*, 2010; Gelbert *et al.*, 2012; Noiray *et al.*, 2011).

2.2.2 Annular Network Reduction (ANR)

Network models which account for one annular cavity connected to N burners usually require a large number of unknown variables (acoustic pressure and velocity in each network tube) and a large matrix describing the system (typically a $2N$-by-$2N$ matrix). To reduce the size of the system (i.e. a matrix of size 2-by-2, independent of the number N of burners), the ANR (Annular Network Reduction) methodology proposed in (Bauerheim *et al.*, 2014*d*) is applied: the full annular combustor is split into N sectors which differ only via the burner/chamber junction (Figs 2.2 and 2.3). Between each sector, the propagation of azimuthal waves (along θ or x) can be modeled by a transfer matrix R_i as proposed by (Parmentier *et al.*, 2012) (Fig. 2.3, propagation):

$$\begin{bmatrix} q^+ \\ q^- \end{bmatrix}_{i+\frac{1}{2}} = \begin{bmatrix} R_i \end{bmatrix} \begin{bmatrix} q^+ \\ q^- \end{bmatrix}_i \text{ where } \begin{bmatrix} R_i \end{bmatrix} = \begin{bmatrix} W & 0 \\ 0 & \frac{1}{W} \end{bmatrix} \tag{2.1}$$

where $q^\pm = p' \pm \rho^0 c^0 u'$, $W = e^{2jkL_c/N}$ and the wavenumber $k = \omega/c^0$.

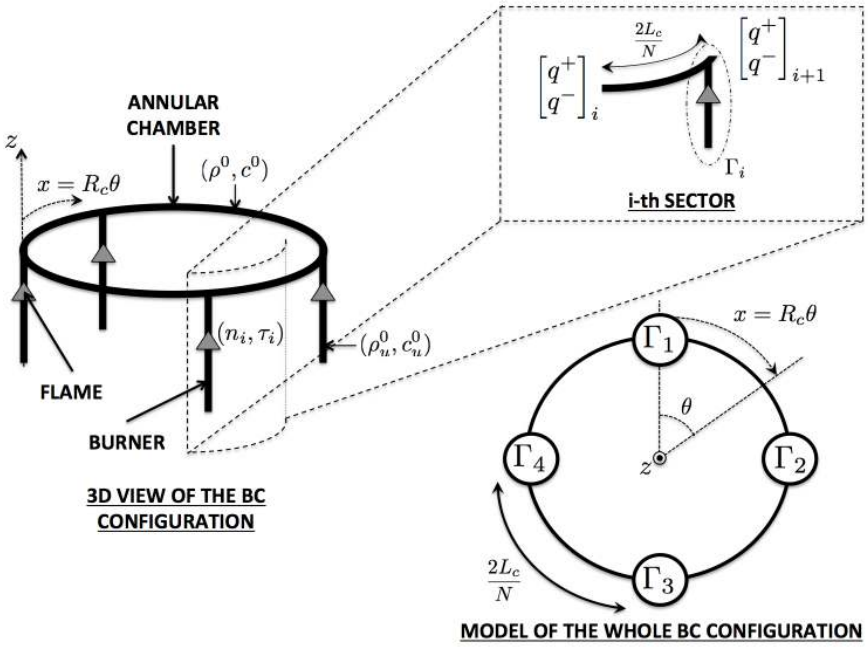

Figure 2.2: 3D view of a BC configuration with $N = 4$ burners (left), zoom on the i^{th} sector (top right) and model of the whole BC configuration (bottom right) where Γ_i represents the burner/chamber interaction (Parmentier *et al.*, 2012)

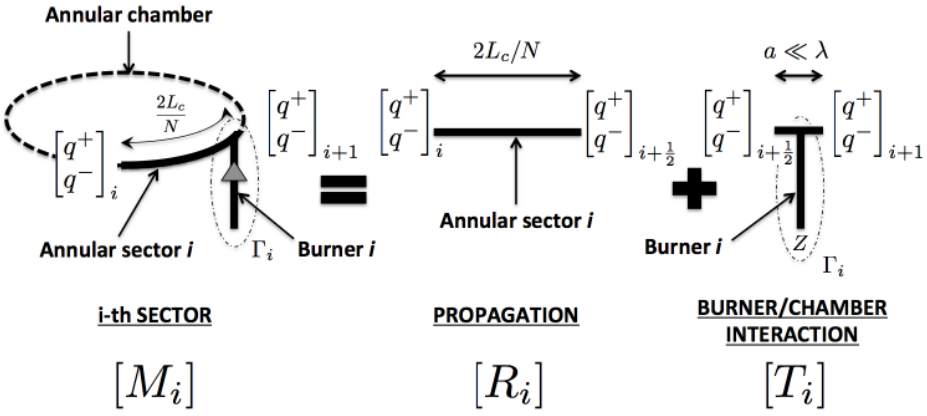

Figure 2.3: ANR methodology: each sector is decomposed into a free propagation of azimuthal waves (characteristic length $2L_c/N$) and a compact burner/chamber interaction (characteristic length $a \ll \lambda$) modeled by the coupling parameter Γ_i

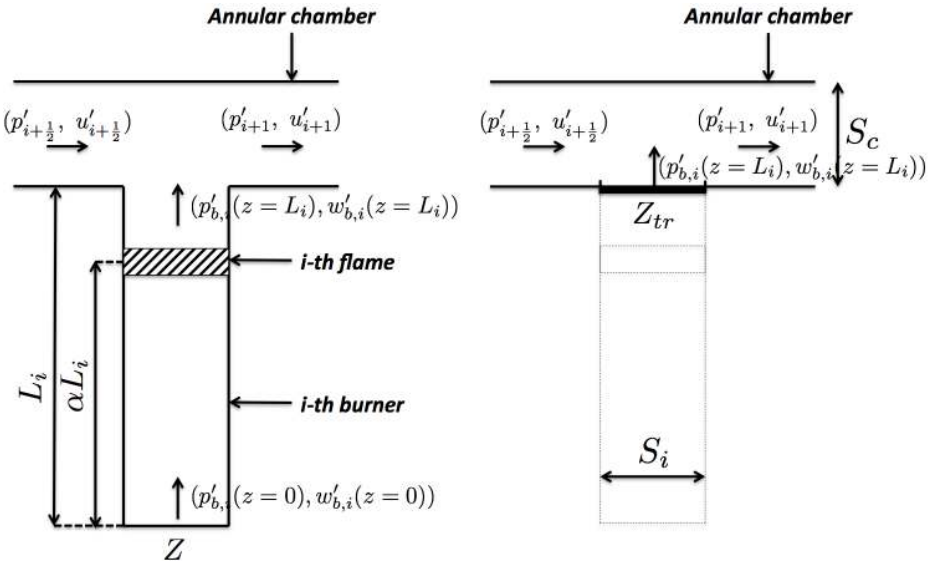

Figure 2.4: Equivalent impedance of the whole i^{th} burner (which includes the i^{th} active flame) near the burner/chamber interaction zone (Fig. 2.3). The translated impedance Z_{tr} at $z = L_i$ takes into account the upstream impedance Z at $z = 0$, the propagation in the cold ($0 < z < \alpha L_i$) and hot ($\alpha L_i < z < L_i$) parts of the burner as well as the active flame effect via the Flame Transfer Function ($n_i,\ \tau_i$)

The area where the i^{th} burner is connected to the annular chamber (--- in Fig. 2.2, top right) was investigated by O'Connor & T.Lieuwen (2012*c*,*b*) and can be assumed to be compact. As shown in Fig. 3.3, using the equations of acoustic propagation in the cold ($0 < z < \alpha L_i$) and hot ($\alpha L_i < z < L_i$) parts of the burner as well as the jump conditions through the i^{th} flame ($z = \alpha L_i$), the effect of the whole i^{th} burner on the annular chamber can be obtained by a translated impedance from $z = 0$ (impedance Z) to the burner/chamber junction at $z = L_i$ (impedance $Z_{tr} = \frac{p'_{b,i}(z=L_i)}{\rho^0 c^0 w'_{b,i}(z=L_i)}$) (Bauerheim *et al.*, 2014*d*; Blimbaum *et al.*, 2012):

$$Z_{tr} = \frac{\mathbb{F}S^k_{1-\alpha}[jC^{k_u}_\alpha - S^{k_u}_\alpha Z] + C^k_{1-\alpha}[C^{k_u}_\alpha Z + jS^{k_u}_\alpha]}{\mathbb{F}C^k_{1-\alpha}[jS^{k_u}_\alpha Z + C^{k_u}_\alpha] + S^k_{1-\alpha}[jC^{k_u}_\alpha Z - S^{k_u}_\alpha]} \tag{2.2}$$

where $\mathbb{F} = \frac{\rho^0 c^0}{\rho^0_u c^0_u}(1 + n_i e^{j\omega\tau_i})$ and notations for sine and cosine functions are $C^{k_u}_\alpha = cos(\alpha k_u L_i)$, $S^{k_u}_\alpha = sin(\alpha k_u L_i)$, $C^k_{1-\alpha} = cos((1-\alpha)kL_i)$, $S^k_{1-\alpha} = sin((1-\alpha)kL_i)$ and wavenumbers are $k = \omega/c^0$ and $k_u = \omega/c^0_u$.

The jump conditions at the burner/chamber junction at null Mach number read (Dowling, 1995; Davies, 1988; Poinsot & Veynante, 2011):

$$p'_{i+\frac{1}{2}} = p'_{i+1} = p'_{b,i}(z = L_i) \tag{2.3}$$

$$u'_{i+\frac{1}{2}} S_c + \underbrace{w'_{b,i}(z=L_i)}_{=\frac{p'_{i+\frac{1}{2}}}{\rho^0 c^0 Z_{tr}}} S_i = u'_{i+1} S_c \tag{2.4}$$

Consequently, a transfer matrix T_i^* for the interaction part of Fig. 2.3 can be deduced:

$$\begin{bmatrix} p' \\ \rho^0 c^0 u' \end{bmatrix}_{i+1} = \begin{bmatrix} T_i^* \end{bmatrix} \begin{bmatrix} p' \\ \rho^0 c^0 u' \end{bmatrix}_{i+\frac{1}{2}} = \begin{bmatrix} 1 & 0 \\ 2j\Gamma_i & 1 \end{bmatrix} \begin{bmatrix} p' \\ \rho^0 c^0 u' \end{bmatrix}_{i+\frac{1}{2}} \tag{2.5}$$

where the coupling parameter Γ_i (Parmentier *et al.*, 2012; Bauerheim *et al.*, 2014*d*; Palies, 2010; Schuller *et al.*, 2012) (Fig. 2.3, burner/chamber interaction) is directly linked to the equivalent admittance $1/Z_{tr}$ of the whole i^{th} burner:

$$\Gamma_i = -\frac{j}{2}\frac{S_i}{S_c Z_{tr}} \tag{2.6}$$

When a velocity node ($Z = \infty$) or a pressure node ($Z = 0$) is imposed at the upstream end of each burner and flames are located at the burner/chamber junction ($\alpha = 1$), the coupling parameters Γ_i reduce to (using (2.2) and (2.6)):

$$\Gamma_i = \frac{1}{2}\frac{S_i \rho^0 c^0}{S_c \rho_u^0 c_u^0} tan(k_u L_i)\left(1 + n_i e^{j\omega\tau_i}\right) \text{ when } Z = \infty \tag{2.7}$$

$$\text{or } \Gamma_i = -\frac{1}{2}\frac{S_i \rho^0 c^0}{S_c \rho_u^0 c_u^0} cotan(k_u L_i)\left(1 + n_i e^{j\omega\tau_i}\right) \text{ when } Z = 0 \tag{2.8}$$

where $k_u = \frac{\omega}{c_u}$ and $(n_i,\ \tau_i)$ are the interaction index and the time-delay of the FTF for the i^{th} flame (Crocco, 1951).

Finally, Eq. (2.5) can be recast to relate characteristic waves $q^{\pm} = p' \pm \rho^0 c^0 u'$ instead of primitive variables p' and u' leading to the scattering matrix T_i:

$$\begin{bmatrix} q^+ \\ q^- \end{bmatrix}_{i+1} = \begin{bmatrix} T_i \end{bmatrix} \begin{bmatrix} q^+ \\ q^- \end{bmatrix}_{i+\frac{1}{2}} \text{ where } \begin{bmatrix} T_i \end{bmatrix} = \begin{bmatrix} 1 + j\Gamma_i & j\Gamma_i \\ -j\Gamma_i & 1 - j\Gamma_i \end{bmatrix} \tag{2.9}$$

The waves at both ends of the i^{th} sector are connected by the $M_i = T_i R_i$ scattering matrix using (2.1) and (2.9) (Fig. 2.3):

$$\begin{bmatrix} q^+ \\ q^- \end{bmatrix}_{i+1} = \begin{bmatrix} T_i \end{bmatrix} \begin{bmatrix} q^+ \\ q^- \end{bmatrix}_{i+\frac{1}{2}} = \begin{bmatrix} T_i \end{bmatrix} \begin{bmatrix} R_i \end{bmatrix} \begin{bmatrix} q^+ \\ q^- \end{bmatrix}_{i} \tag{2.10}$$

Using the periodicity condition $\begin{bmatrix} q^+ \\ q^- \end{bmatrix}_{N+1} = \begin{bmatrix} q^+ \\ q^- \end{bmatrix}_1$ and Eq. (2.10) leads to:

$$\left(\prod_{i=N}^{1} M_i\right) \begin{bmatrix} q^+ \\ q^- \end{bmatrix}_1 = \begin{bmatrix} q^+ \\ q^- \end{bmatrix}_1 \tag{2.11}$$

The system defined by Eq. (2.11) has non-trivial solutions only if its determinant is null. Therefore, the ANR methodology provides an implicit analytical dispersion relation for the pulsation ω for a general non-symmetric BC configuration:

$$det\left(\prod_{i=N}^{1} M_i - I_d\right) = 0 \tag{2.12}$$

where I_d is the 2-by-2 identity matrix.

2.3 Analytical calculation of eigenfrequencies and mode structures

The analytical dispersion relation (Eq. 2.12) provides the frequencies and the structure of the modes of the annular chamber. It allows to study symmetry breaking by investigating the effects of the N burners responses (modelled by the N parameters $\Gamma_i,\ i \in [1, N]$ defined by Eq. (2.6)) on the growth rate and the nature of azimuthal modes. Several configurations are considered here (Fig. 2.5) to understand the effect of symmetry breaking on combustion instabilities.

2.3.1 Unperturbed annular cavity (without burners and flames)

First, an annular chamber with no burner (i.e. $\Gamma_i = 0$, for all $i \in [1, N]$) is studied as a reference case (Fig. 2.5, top left). The sound speed field corresponds to a reactive case: $c = c^0$ in the annular chamber. The transfer matrix of each sector (Eq. (2.10)) reduces to $M_i = R_i$ since $T_i = I_d$: only azimuthal propagation occurs. Consequently Eq. (2.11) reduces to:

$$\begin{bmatrix} W^N & 0 \\ 0 & \frac{1}{W^N} \end{bmatrix} \begin{bmatrix} q^+ \\ q^- \end{bmatrix}_1 = \begin{bmatrix} q^+ \\ q^- \end{bmatrix}_1 \tag{2.13}$$

The dispersion relation is therefore $W^N = 1$ where $W = e^{2jkL_c/N}$. The N solutions of Eq. (2.13) are $W_0 = e^{2jp\pi/N}$ and correspond to real eigenfrequencies of the unperturbed problem:

$$kL_c = p\pi \ \text{ so that } \ f = \frac{pc^0}{2L_c}, \text{ for all } p \in \mathbb{N} \tag{2.14}$$

As expected, Eq. (2.14) corresponds to a family of azimuthal modes where the first one ($p = 1$) is the first azimuthal mode at frequency $c^0/2L_c$ which is the mode observed

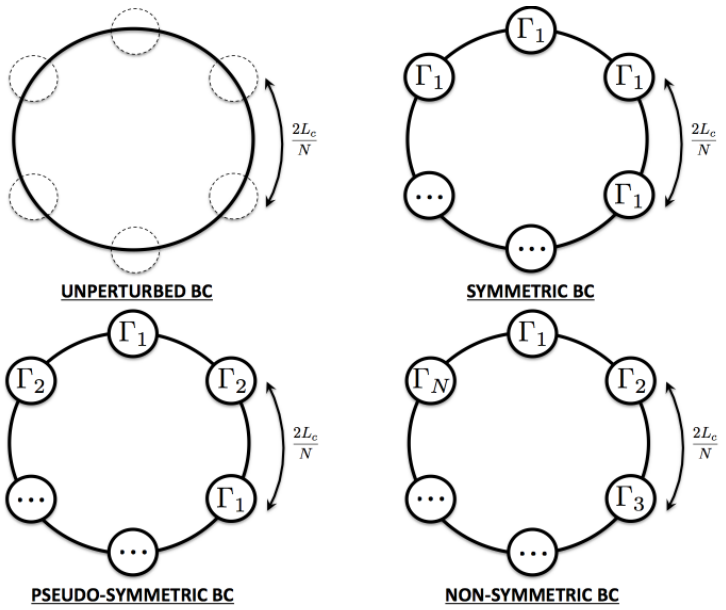

Figure 2.5: Typical configurations: Unperturbed (top left), symmetric with identical burners (top right), pseudo-symmetric configuration (bottom left) and the general non-symmetric configuration (bottom right)

in many practical cases. Eq. (2.13) also provides the eigenvectors V associated to the eigenfrequencies f given by Eq. (2.14). In this situation, the generated eigenspace $\{V\}$ is two-dimensional: all azimuthal modes are degenerate and can be either standing, spinning or mixed. All modes are neutral since no acoustic dissipation is included (zero growth rate: $Im(f) = 0$).

2.3.2 Non-symmetric BC configuration with active flames in the low-coupling limit

Using a combustor with non-identical burners is a promising approach for controlling azimuthal modes (Fig. 2.5, bottom right). An asymptotic expansion of the dispersion relation (Eq. (2.12)) can be used to study this case. Since all burners can be different, all coupling parameters Γ_i (Eq. (2.6)) can be different. A fully analytical solution can be formulated when the solution is "close" to the unperturbed annular cavity case of Section 2.3.1. This is obtained by assuming small coupling parameters Γ_i:

$$\Gamma_i \ll 1, \text{ for all } i \in [1, N] \tag{2.15}$$

Under this assumption, a Taylor expansion of the transfer matrix of the whole system

($M = \prod_{i=N}^{1} T_i R_i$) at second order gives[1]:

$$M = \begin{bmatrix} W^N[1 + j\Sigma - Q(1)] + Q(W) + o(\Gamma_i^2) & j\sum_{i=1}^{N} \Gamma_i \left(\frac{1}{W}\right)^{N-2i+2} + o(\Gamma_i) \\ -j\sum_{i=1}^{N} \Gamma_i W^{N-2i+2} + o(\Gamma_i) & \frac{1}{W^N}[1 - j\Sigma - Q(1)] + Q(\frac{1}{W}) + o(\Gamma_i^2) \end{bmatrix} \tag{2.16}$$

where

$$\begin{cases} \Sigma = \sum_{i=1}^{N} \Gamma_i \\ Q(x) = \sum_{i=1}^{N-1} \sum_{j=i+1}^{N} \Gamma_i \Gamma_j x^{N-2(j-i)} \end{cases} \tag{2.17}$$

and the Landau notation $o(x)$ called "little-o" is used to designate any quantity negligible compared to x.

From Eq. (2.16), the dispersion relation at second order is:

$$\begin{aligned} det\,(M - Id) \approx & -\frac{W^{2N} - 2W^N + 1}{W^N} - \frac{j\Sigma(W^{2N} - 1)}{W^N} \\ + & \sum_{i=1}^{N-1} \sum_{j=i+1}^{N} \Gamma_i \Gamma_j [W^{2N} - W^{N-2(j-i)} - W^{2(j-i)} + 1] = 0 \end{aligned} \tag{2.18}$$

Eq. (2.18) is a dispersion relation which involves terms ($W = e^{2jkL_c/N}$ and $\Gamma_i(k)$) depending on the wave number $k = \omega/c^0$. Under the low coupling assumption (Eq. (2.15)), the wavenumber k is close to the wavenumber of the unperturbed problem $k^0 = p\pi/L_c$ (Section 2.3.1): $k \approx k^0 + \epsilon/L_c$. A proper asymptotic expansion of $W^{\pm} = e^{2jkL_c/N} = e^{2j(p\pi+\epsilon^{\pm})/N} \approx e^{2jp\pi}(1 + 2j\epsilon^{\pm}/N)$ in terms of the wavenumber perturbations ϵ^+ and ϵ^- gives:[2]

$$W^{\pm} = (1 + \mathcal{E}^{\pm})W_0 + o(\mathcal{E}^{\pm}) \;\text{ i.e. }\; kL_c = p\pi + \epsilon^{\pm} \;\text{ or }\; f^{\pm} = \frac{pc^0}{2L_c} + \frac{c^0}{2\pi L_c}\epsilon^{\pm} \tag{2.19}$$

where $W_0 = e^{2jp\pi/N}$ is the solution of the unperturbed problem and corresponds to $kL_c = p\pi$ (i.e. $f = \frac{pc^0}{2L_c}$) where p is the mode order, $\mathcal{E}^{\pm} = 2j\frac{\epsilon^{\pm}}{N}$ and $j^2 = -1$.

The coupling parameters Γ_i also depend on the frequency and therefore on $W^{\pm}$ (or $\epsilon^{\pm}$). This dependency on the frequency can come from (1) the propagation in the burners and (2) the flame response which can depend on the frequency when using FTFs instead of simpler $n - \tau$ formulations. This coupling parameter can be approximated by:

$$\Gamma_i(W) \approx \underbrace{\Gamma_i(W = W_0)}_{\Gamma_i^0} + \mathcal{E}^{\pm} W_0 \underbrace{\left(\frac{\partial \Gamma_i}{\partial W}\right)_{W=W_0}}_{\Gamma_i^1} \approx \Gamma_i^0 + \frac{2j\epsilon^{\pm} W_0}{N}\Gamma_i^1 \tag{2.20}$$

[1] A first-order Taylor expansion of extra-diagonal terms which have no zero order term is sufficient to compute a second-order dispersion relation of $det(M - Id)$.

[2] The two components V^+ and V^- of the azimuthal mode do not necessarily have the same wavenumber perturbation $\epsilon^{\pm}$. Therefore the notation $W^{\pm}$ is used since the azimuthal propagation of waves W depends on the wavenumber perturbation $\epsilon^{\pm}$.

Using (2.19) and (2.20), a Taylor expansion of the terms $W(\epsilon^{\pm})$ and $\Gamma_i(\epsilon^{\pm})$ in the dispersion relation (2.18) at second order ($o(\epsilon^2)$ knowing that Γ_i^0 is of order of $\epsilon^{\pm}$)[3] gives:

$$A - 4B\epsilon^{\pm} + 4C\epsilon^{\pm 2} = 0 \tag{2.21}$$

where

$$\begin{cases} A = -\left[W_0^{2N} - 2W_0^N + 1\right] - j\Sigma_0\left[W_0^{2N} - 1\right] \\ \quad + \sum_{i=1}^{N-1}\sum_{j=i+1}^{N}\Gamma_i^0\Gamma_j^0\left[W_0^{2N} - W_0^{N-2(j-i)} - W_0^{2(j-i)} + 1\right] \\ B = \frac{j}{2}[W_0^{2N} - 1]\left[1 + \frac{\Sigma_1}{N}\right] - \frac{\Sigma_0}{2}[W_0^{2N} + 1] \\ C = \frac{1}{N^2}\left[\binom{N}{N-2}W_0^{2N} + \binom{N+1}{N-1}\right] \end{cases} \tag{2.22}$$

where $\Sigma_0 = \sum_{i=1}^{N}\Gamma_i^0$ and $\Sigma_1 = \sum_{i=1}^{N}\Gamma_i^1$, knowing that $\Gamma_i^{\pm}(\omega) \simeq \Gamma_i^0 + \frac{2j\epsilon^{\pm}}{N}W_0\Gamma_i^1$ (see Eq. (2.20)).

From Section 2.3.1, $W_0^N = 1$ which leads to simplifications of coefficients A, B and C:

$$\begin{cases} A = 4\displaystyle\sum_{i=1}^{N-1}\sum_{j=i+1}^{N}\Gamma_i^0\Gamma_j^0\left[\sin\left(\frac{2p\pi}{N}(j-i)\right)\right]^2 \\ B = -\Sigma_0 \\ C = 1 \end{cases} \tag{2.23}$$

One should note that the term Σ_1 in the coefficient B of Eq. (2.21), which corresponds to the frequency-dependent part of the burner and flame models, naturally vanishes. It suggests that at first order, burners and flames can be characterized only at the angular frequency $\omega = \omega^0$ (i.e. the frequency of the annular cavity alone). Nevertheless, this dependency to frequency is necessary for more accurate estimations, especially when strong coupling occurs (i.e. when the small coupling factor assumption does not hold (Bauerheim *et al.*, 2014*d*)).

Eigenfrequencies are deduced from the quadratic equation Eq. (2.21):

$$\epsilon^{\pm} = \frac{B \pm \sqrt{B^2 - AC}}{2C} \tag{2.24}$$

which leads to a simple expression for the wavenumber perturbations in the case of a general non-symmetric BC configuration:

$$\epsilon^{\pm} = -\frac{1}{2}\left(\Sigma_0 \pm \sqrt{\Sigma_0^2 - A}\right) \tag{2.25}$$

where $\Sigma_0 = \sum_{i=1}^{N}\Gamma_i^0$ will be called the "coupling strength" while A is the non-symmetric part defined in Eq. (2.23) depending on the number of burners N and the mode order p.

[3]The analytical resolution of the dispersion relation will lead to the solution $\epsilon^{\pm} \propto \Gamma_i^0$ which proves that Γ_i^0 is a first order term and $\Gamma_i^0\Gamma_j^0$ or $\Gamma_i^0\epsilon^{\pm}$ are second order terms.

The term $\mathcal{S}_0 = \sqrt{\Sigma_0^2 - A}$ in Eq. (2.25) is called the "splitting strength" because it separates the two eigenvalues ϵ^+ and ϵ^-. It can be recast for simplification (see Appendix A) and highlights the key role of the $2p^{th}$ complex Fourier coefficients $\gamma(\pm 2p)$ of the azimuthal coupling factor distribution $\Gamma^0 = [\Gamma_1^0, ..., \Gamma_N^0]$:

$$\mathcal{S}_0^2 = \Sigma_0^2 - A = \sum_{i,j=1}^{N} \Gamma_i^0 \Gamma_j^0 cos\left(\frac{4p\pi}{N}(j-i)\right) = \gamma(2p) \times \gamma(-2p) \tag{2.26}$$

where $\gamma(k) = \sum_{i=1}^{N} \Gamma_i^0 e^{-j2k\pi i/N}$ is the k^{th} Fourier coefficient of the coupling factor azimuthal distribution Γ^0.

Eq. (2.25) is a generalization of Parmentier *et al.* (2012) and Noiray *et al.* (2011) results to an annular chamber connected by N burners with active flames. It shows that:

1) Stability of the N burners combustor is controlled to first order by the imaginary part of the coupling strength $\Sigma_0 = \sum_{i=1}^{N} \Gamma_i^0$. This coupling strength depends only on the sum of the individual coupling parameters Γ_i, not on the pattern used to distribute these burners when they differ.
2) The splitting strength $\mathcal{S}_0$ defined by Eq. (2.26) controls the nature of the modes: if $\mathcal{S}_0 = 0$ modes are degenerate (i.e. $\epsilon^+ = \epsilon^-$) and if $\mathcal{S}_0 \neq 0$, they are not.

Noiray *et al.* (2011) obtained a similar result where the mode was controlled by $\gamma_{HR}(2p)$, the $2p^{th}$ Fourier coefficient of the heat-release distribution. Eq. (2.26) is a generalization of such a result: the present network model developed in this paper shows that the mode is controlled by the azimuthal distribution of the coupling parameter Γ_i^0 which includes the active flame ($n - \tau$ model) but also by the geometry characteristics, the upstream impedance Z of the burners as well as the density and temperature differences between cold and burnt gases. All these features can affect the asymmetry of the system and therefore the stability: they cannot be neglected when studying combustion instabilities in annular chambers.

A summary of this analytical method providing the frequencies and the stability map of the p^{th} azimuthal mode in a chamber with N burners is given in Appendix B.

2.4 Application to multi-burner annular chambers

Analytical expressions of eigenfrequencies (Eq. (2.25)) of azimuthal modes are compared to results obtained with AVSP (Nicoud *et al.*, 2007), a full 3D Helmholtz solver for two cases:

- A simplified academic configuration with $N = 3$ burners (Section 2.4.2).
- A realistic case with $N = 24$ burners (Section 2.4.3).

The 3D geometries correspond to a BC setup with $N = 3$ or $N = 24$ burners (Fig. 2.6) similar to Fig. 2.1 (physical and geometrical parameters are defined in table 4.1). The burner/chamber interfaces are placed at $z = 0$ and the flames are on the burner side. The flame width is equal to 2 mm which guarantees its compacity with respect to the acoustic wave length. Boundary conditions correspond to impermeable walls everywhere except at the upstream end of burners where an impedance $Z = 0$ (i.e. $p' = 0$) is

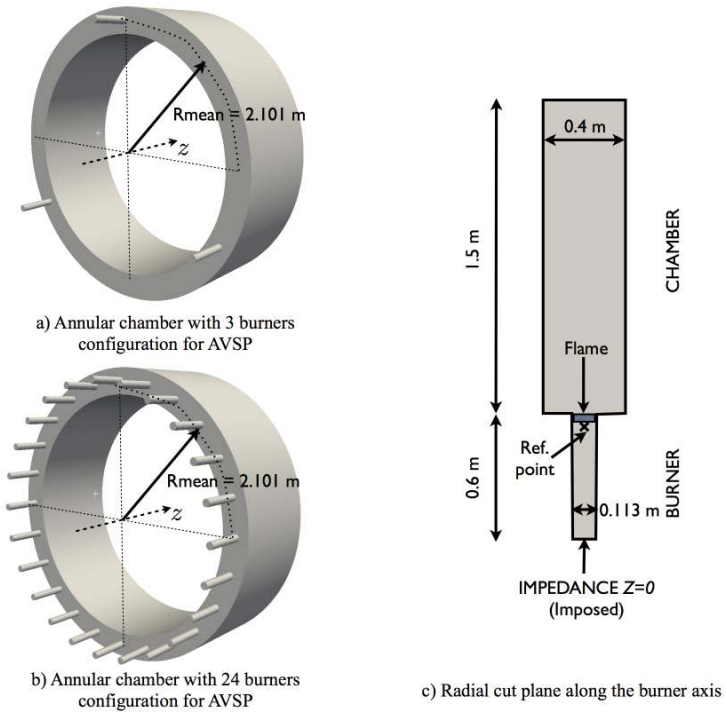

Figure 2.6: Toy-models to validate the ATACAMAC methodology. (a) Perfect annular chamber with $N = 3$, (b) $N = 24$ cylindrical burners, (c) burner/chamber configuration

CHAMBER			
Half perimeter	L_c	6.59	m
Section	S_c	0.6	m^2
BURNER			
Number	N	3 or 24	$-$
Length	L_i^0	0.6	m
Section	S_i	0.01	m^2
FRESH GASES			
Mean temperature	T_u^0	700	K
Mean density	ρ_u^0	9.79	kg/m^3
Mean sound speed	c_u^0	743	m/s
BURNT GASES			
Mean temperature	T^0	1800	K
Mean density	ρ^0	3.81	kg/m^3
Mean sound speed	c^0	1191	m/s
FLAME PARAMETERS			
Interaction index	n_i	1.0	$-$
Time-delay	τ_i	*variable*	s

Table 2.1: Parameters used for numerical applications. They correspond to a typical large scale industrial gas turbine.

NAME	N	CBO	ASYMMETRY PATTERN
B3_C0	3	0	○ ○ ○
B3_C1	3	1	○ ● ○
B24_C0	24	0	○○○○○○○○○○○○○○○○○○○○○○○○
B24_C20_P1	24	20	●●●●●●●●●○○○○●●●●●●●●●●●●
B24_C20_P2	24	20	●●●●●○●●●●○●●●●●●●○●●●●●●○
B24_C20_P3	24	20	●●●●●●●●○○●●●●●○○●●●●●●●●●
B24_C20_P4	24	20	●●●●●○●●●●●○●●●●●●●○●●●●●●○
B24_C24	24	24	●●●●●●●●●●●●●●●●●●●●●●●●●●

Table 2.2: BC configurations investigated with both the 3D Helmholtz solver AVSP and the analytical approach ATACAMAC. ○: Burner without CBO ●: Burner with CBO

imposed to mimic a connection to a large plenum. For the $N = 3$ burners configuration, two cases are investigated (table 2.2): first with identical burners and then with two types of burners with different time-delays τ_1 and τ_2. The interaction index of flames is set to the same value $n = 1.0$ (knowing that typical low-frequency values for n are around $\frac{T^0}{T^0_u} - 1 \simeq 1.57$ here (Poinsot & Veynante, 2011)) in each burner. For the $N = 24$ configuration (Fig. 2.6), two types of burners with different time-delays are mixed to mimic the combustion chamber where burners can be equipped (or not) with CBO's (Cylindrical Burner Outlet) to modify their flame response (Berenbrink & Hoffmann, 2001; Krüger *et al.*, 2000). Table 2.2 displays the circumferential patterns (● for CBO buners and ○ for burners without CBO) which are considered.

2.4.1 Description of the 3D acoustic code

Assumptions and results of ATACAMAC can be validated using a full 3D acoustic solver called AVSP (Nicoud *et al.*, 2007; Silva *et al.*, 2013; Selle *et al.*, 2006; Sensiau *et al.*, 2009) which solves the Helmholtz equation in a reactive flow without the assumptions used in ATACAMAC (Nicoud *et al.*, 2007) but of course at a higher cost. AVSP takes into account the interaction between combustion and acoustics. It solves the eigenvalue problem issued from the discretization on unstructured meshes of the Helmholtz equation at zero Mach number. Meshes contain approximately 2 millions cells (corresponding to the ratio of the wavelength to the longest cell length $\lambda/\Delta h_{max} \simeq 250$) which is sufficient considering the simplicity of the geometry and the wavelength of the first azimuthal modee. Source terms due to flames are modeled using Flame Transfer Functions (FTF) (Crocco, 1951). The local heat release fluctuations are expressed in the burner i as:

$$q'_i = n_{u,i}\, e^{j\omega\tau_i}\, \vec{u}'(\mathbf{x}_{ref,i}) \cdot \vec{n}_{ref,i}. \tag{2.27}$$

where $\mathbf{x}_{ref,i}$ is a reference point upstream of the flame in burner i.

The local interaction index $n_{u,i}$ $[J/m^4]$ describes the local flame-acoustic interactions. The values of $n_{u,i}$ are assumed to be constant in the flame zone Ω_i (Fig. 2.6) and are

chosen to recover the global value of the interaction index n_i $[-]$ corresponding to the infinitely thin flame when integrated over the flame zone Ω_i (Nicoud *et al.*, 2007):

$$\int_{\Omega_i} n_{u,i}(\vec{x}) e^{j\omega\tau_{u,i}(\vec{x})} d\vec{x} = n_g e^{j\omega\tau_i} \tag{2.28}$$

where n_g $[J/m]$ is the global index related to the Crocco index n_i used in ATACAMAC: $n_i = n_g \frac{\gamma-1}{S_f \rho_u c_u^2}$ where S_f is the surface of the infinitely thin flame. One should note that at low frequencies, $n_i \sim T_b/T_u - 1$.

For the sake of simplicity, the flames are also assumed to be independent of frequency. These assumptions allow to use AVSP to check the precision of the analytical techniques developed in ATACAMAC. In annular configurations with multiple burners, the heat release fluctuations in burner i are supposed to be driven by axial velocity fluctuations at the reference point $\mathbf{x_{ref,i}}$. This assumption, called ISAAC (Independence Sector Assumption in Annular Combustor) in (Sensiau *et al.*, 2009) was validated by an LES of a full annular combustor (Staffelbach *et al.*, 2009) and is used in the present study. In the infinitely thin flame model used in ATACAMAC the reference points are chosen at the flame locations $z_{f,i}$. The normalized abscissa of the flame is set to $\alpha \simeq 0.91$ (Bauerheim *et al.*, 2014*d*). 3D effects near the burner/chamber junctions can be accounted for (Pierce, 1981) using a standard length correction in the low-frequency range for a flanged tube (Silva *et al.*, 2009) which is applied at the downstream burner's end ($\Delta L_i = 0.4\sqrt{4S_i/\pi}$). In AVSP, the reference points are placed a few millimeters upstream of the flames (Fig. 2.6) for numerical accuracy issues (Silva *et al.*, 2013).

2.4.2 Symmetry breaking with $N = 3$ burners

Analytical expressions of frequency of azimuthal modes (Eq. (2.25)) can be obtained for a generic annular BC configuration with N burners. First, the symmetric case (Fig. 2.7, left) with $N = 3$ identical burners is studied (Section 2.4.2.a). Then, the effect of circumferential variations on combustion instabilities is investigated (Section 2.4.2.b) and validated on an asymmetric BC configuration where one type 1 burner is replaced by a type 2 (Fig. 2.7, right).

2.4.2.a Symmetric case with $N = 3$ identical burners

In an axisymmetric configuration where burners are the same for all sectors (i.e. $\Gamma_i = \Gamma$, for all $i \in [1, 3]$), only two different mode types exist. Indeed, the splitting strength $\mathcal{S}_0$ in Eq. (2.26) simplifies depending on the mode order p and the number of burners N (Appendix A):

$$\begin{cases} \text{If } p = 3m, \text{ for } m \in \mathbb{N} \text{ then } \mathcal{S}_0 = 3\Gamma^0 \\ \text{For any other mode of order } p: \mathcal{S}_0 = 0 \end{cases} \tag{2.29}$$

Consequently, only two different classes of modes can develop in annular BC configurations with $N = 3$ identical burners:

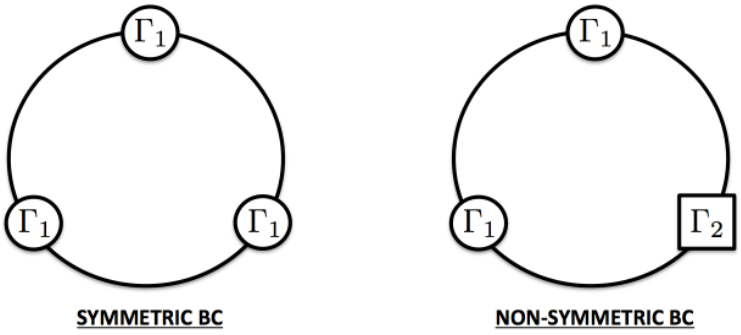

Figure 2.7: Schematic view of the BC configuration with $N = 3$ burners for the validation of numerical and analytical resolutions of Eq. (2.12). Left: symmetric case (all interactions terms Γ_i (Eq. (2.6)) are equal) ; Right: asymmetric case (two identical burners with the same Γ_1 and one burner with Γ_2)

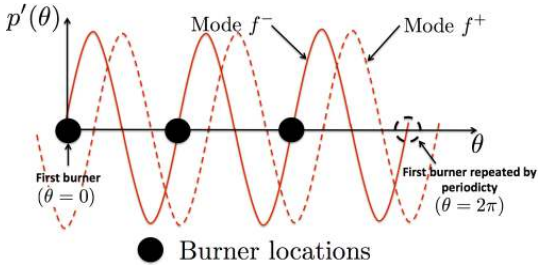

Figure 2.8: Pressure structure of the two components of the azimuthal mode in a $N = 3$ burners configuration: a standing mode imposing a pressure node at every burner locations (——— , f^-) and a standing mode imposing a pressure anti-node at every burner locations (- - - , f^+).

- **Non-degenerate singlets:** If $p = 3m,\ m \in \mathbb{N}$ the splitting strength is not null ($\mathcal{S}_0 = \Sigma_0 = 3\Gamma^0$, Eq. (2.26)) and the azimuthal mode is split into two components V^- and V^+ with different wavenumber perturbations ($\epsilon^\pm$) and frequencies ($f^\pm$) (Eq. (2.19)):

$$\begin{cases} \epsilon^- = 0 \\ \epsilon^+ = -3\Gamma^0 \end{cases} \text{ corresponding to } \begin{cases} f^- = \frac{pc^0}{2L_c} \\ f^+ = \frac{pc^0}{2L_c} - \frac{3}{2}\frac{c^0\Gamma^0}{\pi L_c} \end{cases} \tag{2.30}$$

  Fig. 2.8 displays the mode structure associated to f^+ and f^-: due to symmetry considerations, these modes (e.g. p=3) can lock on burners ($N = 3$) (see Bauerheim *et al.* (2014*a*) for an analytical proof). Their wavelength corresponds to the chamber perimeter (or its half in a case of a configuration with an even number of burners). The first mode V^- with frequency f^- is standing and imposes a pressure node at every burner: therefore it is unperturbed by them ($\epsilon^- = 0$); the mode is neutral. The second mode V^+ at the frequency f^+ is also standing but imposing an azimuthal velocity node (i.e. a pressure anti-node) at every burner ($\epsilon^+ = -3\Gamma^0$).
- **Degenerate doublets:** All other azimuthal modes ($p \neq 3m,\ m \in \mathbb{N}$) are composed of two eigenmodes $V^\pm$ which have the same frequencies (degenerate modes)

because the splitting strength $\mathcal{S}_0 = 0$:

$$\left\{\begin{array}{l}\epsilon^- = -\frac{3}{2}\Gamma^0 \\ \epsilon^+ = -\frac{3}{2}\Gamma^0\end{array}\right. \text{ corresponding to } \left\{\begin{array}{l}f^- = \frac{pc^0}{2L_c} - \frac{3}{4}\frac{c^0\Gamma^0}{\pi L_c} \\ f^+ = \frac{pc^0}{2L_c} - \frac{3}{4}\frac{c^0\Gamma^0}{\pi L_c}\end{array}\right. \tag{2.31}$$

In this configuration, the transfer matrix of the whole system (M defined in Eq. (2.16)) is equivalent to the null matrix. The mode nature is undetermined as pointed out by Noiray *et al.* (2011): a standing, spinning or mixed mode can develop. Noiray *et al.* (2011) have shown that non-linearities on the FTF can however promote one of these natures, a phenomenon which cannot be described by ATACAMAC since it is based on linear FTFs.

Figs. 2.9 and 2.10 provide two validation points (marked by •) of ATACAMAC for symmetric configurations using the full 3D acoustic solver AVSP: modes denoted $A^{\pm}$ when $\tau_1/\tau_c^0 = \tau_2/\tau_c^0 = 0.23$ and $E^{\pm}$ when $\tau_1/\tau_c^0 = \tau_2/\tau_c^0 = 0.68$. A good agreement is obtained between the acoustic code (AVSP) and ATACAMAC.

2.4.2.b Symmetry breaking with $N = 3$ different burners

This section discusses the behavior of azimuthal modes when one of the three burners has a different FTF corresponding to a different value of Γ_i^0 (see Fig. 2.7, right). Especially, the observation in (Perrin & Charnley, 1973; Sensiau *et al.*, 2009) will be investigated: circumferential variations with specific patterns obtained by distributing different burner types along the azimuthal direction could split nominally degenerate doublets into non-degenerate singlets, as observed by (Sensiau *et al.*, 2009). If two burners have a coupling factor Γ_1^0 and the third one Γ_2^0, Eq. (2.25) can be solved with $N = 3$ and gives the following solution:

- **Non-degenerate singlets:** Azimuthal modes with $p = 3m,\ m \in \mathbb{N}$ are non-degenerate singlets characterized by $\mathcal{S}_0 = \Sigma_0 = 2\Gamma_1^0 + \Gamma_2^0$ (Eq. (2.26)) with wavenumber perturbations:

$$\left\{\begin{array}{l}\epsilon^- = 0 \\ \epsilon^+ = -\Sigma_0 = -2\Gamma_1^0 - \Gamma_2^0\end{array}\right. \text{ corresponding to } \left\{\begin{array}{l}f^- = \frac{pc^0}{2L_c} \\ f^+ = \frac{pc^0}{2L_c} - \frac{c^0(2\Gamma_1^0+\Gamma_2^0)}{2\pi L_c}\end{array}\right. \tag{2.32}$$

  where $\Sigma_0 = \sum_{i=1}^{N}\Gamma_i^0$. These modes, as in the symmetric cases, impose a pressure node or pressure anti-node at each burner location leading to two modes with different frequencies: $f^+ \neq f^-$.
- **Nearly degenerate singlets:** For other azimuthal modes ($p \neq 3m,\ m \in \mathbb{N}$), Eq. (2.25) leads to nearly degenerate singlets (Perrin & Charnley, 1973): the degenerate doublet encountered in symmetric configurations (denoted DD with $\epsilon_{DD} = -\frac{1}{2}\Sigma_0 = -\Gamma_1^0 - \frac{1}{2}\Gamma_2^0$, Eq. (2.31)) is split depending on the splitting strength

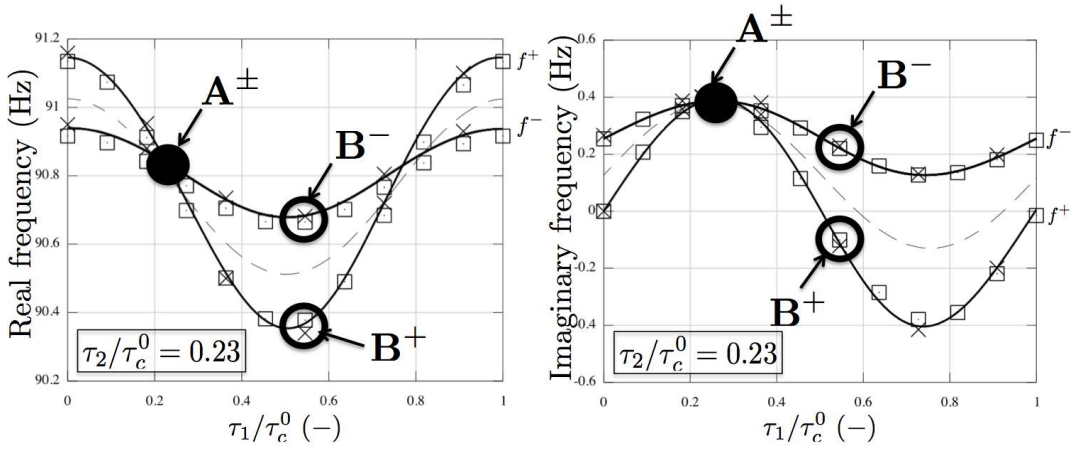

Figure 2.9: Real and imaginary part of the frequency f^+ and f^- of the two components of the first mode ($p = 1$) in the B3_C1 configuration with the pattern 121 ($\circ\bullet\circ$) and a fixed $\tau_2/\tau_c^0 = 0.23$. ——— : Atacamac (numerical resolution of Eq. (2.12)), □: Atacamac (analytical formula Eq. (2.34)), ×: AVSP, - - - : Trajectory of the modes average $(f^+ + f^-)/2$, •: Symmetric case where $\tau_1/\tau_c^0 = \tau_2/\tau_c^0 = 0.23$, τ_c^0 corresponds to $\frac{1}{f_0} \simeq 11\ ms$.

$\mathcal{S}_0 = \Gamma_1^0 - \Gamma_2^0$ (Eq. (2.26) for the $N = 3$ case with the pattern 121 ($\circ\bullet\circ$, table 2.2)):

$$\epsilon^{\pm} = \underbrace{-\frac{1}{2}\Sigma_0}_{\epsilon_{DD}} \pm \underbrace{\frac{1}{2}\mathcal{S}_0}_{\text{Splitting}} \tag{2.33}$$

$$\text{so that } \epsilon^- = -\frac{1}{2}\left(\Gamma_1^0 + 2\Gamma_2^0\right) \text{ and } \epsilon^+ = -\frac{3}{2}\Gamma_1^0 \tag{2.34}$$

These results were validated in Figs. 2.9 and 2.10 for the first azimuthal mode ($p = 1$) of the configuration $B3\_C1$ with the pattern 121 ($\circ\bullet\circ$, table 2.2) where coupling parameters are defined by Eq. (2.8).

When $\mathcal{S}_0 \neq 0$, the nominally doublet is split into two dissimilar azimuthal modes (e.g. modes denoted B^+ and B^- in Fig. 2.9 corresponding to $\tau_1/\tau_c^0 = 0.55$ and $\tau_2/\tau_c^0 = 0.23$) with close frequencies and different growth rates as mentioned in (Perrin & Charnley, 1973; Sensiau *et al.*, 2009). The term $\mathcal{S}_0 = \Gamma_1^0 - \Gamma_2^0$ for the pattern 121 ($\circ\bullet\circ$) measures the differences in flame response between the two burner types and controls the degree of degeneracy of the azimuthal mode[4].

Figure 2.11 displays the associated mode structure of the symmetric (mode A) and asymmetric (mode B) cases. For symmetric configurations, the mode structure is undetermined so that both spinning or standing modes can occur (Fig. 2.11, top). However, breaking the symmetry using two different burner types (e.g. mode B with $\tau_1/\tau_c^0 = 0.55$ and $\tau_2/\tau_c^0 = 0.23$) leads to standing modes only (Fig. 2.11, bottom).

[4]Note that some asymmetry could still give degenerate doublets (i.e. $\mathcal{S}_0 = 0$): for instance, the first order mode ($p = 1$) of a $N = 6$ burners BC configuration with the pattern ($\bullet\circ\bullet\circ\bullet\circ$) or ($\bullet\bullet\bullet\circ\circ\circ$) is a doublet with $\epsilon = -\frac{3}{2}(\Gamma_1^0 + \Gamma_2^0)$.

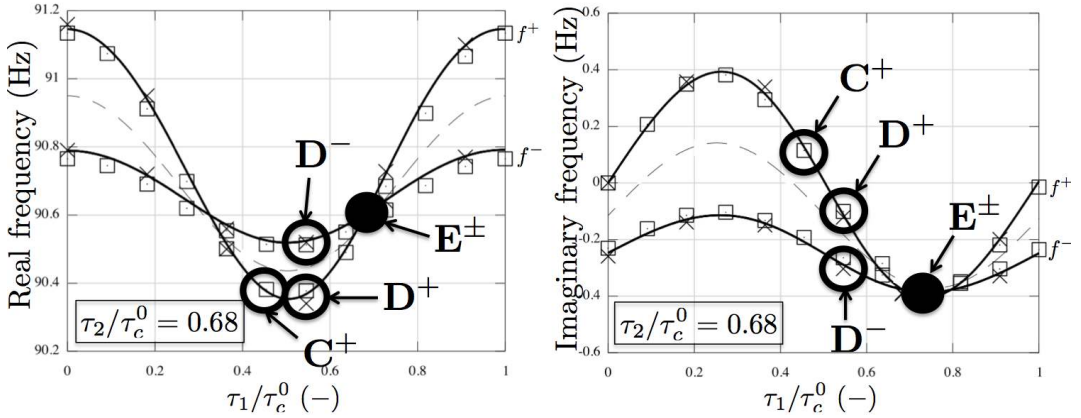

Figure 2.10: Real and imaginary part of the frequency f^+ and f^- of the two components of the first mode ($p = 1$) in the B3_C1 configuration with the pattern 121 ($\circ\bullet\circ$) and a fixed $\tau_2/\tau_c^0 = 68$. —— : Atacamac (numerical resolution of Eq. (2.12)), □: Atacamac (analytical formula Eq. (2.34)), ×: AVSP, - - - : Trajectory of the modes average $(f^+ + f^-)/2$, •: Symmetric case where $\tau_1/\tau_c^0 = \tau_2/\tau_c^0 = 0.68$, τ_c^0 corresponds to $\frac{1}{f_0} \simeq 11\ ms$.

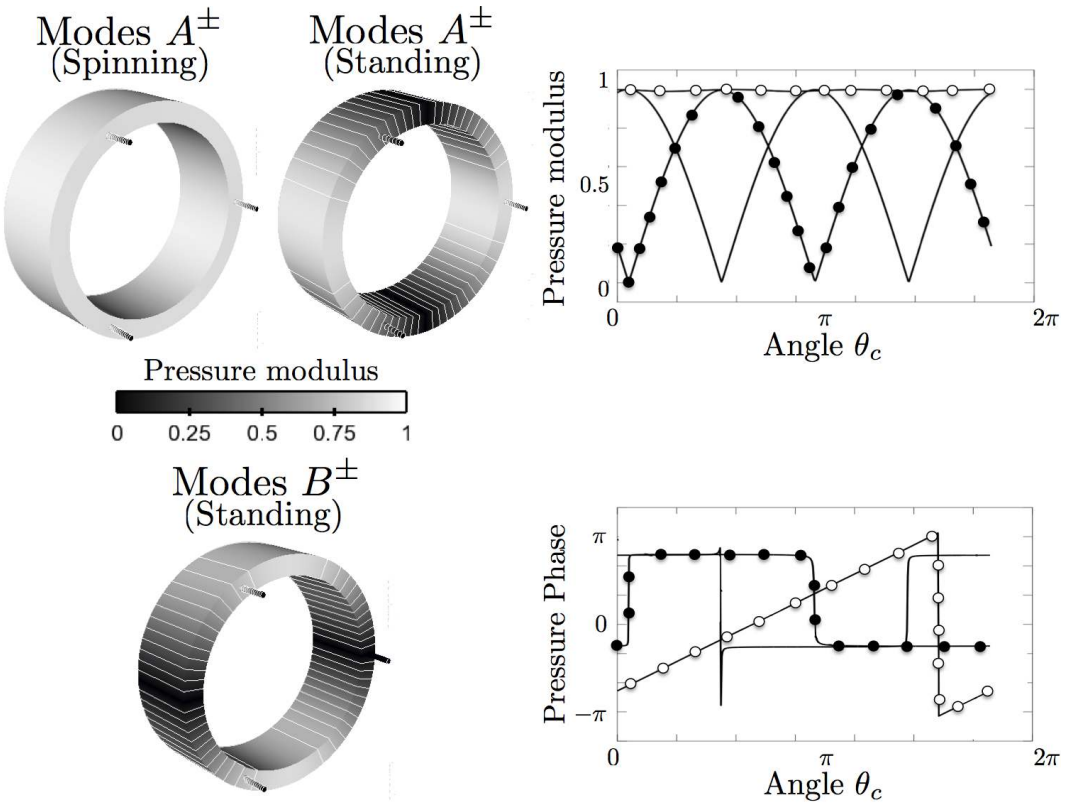

Figure 2.11: 3D and isolines of pressure modulus (left) and modulus and phase of acoustic pressure (right) of the first azimuthal modes ($p = 1$) of the asymmetric case B3_C1 with the pattern 121 ($\circ\bullet\circ$, table 2.2) in two situations: mode A ($\tau_1/\tau_c^0 = \tau_2/\tau_c^0 = 0.23$) and mode B ($\tau_1/\tau_c^0 = 0.55$ and $\tau_2/\tau_c^0 = 0.23$). ○: $A^\pm$ (spinning), •: $A^\pm$ (standing), —— : $B^\pm$ (standing)

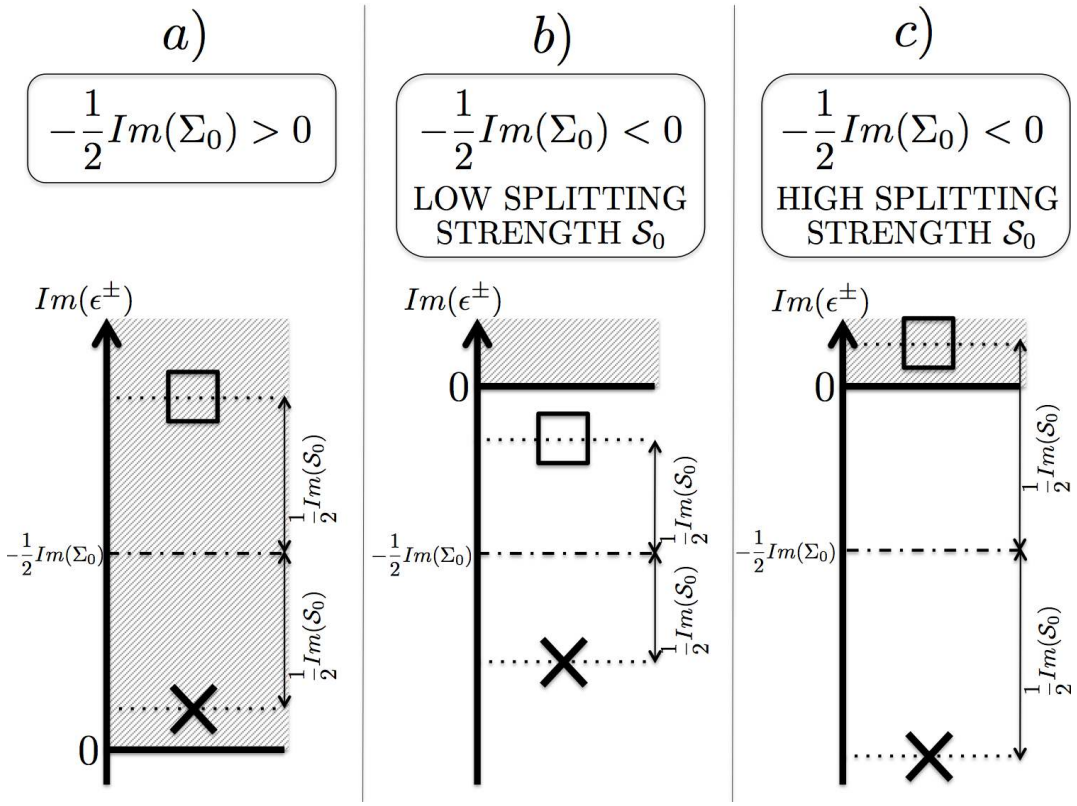

Figure 2.12: Mode stability for an annular chamber with N burners depending on the condition (2.35) and the splitting strength $\frac{1}{2}Im(\mathcal{S}_0)$. $\times$: ϵ^- and $\square$: ϵ^+. The splitting strength is $\mathcal{S}_0^2 = \sum_{i,j=1}^{N} \Gamma_i^0 \Gamma_j^0 cos\left(\frac{4p\pi}{N}(j-i)\right)$ (Eq. (2.26)) and measures the difference between the two burner types 1 and 2. Shaded areas correspond to unstable zones. a) All modes are unstable, b) all modes are stable and c) symmetry breaking makes one mode unstable: the splitting strength $\mathcal{S}_0$ must be reduced to stabilize both modes as in the situation b).

2.4.2.c Conclusion on symmetry breaking in the $N = 3$ case

Sections 2.4.2.a and 2.4.2.b show that the splitting strength $\mathcal{S}_0$ defined by Eq. (2.26) controls both the stability and the mode structure of an annular chamber ($N = 3$) where two types of burners are installed. Nevertheless, a "necessary condition" for stability can be derived independently of the splitting strength value. Indeed, the imaginary part of the modes average $\frac{1}{2}Im(\epsilon^+ + \epsilon^-)$ does not depend on the splitting strength $\mathcal{S}_0$ but only on the total coupling strength $\Sigma_0 = \sum_{i=1}^{N} \Gamma_i^0$ yielding a necessary condition for stability:

$$\frac{1}{2}I_m(\epsilon^+ + \epsilon^-) = -\frac{1}{2}I_m(\Sigma_0) < 0 \tag{2.35}$$

If this condition is not fulfilled (Fig. 2.12, left), there is no hope of stabilizing the mode since at least one of the two components of the azimuthal mode (V^+ or V^-) will remain unstable (e.g. $A^{\pm}$ and B^+ in Fig. 2.9).

For a symmetric case where the splitting strength $\mathcal{S}_0$ is zero, Eq. (2.35) is a necessary and sufficient condition to have a stable mode. However, when symmetry is broken,

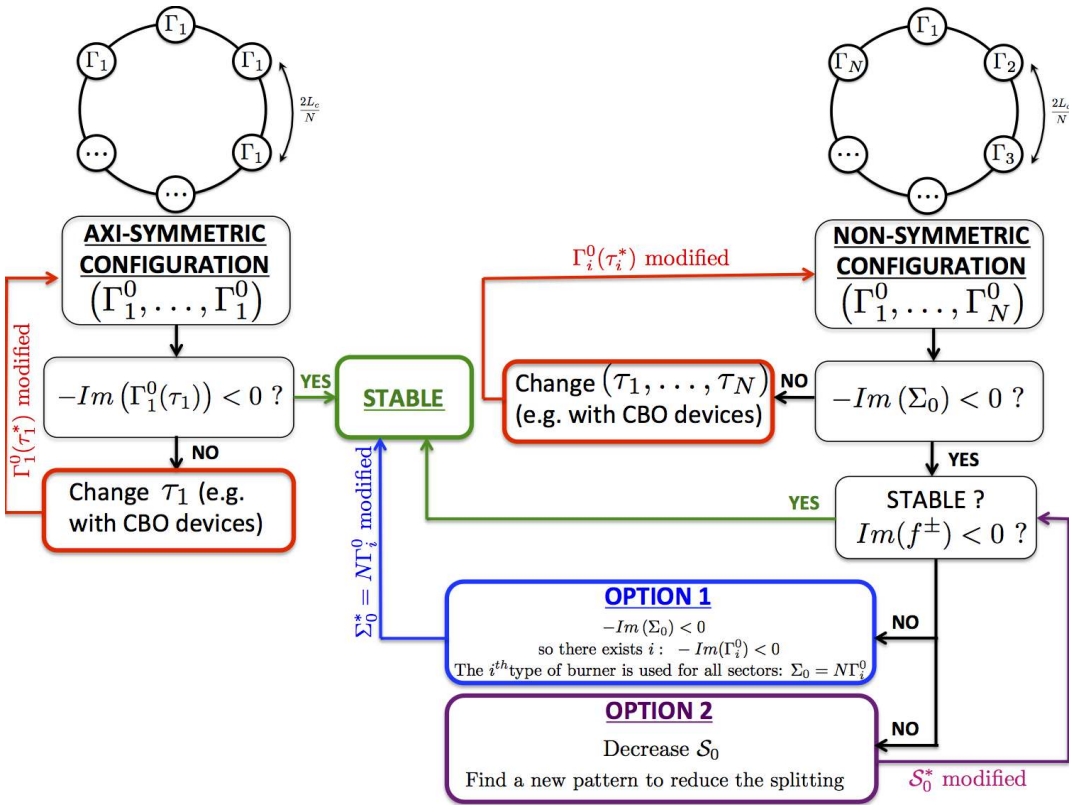

Figure 2.13: Strategy to stabilize an annular combustor.

satisfying condition (2.35) cannot guarantee stability (Fig. 2.12, middle and right). In this case, the necessary and sufficient condition becomes[5]:

$$max(Im(\epsilon^+), Im(\epsilon^-)) < 0 \tag{2.36}$$

because the splitting introduced by symmetry breaking (measured by the splitting strength $\mathcal{S}_0$) has to be taken into account. For weak splitting (Fig. 2.12, middle) the two modes V^+ and V^- remain stable (e.g. eigenmodes $D^{\pm}$ in Fig. 2.10) but for higher splitting (Fig. 2.12, right) one mode can become unstable (e.g. mode C^+ in Fig. 2.10).

2.4.3 Symmetry breaking with $N = 24$ burners

Conclusions of Section 2.4.2.c obtained with $N = 3$ burners suggest a strategy to stabilize the p^{th} mode of a general N burners configuration as described in Fig. 2.13. Axisymmetric configurations (left part of Fig. 2.13) only have one degree of freedom to stabilize the p^{th} mode which is the time-delay τ_1: if τ_1 is such that condition (2.35) is met, then the configuration is stable.

For non-symmetric configurations (right part of Fig. 2.13), however, satisfying Eq. (2.35) does not guarantee the stabilization of the configuration. In this case, the

[5]Note that $max(Im(\epsilon^+), Im(\epsilon^-)) > \frac{1}{2} I_m(\epsilon^+ + \epsilon^-)$ and for a symmetric configuration $\epsilon^+ = \epsilon^-$.

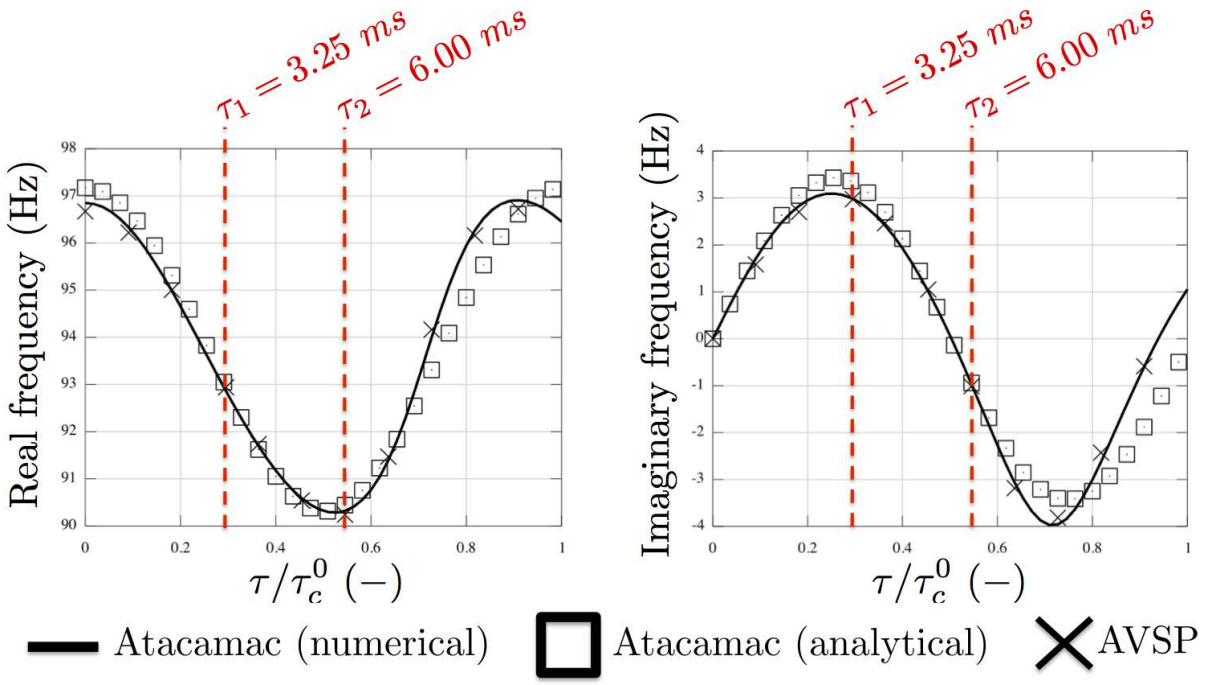

Figure 2.14: Stability map depending on τ of the first azimuthal mode ($p = 1$) of the symmetric BC configuration with 24 burners. τ_c^0 is the period of the first azimuthal mode $\tau_c^0 = 1/f^0 = \frac{2L_c}{pc^0} \simeq 11ms$

asymmetry pattern is an additional degree of freedom and two options are available to ensure the stability of the p^{th} azimuthal mode:

- **Symmetrize the configuration (Option 1)**: if condition (2.35) is satisfied, at least one kind of injector satisfies $-Im(\Gamma_i^0) < 0$: this kind of burner can be used for all sectors which leads to the mode's stabilization. This option is the most efficient method to stabilize an azimuthal mode since no splitting occurs in a symmetrized annular combustor for modes of interest.
- **Reduce the asymmetry effect (Option 2)**: Another solution is to keep the same kind of burners $(\Gamma_1^0, ..., \Gamma_N^0)$ but rearrange them to reduce the splitting of the azimuthal mode and stabilize it. Optimization can be performed to find the best pattern which leads to the smallest value of the splitting strength $\mathcal{S}_0$.

As an example, symmetry breaking is studied here for a $N = 24$ burners configuration (Berenbrink & Hoffmann, 2001; Krüger *et al.*, 2000) representative of real industrial gas turbines. First, the stability of the first azimuthal mode ($p = 1$) of the symmetric configuration is studied as a function of the time-delay τ (which is the same for all burners), with the interaction index $n = 1.0$. Results (Fig. 2.14) show a very good agreement between numerical and analytical solutions given by the 3D Helmholtz solver AVSP and ATACAMAC.

To break symmetry, two different types of burners (called Type 1 and 2) are distributed along the chamber, characterized by different time-delays, τ_1 and τ_2 (Fig. 2.14). A time delay $\tau_1 = 3.25\ ms$ is set for Type 1 burners. This corresponds approximately to the most unstable burner ($Im(f_{AVSP}) = 2.98\ s^{-1}$, in Fig. 2.14 right), which is assimilated here to

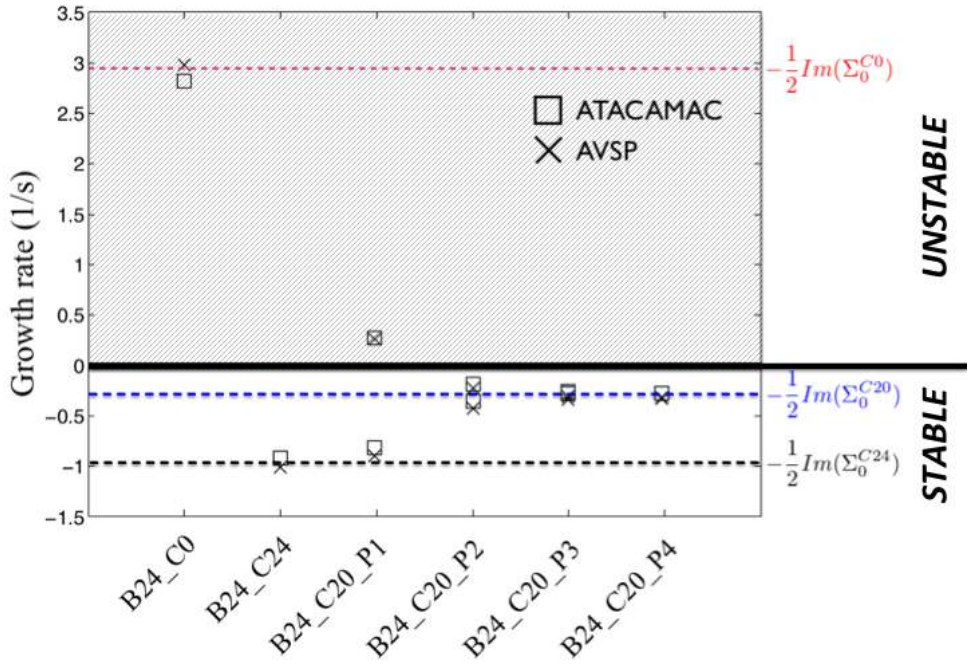

Figure 2.15: Growth rate of the first azimuthal mode ($p = 1$) for various asymmetry combination of burners with and without CBO: B24_C0 (24 noCBO burner), B24_C24 (24 CBO burners) and the four patterns B24_C20 (see table 2.2). **---** : Imaginary part of the modes average $-\frac{1}{2}I_m(\Sigma_0)$ depending on the configuration (C_0, C_{20} and C_{24})

the baseline case, a burner without CBO ($\circ$ in table 2.2). Type 2 burners correspond to systems equipped with CBOs (Cylindrical Burner Outlet). These devices are cylinder extensions which are mounted on some of the burners (Berenbrink & Hoffmann, 2001; Krüger *et al.*, 2000) to modify the flame time-delay and to stabilize the chamber. The length of the cylinder is such that the time lag τ_2 from the injection port to the flame front is increased by approximately a quarter of an acoustic period: $\tau_2 = \tau_1 + \frac{1}{4f^0} \simeq 6ms$ (since the first azimuthal mode has a frequency $f^0 \simeq 90Hz$): it corresponds to a stable burner where $Im(f_{AVSP}) = -1.01\ s^{-1}$ in Fig. 2.14 ($\bullet$ in table 2.2). Note that using 20 Type 2 burners with $\tau_2 = 6\ ms$ and 4 Type 1 burners with $\tau_1 = 3.25\ ms$ respects the necessary stability condition given by Eq. (2.35) (**---** for the configuration C_{20} in Fig. 2.15). The stability of the four patterns proposed in table 2.2 is studied using ATACAMAC and AVSP. Results are plotted in Figs. 2.15 (growth rates) and 2.16 (frequencies) for the first azimuthal mode ($p = 1$)[6]:

- **B24_C0:** This configuration corresponds to the unstable baseline case where only Type 1 burners are used: the necessary condition (Eq. (2.35)) is not satisfied. Some burners have to be changed in order to get a stable combustor.

[6]One should note that conclusions are made only for the first azimuthal modes. For other modes, the conclusion may differ since the splitting strength (Eq. (2.26)) depends on the mode order p. For instance, the pattern $P4$ leads to no splitting for the first azimuthal mode but probably generates a large splitting effect for the second azimuthal mode.

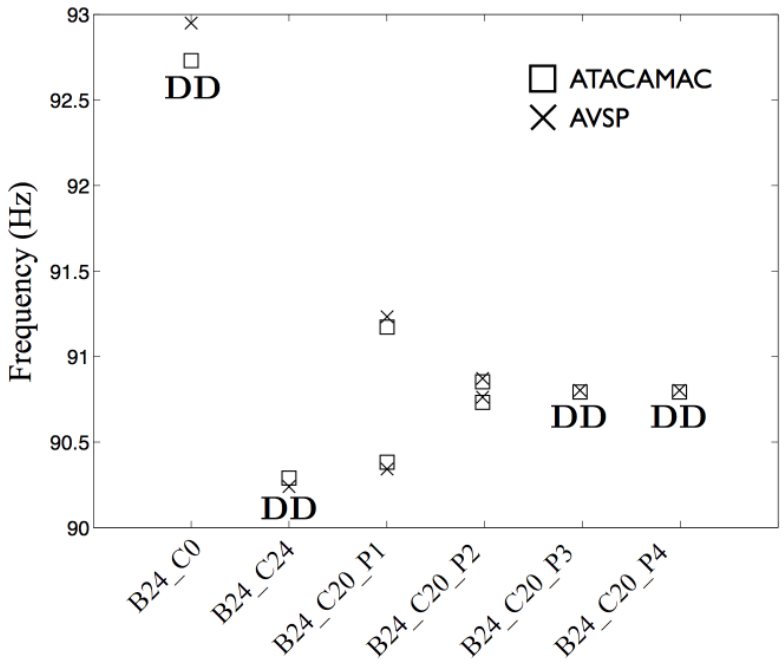

Figure 2.16: Frequencies of the first azimuthal mode ($p = 1$) for various asymmetry combination of burners with and without CBO: B24_C0 (24 noCBO burners), B24_C24 (24 CBO burners) and the four patterns B24_C20 (see table 2.2). **DD**: Degenerate Doublets.

- **B24_C20_P1:** 20 CBOs Type 2 devices have been mounted to try to stabilize the mode. The necessary condition (Eq. (2.35)) is satisfied. However this pattern has a large splitting strength $\mathcal{S}_0$. Consequently it splits azimuthal modes into two singlets with different growth rates making the first azimuthal mode unstable. This case is an excellent example of how, for asymmetric circumferential patterns, one can use stable burners that match the condition $-\frac{1}{2}I_m\left(\Sigma_0\right) < 0$ and yet, due to the asymmetry term $\mathcal{S}_0$, have an unstable mode as shown in Fig. 2.12 (right).
- **B24_C20_P2:** As suggested by Fig. 2.13, a solution to stabilize the mode is to find asymmetry patterns like $B24\_C20\_P2$ with a lower splitting strength $\mathcal{S}_0$ for which both singlets remain stable as mentioned in Fig. 2.12 (middle image).
- **B24_C20_P3 and B24_C20_P4:** The pattern $B24\_C20\_P2$ induces a low splitting strength and stabilizes the mode. However, optimal asymmetry patterns can be found which lead to no or very low splitting and therefore ensure the mode stabilization. Patterns $B24\_C20\_P3$ and $B24\_C20\_P4$ give stable degenerate doublets. In these cases, $\mathcal{S}_0 = 0$ and therefore Eq. (2.35) becomes a necessary and sufficient condition for stability. The mode is stable: $Im(f^{\pm}) \simeq -0.25\ s^{-1}$
- **B24_C24:** As explained in Fig. 2.13, the most efficient option to stabilize a mode is to symmetrize the annular combustor with burners which all satisfy the necessary condition (Eq. (2.35)), i.e. 24 burners with a CBO. The mode is very stable: $Im(f^{\pm}) \simeq -1.0\ s^{-1}$ (Fig. 2.15).

Considering the average imaginary part of the modes $-\frac{1}{2}Im(\Sigma_0)$ (--- in Fig. 2.15), it is interesting to notice that, independently of the asymmetry patterns, combining 20

NAME	ASYMMETRY PATTERN	$\mathcal{K}$
P1	●●●●●●●●●●○○○○●●●●●●●●●●	$\frac{1}{2}\sqrt{3\sqrt{3}+6} \simeq 1.67$
P2	●●●●○●●●●○●●●●●●○●●●●●○	$\frac{1}{2}\sqrt{2-\sqrt{3}} \simeq 0.26$
P3	●●●●●●●○○●●●●○○●●●●●●●●	0
P4	●●●●○●●●●●○●●●●●○●●●●●○	0

Table 2.3: Analytical expressions of the reduced splitting strength $\mathcal{K}$ for the four patterns of Tab. 2.2

CBOs and 4 noCBOs burners give potentially less stable modes than using 24 CBOs: breaking symmetry has a limited interest here compared to adding CBOs on all burners. Nevertheless, if for any reason (ignition, pollution, construction, etc.) one must keep the two types of burner, the present analytical model offers an easy way to optimize the circumferential distribution of the burners by minimizing the imaginary part of the splitting strength $Im(\mathcal{S}_0)$ to stabilize the p^{th} mode. To illustrate this idea, Figs. 2.17 and 2.18 display the effect of several asymmetry patterns on the splitting strength ($\mathcal{S}_0$) using a configuration with 20 CB0 - 4 noCBO burners. When only two types of burners are used, Eq. (2.26) simplifies into a very useful expression as shown by Appendix A. The splitting strength $\mathcal{S}_0$ becomes:

$$\mathcal{S}_0 = \overbrace{2\mathcal{K}}^{\text{Imposed by the pattern}} \underbrace{\left(\Gamma_1^0 - \Gamma_2^0\right)}_{\text{Imposed by the difference between burner types 1 and 2}} \tag{2.37}$$

where the reduced splitting strength $\mathcal{K}$ depends only on the asymmetry pattern (see table 2.3 for the analytical expression of $\mathcal{K}$ for the four patterns studied). In Eq. (2.37), Γ_1^0 and Γ_2^0 are fixed by the burner characteristics so that minimizing $\mathcal{S}_0$ to increase stability is equivalent to minimizing $\mathcal{K}$.

Consequently, an optimization process appears as a promising approach to find patterns with the minimal value of the reduced splitting strength $\mathcal{K}$ which leads to a null or very low splitting and therefore ensure the stability of the p^{th} azimuthal mode. This also highlights the potential of low-order models to perform optimization processes of large problems (here about 1,800 patterns are possible[7]) at very-low cost.

Finally, enumeration and distributions of reduced splitting strengths $\mathcal{K}$ are displayed in Fig. 2.19 depending on N_{noCBO}, the number of noCBO burner types ($N_{noCBO} = 2,\ 4$ and 6): all possible asymmetry patterns are computed where N_{noCBO} burners are chosen as burners without any CBO while the $N - N_{noCBO}$ other ones correspond to burners with a CBO. The first burner of the pattern is always without CBO to avoid circular similarities. Enumeration of patterns according to their reduced splitting strengths $\mathcal{K}$ considering the first order mode ($p = 1$) is obtained numerically using Eqs. (2.26) and (2.37). Results are adimensionalized by the total number of patterns considered to provide the distribution of splitting strengths $\mathcal{K}$. Fig. 2.19 shows that higher reduced splitting

[7]The problem addressed here corresponds to 4 no-CBO burners mixed with 20 CBO burners. When the first burner is fixed as a no-CBO type, the number of patterns is: $\binom{23}{3} = \frac{23!}{20!\times 3!} = 1,771$.

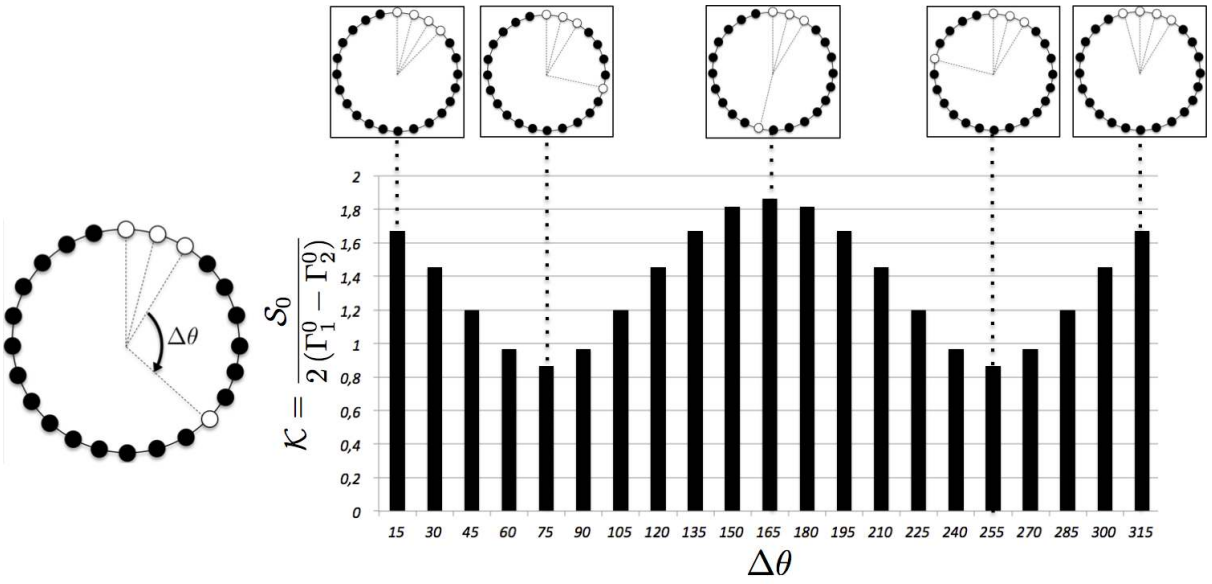

Figure 2.17: The reduced splitting strength ($\mathcal{K}$) for several patterns where three noCBO burners are kept together at the same place and the last noCBO burner's place is changed azimuthally. The splitting is then moderatly affected by the asymmetry pattern.

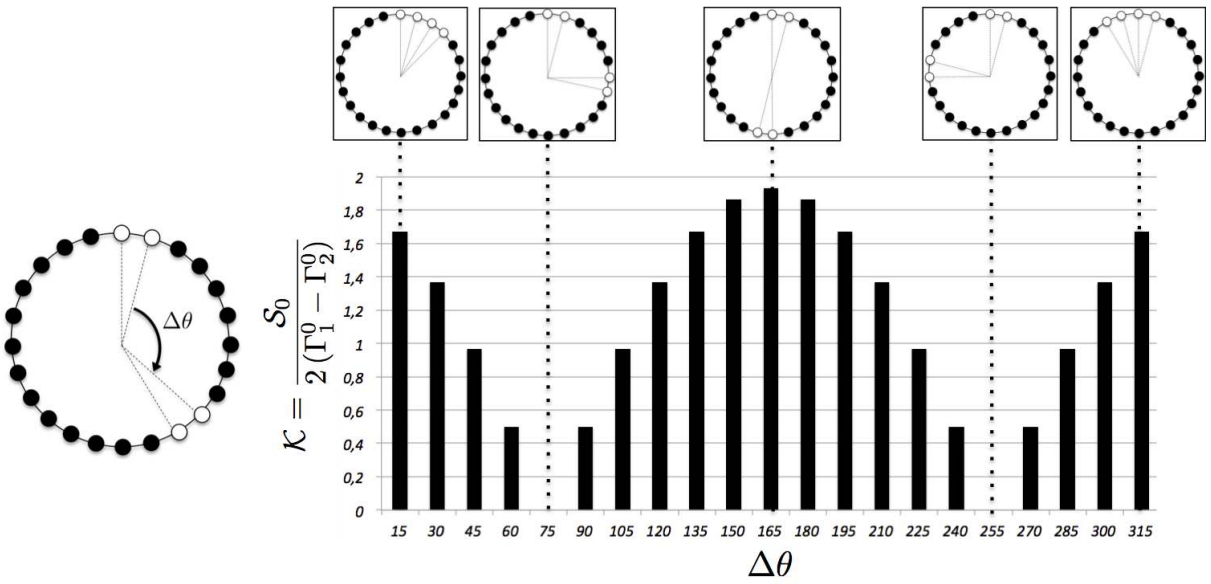

Figure 2.18: The reduced splitting strength ($\mathcal{K}$) for several patterns where two noCBO burners are kept together at the same place and the two other noCBO burner's places are changed azimuthally. The splitting is then strongly affected by the asymmetry pattern.

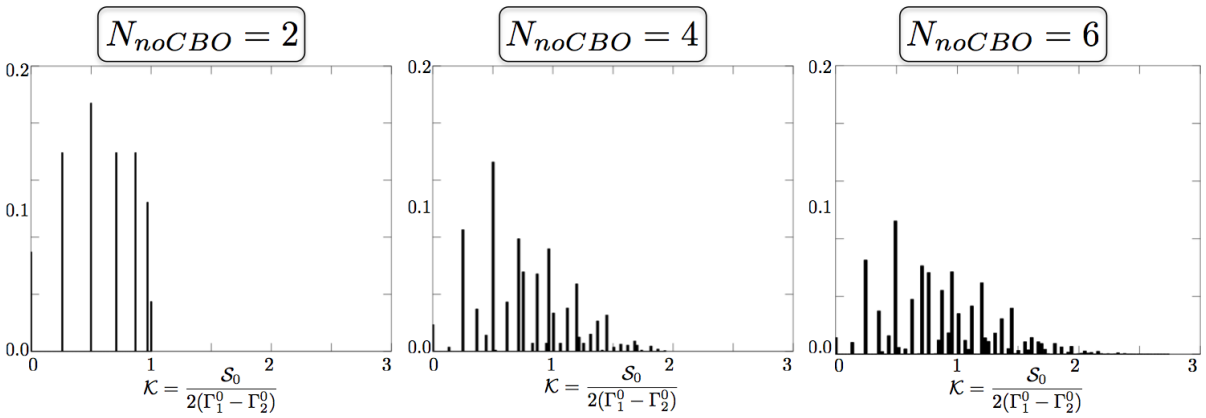

Figure 2.19: Distribution of the reduced splitting strength $\mathcal{K}$ vs. N_{noCBO}, the number of burners without CBO. All possible asymmetry patterns are used to compute each distribution: 23 patterns for $N_{noCBO} = 2$; 2275 for $N_{noCBO} = 4$ and 77804 for $N_{noCBO} = 6$).

strength values are obtained when the number of noCBO burners (N_{noCBO}) is increased. Distributions of $\mathcal{K}$ are also larger when N_{noCBO} is higher: these situations are more complex to analyze and optimize. Moreover, only a few patterns lead to a small splitting strength in this case.

Symmetry breaking can also modify the dynamic nature of the acoustic modes. The modulus and phase of acoustic pressure of the first azimuthal mode ($p = 1$) [8] are plotted in Fig. 2.20 for the four patterns of Tab. 2.2, showing two distinct behaviors.

- **Patterns P1 and P2:** Patterns P1 and P2 give non-degenerate doublets: the two components V^+ and V^- of the azimuthal mode are standing (• in Fig. 2.20) and oscillate in opposite phase with different (yet very close) frequencies (e.g. 90.3 Hz and 91.3 Hz for the pattern P1). Figure 2.15 shows that for pattern P1, one mode is amplified whereas the other one is damped, resulting in a single unstable standing mode.
- **Patterns P3 and P4:** On the other hand, asymmetry patterns leading to degenerate doublets have an undetermined mode structure: the two components V^+ and V^- of the azimuthal modes have the same frequencies so that they can be combined to obtain either a spinning (—— in Fig. 2.20), a standing (• in Fig. 2.20) or a mixed mode.

2.5 Conclusion

This chapter describes a fully analytical approach, completed by a 3D numerical validation, of the stability of azimuthal thermoacoustic modes in annular chambers. The analytical model is based on a quasi-one-dimensional zero-Mach number natural formulation where N burners are connected to a downstream annular chamber. Flames are supposed to be compact and are modeled using a Flame Transfer Function, character-

[8] Only one of the two components of a given azimuthal mode is shown in Fig. 2.20.

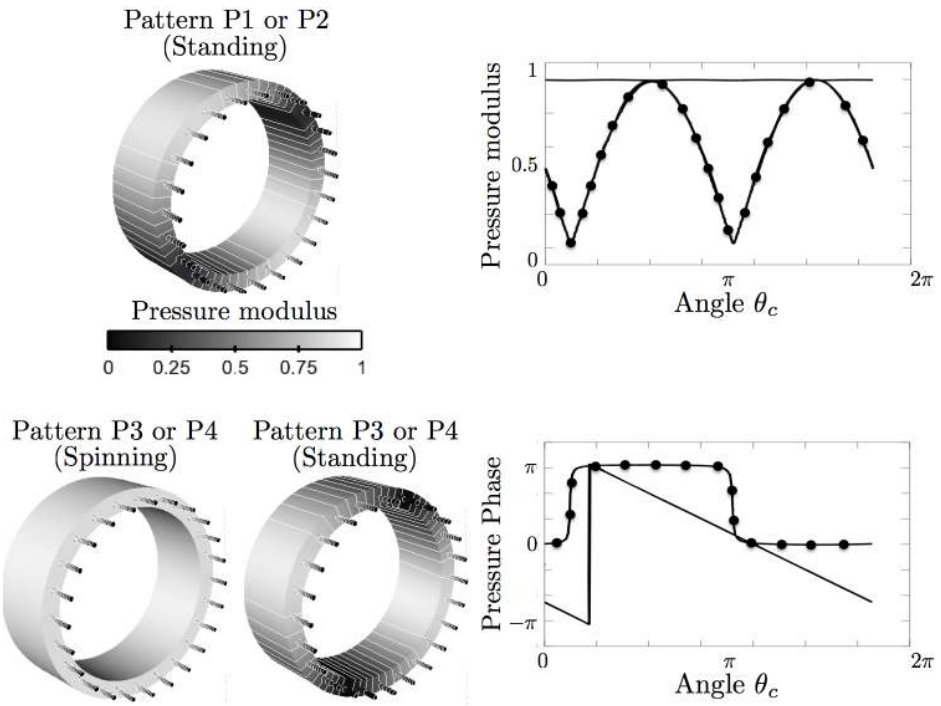

Figure 2.20: Effect of the asymmetry pattern on the azimuthal mode nature. 3D and isolines of the pressure modulus (left) and modulus and phase of the acoustic pressure over the circumference (right). P1 or P3: necessarily standing (•) ; P3 or P4: any combination of standing (•) or spinning(———).

ized by a coupling factor and a phase shift. Manipulation of the corresponding acoustic equations yields a simple dispersion relation which can be solved analytically in specific situations where coupling factors are small (weak coupling). This analytical approach allows to predict the stability of azimuthal modes in symmetric cases where all burners are identical but also to study cases where different burner types are mixed in a chamber, using a predefinite pattern. The analytical method highlights the importance of two parameters:

- A "coupling strength" Σ_0 which is the sum of the individual coupling factors Γ_i^0 of each burner and controls the stability at first order.
- A "splitting strength" $\mathcal{S}_0$ defined in equation(2.26) which affects the stability and the mode structure and depends on a combination of the coupling parameters of each burner.

First, a symmetric configuration with N identical burners with null inlet impedances (i.e. $p' = 0$) is studied. Only two mode behaviors are observed: degenerate doublets and non-degenerate singlets, the latter being capable of generating warbles (low frequency oscillations due to a non-degenerate mode (Perrin & Charnley, 1973)). Then, a non-symmetric case where two different types of burners are distributed in the chamber is studied: symmetry breaking is proved to modify the azimuthal modes behavior in a simple case with only three burners in an annular chamber. The staging patterns can split nominally degenerate azimuthal modes (doublets) into non-degenerate pairs (singlets), a situation already mentioned in the literature and observed in recent Helmholtz

simulations (Sensiau *et al.*, 2009).

Finally, the effect of the asymmetry pattern itself is investigated in a $N = 24$ burners case representative of industrial gas turbines. A very good agreement is found for all cases between analytical (ATACAMAC) and numerical (AVSP) results, obtained with a 3D Helmholtz solver. Results are compared to experimental observations where CBOs (Cylindrical Burner Outlet) are added to certain burners to control combustion instabilities. A simple criterion is derived to provide a necessary condition to stabilize an annular combustor. Since the asymmetry pattern does not appear in this criterion and the splitting strength is the only control parameter, this shows that symmetry breaking can modify the mode nature but has no real impact on mitigating combustion instabilities in annular chambers. The best method to control a chamber with $N = 24$ sectors is to use 24 identical burners with an FTF leading to stable azimuthal modes. However if keeping only one type of burner is not possible, a strategy to stabilize the mode is proposed: find an optimal pattern which leads to a low splitting of the corresponding azimuthal mode. The general character of this conclusion[9] is limited by the low coupling assumption which implies no interaction between burners. Strongly coupled situations where burners interfere (Bauerheim *et al.*, 2014*d*; Worth & Dawson, 2013*b*) may lead to an effect of the asymmetry pattern on the overall stabilization of the annular engines.

[9] A summary of this method is provided in Appendix B: it allows the computation of the "coupling strength", the "splitting strength", the frequency and the growth rates of all modes as soon as the FTF of each burner is known.

Chapter 3

Theoretical study of mean azimuthal flow and asymmetry effects on thermo-acoustic modes in annular combustors

Contents

The objective of this chapter is to extend the previous analytical model for BC configurations to capture flow symmetry (FS) breaking and investigate its effect on the frequency and nature (spinning, standing or mixed) of azimuthal modes. FS breaking is due to the mean azimuthal flow induced by swirlers or effusion cooling systems. The ATACAMAC (Analytical Tool to Analyze and Control Azimuthal Modes in Annular Chambers) methodology is applied using the linearized acoustic equations with a steady and uniform azimuthal mean flow. It provides an analytical implicit dispersion relation which can be solved numerically. A fully analytical resolution is possible when the annular chamber is weakly coupled to the burners. Results show that symmetry breaking, either by mixing burners types (GS) or with a mean azimuthal flow (FS), splits the azimuthal modes into two waves with different frequencies and structures. GS breaking promotes standing modes but adding even a low azimuthal mean flow fosters spinning modes so that the azimuthal mean flow must be taken into account to study azimuthal modes.

3.1 Introduction

The previous chapter has emphasized on an analytical tool to study geometrical symmetry breaking in BC (Burners+Chamber) annular combustors showing that breaking symmetry affects the frequency, the stability as well as the nature of azimuthal modes. In particular, the nature of azimuthal modes has been the topic of multiple past studies since the pioneering works of companies like Siemens (Krebs *et al.*, 2002) or Alstom (Noiray *et al.*, 2011) who showed that both spinning or standing azimuthal modes could be observed in an annular gas turbine. Five years ago, the development of powerful LES techniques applied to full annular combustors (Staffelbach *et al.*, 2009; Wolf *et al.*, 2012) showed that azimuthal modes could change nature randomly, evolving from spinning to standing structure at random instants. Experiments have also been developed (Bourgouin *et al.*, 2013; Worth & Dawson, 2013*b*), confirming LES results but also raising additional questions, for example linked to the effect of outlet conditions on the development of modes. Various theories have been proposed (Noiray *et al.*, 2011; Noiray & Schuermans, 2013; Schuermans *et al.*, 2006; Sensiau *et al.*, 2009; Ghirardo & Juniper, 2013), focusing on two questions: (1) what controls the nature and the occurrence of azimuthal modes ? and (2) is it possible to suppress them ? Most solutions focus on breaking symmetry, for example by mixing burners with different unsteady responses in a given chamber as studied in Chapter 2.

Analytical studies are usually performed to determine the stability of the configuration but can also predict linear effects on the mode structure. Non-linear theories based on linearized Galerkin methods (Noiray *et al.*, 2011; Ghirardo & Juniper, 2013) are also developed where the configuration is usually reduced to a simple annulus with zero or an infinite number of burners and no plenum but the acoustic-flame behavior is non-linear and modeled using a Flame Describing Function (FDF). Non-linear approaches are especially designed to study limit cycles and mode structures but they require simplifications.

Linear effects of geometrical symmetry breaking on more realistic configurations, due to different burner types, has been proved to change the nature of azimuthal modes (Chapter 2) but other elements may also break the rotation symmetry. For example, the flow itself can possess a non-symmetric component which breaks the symmetry of the annular configuration and may modify both the stability and the mode structure of the system, as observed in recent experiments (Worth & Dawson, 2013*b*,*a*). Therefore, this chapter is dedicated to the investigation of this second symmetry breaking mechanism.

This chapter extends the previous linear approach to investigate two linear mechanisms controlling azimuthal by breaking symmetry: 1) Geometrical symmetry (GS) breaking studied in Chapter 2 by mixing burners with different responses and 2) Flow symmetry breaking by introducing a mean swirling motion (SM) in the annular chamber. These two mechanisms have to be studied together to highlight their interactions and respective strength on mode structures and frequencies. The SM mechanism is shown to play a strong role: it makes the period of the two modes (co-rotating with the mean swirl and counter rotating) different because propagating at $c+w$ or $c-w$ (where w is the swirl velocity and c the sound speed in the chamber). This 'splits' azimuthal modes (which are usually degenerate at zero Mach number) into two distinct modes. This effect is dominant compared to GS breaking and results suggest that the nature of azimuthal modes in annular chambers cannot be analyzed in the zero Mach number limit but must incorporate the effects of a mean azimuthal velocity. All applications are performed for a chamber containing 4 burners but conclusions are expected to be valid for real chambers ($N \simeq 10$ to 30). The configuration corresponds to a BC (Burners+Chamber) case where the plenum is not included in the analysis.

3.2 The analytical model

3.2.1 Model description

A similar configuration studied in Chapter 2, where N burners feed a 1D annular chamber (Fig. 3.1) is investigated in this Chapter. Different types of burners are used to study GS breaking (Section 3.3.4) but here a mean azimuthal flow is imposed in the chamber (Fig. 3.1) to study SM breaking (Section 3.3.3). This mean flow field is supposed to be one dimensional, steady and uniform:

$$\vec{u_0}(x,t) = u_0(x,t)\vec{e_\theta} = M_\theta c^0 \vec{e_\theta} \tag{3.1}$$

where $\vec{e_\theta}$ is the azimuthal vector and $M_\theta = u_0/c^0$ is the azimuthal Mach number. Such swirling motions are often observed in annular chambers because all swirlers have the same rotation direction. In many recent chamber designs, where effusion systems are used to introduce additional azimuthal rotation and modify residence times, the azimuthal local Mach number can be fairly large (M_θ up to $0.01-0.1$). Even if this azimuthal flow is not one-dimensional (for instance, swirlers induce an azimuthal flow in opposite directions in the outer and inner part of the annular rig leading to a low bulk swirl and a complex interaction between the acoustic mode and the swirl motion (Worth & Dawson, 2013*b*,*a*)),

this present study will consider a simplified case with a one-dimensional mean azimuthal flow to unravel the interaction between acoustic with such a swirl motion.

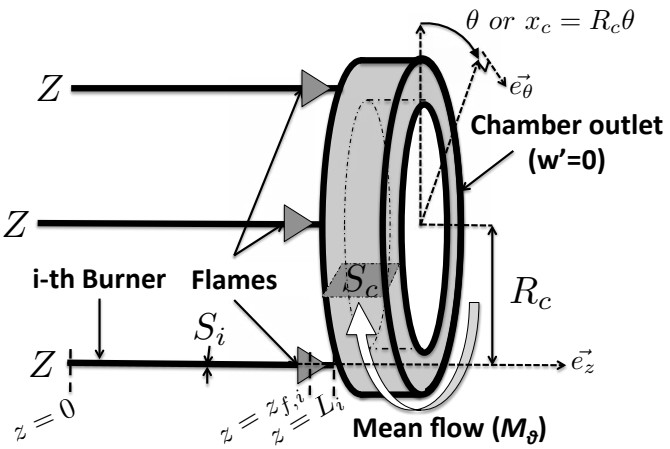

Figure 3.1: BC configuration to study unstable modes in annular chambers with a steady and uniform azimuthal flow (constant Mach number M_θ).

3.2.2 ATACAMAC methodology and analytical dispersion relation

The ATACAMAC (Analytical Tool to Analyze and Control Azimuthal Modes in Annular Chambers) (Parmentier *et al.*, 2012; Bauerheim *et al.*, 2014*d*) methodology proposed in Chapter 2 is used to reduce the size of the system by splitting the annular combustor into N sectors (Fig. 3.2). Each sector is split into two parts: an azimuthal propagation in the annular chamber and an interaction area at the burner/chamber junction. which now depends on the mean azimuthal Mach number M_θ.

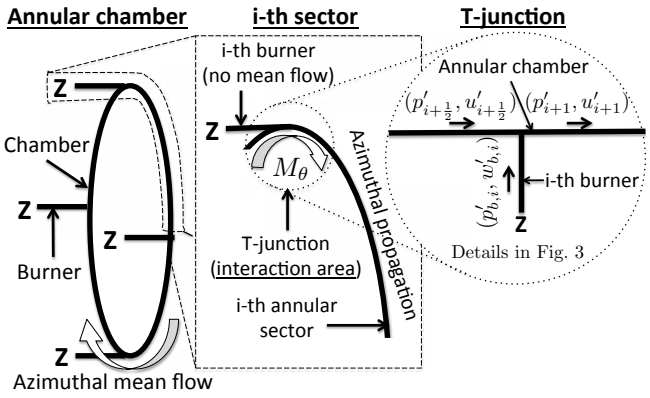

Figure 3.2: Configuration with $N = 4$ burners (left) and zoom on i^{th} sector (middle) and i^{th} T-junction (right).

3.2.2.a Interaction area at the burner/chamber junction

The area where the acoustic interaction between the i^{th} burner and the annular chamber occurs (Fig. 3.2) is compact (O'Connor & T.Lieuwen, 2012*c*). The effect of the i^{th} burner on the acoustic field can be modeled by a translated impedance $Z_{tr}(Z, \alpha, L_i, n_i, \tau_i) = \frac{p'_{b,i}(z=Li)}{\rho^0 c^0 w'_{b,i}(z=L_i)}$ (Blimbaum *et al.*, 2012).

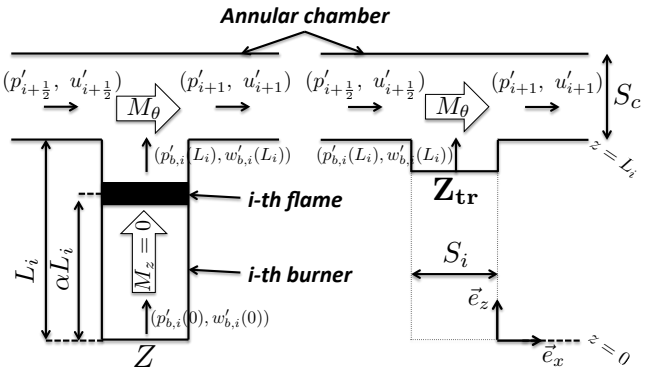

Figure 3.3: Equivalent impedance of the i^{th} burner: the translated impedance Z_{tr} takes into account the upstream impedance Z, the propagation in the cold ($0 < z < \alpha L_i$) and hot ($\alpha L_i < z < L_i$) parts of the burner as well as the active flame (at $z = \alpha L_i$).

The linearized equations of conservation of mass and momentum for isentropic ($p' = c^{0^2}\rho'$) configurations with non-zero azimuthal Mach number (Fig. 3.3) discussed in (Stow & Dowling, 2003; Dowling, 1995; Stow & Dowling, 2001; Motheau *et al.*, 2012) are applied at the T-junction (mean flow is added only in the chamber but no mean flow is introduced in the burners along the longitudinal direction $\vec{z}$, i.e. $M_z = 0$) which contains only burnt gases (Figs. 3.2 and 3.3):

$$m'_{i+\frac{1}{2}} + m'_{b,i} = m'_{i+1} \quad \text{and} \quad D'_{i+\frac{1}{2}} = D'_{i+1} = D'_b \tag{3.2}$$

where $m' = (\bar{\rho}u' + \rho'\bar{u})S$ is the linearized mass flow rate through the surface S and $D' = p' + 2\bar{\rho}\bar{u}u' + \rho'\bar{u}^2$ is the linearized acoustic momentum where $\bar{f}$ and f' designates the mean and fluctuating quantity of f respectively.

With an azimuthal mean flow in the chamber, these equations become at the T-junction:

$$[p'_{i+1} - p'_{i+\frac{1}{2}}]M_\theta S_c = \rho^0 c^0 [u'_{i+\frac{1}{2}} S_c + w'_{b,i}(z = L_i)S_i - u'_{i+1} S_c] \tag{3.3}$$

$$p'_{i+\frac{1}{2}}(1 + M_\theta^2) + 2\rho^0 c^0 M_\theta u'_{i+\frac{1}{2}} = p'_{b,i}(z = L_i) = p'_{i+1}(1 + M_\theta^2) + 2\rho^0 c^0 M_\theta u'_{i+1} \tag{3.4}$$

or in matrix form:

$$\begin{bmatrix} p' \\ -j\rho^0 c^0 u' \end{bmatrix}_{i+1} = T_i \begin{bmatrix} p' \\ -j\rho^0 c^0 u' \end{bmatrix}_{i+\frac{1}{2}} \tag{3.5}$$

where the interaction matrix T_i is:

$$T_i = I_d + \mathcal{G}_i \begin{bmatrix} -4j\frac{M_\theta}{1+M_\theta^2} & 8\left(\frac{M_\theta}{1+M_\theta^2}\right)^2 \\ 2 & 4j\frac{M_\theta}{1+M_\theta^2} \end{bmatrix} \tag{3.6}$$

where $\mathcal{G}_i = \frac{(1+M_\theta^2)^2}{1-M_\theta^2}\Gamma_i$ is the coupling parameter at non-null Mach number and $j = \sqrt{-1}$. It is related to the coupling parameter without mean flow Γ_i introduced in Chapter 2 (Parmentier *et al.*, 2012; Bauerheim *et al.*, 2014*d*; Palies, 2010; Schuller *et al.*, 2012) linked to the equivalent impedance Z_{tr} of the i^{th} burner (Fig. 3.3):

$$\Gamma_i = S_c/(2jS_iZ_{tr}) \tag{3.7}$$

3.2.2.b Propagation in the i^{th} annular sector

Pressure and velocity fluctuations can be written at any location x in the annular chamber as (Parmentier *et al.*, 2012; Krebs *et al.*, 2001):

$$\begin{cases} p'_x &= (Ae^{jk^+x} + Be^{-jk^-x})e^{-j\omega t} \\ \rho^0 c^0 u'_x &= (Ae^{jk^+x} - Be^{-jk^-x})e^{-j\omega t} \end{cases} \tag{3.8}$$

where $k^\pm = \frac{\omega/c^0}{1\pm M_\theta}$.

Equation (3.8) yields:

$$\begin{bmatrix} p' \\ -j\rho^0 c^0 u' \end{bmatrix}_{x+\Delta x} = R(\Delta x) \begin{bmatrix} p' \\ -j\rho^0 c^0 u' \end{bmatrix}_x \tag{3.9}$$

where the propagation matrix $R(\Delta x)$ is:

$$R(\Delta x) = \frac{e^{jk^+\Delta x}}{2}\begin{bmatrix} 1 & j \\ -j & 1 \end{bmatrix} + \frac{e^{-jk^-\Delta x}}{2}\begin{bmatrix} 1 & -j \\ j & 1 \end{bmatrix} \tag{3.10}$$

Knowing that for each sector the azimuthal propagation distance is the same ($\Delta x = 2L_c/N$), all propagation matrices are equal and written $R(2L_c/N)$.

3.2.2.c Analytical dispersion relation

Since interaction (Eq. (3.5)) and propagation (Eq. (3.10)) matrices are known, the transfer matrix M_i of the i^{th} sector can be obtained:

$$\begin{bmatrix} p' \\ -j\rho^0 c^0 u' \end{bmatrix}_{i+1} = \underbrace{[T_i].[R(2L_c/N)]}_{M_i} \begin{bmatrix} p' \\ -j\rho^0 c^0 u' \end{bmatrix}_i \tag{3.11}$$

Finally, the periodicity of the system and the equation of one sector (Eq. (3.11)) lead to:

$$\begin{bmatrix} p' \\ -j\rho^0 c^0 u' \end{bmatrix}_N = \left(\prod_{i=N}^{1} M_i\right) \begin{bmatrix} p' \\ -j\rho^0 c^0 u' \end{bmatrix}_N \tag{3.12}$$

The system (3.12) has non trivial solutions only if its determinant is null leading to an implicit analytical dispersion relation for the frequency f:

$$det\left(\prod_{i=N}^{1} M_i - I_d\right) = 0 \tag{3.13}$$

where I_d is the 2-by-2 identity matrix.

3.2.3 Analytical resolution for a chamber with $N = 4$ burners

The implicit dispersion relation (Eq. (3.13)) can be solved analytically using an asymptotic approach for low coupling factor Γ_i or $\mathcal{G}_i$:

$$\forall i \in [1, N],\ \|\mathcal{G}_i\| \ll 1 \tag{3.14}$$

The matrix $M = \prod_{i=4}^{1} M_i = M_2 M_1 M_2 M_1$ corresponds to the geometrical asymmetry pattern 1212 and to the symmetric configuration if $M_1 = M_2$ is enforced ($\Gamma_1 = \Gamma_2$). The Taylor expansion of this matrix (called $\widetilde{M}$) around the frequency of the annular rig alone ($f = f^0 + \delta f$ (Parmentier *et al.*, 2012; Bauerheim *et al.*, 2014*d*) where $f^0 = c^0/2L_c$ for the first azimuthal mode) at first order assuming low coupling factors (Eq. (3.14)) and low Mach number $M_\theta \ll 1$ is:

$$\widetilde{\prod_{i=4}^{1} M_i} = I_d + 2\pi \begin{bmatrix} -jM_\theta & -\frac{2L_c}{c^0}\delta f - \frac{2}{\pi}\mathcal{G}_1^{0,\pm M_\theta} \\ \frac{2L_c}{c^0}\delta f + \frac{2}{\pi}\mathcal{G}_2^{0,\pm M_\theta} & -jM_\theta \end{bmatrix} \tag{3.15}$$

where $\mathcal{G}_1^{0,\pm M_\theta}$ and $\mathcal{G}_2^{0,\pm M_\theta}$ are the values of the coupling parameters $\mathcal{G}_1$ and $\mathcal{G}_2$ evaluated at the frequency $f^0(1 \pm M_\theta)$.

Equation (3.15) yields an explicit dispersion relation:

$$\left(2\pi\frac{L_c}{c^0}\delta f\right)^2 + 4\pi\frac{L_c}{c^0}\left(\mathcal{G}_1^{0,\pm M_\theta} + \mathcal{G}_2^{0,\pm M_\theta}\right)\delta f + 4\mathcal{G}_1^{0,\pm M_\theta}\mathcal{G}_2^{0,\pm M_\theta} - \pi^2 M_\theta^2 = 0 \tag{3.16}$$

Frequencies of the first azimuthal mode can be obtained by solving the quadratic equation (Eq. (3.16)). They are recast using nondimensionalized numbers such as the mean azimuthal Mach number, the total coupling factor ($\Sigma_0 = 2(\mathcal{G}_1^{0,\pm M_\theta} + \mathcal{G}_2^{0,\pm M_\theta})$) and the splitting strength ($\mathcal{S}$) defined in Chapter 2 for the pattern 1212 as:

$$\mathcal{S} = 2(\mathcal{G}_1^{0,\pm M_\theta} - \mathcal{G}_2^{0,\pm M_\theta}) \tag{3.17}$$

so that solutions of Eq. (3.16) are:

$$\delta f_{1,2} = -c^0\left(\Sigma_0 \pm \sqrt{\mathcal{S}^2 + 4\pi^2 M_\theta^2}\right)/4\pi L_c \tag{3.18}$$

where $+$ corresponds to Wave 1 (co-rotating if $M_\theta \neq 0$) and $-$ to Wave 2 (counter-rotating if $M_\theta \neq 0$): the frequencies are split.

The eigenspace associated to each frequency ($f_1 = f^0 + \delta f_1$ and $f_2 = f^0 + \delta f_2$) is one-dimensional and the mode nature is fixed by M_θ and $\|\mathcal{S}\|$. The system defined by Eq. (3.12) can be evaluated at the frequencies f_1 and f_2 obtained in Eq. (3.18) which provides the relation:

$$\begin{bmatrix} -2\pi j M_\theta & -\mathcal{S} \pm \mathcal{S}_M \\ -\mathcal{S} \mp \mathcal{S}_M & -2\pi j M_\theta \end{bmatrix} \begin{bmatrix} p' \\ -j\rho^0 c^0 u' \end{bmatrix}_4 = \begin{bmatrix} 0 \\ 0 \end{bmatrix} \tag{3.19}$$

where $\mathcal{S}_M = \sqrt{\mathcal{S}^2 + 4\pi^2 M_\theta^2}$ corresponds to the interaction of GS ($\mathcal{S}$) and SM (M_θ) breaking.

For Waves 1 and 2, Eq. (3.19) gives the ratio $\frac{q^+}{q^-} = \frac{p'_4 + \rho^0 c^0 u'_4}{p'_4 - \rho^0 c^0 u'_4}$:

$$\frac{q^+}{q^-} = \frac{-\mathcal{S}}{2\pi M_\theta + \mathcal{S}_M} \quad \text{and} \quad \frac{q^+}{q^-} = \frac{2\pi M_\theta + \mathcal{S}_M}{\mathcal{S}} \tag{3.20}$$

Consequently the frequency and nature of azimuthal modes are controlled by the splitting strength $\|\mathcal{S}\|$, the Mach number M_θ and their interaction $\|\mathcal{S}_M\|$.

3.3 FS and GS breaking in annular combustors

3.3.1 Description of the configurations

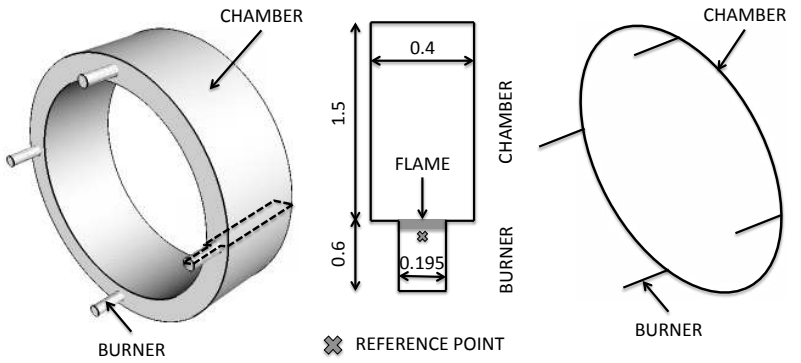

a) 3D view of the BC configuration b) Axial cut c) 1D model for ATACAMAC

Figure 3.4: Configuration with $N = 4$ burners

The effect of geometrical and flow symmetry breaking on frequency and nature of azimuthal modes will be investigated using the analytical results (Eqs. (3.18) and (3.20)) in an idealized annular combustor with $N = 4$ burners (Fig. 3.4). Only the first azimuthal mode is considered. Physical and geometrical parameters are defined in Tab. 3.1 and Fig. 3.4. The upstream impedance Z is set to zero to mimic a large plenum connected to the burners and the flames are placed at the burner/chamber junction ($\alpha = 1$) which leads to (Bauerheim *et al.*, 2014*d*):

$$\Gamma_i = -\frac{1}{2}\frac{S_i}{S_c}\frac{\rho^0 c^0}{\rho_u^0 c_u^0}\left(1 + n_i e^{j\omega\tau_i}\right)\text{cotan}(k_u L_i) \tag{3.21}$$

where $k_u = \omega/c_u$.

Four different cases (Fig. 3.5) are studied in this chapter:

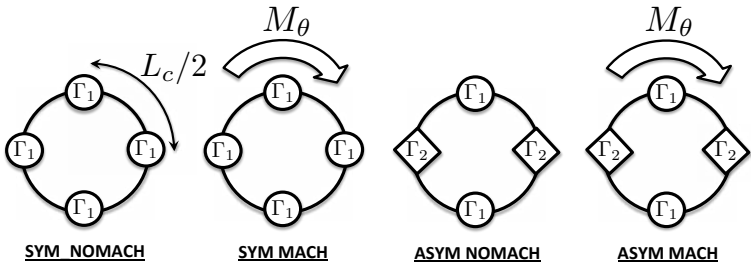

Figure 3.5: Configurations leading to symmetry breaking

- **Sym-NoMach:** First, a symmetric configuration where burners and flames are identical is studied (Section 3.3.2, (Parmentier *et al.*, 2012)). The Mach number M_θ is zero.
- **Sym-Mach:** A constant mean azimuthal flow ($M_\theta \neq 0$) is added to the previous case.
- **Asym-NoMach:** At zero Mach number ($M_\theta = 0$), the configuration is disymmetrized using two burner types with different Flame Transfer Functions (n_1, τ_1) and (n_2, τ_2) with the pattern 1212 (Section 3.3.4).
- **Asym-Mach:** Finally, an azimuthal mean flow corresponding to a mean Mach number M_θ is added to the previous case (Section 3.3.5).

Chamber	L_c	6.59	m
	S_c	0.6	m^2
Burner	L_i^0	0.6	m
	S_i	0.01	m^2
Fresh gases	ρ_u^0	9.79	kg/m^3
	c_u^0	743	m/s
Burnt gases	ρ^0	3.81	kg/m^3
	c^0	1191	m/s
Flame	n_i	1.57	$-$
	τ_i	*variable*	s

Table 3.1: Parameters used for numerical applications corresponding to a large scale industrial gas turbine.

Analytical results are systematically compared to numerical solutions of the eigenproblem (3.12): the frequencies are computed using a non-linear solver (Newton-Raphson) searching for zeros of $det\left(\prod_{i=N}^{1} M_i - I_d\right)$.

Knowing the frequency, the state at the N^{th} burner location ($V_N = (p'_N, -j\rho^0 c^0 u'_N)^T$) is computed as an eigenvector satisfying Eq. (3.12). The acoustic pressure p'_N and velocity u'_N are propagated at any azimuthal location x in the chamber using Eqs. (3.5) and (3.10).

The azimuthal variation of the pressure modulus ($\|p'\|$) and phase ($\phi = \arg(p')$) with the azimuthal coordinate (x or θ) indicates the mode nature: spinning (linear phase), standing (constant phase) or mixed. A structure diagram ($\|p'\|\cos(\phi)$,$\|p'\|\sin(\phi)$, M_θ or $\|\mathcal{S}\|$) is constructed to track the evolution of the mode structure with the Mach number (M_θ) or the splitting strength ($\|\mathcal{S}\|$). It allows to compare effect of GS breaking already studied in the previous chapter with FS breaking in terms of mode structure. Analytical results with no mean flow will be also validated using a 3D acoustic solver called AVSP devoted to the resolution of acoustic modes at zero Mach number of combustion chambers (Nicoud *et al.*, 2007).

3.3.2 Symmetric case with no mean flow (Sym NoMach)

All 4 burners are identical thus matrices $M_i = T_i R_i$ and coupling factors Γ_i are all equal (the subscript i can be omitted here). The dispersion relation (Eq. (3.16) with $\|\mathcal{S}\| = 0$ and $M_\theta = 0$) has a double root: the mode is degenerate and the expression of the first azimuthal mode frequency (Eq. (3.18)) reduces to:

$$f = \underbrace{c^0/(2L_c)}_{f^0} - \underbrace{c^0\Gamma^0/(\pi L_c)}_{\delta f} \tag{3.22}$$

Eq. (3.22) is compared to results provided by the numerical resolution of Eq. (3.13) and the 3D acoustic solver in Fig. 3.6 showing a very good agreement on frequency and growth rate.

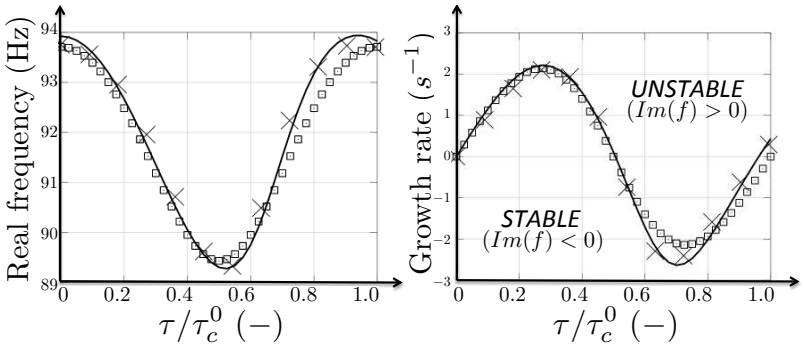

Figure 3.6: Freqency (left) and growth rate (right) vs normalized time-delay τ/τ_c^0 (where $\tau_c^0 = 1/f^0$) of the first azimuthal mode in a configuration with $N = 4$ burners. —— : Atacamac (numerical resolution Eq. (3.13)), □: Atacamac (analytical - Eq. (3.22)) and ×: 3D acoustic solver

In a symmetric configuration, the eigenspace associated to the first azimuthal mode is two-dimensional (the matrix of the system $\prod_{i=4}^{1} M_i$ (Eq. (3.19)) is the null matrix) so that spinning, standing or mixed mode can occur and have the same growth rate: the mode structure is undetermined. Noiray *et al.* (2011) have shown that non-linearities on the FTF can promote one of these types, a phenomenon which cannot be described by the present linear model.

3.3.3 Flow symmetry breaking (Sym Mach)

Consider now a case with a mean flow (SM effect: $M_\theta \neq 0$) where all burners are identical (i.e. all coupling factors $\mathcal{G}_i$ are equal so that $\|\mathcal{S}\| = 0$). The dispersion relation (Eq. (3.16) with $\|\mathcal{S}\| = 0$ and $M_\theta \neq 0$) has two distinct solutions so that waves 1 and 2 have different frequencies and growth rates:

$$f_{1,2} = \underbrace{\frac{c^0}{2L_c}}_{f^0} - \underbrace{\frac{c^0 \mathcal{G}^{0,\pm M_\theta}}{\pi L_c} \pm \frac{c^0}{2L_c} M_\theta}_{\delta f_1 \ (+),\ \delta f_2 \ (-)} \tag{3.23}$$

The mean azimuthal flow modifies the nature of the system: the eigenspace is only one dimensional because the matrix of the system ((Eq. (3.19) where $\mathcal{S} = 0$ and $M_\theta \neq 0$) does not reduce to the null matrix and (Eq. (3.20)) gives the nature of the two waves:

- **Wave 1:** $q_4^+ \neq 0$ and $q_4^- = 0$ corresponding to a co-rotating spinning mode.
- **Wave 2:** $q_4^+ = 0$ and $q_4^- \neq 0$ corresponding to a counter-rotating spinning mode.

Adding an azimuthal mean flow (M_θ) splits azimuthal modes into two spinning waves with different frequencies and growth rates.

3.3.4 GS breaking with no mean flow (Asym NoMach)

The Sym-NoMach case (Section 3.3.2) is now investigated with two distinct Flame Transfer Functions corresponding to the introduction of two different burner types (i.e. two different coupling parameters Γ_1 and Γ_2) to break symmetry with the pattern 1212 (Fig. 3.5). The time-delay τ_1 varies from $0ms$ to $11ms$ while the other time-delay τ_2 is fixed to $2.21ms$.

The dispersion relation (3.16) gives two different frequencies f_1 and f_2:

$$f_1 = \frac{c^0}{2L_c} - \frac{c^0 \Gamma_1^0}{\pi L_c} \quad \text{and} \quad f_2 = \frac{c^0}{2L_c} - \frac{c^0 \Gamma_2^0}{\pi L_c} \tag{3.24}$$

GS breaking splits the first azimuthal mode in two classes. Mode 1 depends only of Γ_1 and is driven only by the type 1 burners. Mode 2 depends only on Γ_2 and type 2 burners, leading to a constant stability map (Fig. 3.7) since only τ_1 is varying while τ_2 is fixed.

The splitting strength (Eq. (3.17)) is non null and controls the degeneracy of the mode ($\|\mathcal{S}\| = 2\|\Gamma_1^0 - \Gamma_2^0\| = \frac{2\pi L_c}{c^0}\|f_2 - f_1\|$) which generalizes the results of Noiray *et al.* (2011) obtained in a simple annular rig not connected to burners.

Due to this splitting, the eigenspace associated to each frequency (f_1 and f_2) is one-dimensional and Eq. (3.20) gives the nature of the two waves:

- **Wave 1:** $q_4^+/q_4^- = -1$ ($p'_4 = 0$) corresponding to a mode locked on the 4^{th} burner (which is of type 2 for the pattern 1212) and imposing a pressure node. This mode is standing and not perturbed by burners of type 2.
- **Wave 2:** $q_4^+/q_4^- = +1$ ($u'_4 = 0$) corresponding to a standing mode imposing a velocity node at each burner of type 2 and a pressure node at every burner of type

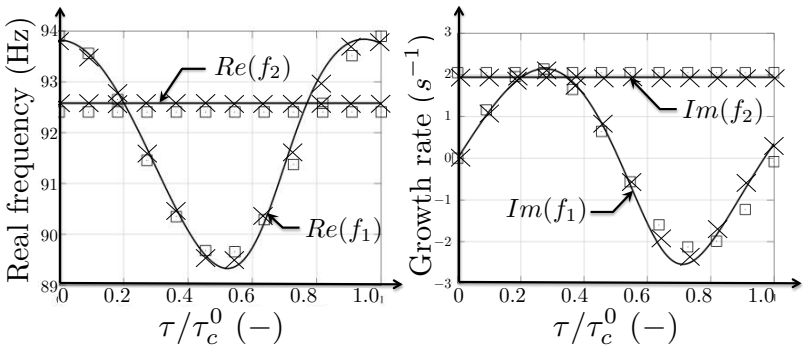

Figure 3.7: Freqency (left) and growth rate (right) vs normalized time-delay τ_1/τ_c^0 (where $\tau_c^0 = 1/f^0 \simeq 11\ ms$) while τ_2 is fixed to 2.21 ms of the first azimuthal mode in a configuration with $N = 4$ burners. —— : Atacamac (numerical resolution Eq. (3.13)) and □: Atacamac (analytical - Eq. (3.24)) and ×: 3D acoustic solver (AVSP)

1: it is perturbed only by burners of type 2 (constant stability map in Fig. 3.7 since τ_2 is fixed).

A structure diagram (Noiray *et al.*, 2011) ($(\|p'\|\cos(\phi),\ \|p'\|\sin(\phi),\ \|\mathcal{S}\|)$, Section 3.3.1) can be constructed (Fig. 3.8) to highlight the wave nature: if the trajectory at a fixed splitting strength $\|\mathcal{S}\|$ is a circle the wave is spinning ($\phi = \theta$). If the trajectory is a line the wave is standing ($\phi = 0$ or π). Fig. 3.8 shows the transition of the nature of "Wave 1" from spinning to standing when the splitting strength $\|\mathcal{S}\|$ increases (the time-delay τ_2 is fixed to $2.21ms$ and τ_1 can vary). This result is a generalization of the graph "(η_1, η_2, C_{2p})" in (Noiray *et al.*, 2011) for the p^{th} azimuthal mode in the non-linear regime.

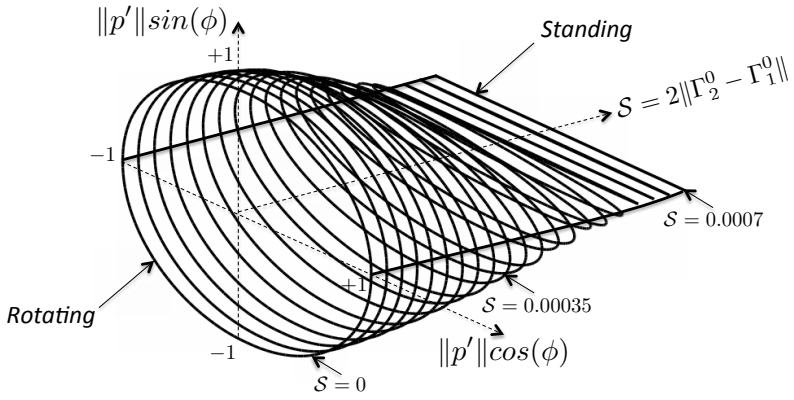

Figure 3.8: Structure diagram ($\|p'\|\cos(\phi)$, $\|p'\|\sin(\phi)$) of the Wave 1 vs splitting strength $\|\mathcal{S}\|$. For each splitting strength, the trajectory corresponds to azimuthal positions θ going from 0 to 2π.

3.3.5 GS and SM breaking (Asym Mach)

Using different burner types ($\tau_1 = 2.21ms$ and $\tau_2 = 4.98ms$ leading to a strong splitting term $\|\mathcal{S}\| \simeq 0.145$) and adding a mean azimuthal flow (M_θ can vary) combines GS and SM effects.

The azimuthal mode frequency and structure are given by Eqs. (3.18) and (3.20): the mode is mixed and split by both the geometrical (GS, $\|\mathcal{S}\| \neq 0$, Section 3.3.4) and flow (SM, $M_\theta \neq 0$, Section 3.3.3) symmetry breaking (Fig. 3.9 when $M_\theta = 0.1$).

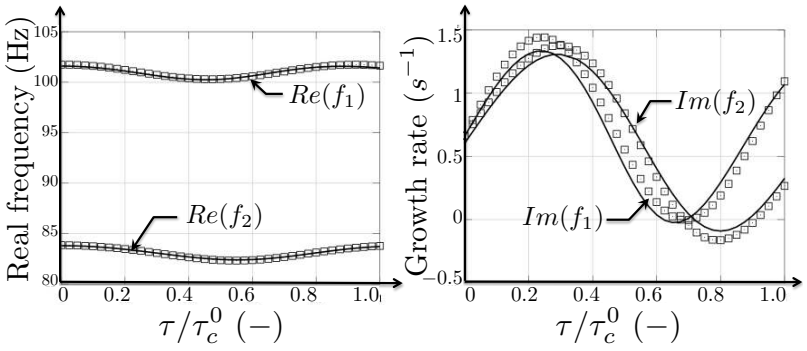

Figure 3.9: Freqency (left) and growth rate (right) vs normalized time-delay τ_1/τ_c^0 (where $\tau_c^0 = 1/f^0$) while $\tau_2 = 2.21\ ms$ of the first azimuthal mode in a configuration with $N = 4$ burners and a mean flow $M_\theta = 0.1$. —— : Atacamac (numerical resolution Eq. (3.13)) and □: Atacamac (analytical - Eq. (3.18)).

A configuration where $\tau_1 = 2.21ms$ and $\tau_2 = 4.98ms$ with a pattern 1212 (corresponding to $\mathcal{S} \simeq 0.145$) is studied by increasing the mean flow from $M_\theta = 0$ to 10^{-3}. The structure diagram (Fig. 3.10, Section 3.3.1) shows a transition from a standing mode (when the Mach number M_θ is low) to a spinning mode (when M_θ is higher): a small swirl motion (SM) can affect the mode structure even with a strong geometrical symmetry (GS) breaking.

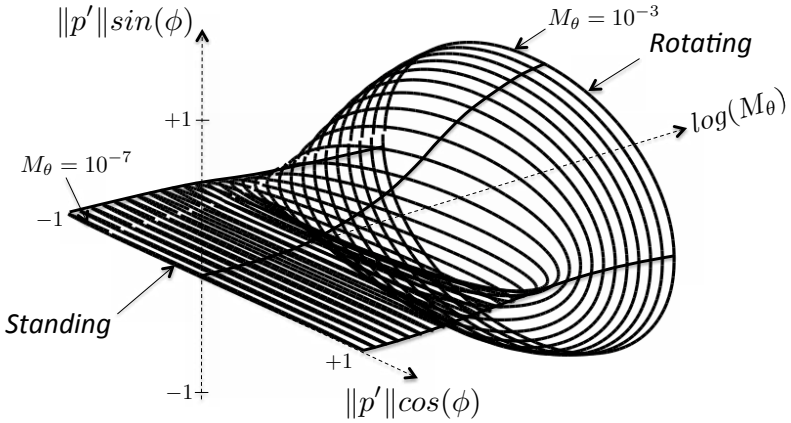

Figure 3.10: Structure diagram ($\|p'\|\cos(\phi)$, $\|p'\|\sin(\phi)$) vs Mach number M_θ of the wave associated to the frequency f_1 of a configuration with an initial splitting strength $\mathcal{S} \simeq 0.145$.

3.4 Conclusion

This chapter extends the analytical approach described in Chapter 2 to study a second mechanism controlling azimuthal modes frequency and nature (spinning, standing or

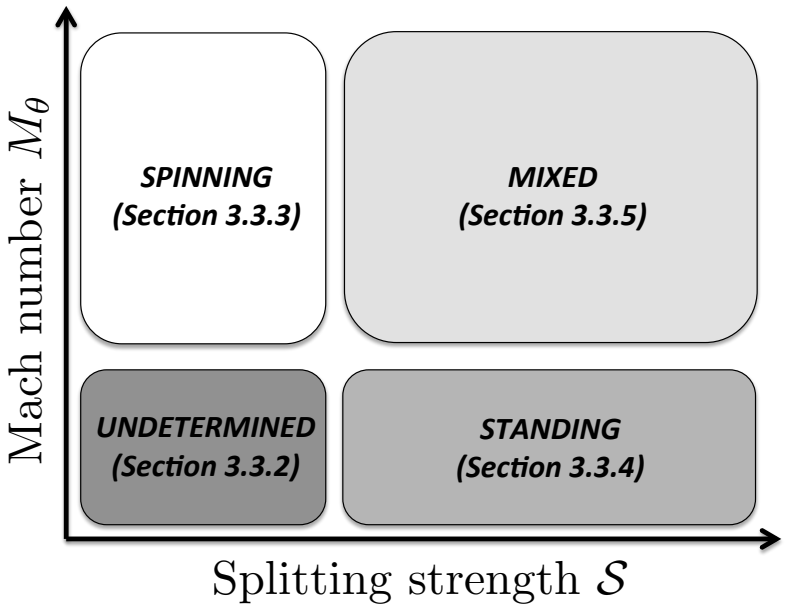

Figure 3.11: Effects of geometrical (GS) and flow (SM) symmetry breaking on the mode nature.

mixed) in annular combustors containing 4 burners: the existence of a mean azimuthal flow (FS breaking). The ATACAMAC methodology (Bauerheim *et al.*, 2014*d*) is extended to solve the linearized acoustic equations with a steady and uniform azimuthal mean flow in the annular chamber. It provides an analytical implicit dispersion relation for the frequency f which can be solved numerically. An analytical resolution is possible in specific situations where the annular chamber is weakly coupled to the burners. Results show that symmetry breaking, either by modifying burner characteristics (GS) or with a swirl motion (FS), splits the azimuthal mode into two waves which can have different but close frequencies and structures. Results are summarized in Fig. 3.11 showing the nature of the two components of the azimuthal mode as a function of mean Mach number M_θ and splitting strength $\mathcal{S}$. However, as for non-linear theories (Noiray *et al.*, 2011; Ghirardo & Juniper, 2013) or acoustic simulations, only the nature of these two components A and B can be determined but their ratio A/B fixing the final mode structure remains unknown and would requires high fidelity simulations or the complete resolution of the mode dynamics (where the critical issue would be the determination of the initial condition), a point discussed in thesis in Chapter 9. Nevertheless, this theory could be validated by the extraction of the splitting frequency as well as the nature of the two components from LES or experiments. No experimental validation has been performed yet but annular systems available at Cambridge (Worth & Dawson, 2013*b*) or EM2C (Bourgouin *et al.*, 2013) would be excellent setups to verify the validity of this model which was derived here for 4 burners but is expected to be also valid for real chambers with more burners.

Chapter 4

Theoretical analysis of azimuthal thermo-acoustics modes in a PBC (Plenum-Burners-Chamber) configuration

Contents

This chapter extends the analytical method (ATACAMAC of Chapters 2 and 3) to PBC configurations where an annular chamber is fed by N burners connected to an annular plenum. Like for BC configurations, the ANR (Annular Network Reduction) methodology allows to retain only the useful information related to the azimuthal modes of the two annular cavities and yields a simple dispersion relation which can be solved numerically. In specific situations where coupling factors are small (weak coupling), a fully analytical solution for the frequencies and growth rates can be derived. Results show that for low coupling parameters, the two annular cavities are decoupled: chamber and plenum modes coexist with little interaction. However, a bifurcation appears at high coupling factors leading to a frequency lock-in of the two annular cavities (strong coupling) which modifies the stability of the whole system. This tool is finally applied to an academic case where four burners connect an annular plenum to a chamber. For this configuration, analytical results are compared to a full three-dimensional Helmholtz solver to validate the analytical model in both weak and strong coupling regimes. Results show that this simple analytical tool allows to predict modes in annular combustors and investigate strategies to control them.

4.1 Introduction

The previous Chapters (2 and 3) have presented the development of an analytical tool to analyze azimuthal modes in a simplified configuration called BC, where an annular chamber is connected to N burners. The inlet of each burner was described by an impedance and they are not connected. However, modern gas turbines are much more complex and exhibit numerous azimuthal modes coupling multiple annular cavities as presented by Campa *et al.* (2011). The most important one is the plenum which feeds all burners. Since this plenum is also annular, it can develop azimuthal modes like chamber does. One interesting is therefore to classify these modes and understand which cavity drives the instability. For example, standing and turning modes (Krebs *et al.*, 2002; Evesque *et al.*, 2003) are both observed (Krebs *et al.*, 2002; Noiray *et al.*, 2011; Wolf *et al.*, 2012; Schuermans *et al.*, 2006) but predicting which mode type will appear in practice and whether they can be studied and controlled with the same method remains difficult (Ghirardo & Juniper, 2013). Similarly, most large scale annular chambers exhibit multiple acoustic modes in the frequency range of interest (typically 10 to 30 acoustic modes can be identified in a large scale industrial chamber between 0 and 300 Hz) and classifying them into categories is the first step to control them. These categories are typically 'longitudinal vs azimuthal modes' or 'modes involving only a part of the chamber (decoupled modes) vs modes involving the whole system (coupled modes)' (Krebs *et al.*, 2002; Lieuwen & Yang, 2005; Campa *et al.*, 2011; Pankiewitz & Sattelmayer, 2003). Knowing that a given unstable mode is controlled only by a certain part of the combustor is an obvious asset for any control strategy. In the case of combustors including an annular plenum, burners and an annular chamber (PBC configurations), such a classification is useful to understand how azimuthal modes in the plenum and in the chamber (which have a different radius

and sound speed and therefore different frequencies) can interact or live independently. For example, FEM simulations of a real industrial gas turbine (Campa *et al.*, 2011; Campa & Camporeale, 2014) produce numerous complex modes which involve several cavities (plenum, burners and chamber) at the same time. Unfortunately determining whether certain parts of a chamber can be 'decoupled' from the rest of the chamber is a task for which there is no clear strategy. 'Decoupling' factors have been derived for longitudinal modes in academic burners where all modes are longitudinal (Schuller *et al.*, 2012). Extending these approaches to annular systems requires first to derive analytical solutions allowing to isolate the effect of parameters on the modes structure. This is one of the objectives of this chapter.Thus, no full analytical resolution of frequency and nature of azimuthal modes has been performed in PBC configurations. The present chapter extends the analytical methodology of Schuller *et al.* (2012) for longitudinal tubes and of Parmentier *et al.* (2012) for BC configurations to a PBC configuration with N burners in order to highlight key parameters involved in the coupling mechanisms.

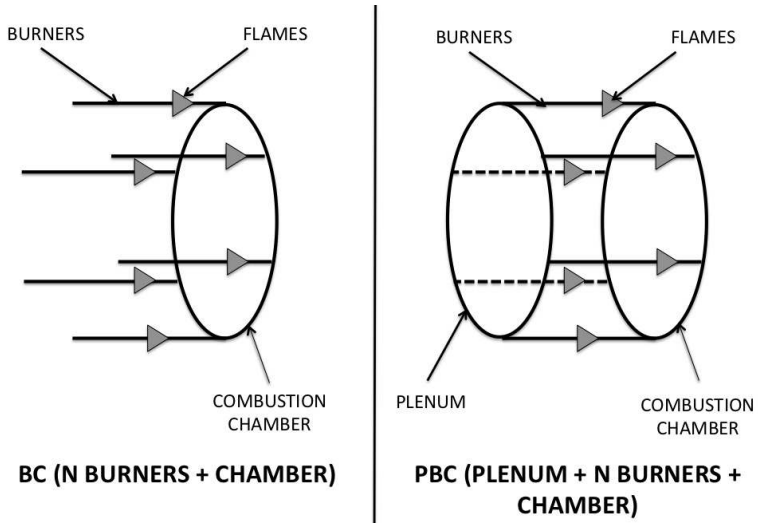

Figure 4.1: Configurations to study unstable modes in annular chambers

The chapter is organized as follows: Section 4.2 describes the principle of the ANR (Annular Network Reduction) methodology and the submodels to account for active flames. As for BC configurations, the network model is decomposed into azimuthal propagators and H-shaped connectors coupling the annular plenum to the chamber (compared to T-shaped connectors in BC setups where the chamber is connected only to the N burners). This approach allows to build an explicit dispersion relation giving the frequency, growth rate and structure of all modes. In Section 4.3, thermo-acoustic regimes (from fully decoupled to strongly coupled) are defined depending on the analytical coupling parameters conducted in Section 4.2. Finally, this analytical model is validated using the model annular chamber described in Section 4.4 with simplistic shapes to construct coupling factors and study azimuthal modes for a case where a plenum is connected to a chamber by four similar burners ($N = 4$, no symmetry breaking). First the weakly coupled regime (Section 4.5) and then the strongly coupled regime (Section 4.6) are in-

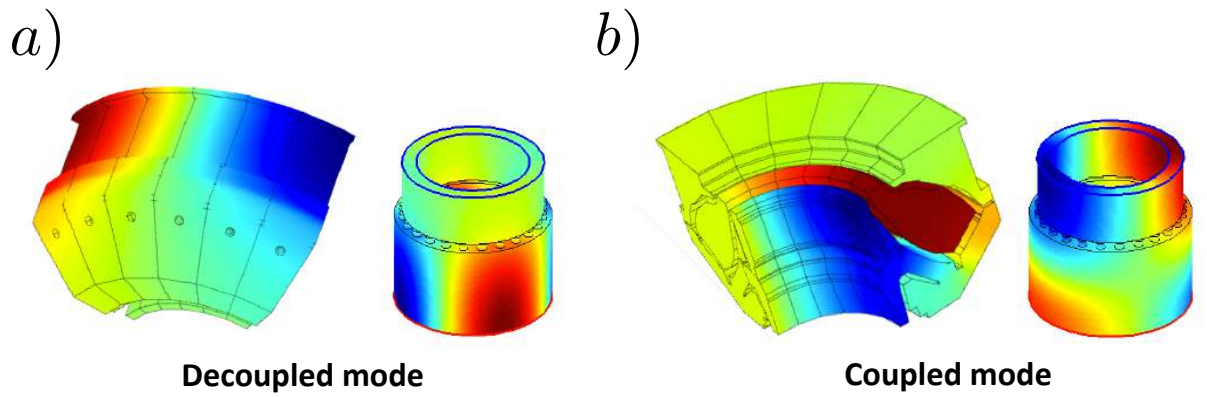

Figure 4.2: FEM simulations performed by Campa *et al.* (2011) on a complex industrial gas turbine (only 6 sectors are displayed) and its PBC configuration model. Two kinds of eigenmodes are observed: a) Decoupled mode and b) Coupled mode

vestigated. The bifurcation from weakly to strongly coupled situations is triggered by increasing the flame interaction index controlling the flame response to the acoustic flow. Results show that ATACAMAC allows to predict azimuthal turning and standing modes in a PBC configuration and performs as well as a 3D Helmholtz solver for all regimes while simple annular rigs (Noiray *et al.*, 2011; Ghirardo & Juniper, 2013) or BC models (Parmentier *et al.*, 2012; Stow & Dowling, 2004) are not able to capture the bifurcation from weakly to strongly coupled regimes. In this chapter, all configurations are perfectly axisymmetric. The effect of the annular plenum and potential coupling mechanisms on symmetry breaking is studied in the next chapter (Chapter 5).

4.2 A network model for PBC configurations

4.2.1 Model description

The model is based on a network view of the annular chamber fed by burners connected to an annular plenum (PBC, Fig. 4.3). This model is limited to situations where pressure fluctuations depend on the angle θ (or x) but not on z in the chamber and the plenum (they depend on the coordinate z only in the N burners). This case can be observed in combustors terminated in choked nozzles which behave almost like a rigid wall (i.e. $w' = 0$ under the low upstream Mach number assumption). Note however that this restriction prevents the present model to represent academical combustors where the combustion chamber is open to the atmosphere (Worth & Dawson, 2013*b*; Moeck *et al.*, 2010; Bourgouin *et al.*, 2013) or to predict "mixed modes" appearing at higher frequencies in configurations terminated by choked nozzles (Campa *et al.*, 2011).

Since the chamber inlet is also close to a velocity node, modes which have no variation along z can develop in the chamber, as shown by recent LES (Staffelbach *et al.*, 2009). Radial modes (where p' depends on r) are neglected because often occurring at high frequency. Gas dynamics are described using standard linearized acoustics for perfect gases in the low Mach number approximation. The mean flow induced by swirlers remains

slow (Staffelbach *et al.*, 2009) and azimuthal waves propagate at the sound speed which is different in the plenum (fresh gas at sound speed c_u^0) and the chamber (burnt gas at sound speed c^0).

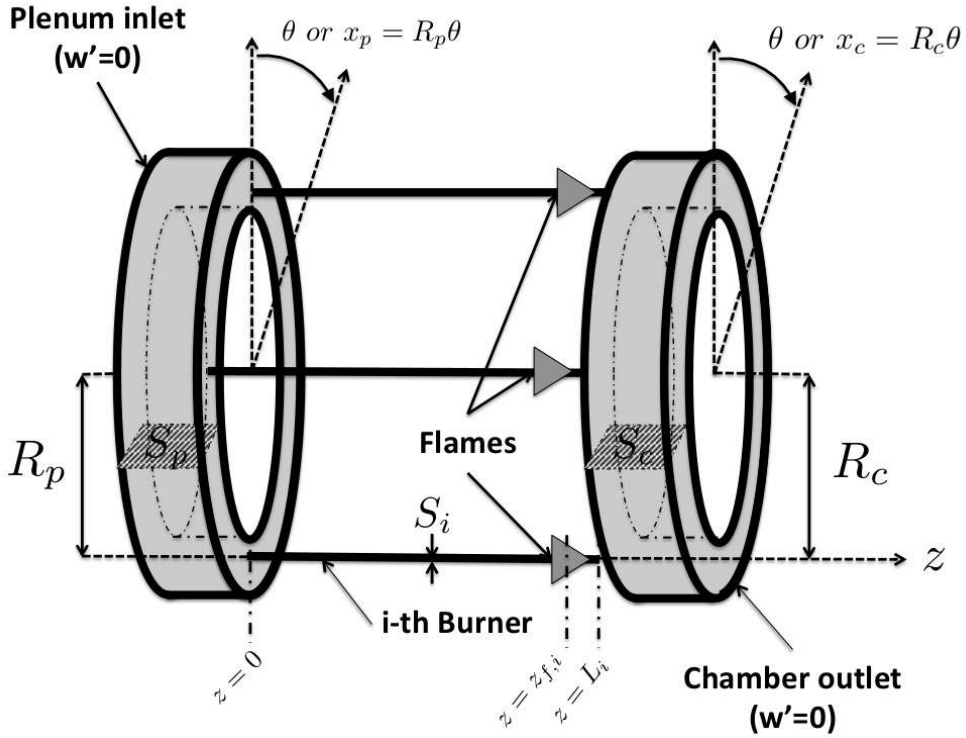

Figure 4.3: Network representation of the plenum, burners and chamber (PBC configuration)

In the previous chapters, a BC (Burners+Chamber) configuration was considered: an annular chamber is fed by N burners without taking into account the existence of a plenum ; the impedance imposed at the inlet of the N burners corresponded to a closed end ($w' = 0$) and flames were located at the burners extremity ($z_{f,i} \simeq L_i$ where L_i is the length of the i^{th} burner). This section describes how this BC case is extended to PBC (Plenum+Burners+Chamber) configurations where an annular plenum feeds N ducts ("burners") which are all connected to an annular chamber. Most annular gas turbine chambers can be modeled using this scheme (Fig. 4.3).

In a PBC configuration, burners are connected at both ends to the annular plenum and chamber. The boundary conditions $w' = 0$ used for BC configurations are retained here only on walls of the annular cavities but not at the inlet/outlet sections of the burners. Mean density in the annular chamber is noted ρ^0 (ρ_u^0 in the plenum). The subscript u stands for unburnt gases. The perimeter and the section of the annular plenum are noted $2L_p = 2\pi R_p$ and S_p respectively while L_i and S_i stand for the length and cross section area of the i^{th} burner. The perimeter and the section of the annular chamber are noted $2L_c = 2\pi R_c$ and S_c respectively. The position along the annular plenum and chamber is given by the angle θ defining abscissa $x_p = R_p\theta$ for the plenum and $x_c = R_c\theta$ for the chamber. The location of the flames in the burners is given by the normalized abscissa

$\alpha = z_{f,i}/L_i$ (Fig. 4.3).

4.2.2 Acoustic waves description and ANR methodology

To reduce the size of the system, the ANR methodology (Annular Network Reduction) introduced for BC cases in Chapter 2 is extended here to PBC cases. First, the combustor is decomposed into N sectors (Fig. 4.4) by assuming that every sector can be studied separately and that no flame-to-flame interaction occurs between neighboring sectors, a question which is still open today (O'Connor & T.Lieuwen, 2012*c*,*a*). Staffelbach *et al.* (2009) have shown that this was the case in LES of azimuthal modes for Siemenc/Ansaldo and Snecma type turbines. Worth & Dawson (2013*b*,*a*) have also demonstrated experimentally that this assumption in annular combustors is valid when the distance between burners is large enough to avoid flames merging.

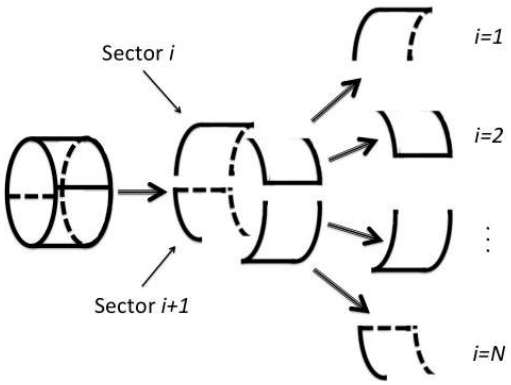

Figure 4.4: Decomposition of an annular combustor in N sectors

For each individual sector, the acoustic problem may be split into two parts: propagation (Section 4.2.2.a already described in previous chapters) and H-shaped connector (Section 4.2.2.b) (Fig. 4.5). The angle θ and the coordinates of the plenum x_p and chamber x_c take their origin at the burner i. The end of the sector i is located at $x_p = \frac{2L_p}{N}$ and $x_c = \frac{2L_c}{N}$ (thus assuming that burners are evenly located around the annular combustor). H-shaped connectors are supposed to be compact regarding the acoustic wavelength.

4.2.2.a Propagation

As presented in the two previous chapters, the pressure and velocity perturbations inside the i^{th} sector of the annular chamber (denoted via the subscript c,i) can be written as:

$$p'_{c,i}(x_c,t) = (A_i \cos(kx_c) + B_i \sin(kx_c))e^{-j\omega t} \tag{4.1}$$

$$\rho^0 c^0 u'_{c,i}(x_c,t) = j(A_i \sin(kx_c) - B_i \cos(kx_c))e^{-j\omega t} \tag{4.2}$$

where $j^2 = -1$, $k = \omega/c^0$ is the wavenumber, A_i and B_i are complex constants.

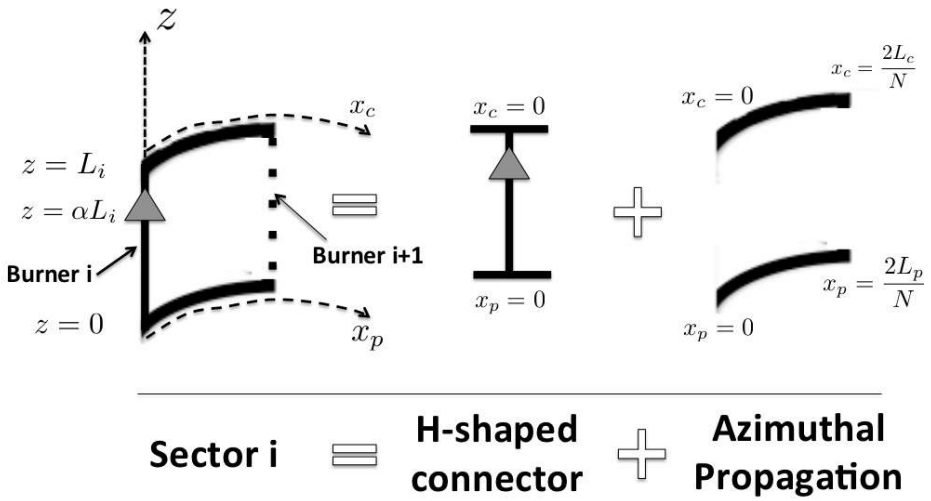

Figure 4.5: ANR methodology: splitting of one sector into propagation and H-shaped section parts for a PBC configuration

From Eqs. (4.1) and (4.2), pressure and velocity perturbations at two positions in the chamber x_{c0} and $x_{c0} + \Delta x_c$ are linked by:

$$\begin{bmatrix} p'_{c,i} \\ \frac{1}{j}\rho^0 c^0 u'_{c,i} \end{bmatrix}_{(x_{c0}+\Delta x_c,t)} = \underbrace{\begin{bmatrix} \cos(k\Delta x_c) & -\sin(k\Delta x_c) \\ \sin(k\Delta x_c) & \cos(k\Delta x_c) \end{bmatrix}}_{R(k\Delta x_c)} \begin{bmatrix} p'_{c,i} \\ \frac{1}{j}\rho^0 c^0 u'_{c,i} \end{bmatrix}_{(x_{c0},t)} \tag{4.3}$$

The matrix $R(k\Delta x_c)$ is a 2D rotation matrix of angle $k\Delta x_c$. In the case where N burners are equally distributed over the annular chamber, the propagation in the chamber between each burner is fully described by the transfer matrix $R(k\frac{2L_c}{N})$ where $2L_c$ is the chamber perimeter.

Wave propagation in the i^{th} sector of the plenum satisfies the same equation than in the chamber Eq. (4.3) but the sound speed in fresh gases c_u^0 must be used:

$$\begin{bmatrix} p'_{p,i} \\ \frac{1}{j}\rho_u^0 c_u^0 u'_{p,i} \end{bmatrix}_{(x_0+\Delta x_p,t)} = \underbrace{\begin{bmatrix} \cos(k_u\Delta x_p) & -\sin(k_u\Delta x_p) \\ \sin(k_u\Delta x_p) & \cos(k_u\Delta x_p) \end{bmatrix}}_{R(k_u\Delta x_p)} \begin{bmatrix} p'_{p,i} \\ \frac{1}{j}\rho_u^0 c_u^0 u'_{p,i} \end{bmatrix}_{(x_0,t)} \tag{4.4}$$

where $k_u = \omega/c_u^0$.

Propagation in the i^{th} burner from the plenum ($z = 0$) to the flame ($z = \alpha L_i$) and from $z = \alpha L_i$ to $z = L_i$ (Fig. 4.6) can be described in the same way considering propagation in fresh gases for the first part ($0 < z < \alpha L_i$) and hot gases in the second part ($\alpha L_i < z < L_i$):

Therefore, equations for the wave propagation in the i^{th} burner are:

$$\begin{bmatrix} p'_i \\ \frac{1}{j}\rho_u^0 c_u^0 w'_i \end{bmatrix}_{(\alpha L_i,t)} = R(k_u \alpha L_i) \begin{bmatrix} p'_i \\ \frac{1}{j}\rho_u^0 c_u^0 w'_i \end{bmatrix}_{(0,t)} \quad \text{(Cold part of the i-th burner)} \tag{4.5}$$

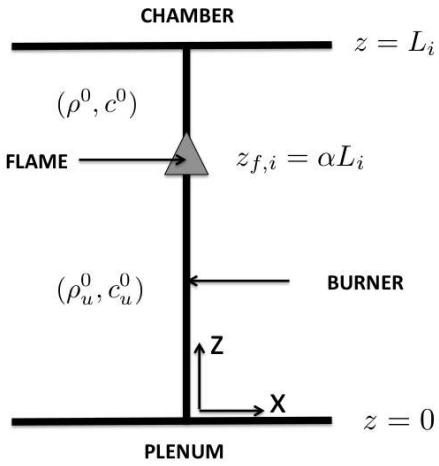

Figure 4.6: Propagation in the i^{th}burner for a PBC configuration in the ANR method

and

$$\begin{bmatrix} p_i' \\ \frac{1}{j}\rho^0 c^0 w_i' \end{bmatrix}_{(L_i,t)} = R(k(1-\alpha)L_i) \begin{bmatrix} p_i' \\ \frac{1}{j}\rho^0 c^0 w_i' \end{bmatrix}_{(\alpha L_i,t)} \text{(Hot part of the i-th burner)} \quad (4.6)$$

4.2.2.b H-shaped connector

The physical parameters at the entrance (located at the end of the $i-1^{th}$ sector corresponding to $\theta = \frac{2\pi}{N}$ and consequently $x_p = \frac{2L_p}{N}$ and $x_c = \frac{2L_c}{N}$) must be linked to the output parameters (corresponding to the beginning of the i^{th} sector located at $\theta = 0$ and consequently $x_p = x_c = 0$) as shown in Fig. 4.7.

The H-shaped connectors are treated as compact elements in the azimuthal direction. Jump conditions are first written along the x direction at $z = 0$ and $z = L_i$: at low Mach number (Poinsot & Veynante, 2011), they correspond to the continuity of pressure and volume rate through the interface. For the sake of simplicity, more complex interactions (e.g. effective length or pressure drop effects) (Campa *et al.*, 2011) are neglected knowing they could affect the coupling mechanisms between cavities. At $z = L_i$:

$$p'_{c,i-1}(x_c = \frac{2L_c}{N}, t) = p'_{c,i}(x_c = 0, t) = p'_i(z = L_i) \quad (4.7)$$

$$S_c u'_{c,i-1}(x_c = \frac{2L_c}{N}, t) + S_i w'_i(z = L_i) = S_c u'_{c,i}(x_c = 0, t) \quad (4.8)$$

and at $z = 0$:

$$p'_{p,i-1}(x_p = \frac{2L_p}{N}, t) = p'_{p,i}(x_p = 0, t) = p'_i(z = 0) \quad (4.9)$$

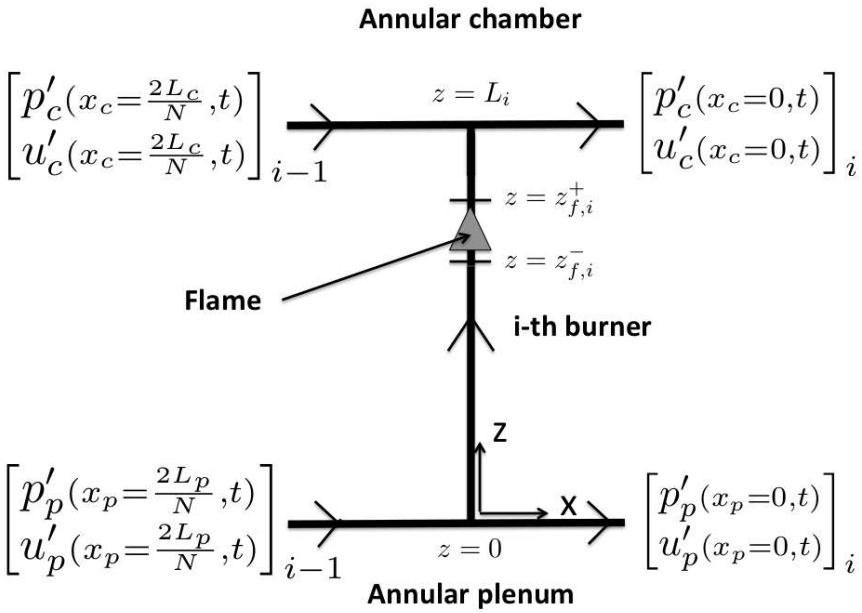

Figure 4.7: H-shaped overview in the ANR method

$$S_p u'_{p,i-1}(x_p = \frac{2L_p}{N}, t) = S_i w'_i(z = 0) + S_p u'_{p,i}(x_p = 0, t) \tag{4.10}$$

Jump conditions are also required in the burners through the flames located at $z = z_{f,i}$. They are assumed to be planar and compact: their thickness is negligible compared to the acoustic wavelength. Flames are located at $z = z^+_{f,i} = z^-_{f,i} \simeq \alpha L_i$ where superscripts $+$ and $-$ denote the downstream and upstream positions of the i^{th} flame. At low Mach number, jump conditions through the flame imply equality of pressure and flow rate discontinuity due to an extra volume source term related to unsteady combustion (Poinsot & Veynante, 2011):

$$p'_i(z^+_{f,i}) = p'_i(z^-_{f,i}) \tag{4.11}$$

$$S_i w'_i(z^+_{f,i}) = S_i w'_i(z^-_{f,i}) + \frac{\gamma_u - 1}{\gamma_u P^0} \dot{\Omega}'_{T,i} \tag{4.12}$$

where P^0 is the mean pressure and γ_u is the heat capacity ratio of fresh gases. The unsteady heat release $\dot{\Omega}'_{T,i}$ is expressed using the FTF model (Flame Transfer Function) (Crocco, 1951):

$$\frac{\gamma_u - 1}{\gamma_u P^0} \dot{\Omega}'_{T,i} = S_i n_i e^{j\omega\tau_i} w'_i(z^-_{f,i}) \tag{4.13}$$

where the interaction index n_i[1] and the time-delay τ_i are input data (depending on

[1]Typical values of the interaction index n_i can reach $T_b/T_u - 1$ at low frequency.

frequency) describing the interaction of the i^{th} flame with acoustics. Therefore, the jump condition in Eq. (4.12) is recast using Eq. (4.13):

$$S_i w_i'(z_{f,i}^+) = S_i(1 + n_i e^{j\omega\tau_i}) w_i'(z_{f,i}^-) \tag{4.14}$$

Thanks to Eqs. (4.7 - 4.14), a transfer matrix T_i of the H-shaped connector of Fig. 4.7 is defined as:

$$\begin{bmatrix} p'_{p(x_p=0,t)} \\ \frac{1}{j}\rho_u^0 c_u^0 u'_{p(x_p=0,t)} \\ p'_{c(x_c=0,t)} \\ \frac{1}{j}\rho^0 c^0 u'_{c(x_c=0,t)} \end{bmatrix}_i = T_i \begin{bmatrix} p'_{p(x_p=\frac{2L_p}{N},t)} \\ \frac{1}{j}\rho_u^0 c_u^0 u'_{p(x_p=\frac{2L_p}{N},t)} \\ p'_{c(x_c=\frac{2L_c}{N},t)} \\ \frac{1}{j}\rho^0 c^0 u'_{c(x_c=\frac{2L_c}{N},t)} \end{bmatrix}_{i-1} \tag{4.15}$$

where the transfer matrix T_i is:

$$T_i = I_d + 2\begin{bmatrix} 0 & 0 & 0 & 0 \\ \Gamma_{i,1} & 0 & \Gamma_{i,2} & 0 \\ 0 & 0 & 0 & 0 \\ \Gamma_{i,3} & 0 & \Gamma_{i,4} & 0 \end{bmatrix} \tag{4.16}$$

and the coefficients $\Gamma_{i,k},\ k = 1$ to 4 are:

$$\Gamma_{i,1} = -\frac{1}{2}\frac{S_i}{S_p}\frac{\cos(k(1-\alpha)L_i)\cos(k_u\alpha L_i) - \mathbb{F}\sin(k(1-\alpha)L_i)\sin(k_u\alpha L_i)}{\cos(k(1-\alpha)L_i)\sin(k_u\alpha L_i) + \mathbb{F}\sin(k(1-\alpha)L_i)\cos(k_u\alpha L_i)} \tag{4.17}$$

$$\Gamma_{i,2} = \frac{1}{2}\frac{S_i}{S_p}\frac{1}{\cos(k(1-\alpha)L_i)\sin(k_u\alpha L_i) + \mathbb{F}\sin(k(1-\alpha)L_i)\cos(k_u\alpha L_i)} \tag{4.18}$$

$$\Gamma_{i,3} = \frac{1}{2}\frac{S_i}{S_c}\frac{\mathbb{F}}{\cos(k(1-\alpha)L_i)\sin(k_u\alpha L_i) + \mathbb{F}\sin(k(1-\alpha)L_i)\cos(k_u\alpha L_i)} \tag{4.19}$$

$$\Gamma_{i,4} = -\frac{1}{2}\frac{S_i}{S_c}\frac{\mathbb{F}\cos(k(1-\alpha)L_i)\cos(k_u\alpha L_i) - \sin(k(1-\alpha)L_i)\sin(k_u\alpha L_i)}{\cos(k(1-\alpha)L_i)\sin(k_u\alpha L_i) + \mathbb{F}\sin(k(1-\alpha)L_i)\cos(k_u\alpha L_i)} \tag{4.20}$$

with the flame parameter $\mathbb{F}$:

$$\mathbb{F} = \frac{\rho^0 c^0}{\rho_u^0 c_u^0}(1 + n e^{j\omega\tau}) \tag{4.21}$$

These coefficients are the coupling parameters for PBC configurations. $\Gamma_{i,1}$ and $\Gamma_{i,2}$ are linked to the plenum/burner junction (depending on S_i/S_p which measures the ratio between the burner section S_i and the plenum section S_p) while $\Gamma_{i,3}$ and $\Gamma_{i,4}$ are linked to the chamber/burner junction (depending on S_i/S_c which measures the ratio of the burner section to the chamber section (Fig. 4.3)).

4.2.3 Dispersion relation calculation given by the ANR method

In previous sections, the overall problem has been split into smaller parts and now has to be reconstructed in order to obtain the dispersion relation for the whole system. First, the pressure and velocity fluctuations at the end of the $i-1^{th}$ sector are linked to those at the end of the i^{th} sector using Eqs. (4.3), (4.4) and (4.15).

$$\begin{bmatrix} p'_{p(x_p=\frac{2L_p}{N},t)} \\ \frac{1}{j}\rho_u^0 c_u^0 u'_{p(x_p=\frac{2L_p}{N},t)} \\ p'_{c(x_c=\frac{2L_c}{N},t)} \\ \frac{1}{j}\rho^0 c^0 u'_{c(x_c=\frac{2L_c}{N},t)} \end{bmatrix}_i = R_i \begin{bmatrix} p'_{p(x_p=0,t)} \\ \frac{1}{j}\rho_u^0 c_u^0 u'_{p(x_p=0,t)} \\ p'_{c(x_c=0,t)} \\ \frac{1}{j}\rho^0 c^0 u'_{c(x_c=0,t)} \end{bmatrix}_i = R_i T_i \begin{bmatrix} p'_{p(x_p=\frac{2L_p}{N},t)} \\ \frac{1}{j}\rho_u^0 c_u^0 u'_{p(x_p=\frac{2L_p}{N},t)} \\ p'_{c(x_c=\frac{2L_c}{N},t)} \\ \frac{1}{j}\rho^0 c^0 u'_{c(x_c=\frac{2L_c}{N},t)} \end{bmatrix}_{i-1} \tag{4.22}$$

where T_i is the matrix defined in Eq. (4.16) and R_i is the propagation matrix inside the plenum and chamber in the i^{th} sector defined by:

$$R_i = \begin{bmatrix} R(k_u\frac{2L_p}{N}) & \begin{matrix} 0 & 0 \\ 0 & 0 \end{matrix} \\ \begin{matrix} 0 & 0 \\ 0 & 0 \end{matrix} & R(k\frac{2L_c}{N}) \end{bmatrix} \tag{4.23}$$

where $R(k_u\frac{2L_p}{N})$ and $R(k\frac{2L_c}{N})$ are 2-by-2 matrices defined in Eqs. (4.3) and (4.4)

Then, Eq. (4.22) can be repeated through the N sectors and periodicity imposes that:

$$\begin{bmatrix} p'_{p(x_p=\frac{2L_p}{N},t)} \\ \frac{1}{j}\rho_u^0 c_u^0 u'_{p(x_p=\frac{2L_p}{N},t)} \\ p'_{c(x_c=\frac{2L_c}{N},t)} \\ \frac{1}{j}\rho^0 c^0 u'_{c(x_c=\frac{2L_c}{N},t)} \end{bmatrix}_{i=1} = \left(\prod_{i=N}^{1} R_i T_i\right) \begin{bmatrix} p'_{p(x_p=\frac{2L_p}{N},t)} \\ \frac{1}{j}\rho_u^0 c_u^0 u'_{p(x_p=\frac{2L_p}{N},t)} \\ p'_{c(x_c=\frac{2L_c}{N},t)} \\ \frac{1}{j}\rho^0 c^0 u'_{c(x_c=\frac{2L_c}{N},t)} \end{bmatrix}_{i=1} \tag{4.24}$$

System Eq. (4.24) leads to non-null solutions if and only if its determinant is null:

$$det\left(\prod_{i=N}^{1} R_i T_i - I_d\right) = 0 \tag{4.25}$$

where I_d is the 4-by-4 identity matrix and the matrix $M = \prod_{i=N}^{1} R_i T_i$ is the transfer matrix of the overall system. Eq. (4.25) provides an implicit equation for the pulsation ω and gives the stability limits and the frequency of unstable modes. Note that Eq. (4.25) given by the ANR methodology only involves a 4-by-4 determinant[2] irrespective of the number of burners N.

[2]The ANR methodology retains only useful information related to azimuthal modes of the annular cavities. Knowing that these modes are a combination of two characteristic waves, the minimum size of the matrix system is $2\mathcal{C}$-by-$2\mathcal{C}$ where $\mathcal{C}$ is the number of annular cavities (here $\mathcal{C} = 2$: plenum + chamber)

4.3 Analytical procedure and coupling limits

Due to significant non linearities, Eq. (4.25) cannot be solved analytically in the general case. However different situations (Fig. 4.8) can be exhibited where Eq. (4.25) can be solved depending on values taken by the coupling parameters $\wp_{p,i}$ and $\wp_{c,i}$:

$$\wp_{p,i} = \max(|\Gamma_{i,1}|, |\Gamma_{i,2}|) \tag{4.26}$$

and

$$\wp_{c,i} = \max(|\Gamma_{i,3}|, |\Gamma_{i,4}|) \tag{4.27}$$

The parameters $\wp_{p,i}$ and $\wp_{c,i}$ measure the coupling effect of the plenum/burner junction and the chamber/burner junction respectively for the i^{th} sector. They depend only on the geometry (section ratios S_i/S_p and S_i/S_c as well as the burners length L_i) and the flame (the flame interaction factor $\mathbb{F}$ and the flame position α). Longitudinal modes in the burners can be also obtained with this model but only purely azimuthal modes will be studied in this chapter (Fig. 4.8).

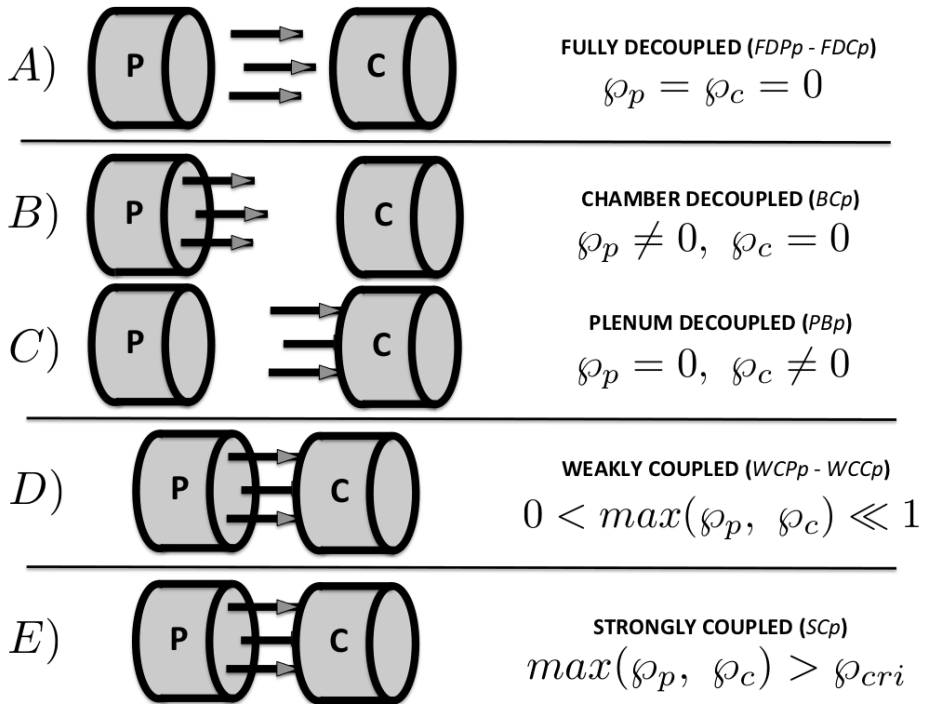

Figure 4.8: The four coupling situations depending on the parameters $\wp_p$ and $\wp_c$

4.3.1 Fully decoupled situations (FDPp and FDCp)

If the coupling parameters have vanishing small values ($\wp_{p,i} = 0$ and $\wp_{c,i} = 0$), the coupling matrices of each sector (T_i in Eq. (4.25)) are the identity matrix. As a consequence,

the dispersion relation (Eq. (4.25)) reduces to:

$$det\left(\prod_{i=N}^{1} R_i - I_d\right) = 0 \tag{4.28}$$

The matrices R_i being block matrices of 2-by-2 rotation matrices which satisfy $R(\theta_1)R(\theta_2) = R(\theta_1 + \theta_2)$, Eq. (4.28) becomes:

$$\begin{aligned} det\left(\prod_{i=N}^{1} R_i - I_d\right) &= det\left(\begin{bmatrix} R(2k_uL_p) - I_d & \begin{matrix} 0 & 0 \\ 0 & 0 \end{matrix} \\ \begin{matrix} 0 & 0 \\ 0 & 0 \end{matrix} & R(2kL_c - I_d) \end{bmatrix}\right) \\ &= det\left(R(2k_uL_p) - I_d\right)\, det(R(2kL_c) - I_d) = 0 \end{aligned} \tag{4.29}$$

Solutions of Eq. (4.29) are $k_uL_p = p\pi$ and $kL_c = p\pi$ where p is an integer. They correspond to two families of modes which live separately (case A in Fig. 4.8):

- **FDPp - Fully Decoupled Plenum mode of order p:** they satisfy the relation $k_uL_p = p\pi$ and correspond to the azimuthal modes of the annular plenum alone (Fig. 4.8).
- **FDCp - Fully Decoupled Chamber mode of order p:** they satisfy the relation $kL_c = p\pi$ and correspond to the azimuthal modes of the annular chamber alone (Fig. 4.8).

4.3.2 Chamber or plenum decoupled situations (PBp and BCp)

These situations correspond to the cases considered in the two previous chapters (Chapters 2 and 3) where either the plenum or the chamber are fully decoupled from the burners, i.e. respectively $\wp_p = 0$ or $\wp_c = 0$ (cases B and C in Fig. 4.8). The transfer matrices of each sector are block-triangular leading to a simple relation for the determinant and consequently for the dispersion relation (Eq. 4.25) without assumption on the non-null parameter $\wp_p$ or $\wp_c$. As for the fully decoupled situations, two families of modes can be exhibited (cases B and C in Fig. 4.8):

- **PBp - Plenum/Burners mode of order p:** in this situation, $\wp_c = 0$. The annular chamber is fully decoupled from the system (burners+plenum) and the dispersion relation Eq. (4.25) reduces to two equations:

$$det(R(2kL_c) - 1) = 0 \tag{4.30}$$

$$det\left(\prod_{i=N}^{1} R\left(\frac{2k_uL_p}{N}\right)\begin{bmatrix} 1 & 0 \\ \Gamma_{i,1} & 1 \end{bmatrix} - I_d\right) = 0 \tag{4.31}$$

  Eq. (4.30) corresponds to the dispersion relation of a FDCp mode while Eq. (4.31) is the dispersion relation of a PB (Plenum + Burners) configuration where an impedance $Z = 0$ is imposed at the downstream end of the burner simulating the

large chamber decoupled from the system (case B in Fig. 4.8). This latter mode is referred to as "PBp" standing for Plenum/Burners mode of order p. These situations are, however, unrealistic because they neglect all interactions between the annular plenum and chamber: the only solution to obtain $\wp_c \to 0$ in a PBC configuration is an infinite cross section of the chamber ($S_c \to \infty$ in Eqs. (4.19 - 4.20)). Therefore, this chapter will focus on other situations (e.g. cases D and E in Fig. 4.8) which are more representative of real engines by including the interaction between annular cavities.

- **BCp - Burners/Chamber mode of order p:** in this situation, $\wp_p = 0$ so that the annular plenum is fully decoupled from the rest of the system and the dispersion relation Eq. (4.25) reduces to two equations:

$$det(R(2k_u L_p) - 1) = 0 \tag{4.32}$$

$$det\left(\prod_{i=N}^{1} R\left(\frac{2kL_c}{N}\right)\begin{bmatrix}1 & 0\\ \Gamma_{i,4} & 1\end{bmatrix} - I_d\right) = 0 \tag{4.33}$$

The first equation (Eq. (4.32)) is the dispersion relation of a FDPp mode while Eq. (4.33) is the dispersion relation of a BC (Burners + Chamber) configuration where a pressure node ($Z = 0$) is imposed at the upstream end of the burner modeling the large plenum decoupled from the burners and the annular chamber (case C in Fig. 4.8). This latter mode is called "BCp" for Burners/Chamber mode of order p and was already studied by Parmentier *et al.* (2012).

4.3.3 Weakly coupled situations (WCPp and WCCp)

When $\wp_p$ and $\wp_c$ are both non zero, both azimuthal modes of the plenum and the chamber can exist and interact through the burners. If $\wp_p$ and $\wp_c$ remain small (Eq. (4.34)), an asymptotic solution can be constructed.

$$\forall i,\ 0 < \wp_{p,i} << 1 \text{ and } 0 < \wp_{c,i} << 1 \tag{4.34}$$

The parameters $\wp_{p,i}$ (Eq. 4.26) and $\wp_{c,i}$ (Eq. 4.27) measure the strength of the coupling effect of the plenum/burner junction and the chamber/burner junction respectively for the i^{th} sector. If they are small, the transfer matrices of each sector ($T_i R_i$ in Eq. (4.25)) are close to the rotation matrix R_i defined in Eq. (4.4) so that the eigenfrequencies of the system will be close to a FDPp or a FDCp mode. Consequently, as for fully decoupled modes, two families of modes can be exhibited (case D in Fig. 4.8):

- **WCPp - Weakly Coupled Plenum mode of order p:** this mode is close to a FDPp mode and the solution for the wavenumber k_u can be searched as an expansion around this case:

$$k_u L_p = p\pi + \epsilon_p \tag{4.35}$$

where $\epsilon_p \ll p\pi$

- **WCCp - Weakly Coupled Chamber mode of order p:** this mode is close to a FDCp mode and the solution for the wavenumber k can be searched as an expansion around this case:

$$kL_c = p\pi + \epsilon_c \tag{4.36}$$

where $\epsilon_c \ll p\pi$

For weakly coupled modes, this low coupling assumption allows a Taylor expansion of the dispersion relation (Eq. 4.25) which can be truncated and solved providing analytical solutions for ϵ_c and ϵ_p. This expansion is case-dependent: the $N = 4$ case will be detailed in Section. 4.5. Basically, results show that azimuthal modes will be either Chamber or Plenum modes slightly modified by their interaction with the rest of the combustor.

Note that the low coupling assumption ($\wp_{p,i} \ll 1$ and $\wp_{c,i} \ll 1$) does not imply low thermo-acoustic coupling ($n_i \ll 1$) because surface ratios between burner and plenum or chamber are usually small ($S_i/S_c \ll 1$ and $S_i/S_p \ll 1$).

In the specific configuration where the flames are located at the end of the burner ($\alpha = z_{f,i}/L_i = 1$ in Fig. 4.3), however, the coupling parameters simplify as:

$$\Gamma_{i,1} = -\frac{1}{2}\frac{S_i}{S_p}\,\mathrm{cotan}(k_u L_i) \tag{4.37}$$

$$\Gamma_{i,2} = \frac{1}{2}\frac{S_i}{S_p}\frac{1}{\sin(k_u L_i)} \tag{4.38}$$

$$\Gamma_{i,3} = \frac{1}{2}\frac{S_i}{S_c}\frac{\mathbb{F}}{\sin(k_u L_i)} \tag{4.39}$$

$$\Gamma_{i,4} = -\frac{1}{2}\frac{S_i}{S_c}\mathbb{F}\,\mathrm{cotan}(k_u L_i) \tag{4.40}$$

where $\mathbb{F}$ is the flame parameter defined in Eq. (4.21). Equations (4.37) to (4.40) correspond to an extension of the coupling parameters proposed by Schuller *et al.* (2012) for longitudinal instabilities and Parmentier *et al.* (2012) for azimuthal instabilities in a BC configuration. They show that decoupling ($\wp_{p,i} \ll 1$ and $\wp_{c,i} \ll 1$) can be expected in this case for small sections ratios $S_i/S_p << 1$ and $S_i/S_c << 1$, when the flame parameter $\mathbb{F}$ (Eq. (4.21)) is small too.

4.3.4 Strongly coupled situations (SCp)

The low coupling assumption ($\wp_{p,i} \ll 1$ and $\wp_{c,i} \ll 1$) is not valid at high flame interaction factor ($\mathbb{F} = \frac{\rho^0 c^0}{\rho_u^0 c_u^0}(1 + ne^{j\omega\tau})$) or high surface ratios (S_i/S_p or S_i/S_c). In these situations (case E in Fig. 4.8), a numerical resolution of the analytical dispersion relation (Eq. (4.25)) is required. It can be achieved by a non-linear solver based on the Newton-Raphson algorithm.

In the rest of this chapter, the weakly and strongly coupled situations (Fig.4.8) will be studied on the PBC configuration with four burners ($N = 4$) described in Section 4.4. The transition from weakly (Section 4.5) to strongly coupled (Section 4.6) regimes is controlled

by a critical coupling limit factor $\wp_{crit}$. The transition occurs when $max(\wp_p,\ \wp_c) > \wp_{crit}$. The geometry being fixed (Table 4.1) and the coupling parameters ($\wp_p$ and $\wp_c$) depending only on the geometry and the flame, the transition will be triggered by increasing the flame interaction index n_i of the flames from $n_i = 1.57$ (weak coupling) to $n_i = 8.0$ (strong coupling).

4.4 Validation in a simplified model chamber

Eigenfrequencies and mode structures of the analytical resolution of the dispersion relation under the low coupling factors assumption (Fig. 4.8, all modes except SCp) are first compared to a full 3D acoustic code and to the direct resolution of Eq. (4.25) in the case of a simplified 3D PBC configuration which is used as a toy-model for ATACAMAC and corresponds to a typical industrial gas turbine.

4.4.1 Description of the simplified PBC configuration

The 3D geometry (Fig. 4.9) corresponds to a PBC setup with $N = 4$ burners similar to Fig. 4.3 (characteristics defined in Tab. 4.1). The mean radii R_p and R_c of the cylindrical chamber and plenum are derived from the half perimeter L_p and L_c of the analytical model. Boundary conditions correspond to impermeable walls everywhere.

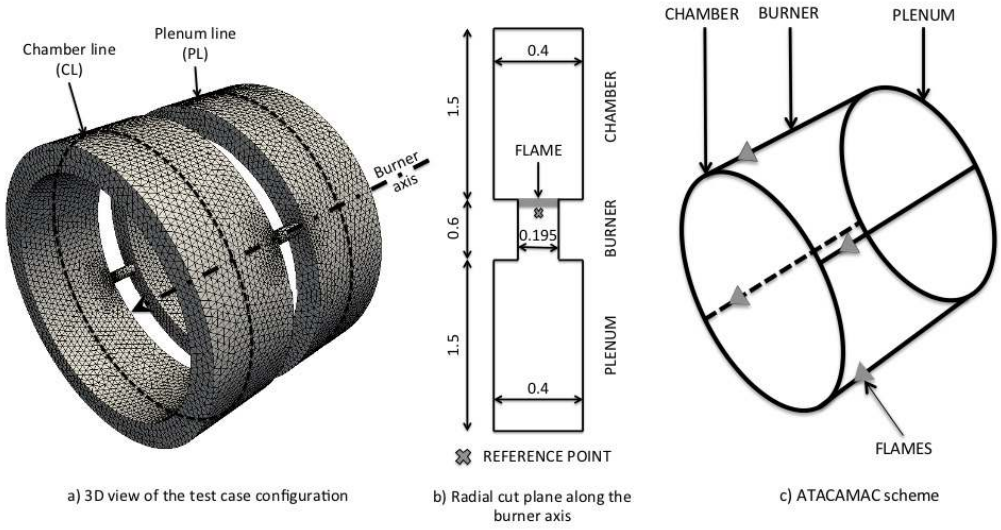

Figure 4.9: 3D toy-model to validate the ATACAMAC methodology. Perfect annular chamber and plenum connected by four burners ($N = 4$). `---` : line in the plenum (PL) and in the chamber (CL) along which absolute pressure and phase will be plotted

4.4.2 Description of the 3D acoustic code

To validate the assumptions used in ATACAMAC formulation, it is interesting to compare its results to the output of a full 3D acoustic solver. Here, AVSP was used: AVSP is

Chamber			
Half perimeter	L_c	6.59	m
Section	S_c	0.6	m^2
Plenum			
Half perimeter	L_p	6.59	m
Section	S_p	0.6	m^2
Burner			
Length	L_i^0	0.6	m
Section	S_i	0.03	m^2
Fresh gases			
Mean pressure	p^0	$2 \cdot 10^6$	Pa
Mean temperature	T_u^0	700	K
Mean density	ρ_u^0	9.79	kg/m^3
Mean sound speed	c_u^0	743	m/s
Burnt gases			
Mean pressure	p^0	$2 \cdot 10^6$	Pa
Mean temperature	T^0	1800	K
Mean density	ρ^0	3.81	kg/m^3
Mean sound speed	c^0	1191	m/s
Flame parameters			
Interaction index	n_i	*variable*	$-$
Time-delay	τ_i	*variable*	s
Thickness	e_{fl}	0.03	m

Table 4.1: Parameters used for numerical applications. They correspond to a typical large scale industrial gas turbine.

a parallel 3D code devoted to the resolution of acoustic modes of industrial combustion chambers (Nicoud *et al.*, 2007). It solves the eigenvalues problem issued from a discretization on unstructured meshes of the Helmholtz equation with a source term due to the flames. The mesh used here (Fig. 4.9, left) is composed of 230,000 cells which ensures grid independence. The flame-acoustic interaction is taken into account via the FTF model (Crocco, 1951) similar to the expression used in Eq. (4.13). The local reaction term is expressed in burner i as:

$$\dot{\omega}_i = n_{u,i}\, e^{j\omega\tau_i}\, w'(\mathbf{x}_{ref,i}) \tag{4.41}$$

The local interaction index $n_{u,i}$ describes the local flame-acoustic interactions. The values of $n_{u,i}$ are assumed to be constant in the flame zone i (Fig. 4.9) and are chosen to recover the global value of interaction index n_i of the infinitely thin flame when integrated over the flame zone i (Nicoud *et al.*, 2007). They are also assumed to be independent on frequency for simplicity. Heat release fluctuations in each flame zone are driven by the velocity fluctuations at the reference points $\mathbf{x_{ref,i}}$ located in the corresponding burner. In the infinitely thin flame model these reference points are the same as the flame locations

z_f. In AVSP, the reference points were placed a few millimeters upstream of the flames (Fig. 4.9) in order to avoid numerical issues. This was proved to have only a marginal effect on the computed frequency (Nicoud *et al.*, 2007).

4.4.3 Construction of a quasi-1D network from a real 3D combustor

A quasi-one-dimensional model of a simplified PBC configuration described in Section 4.4.1 can be constructed using Tab. 4.1. Even though the present model is quasi-one-dimensional, simple corrections can be incorporated to capture 3D effects.

First, the burners considered in Fig. 4.9 are long narrow tubes for which end effects modify acoustic modes. In the low frequency range, this can be accounted for (Pierce, 1981) and a standard length correction for a flanged tube (Silva *et al.*, 2009) is applied at the two burner's ends. The corrected length L_i for the burners is:

$$L_i = L_i^0 + 2 \times 0.4\sqrt{4S_i/\pi} \tag{4.42}$$

where L_i^0 is the i^{th} burner length without correction and S_i is the surface of the i^{th} burner.

Second, the position of the compact flames is defined via the parameter $\alpha = z_{f,i}/L_i$ where L_i is the corrected burner length and $z_{f,i}$ is the position of the center of the flame. In Sections 4.5 and 4.6, the flame position parameter is set to $\alpha = 0.88$, a location chosen because it is far away from all pressure nodes.

4.5 Mode analysis of a weakly coupled PBC configuration with four burners ($N = 4$)

Under the weak coupling factors assumption ($0 < \wp_{p,i} \ll 1$ and $0 < \wp_{c,i} \ll 1$) frequencies of the whole system can be analyzed considering small perturbations around the chamber alone (FDCp mode at $k^0 L_c = p\pi$) or plenum alone (FDPp mode at $k_u^0 L_p = p\pi$) wave numbers leading to two families of modes which appear separately (Section 4.3.3):

$$kL_c = p\pi + \epsilon_c \text{ (WCCp)} \tag{4.43}$$

or

$$k_u L_p = p\pi + \epsilon_p \text{ (WCPp)} \tag{4.44}$$

where p is the mode order, $\epsilon_c << p\pi$ and $\epsilon_p << p\pi$. Since the two families of modes behave in the same manner (only radius, density and sound speed are changed), only weakly coupled chamber modes will be detailed in this Section.

Due to symmetry considerations of the case $N = 4$, odd-order modes ($p = 2q+1,\ q \in \mathbb{N}$) and even-order modes ($p = 2q,\ q \in \mathbb{N}$) will not behave in the same manner and are analyzed in Section 4.5.1 and 4.5.2 respectively. A similar situation was also observed in previous chapters and appears for specific values of the number of burners.

4.5.1 Odd-order weakly coupled modes of the PBC configuration with four burners ($N = 4$)

Considering odd order modes ($p = 2q+1,\ q \in \mathbb{N}$) with the low coupling limit assumption ($0 < \wp_{p,i} \ll 1$ and $0 < \wp_{c,i} \ll 1$) leads to the expansion $kL_c = p\pi + \epsilon_c$ (for a WCCp mode). A Taylor expansion can therefore be used to obtained a simplified analytical expression of the transfer matrix of the i^{th} sector and consequently of the dispersion relation (Eq. (4.25)). This approach is fully detailed in Appendix D for the first mode on a single burner case ($N = 1$) for simplicity. The same approach for the p^{th} mode and four burners ($N = 4$) leads to (see Tab. D.1):

$$\sin(p\pi\beta)^2[\epsilon_c^2 + 4\epsilon_c\Gamma_4^0 + 4{\Gamma_4^0}^2] + o(\epsilon_c^2) = 0 \tag{4.45}$$

where $\beta = \frac{c^0 L_p}{c_u^0 L_c}$ and Γ_4^0 is the value of Γ_4 when $kL_c = p\pi$. Note that all the burners share the same length and cross section in this configuration so that the index i of Eq. (4.20) was removed for simplicity.

The β parameter can be viewed as a tuning parameter between cavities: it compares the period of the azimuthal modes in the plenum alone ($\tau_p^0 = \frac{2L_p}{pc_u^0}$) and in the chamber alone ($\tau_c^0 = \frac{2L_c}{pc^0}$). In general, the two annular volumes are not tuned and the periods τ_p^0 and τ_c^0 of the azimuthal modes of the plenum and the chamber do not match, i.e. $\beta = \tau_p^0/\tau_c^0 \neq l,\ l \in \mathbb{N}$ (for example for the first chamber and plenum modes ($p = 1$) of Table 4.1 where $\beta \simeq 1.60$) so that the only solution to satisfy Eq. (4.45) is:

$$\epsilon_c^2 + 4\epsilon_c\Gamma_4^0 + 4{\Gamma_4^0}^2 + o(\epsilon_c^2) = 0 \tag{4.46}$$

This quadratic equation has a double root [3] :

$$\epsilon_c = -2\Gamma_4^0 \tag{4.47}$$

where Γ_4^0 is the value of Γ_4 (Eq. (4.20)) at $\omega = \omega^0 = p\pi c^0/L_c$.

Real and imaginary parts of the frequency obtained in Eq. (4.47) are compared to the exact numerical resolution of the dispersion relation Eq. (4.25) and to AVSP results in Fig. 4.10. A very good agreement is found showing that the asymptotic expression of Eq. (4.47) is correct.

From Eq. (4.47), a simple analytical stability criterion can be derived as explained in Appendix E for weakly coupled chamber modes (Eq. (E.3)):

$$\underbrace{\sin\left(2\pi\frac{\tau}{\tau_c^0}\right)}_{\text{effect of } \tau}\underbrace{\sin\left(2p\pi\frac{\alpha L_i c^0}{L_c c_u^0}\right)}_{\text{effect of } \alpha} < 0 \quad \text{(WCCp modes)} \tag{4.48}$$

[3] This approach can be extended at higher orders to unveil plenum/chamber interactions. From a third-order truncation of the dispersion relation (Eq. 4.25), a second-order correction on eigenfrequencies found in Eq. (4.47) is obtained for WCCp modes:

$$\epsilon_c = -2\Gamma_4^0 - H(\beta)\Gamma_2^0\Gamma_3^0 \quad \text{(WCCp modes)}$$

where $H(\beta) = 4\tan(p\pi\beta/2)$.

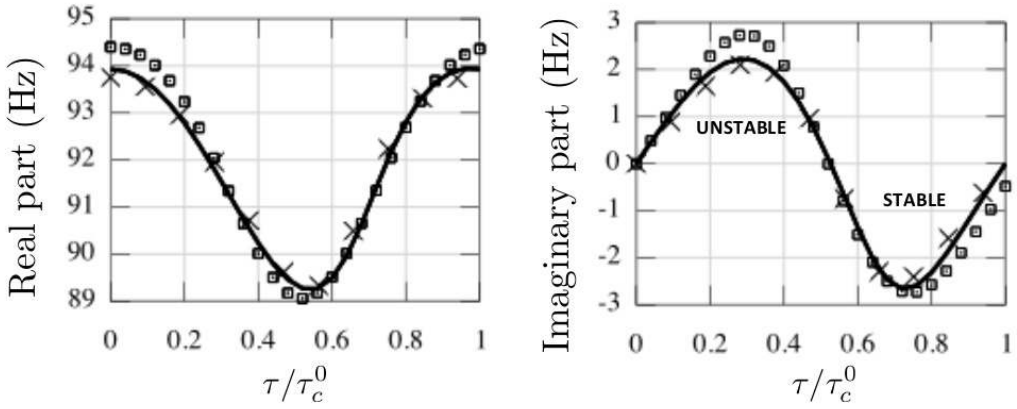

Figure 4.10: Eigenfrequency of the WCC1 mode for four burners ($N = 4$) with $n_i = 1.57$ as a function of τ/τ_c^0. —— : Numerical resolution of the dispersion relation Eq. (4.25), □: Analytical model prediction Eq. (4.47), ×: AVSP results

where $\tau_c^0 = \frac{2c^0}{pL_c}$

Time-delay τ of the FTF and flame position α have an effect on the stability and can be studied separately:

- **Time-delay -** From Eq. (4.48), a critical time-delay controlling the transition from stable to unstable regimes can be obtained: $\tau_{crit} = \tau_c^0/2 = \frac{L_c}{pc^0}$ for WCCp modes. This result being also valid for plenum modes (i.e. WCPp modes, see Eq. (E.4) leading to the critical time-delay $\tau_p^0/2 = \frac{L_p}{pc_u^0}$), stability ranges of the two first azimuthal modes WCC1 and WCP1 can be displayed simultaneously (Fig. 4.11). It shows that the region where both the chamber and plenum modes are stable is smaller than the stability ranges of modes taken separately: stabilizing one mode of the system cannot ensure the stability of the whole system. Of course, this result does not include any dissipation or acoustic fluxes through the boundaries (Nicoud & Poinsot, 2005) which would increase stability regions.
- **Flame position -** Similarly to longitudinal modes in the Rijke tube (Schuller *et al.*, 2012; Poinsot & Veynante, 2011), the flame position (defined by α) also controls the stability (Eq. (4.48)). Appendix F demonstrates an analytical expression of the critical flame position for weakly couple modes (Eq. (F.2)) at which the stability change occurs. These expressions are close to the solution found in Rijke tubes (Eq. (F.1)) and have been validated for several weakly coupled modes (Tab. F.1 and Fig. F.1).

4.5.2 Even-order modes of the PBC configuration with four burners ($N = 4$)

Considering even-order weakly coupled chamber modes ($p = 2q$, $q \in \mathbb{N}$) and using Eq. (4.25) with the low coupling limit assumption ($0 < \wp_{p,i} \ll 1$ and $0 < \wp_{c,i} \ll 1$),

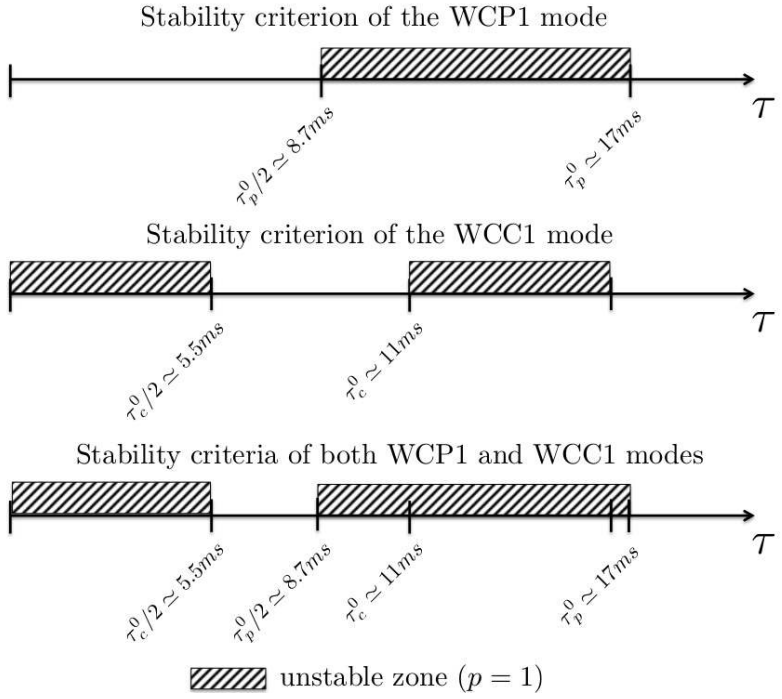

Figure 4.11: Stability maps (Eq. (4.48)) of the two first azimuthal modes ($p = 1$) for a flame located at $\alpha \simeq 0.88$: WCP1 (top), WCC1 (middle) and both WCP1 and WCC1 (bottom)

the dispersion relation (Eq. (4.25)) becomes (Tab. D.1):

$$\sin(p\pi\beta/2)^2[\epsilon_c^2 + 4\epsilon_c\Gamma_4^0] + o(\epsilon_c^2) = 0 \tag{4.49}$$

where $\beta = \frac{k_u L_p}{k L_c}$ and Γ_4^0 is the value of Γ_4 when $kL_c = p\pi$.

When chamber and plenum frequencies do not match, i.e. $\beta \neq 1$ (for example for the second ($p = 2$) mode of Table 4.1 where $\beta \simeq 1.60$), the only solution to satisfy Eq. (4.49) is to have:

$$\epsilon_c^2 + 4\epsilon_c\Gamma_4^0 + o(\epsilon_c^2) = 0 \tag{4.50}$$

This quadratic equation has two distinct roots:

$$\epsilon_c = 0 \text{ and } \epsilon_c = -4\Gamma_4^0 \tag{4.51}$$

The first solution ($\epsilon_c = 0$) of Eq. (4.51) corresponds to modes which are not affected by the flames: the symmetry of the four burners case ($N = 4$) allows even-order modes to impose a pressure node at each burner location suppressing the flame effect on these modes which become neutral. The second solution of Eq. (4.51) ($\epsilon_c = -4\Gamma_4^0$) correspond to modes which are modes strongly affected by the flame because it imposes a pressure anti-node (maximum pressure) downstream of each burner.

Real and imaginary parts of the frequency obtained from Eq. (4.51) are compared to the numerical solutions of the dispersion relation Eq. (4.25) and to AVSP results in

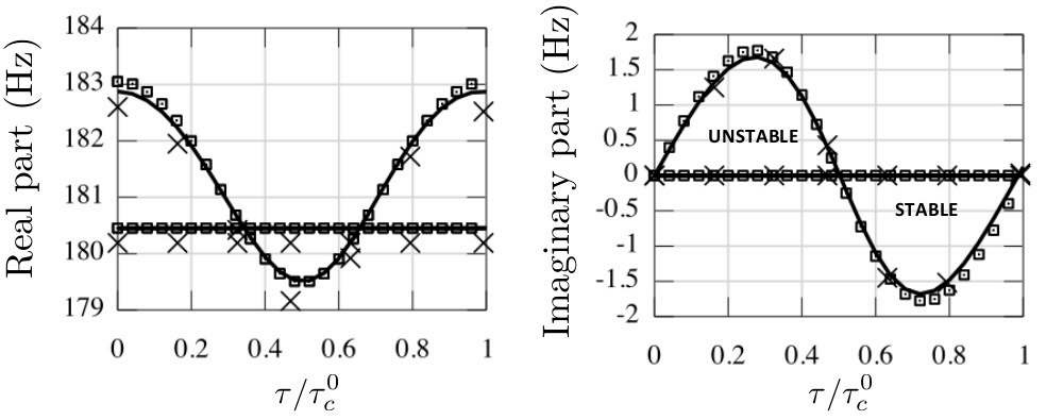

Figure 4.12: Eigenfrequency of the WCC2 mode for four burners ($N = 4$) with $n_i = 1.57$ as a function of τ/τ_c^0. —— : Numerical resolution of the dispersion relation Eq. (4.25), □: Analytical model prediction Eq. (4.51), ×: AVSP results

Fig. 4.12. A very good agreement is found and the non-perturbed mode ($\epsilon_c = 0$) is correctly captured (straight lines).

Using Eq. (4.51) and Appendix E leads to an analytical stability criterion for WCCp even-order modes (Eq. (E.3)). This result being also valid for WCPp modes (Eq. (E.4)) and using the results from Section 4.5.1, stability maps of the weakly coupled plenum and chamber modes (WCC1, WCC2, WCP1 and WCP2) can be plotted together (Fig. 4.13) highlighting the difficulty to get a stable system in the absence of dissipation as supposed here: considering only these four modes, no stable region is found for time-delays lower than $19.1ms$ in the case described in Tab. 4.1 (Fig. 4.13).

4.5.3 Mode structure of weakly coupled modes

In weakly coupled situations, acoustic activity is present only in one annular cavity and in the burners as shown in Fig. 4.14 for the WCC1 mode (the same mode with the opposite rotation direction is also captured by AVSP but not shown here). Fig. 4.15 shows that this mode is purely rotating in the chamber while it is mixed in the plenum. Therefore, the combination of the two weakly coupled chamber modes with the clockwise rotation (show in Fig. 4.15) and the anti-clockwise rotation (not shown) enable to have purely rotating or purely standing modes but not necessarily in the two annular cavities at the same time.

4.5.4 Stability map of weakly coupled situations

Sections 4.5.1 and 4.5.2 focused on weakly coupled situations where the low coupling factor assumption ($\wp_p \ll 1$ and $\wp_c \ll 1$) is valid. Stability maps of perturbed modes (i.e. $\epsilon \neq 0$) in the complex plane $[R_e(f), I_m(f)]$ are well suited to show differences between the several regimes - weakly coupled and strongly coupled situations. These maps are oriented circles (--- (WCP1) and —— (WCC1) in Fig.4.16) centered at the frequency $f(n_i = 0) \simeq f_0$ which corresponds to a passive flame mode ($n_i = 0$: × in Fig.4.16) and

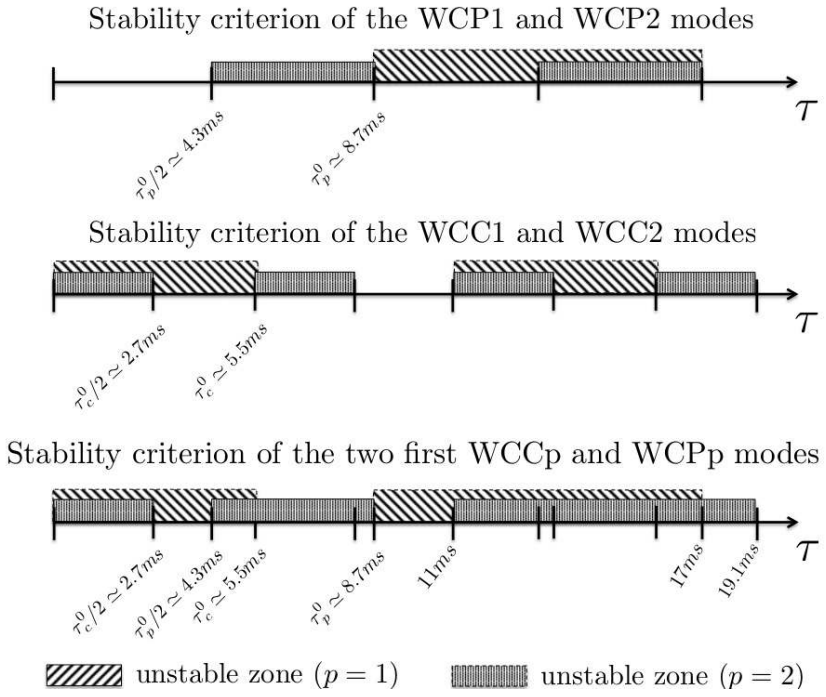

Figure 4.13: Stability maps of the WCC1, WCC2, WCP1 and WCP2 modes

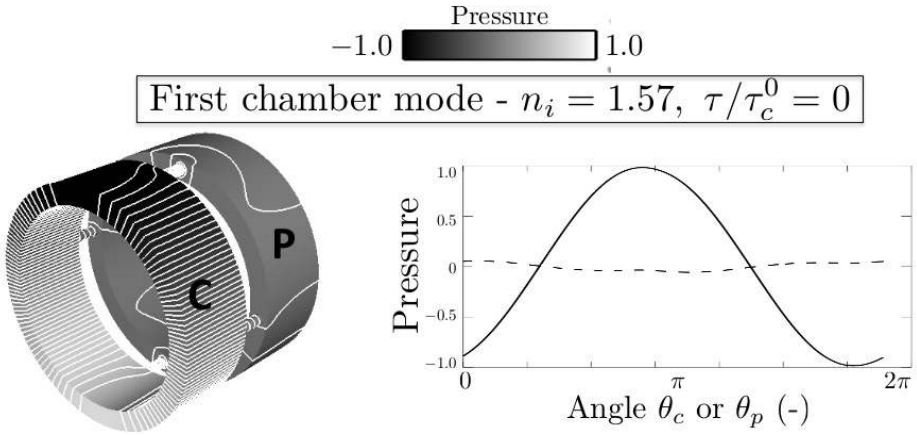

Figure 4.14: Pressure mode structures ($p' = |p'|cos(arg(p'))$) obtained with AVSP with pressure isolines (left) and pressure along the azimuthal direction in the annular chamber (———) and annular plenum (- - -) for the WCC1 mode of a PBC configuration with four burners ($N = 4$) and $n_i = 1.57$ at the time-delay: $\tau/\tau_c^0 = 0$

is approximately the frequency of the cavity alone ($f_0 = \frac{pc^0}{2L}$). The radius is proportional to the coupling factor which can be increased via the surface ratios (S_i/S_p and S_i/S_c) or the flame interaction index n_i. In the weakly coupled regime, WCCp and WCPp modes do not strongly interact as shown in Fig. 4.16: modes in the plenum and in the chamber live separately.

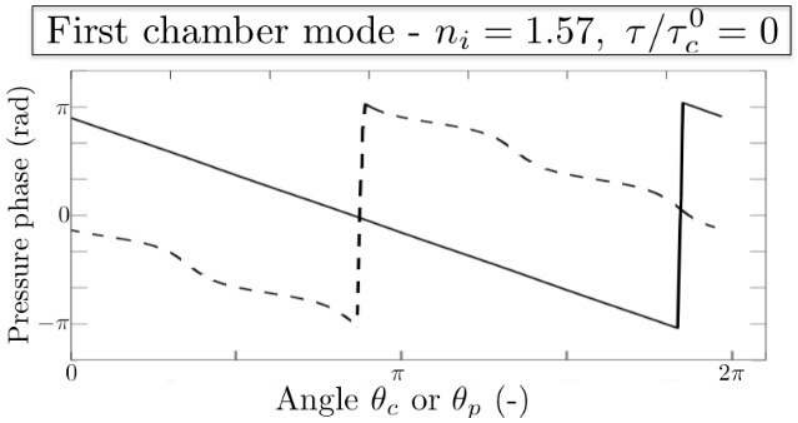

Figure 4.15: Pressure phase of the WCC1 mode obtained with AVSP at $n_i = 1.57$ along the azimuthal direction in the annular chamber (——) and the annular plenum (- - -) for time-delay: $\tau/\tau_c^0 = 0$

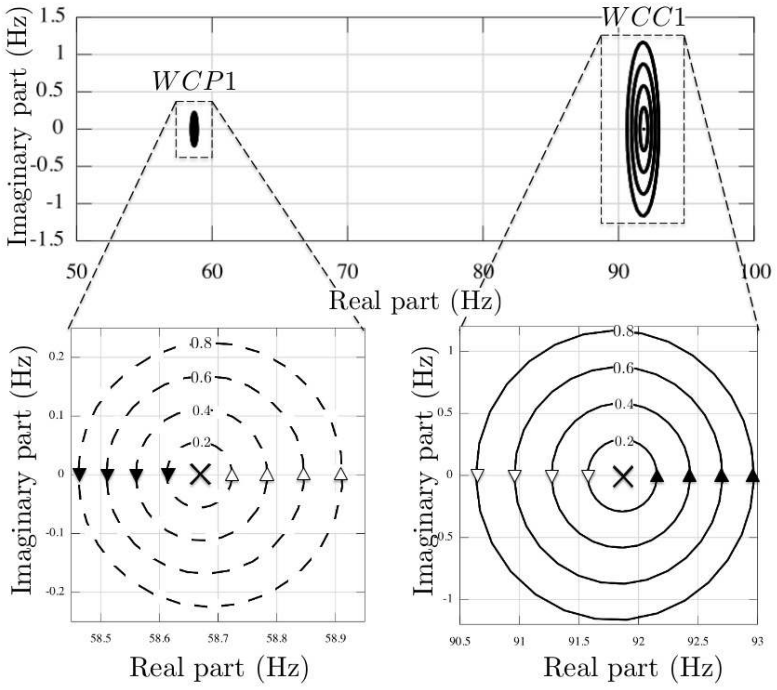

Figure 4.16: Eigenfrequencies of both WCP1 and WCC1 modes (top) and zoom on WCP1 (bottom left) and WCC1 (bottom right) when the flame delay changes for PBC configuration with four burners ($N = 4$) with $n_i = 0.2$, 0.4, 0.6 and 0.8, ×: Passive flame ($n_i = 0$), - - - : WCP1 mode, —— : WCC1 mode, ►: $\tau/\tau_p^0 = 0$ or $\tau/\tau_c^0 = 0$ oriented in the increasing τ direction, ▷: $\tau/\tau_p^0 = 1/2$ or $\tau/\tau_c^0 = 1/2$

4.6 Mode analysis of a strongly coupled PBC configuration with four burners ($N = 4$)

For weakly coupled cases (Section 4.5), the frequencies of the azimuthal modes in the plenum and in the chamber are only marginally affected by the flame (Figs. 4.10 and 4.12) so that they can never match (Fig. 4.16). However, if the flame interaction index

(n_i) is larger, the frequencies of the azimuthal modes of the annular plenum and the annular chamber change more and the possibility of having there two frequencies match opens an interesting situation where the whole system can resonate. This corresponds to the strongly coupled modes of order p (referred as "SCp" modes) studied in this section.

Figure 4.17 shows the stability maps of the WCC1 (——) and WCP1 (---) modes obtained with low flame interaction index ($n_i = 5.0$ and 6.0) as well as the SC1 (∘) and SC2 modes (•) obtained for higher flame interaction index ($n_i = 7.0$ and 8.0[4] at the zero frequency limit). Three points in the SC2 trajectory with $n_i = 8.0$ corresponding to several time-delays ($\tau/\tau_c^0 = 0$ (A), $\tau/\tau_c^0 = 0.54$ (B) and $\tau/\tau_c^0 = 0.9$ (C)) are displayed in Fig. 4.17 and will be used as typical cases to show pressure structures in the annular plenum and chamber.

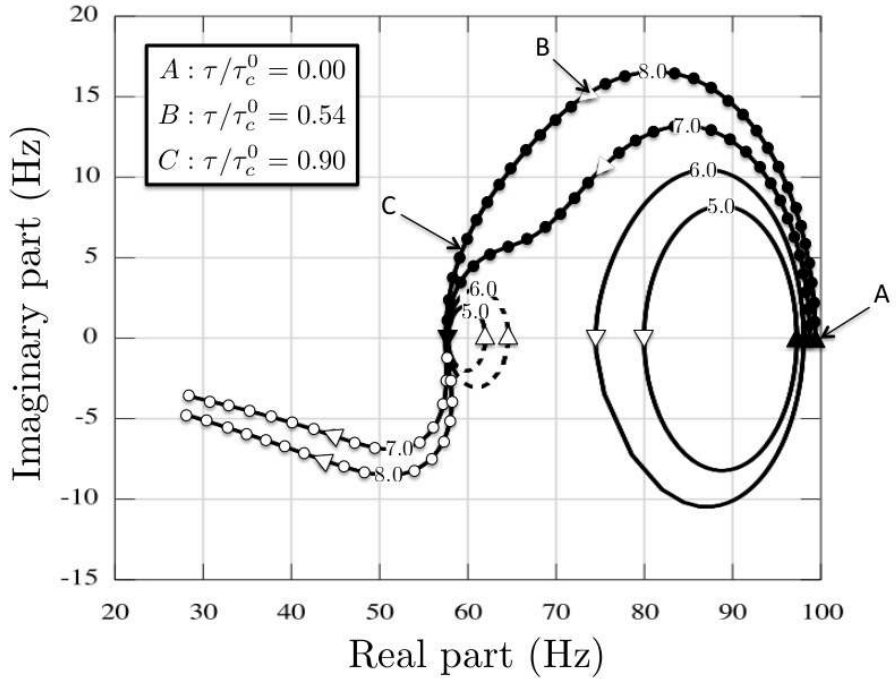

Figure 4.17: Eigenfrequencies on the complex plane for a PBC configuration with four burners ($N = 4$), ---- : WCP1 mode ($n_i = 5.0$ and 6.0), —— : WCC1 mode ($n_i = 5.0$ and 6.0), ∘: SC1 mode ($n_i = 7.0$ and 8.0), •: SC2 mode ($n_i = 7.0$ and 8.0), ▶: $\tau/\tau_p^0 = 0$ or $\tau/\tau_c^0 = 0$ oriented in the increasing τ direction and ▷: $\tau/\tau_p^0 = 1/2$ or $\tau/\tau_c^0 = 1/2$

For low flame interaction index ($n_i = 5.0$ and 6.0), the first two modes always have different frequencies and can be identified as plenum (WCPp: ---) or chamber modes (WCCp: ——) as studied in Section 4.5.

However, for higher flame interaction indices ($n_i = 7.0$ and 8.0) a bifurcation occurs: frequencies of the annular plenum, burners and annular chamber can match leading to strongly coupled modes where the whole system resonates. The trajectory of the first strongly coupled mode (SC1: ∘) goes from the WCP1 mode (for small time-delays $\tau < \tau_p^0/2$) to a longitudinal mode (not presented here around 40Hz, for large time-delays

[4]Note that the typical order of magnitude of the interaction index n_i is $T_b/T_u - 1$

$\tau > \tau_p^0/2$). A second strongly coupled mode (SC2: •) has a trajectory in the complex plane coming from the WCC1 mode (for small time-delays $\tau < \tau_c^0/2$) and going to the WCP1 mode (for large time-delays $\tau > \tau_c^0/2$).

The stability map of the SC2 mode (•) at $n_i = 8.0$ has been validated against the 3D finite element solver AVSP (Fig. 4.18). A good agreement between AVSP (×) and the numerical resolution of Eq. (4.25) (——) is found. The growth rate is slightly underestimated but the global trend is well captured: the mode is fully unstable for all time-delays which corresponds to a new behavior compared to the weakly coupled modes. The analytical approach developed in Section 4.5 for the weakly coupled regime (□ in Fig. 4.18) is not able to capture this new highly non-linear behavior.

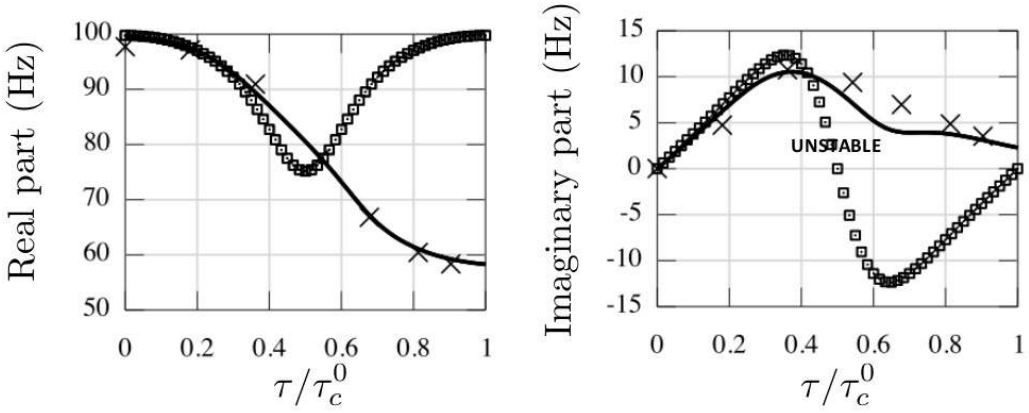

Figure 4.18: Eigenfrequency of the first order chamber mode ($p = 1$) for four burners ($N = 4$) as a function of τ/τ_c^0 with $n_i = 8.0$. —— : Numerical resolution of Eq. (4.25), □: Analytical model prediction for weakly coupled situations (Eq. (4.47)), ×: AVSP results

When the flame interaction index is sufficiently large ($n_i > 7.0$), i.e. when the flame is sufficiently intense, the modes of plenum and chamber lock-in and become unstable for all time delays. Fig. 4.19 shows the modulus of the coupling factors $\|\Gamma_1\|$, $\|\Gamma_4\|$ and the interaction product $\|\Gamma_2\Gamma_3\|$ (terms appearing in analytical results summarized in Tab. E.1) as a function of the time-delay τ_1 for the three different cases corresponding to the first order ($p = 1$) chamber mode: $n_1 = 1.57$ (weakly coupled regime), $n_1 = 4.0$ (limit case between weakly/strongly coupled regimes) and $n_1 = 8.0$ (strongly coupled regime). It highlights the tuning mechanism:

- In the weakly coupled regime ($n_1 = 1.57$), both Γ_1 and Γ_4 have the same order of magnitude and they vary in opposite directions. The low coupling factors assumption is satisfied.
- Then, at the limit case between weakly/strongly coupled regime ($n = 1.40$), $\|\Gamma_4\|$ is almost constant with the time-delay τ_1. The other coupling factors are not affected.
- Finally, in the strongly coupled regime ($n_1 = 8.0$), the coupling parameter of the burner/chamber junction Γ_4 is amplified which indicates that this junction is tuned. The evolution of the eigenmode versus the time-delay is reversed compared to the weakly coupled regime: now, the two annular cavities (plenum and chamber) act together in the same manner ; they are coupled. Consequently, the interaction term

($\|\Gamma_2\Gamma_3\|$) is also increased. The low coupling factors assumption is not satisfied in this case.

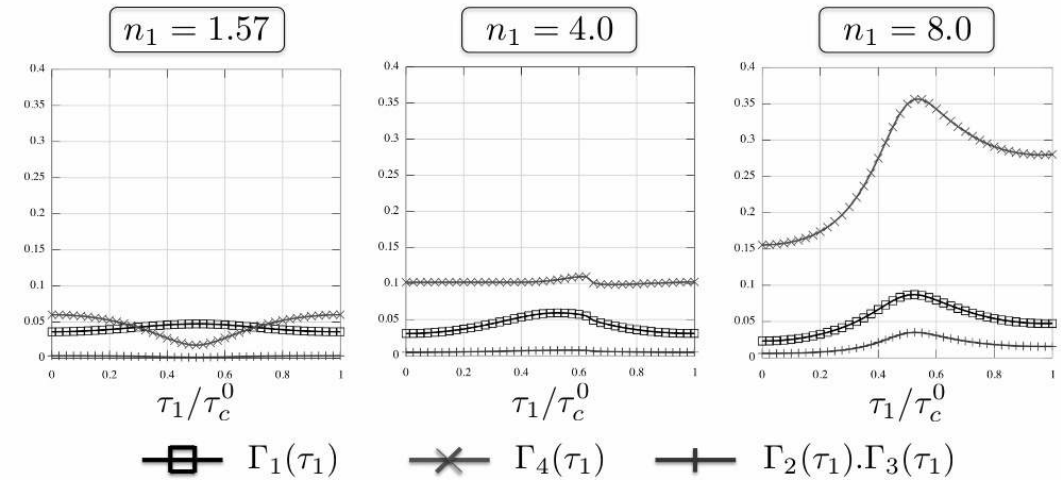

Figure 4.19: Modulus of the coupling factors $\|\Gamma_1\|$ ($\square$), $\|\Gamma_4\|$ ($\times$) and $\|\Gamma_2 * \Gamma_3\|$ ($+$) varying with the time delay τ_1 for three cases: $n_1 = 1.57$ (weakly coupled regime), $n_1 = 4.0$ (limit case) and $n_1 = 8.0$ (strongly coupled regime)

Pressure structures ($p' = |p'|cos(arg(p'))$) along the azimuthal direction in the plenum (PL line in Fig. 4.9) and in the chamber (CL line in Fig. 4.9) obtained with AVSP for the second strongly coupled mode are displayed in Fig. 4.20 for a high flame interaction index ($n_i = 8.0$) and several time-delays (A: $\tau/\tau_c^0 = 0$, B: $\tau/\tau_c^0 = 0.54$ and C: $\tau/\tau_c^0 = 0.9$ from Fig. 4.17). For null time-delays (A in Fig. 4.17), acoustic activity is only present in the chamber (——) and the frequency is close to the weakly coupled chamber mode. The acoustic activity in the second annular cavity (i.e. the plenum: ---) grows with the time-delay τ. For $\tau/\tau_c^0 = 0.54ms$ (B in Fig. 4.17) a strong interaction with the burners appears leading to higher growth rates. Surprisingly, this case corresponds only to a moderate acoustic activity in the second annular cavity (i.e. the annular plenum: ---). For $\tau/\tau_c^0 = 0.9$ (C in Fig. 4.17) a first order mode is present in both annular cavities highlighting a strongly coupled situation. This strong interaction between plenum and chamber revealed by the presence of acoustic activity in both annular cavities leads, however, to a marginally unstable mode.

Fig. 4.21 shows the pressure phase in the annular plenum (---) and in the annular chamber (——) for several time-delays. The same mode with opposite direction is also found with AVSP but not shown here. For small time-delay ($\tau/\tau_c^0 = 0$ for case A and $\tau/\tau_c^0 = 0.54$ for case B of Fig. 4.17), pressures in the plenum and in the chamber have different natures: purely spinning mode in the chamber (linear phase) and a mixed mode in the plenum (wave shape of the phase). The combination of clockwise and anti-clockwise mode can generate purely spinning or purely standing mode but not necessarily in both annular cavities at the same time. However, higher time-delays cases (as for case C where $\tau/\tau_c^0 = 0.9$) correspond to strongly coupled situations where both annular cavities lock-in (Fig. 4.20 C). In such a case, pressure in the chamber and plenum exhibit the same

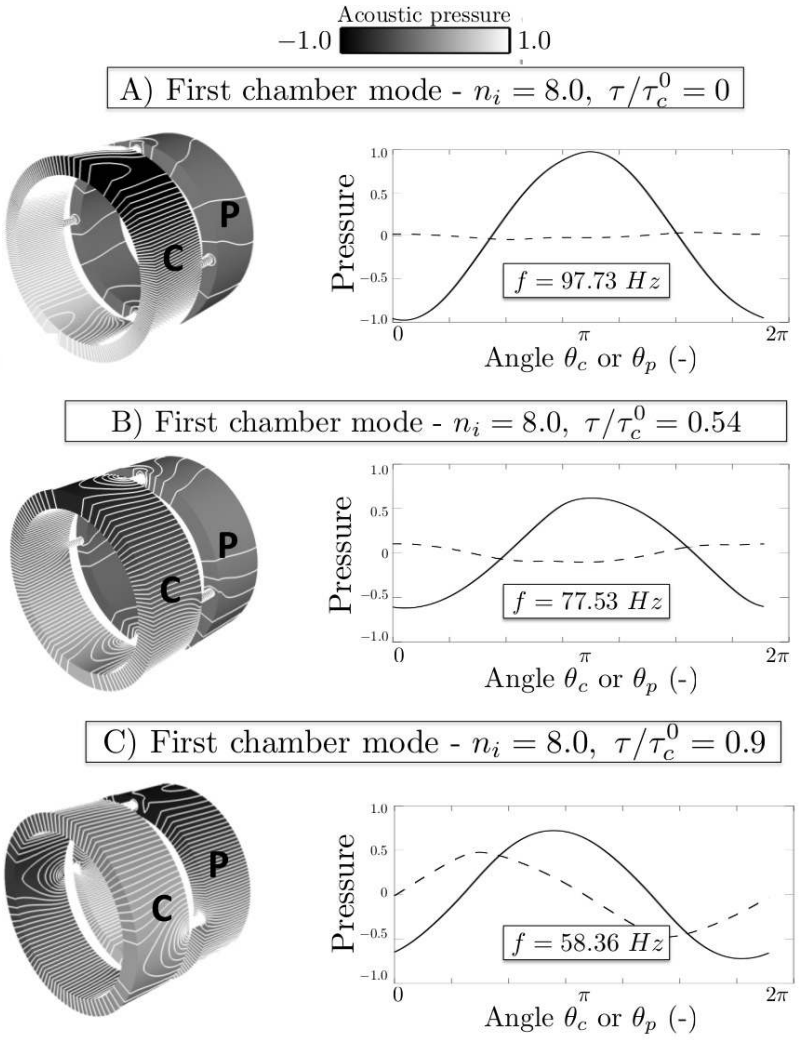

Figure 4.20: Pressure structures and isolines ($p' = |p'|cos(arg(p'))$) obtained with AVSP (left) and pressure along the azimuthal direction in the annular chamber (——) and annular plenum (- - -) for the SC2 mode of a PBC configuration with four burners ($N = 4$) and $n_i = 8.0$ at several time-delay: $\tau/\tau_c^0 = 0$ (top), 0.54 (middle) and 0.9 (bottom). The configuration corresponds to $f_{FDP1} = 56$ Hz and $f_{FDC1} = 90$ Hz

nature: purely spinning in both cavities in Fig. 4.21 C (the same mode with the opposite rotating direction is also found by AVSP but not shown here). The combination of the purely spinning modes (clockwise and anti-clockise) can also lead to standing modes in both annular cavities at the same time: this is a specific behavior only encountered in locked-in modes as case C.

Finally, it demonstrates that a highly unstable mode does not necessarily exhibit strong acoustic activity in both annular cavities (as for case B) and that a mode where acoustic activity appears in the whole system can be only marginally unstable (as for case C). Moreover, the phase-lag between pressure in the annular cavity and the annular chamber as well as the nature of the mode (spinning, standing or mixed) changes when acoustic activity is present in both annular cavities, a property which has been then

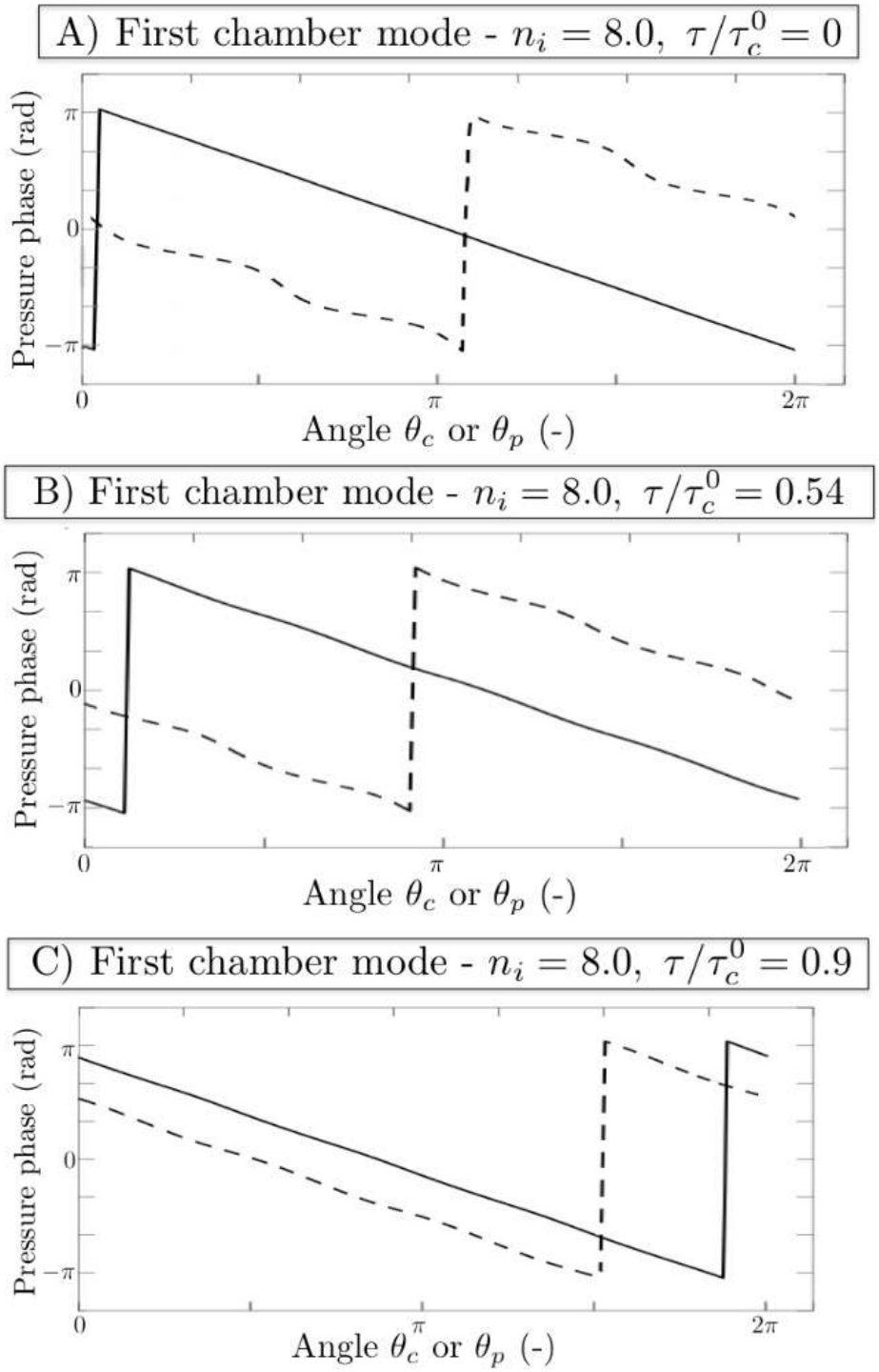

Figure 4.21: Pressure phase obtained with AVSP for the SC2 mode at $n_i = 8.0$ along the azimuthal direction in the annular chamber (——) and the annular plenum (- - -) for several time-delays: $\tau/\tau_c^0 = 0$ (top), 0.54 (middle) and 0.9 (bottom).

further investigated theoretically and experimentally by Bourgouin *et al.* (2014).

4.7 Conclusion

This chapter describes an extension of the analytical theory developed in previous chapters of this PhD thesis to more realistic configurations where the both the annular chamber and plenum are considered. A manipulation of the corresponding acoustic equations in this configuration leads to a simple analytical dispersion relation which can be solved numerically. This method allows to exhibit coupling factors between plenum, burners and chamber which depend on area ratios and flame transfer function (FTF). For $N = 4$, a fully analytical resolution can be performed in specific situations where coupling factors of the FTF (Parmentier *et al.*, 2012; Schuller *et al.*, 2012) are small and simple stability criteria can be proposed. For higher coupling factors, a bifurcation occurs yielding a strongly coupled regime where acoustic activity is present in both annular cavities. The nature of such a mode (standing, spinning or mixed) changes with the time-delay. Purely spinning or purely standing modes in the annular plenum and in the chamber were found simultaneously only when a strongly coupled situation occurs (Fig. 4.21 C). For these cases, a PBC configuration where two annular cavities are connected to N burners is required to predict correctly eigenmodes and stability maps. This analytical tool has been compared systematically to the predictions of a full three-dimensional Helmholtz solver. A very good agreement is found showing that the present asymptotic resolution is correct. In this chapter, all configurations were considered as axisymmetric but symmetry breaking effects in PBC configurations for both weakly and strongly coupled regimes are studied in the next chapter.

Chapter 5

Uncertainty Quantification of thermo-acoustic modes in annular gas turbines

Contents

An Uncertainty Quantification (UQ) method based on active subspace and low-order models is applied on a gas turbine geometry to determine its modal risk factor: ten probability of an acoustic mode to be unstable. The system considered is a PBC configuration equipped with 19 *burners which is operated in the 'weakly' and 'strongly' coupled regimes identified in the previous chapter. Each flame is modeled by two uncertain parameters leading to a large UQ problem involving* 38 *parameters. The combustor is modeled as a network of* 4×19 *interconnected 1D acoustic elements which is solved quasi-analytically (ATACAMAC) as proposed recently by Bauerheim et al. (2014d). This allows to perform a Monte Carlo analysis (approx.* $10,000$ *ATACAMAC calculations) assuming that the uncertainties on the inputs (the* n *and* τ *of each burner:* 38 *parameters) are known: results of this full Monte Carlo method constitute a reference case which can be affordable when using ATACAMAC but not Helmholtz solvers. Results show that uncertainties on FTF induce a symmetry breaking of the configuration. The reference Monte Carlo risk factor is then compared with that obtained by a less demanding UQ method to prepare for situations where the analytical method of ATACAMAC would have to be replaced by a full 3D solver such as AVSP. First, the dimension of the problem is reduced from* 38 *to only* 5 *parameters for the two regimes considered by the active subspace approach based on gradients correlations. Then, linear and quadratic analytical models based on the five active variables are fit using* 100 *ATACAMAC simulations. These low-order models are then replayed* $100,000$ *times to obtain the PDF of the growth rate as well as the risk factor estimation. Results show that for both regimes, the UQ method is able to accurately predict the risk factor of the configuration.*

5.1 Introduction

All experimentalists and engineers in the field of combustion know that instabilities are phenomena which depend strongly on small variations of parameters: a chamber which is stable when the weather is nice can become unstable if it is raining ; ten boosters built on the same design can exhibit different stability properties with 8 stable systems and 2 unstable ones. These observations call for the introduction of UQ (Uncertainty Quantification) in the study of combustion instabilities. UQ methods have been spreading in CFD community for a few years (Roache, 1997; Chantrasmi *et al.*, 2006). These methods basically aim at qualifying uncertainties on a CFD result, knowing uncertainties on the inputs of the computation. In the field of thermoacoustics, the main question is to predict whether a mode is damped or not. The natural next question is "what is the dependency of this answer to small variations of the input parameters of the code ?" which can also be expressed as "knowing uncertainties on input parameters, is it possible to obtain the probability that a mode will be unstable ?": this question is known as the forward uncertainty propagation problem.

This question cannot be studied with LES which is too expensive but it can be with Helmholtz solvers. However the best candidate to test and compare new UQ methods is

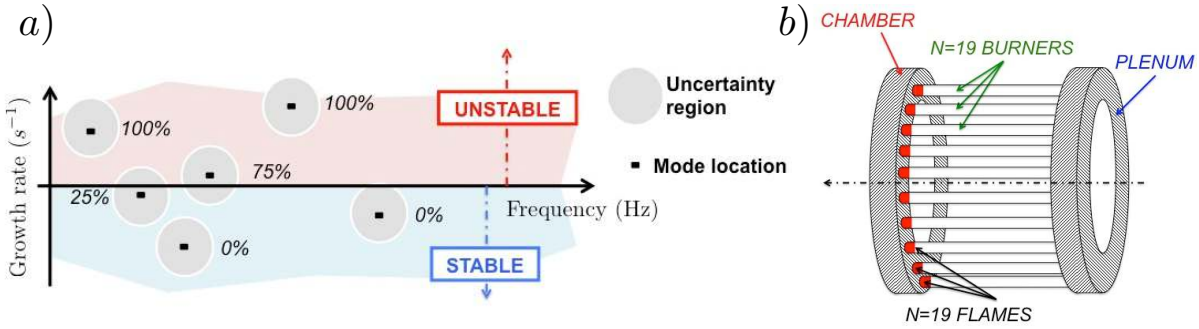

Figure 5.1: a) Location in the frequency plane of the first six thermo-acoustic modes in a typical combustor without uncertainties (single point, black symbols) and with uncertainties (each mode belongs to an admissible region of the frequency plane with an associated risk factor to be unstable). b) The annular configuration studied with one plenum connecting $N = 19$ burners and an annular chamber.

to use the analytical tool developed here (ATACAMAC) which allows fast computation of problems involving complex phenomena (non-linear problem, stability margin, bifurcations etc.) while retaining most characteristics of 3D Helmholtz solvers. These 3D solvers characterize the stable/unstable modes in the frequency domain. An approximate linear wave equation for the small pressure perturbations $p(\vec{x},t) = \tilde{p}(\vec{x})exp(-j\omega t)$ in reacting flows may be derived from the Navier-Stokes equations (Poinsot & Veynante, 2005) and reads:

$$\nabla \cdot \left(c_0^2 \nabla \tilde{p}\right) + \omega^2 \tilde{p} = j\omega(\gamma - 1)\tilde{\dot{\omega}_T} \tag{5.1}$$

where $\dot{\omega}_T(\vec{x},t) = \tilde{\dot{\omega}_T}(\vec{x})exp(-j\omega t)$ is the unsteady heat release, c_0 the speed of sound and ω is the complex pulsation.

In order to close the problem, the flame is often modeled as a purely acoustic element thanks to a $n-\tau$ type of model (Crocco, 1952) or a matrix transfer (Polifke *et al.*, 2001*b*), which essentially relates the unsteady heat release to acoustic quantities at reference locations. Equation 5.1 then corresponds to a non-linear eigenvalue problem which can be solved efficiently at reduced cost (Nicoud *et al.*, 2007). The output of such low-order tool is typically a map of the thermo-acoustic modes in the complex plane (see the black symbols, in Figure 5.1-a). In this view, each mode is either stable or unstable, depending on the input parameters of the thermacoustic analysis. Each mode corresponding to a positive imaginary frequency (positive growth rate) is linearly unstable and must be controlled (e.g. by including acoustic dampers) for the combustor to be stable. The design process is made much more complex by the fact that the input parameters of the low-order model described by Eq. 5.1, are uncertain. For example, the speed of sound c_0, the boundary impedances and the flame forcing $\dot{\omega}_T(\vec{x},t)$ are very sensitive to multiple physical parameters such as the flow regime, manufacturing tolerances, fuel changes, acoustic and heat losses which are themselves (partly) unknown. As a consequence, each mode actually belongs to an uncertain region in the complex plane as illustrated in Figure 5.1-a and quantified by the risk factor, the probability for the mode to be unstable. Moreover, manufacturing uncertainties lead to small differences in the burners and flames

behaviors which can induce a symmetry breaking and a potential destabilization of the system as shown in Chapters 2 and 3.

In academic situations containing only one burner, the shape and size of these uncertain regions depend only on a few uncertain parameters such as the inlet air temperature, the amplitude and phase of the flame response and the boundary impedances (Duchaine *et al.*, 2011). The situation is more complex in actual industrial combustors used for power generation or aero-engines: they usually contain an annular chamber hosting several burners, typically from 15 to 24, and are prone to azimuthal combustion instabilities. In this case, the number of uncertain parameters may reach several tens since the gain and time delay of each burner (and associated flame) are highly sensitive to manufacturing tolerances. The "curse of dimensionality", well known in the UQ field, is thus becoming a problem when applying UQ to such systems. Moreover, the coupling between the combustion chamber, the burners and the upstream plenum is also rather complex as revealed by recent experimental (Worth & Dawson, 2013*b*) and numerical (Wolf *et al.*, 2012; Bourgouin *et al.*, 2013) studies.

Even though our objective is to apply UQ in full 3D Helmholtz solvers, it is applied first here using the ATACAMAC tool presented in previous chapters because it is much more faster. The analytical descriptions performed in Chapter 4 for thermoacoustic modes in annular PBC combustors with burners heterogeneities indeed open new perspectives regarding parametric studies and uncertainty quantification (UQ) at low cost. Consequently, in this chapter ATACAMAC is used to test a novel approach in UQ, called active subspace (Constantine *et al.*, 2014), dedicated to reduce the input space dimensionality. To the best of our knowledge, introducing UQ for thermoacoustics and symmetry breaking was never done before although this is a necessary step to better control the risk associated with each mode during the design process. This is the objective of this chapter. The application of UQ to full 3D solvers is left for further studies.

5.2 Thermo-acoustics of a PBC annular combustor

5.2.1 Mathematical framework

In the last decade, theoretical approaches for thermoacoustics in annular chambers have been applied on simplified annular configurations (Noiray *et al.*, 2011; Parmentier *et al.*, 2012) to complement 3D Helmholtz simulations (Campa *et al.*, 2011; Pankiewitz & Sattelmayer, 2003) and LES (Wolf *et al.*, 2012). In Chapters 2 and 3, the analytical ATACAMAC tool (Analytical Tool to Analyze and Control Azimuthal Mode in Annular Chambers) has been developed to handle a BC configuration where an annular chamber connects N burners. This tool has been extended to more complex geometries with two annular cavities (Bauerheim *et al.*, 2014*a*) in the previous chapter: one annular chamber fed by N burners connected to an annular plenum, as illustrated in Figure 5.1-b. In such systems, the two annular cavities can couple and may impact the symmetry breaking mechanisms. This chapter focuses on such a configuration where a 1D annular plenum connects $N = 19$ burners and a 1D annular combustion chamber, representative of real industrial gas turbines (Figure 5.1-b). The ANR methodology applied on PBC geometries

detailed in Chapter 4 leads to the analytical dispersion relation:

$$\det\left(\prod_{k=N}^{1} R_i T_i - I_d\right) = 0 \tag{5.2}$$

where R_i is the 4-by-4 propagation matrix defined in Eq. (4.23) and T_i is the 4-by-4 interaction matrix obtained in Eq. (4.16) which depends on four coupling parameters $\Gamma_{i,k=1..4}$ described in Eqs. (4.17)-(4.20). In the previous chapter (Chapter 4), two different regimes have been identified:

- **Weakly coupled modes:** A fully analytical expression of frequencies and growth rates has been derived in Chapter 4 assuming low coupling parameters between burners and combustion chamber: $\|\Gamma_{i,k=1..4}\| \ll 1$. When this assumption is valid, the annular chamber and the annular plenum can be considered as decoupled and growth rates can be expressed using analytical results obtained for BC configurations in Chapters 2 and 3. This regime is called weakly coupled.
- **Strongly coupled modes:** When the coupling parameters increase (i.e. when flames become more sensitive to acoustics), a bifurcation can occur corresponding to a strong coupling between the two annular cavities which can change the stability of the whole system. Acoustic activity is present in both annular cavities with a phase-lag between the fluctuating pressure in the chamber and in the plenum, modifying the mode structure and therefore may have an impact on symmetry breaking effects. This regime is called strongly coupled and cannot be analyzed analytically.

5.2.2 Thermo-acoustic modes in an axisymmetric PBC configuration with $N = 19$ burners

The mathematical framework described previously in Chapter 4 for a simplified combustor with $N = 4$ burners is applied here on a realistic PBC combustor equipped with $N = 19$ burners (Fig. 5.1-a). This section considers an axisymmetric case and reproduce the work of Chapter 4 to classify plenum/chamber and weakly/strongly coupled modes of this new configuration where geometrical and mean flow characteristics are known perfectly (no uncertainty here) and given in Tab. 5.1. UQ and symmetry breaking will be investigated in the next sections.

The annular configuration is perfectly axisymmetric with identical burners and flames so that all flame parameters (n_i, τ_i), coupling parameters Γ_i and matrices R_i or T_i are exactly the same (the subscript i can be omitted in this section). Parameters of the FTF are varied to produce stability maps and unveil mode trajectories as well as coupling between cavities (Bauerheim *et al.*, 2014*d*).

Figure 5.2 highlights three different mode types: weakly coupled chamber modes (red zone), weakly coupled plenum modes (blue zone) and strongly coupled modes (green zone). This chapter will focus on the first azimuthal mode of the combustion chamber (red and green zones). Two operating points are identified using this stability map of the

Chamber	L_c	0.54	m
	S_c	0.00785	m^2
Plenum	L_p	0.54	m
	S_p	0.00785	m^2
Burner	L_i^0	0.04	m
	S_i	0.00028	m^2
Fresh gases	ρ_u^0	10.93	kg/m^3
	c_u^0	519	m/s
Burnt gases	ρ^0	4.70	kg/m^3
	c^0	832	m/s
Flame	n_i	variable	$-$
	τ_i	variable	s

Table 5.1: Parameters used for numerical applications corresponding to a PBC configuration equipped with $N = 19$ burners. They correspond to a typical aircraft engine.

axisymmetric case provided in Fig. 5.2. These operating points characterize the values for n and τ of the N identical flames:

- Weakly coupled chamber mode with $n = 0.5$ and $\tau = 0.635\ ms$ (white cross if Fig. 5.2).
- Strongly coupled chamber mode with $n = 1.75$ and $\tau = 0.735\ ms$ (black cross in Fig. 5.2).

Figure 5.3 shows the associated structure of the acoustic mode obtained in the annular plenum and the annular chamber by ATACAMAC for the two operating points: the weakly (white cross in Fig. 5.2) and strongly (black cross in Fig. 5.2) coupled cases. It shows that changing the flames (i.e. changing the FTF) modifies the coupling between the two annular cavities. The strongly coupled case, where the acoustic pressure is present in the two cavities, cannot be investigated analytically since the low coupling factors assumption is not valid. However, combining the numerical resolution of the analytical dispersion relation provided by ATACAMAC with a UQ approach can unveil coupling mechanism effects on symmetry breaking and stability of the system. In the following sections, the weakly and strongly coupled cases will be studied using the numerical resolution of the dispersion relation (Eq. (5.2)).

5.3 UQ analysis of thermo-acoustic modes

5.3.1 Description of the UQ cases

The deterministic approach performed in the previous Section was useful to classify modes in the PBC combustor in absence of any uncertainty on the input data (n and τ's). The probabilistic UQ methods will be applied now to the same combustor but taking into account uncertainties on the 38 values of n and τ. To do this, it is necessary to specify how these uncertainties are distributed on n and τ:

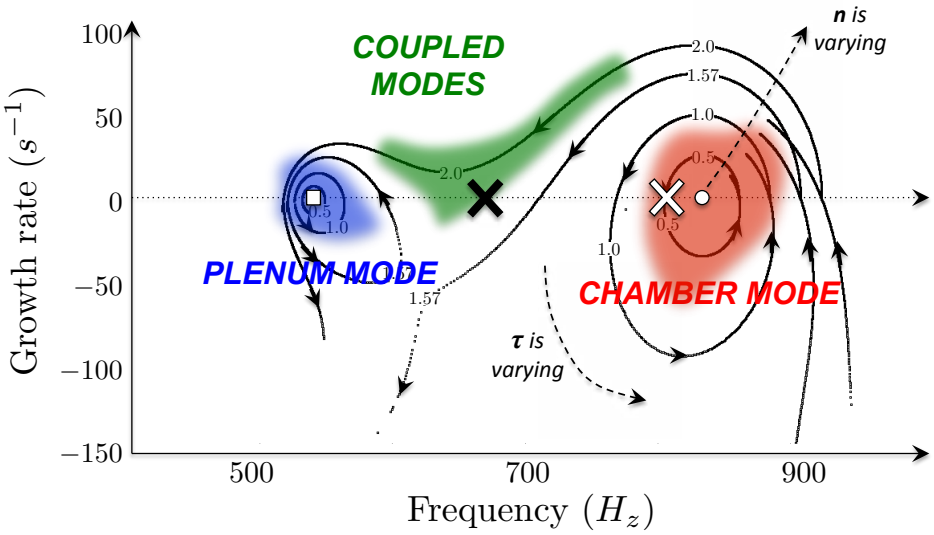

Figure 5.2: Frequencies and growth rates of modes computed using Eq. (5.2) for identical flames with FTF inputs: $n = 0.5,\ 1.0,\ 1.57$ and 2.0 ; $\tau = 0\ ms$ to $0.55\ ms$. Plenum (□) and chamber (○) modes with passive flames are also displayed. Three different mode types are identified: weakly coupled chamber modes (red zone), weakly coupled plenum modes (blue zone) and strongly coupled modes (green zone). Only two operating points are chosen for UQ which correspond to marginally stable weakly (white cross) or strongly (black cross) chamber modes.

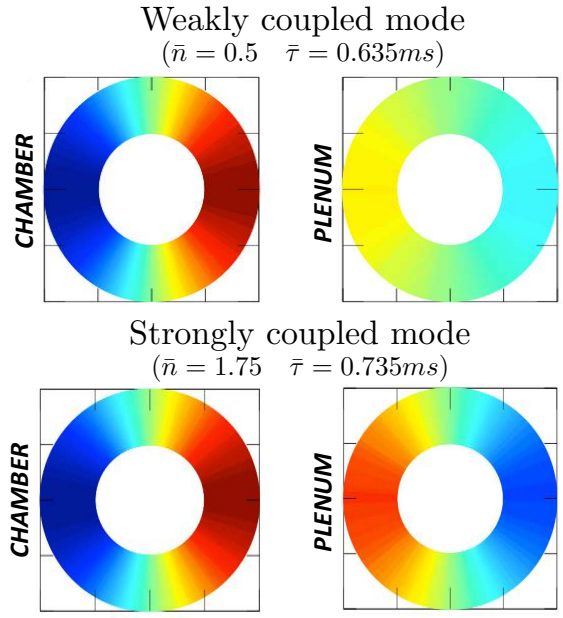

Figure 5.3: Structure of the acoustic mode (acoustic pressure $p' = \|\hat{p}\| \cos(\arg(\hat{p}))$) in the annular plenum and the annular chambers obtained by ATACAMAC for the two regimes: weakly (top) and strongly (bottom) coupled cases.

1) It is possible to assume that n and τ are uncertain parameters but that all burners still have exactly the same n and τ. In other words, it corresponds to a probabilistic model of a perfectly symmetric combustor: all flames are exactly identical (same n and τ) but these parameters are uncertain randomly because of fuel or overall operating condition uncertainties. We will call this case 'Identical' and right away notice that it only involves two uncertain parameters (since all flames are statistically dependent). Thus no sophisticated UQ techniques are needed to solve this problem compared to the second one.
2) We can also assume that each burner will have a specific n_i and τ_i independently of the others. This is a more realistic point of view for example when uncertainties are due to random tolerance margins and the 19 burners are picked-up from a set of burners produced with the same tool but exhibiting random changes from on burner to the other. We will call this case 'Different'.

At this point, it is interesting to notice that the 'Identical/Different' notion introduced above is also related to the 'Axisymmetry/Symmetry breaking' ideas introduced in Part I. Instead of studying burners which are all the same, we accept or even introduce perturbations on burners. The 'Different' case corresponds to a situation where symmetry is broken by uncertainties. Note however that the 'Different' term used here does not correspond to the controlled Symmetry Breaking introduced in Part I where two burner types where mixed on purpose with very different τ_i. Here, only one type of burner is used and 'Different' only describes variation around its mean characteristics. Applying UQ to Symmetry Breaking cases was not done here and is left for further studied as shown in Fig. 5.4.

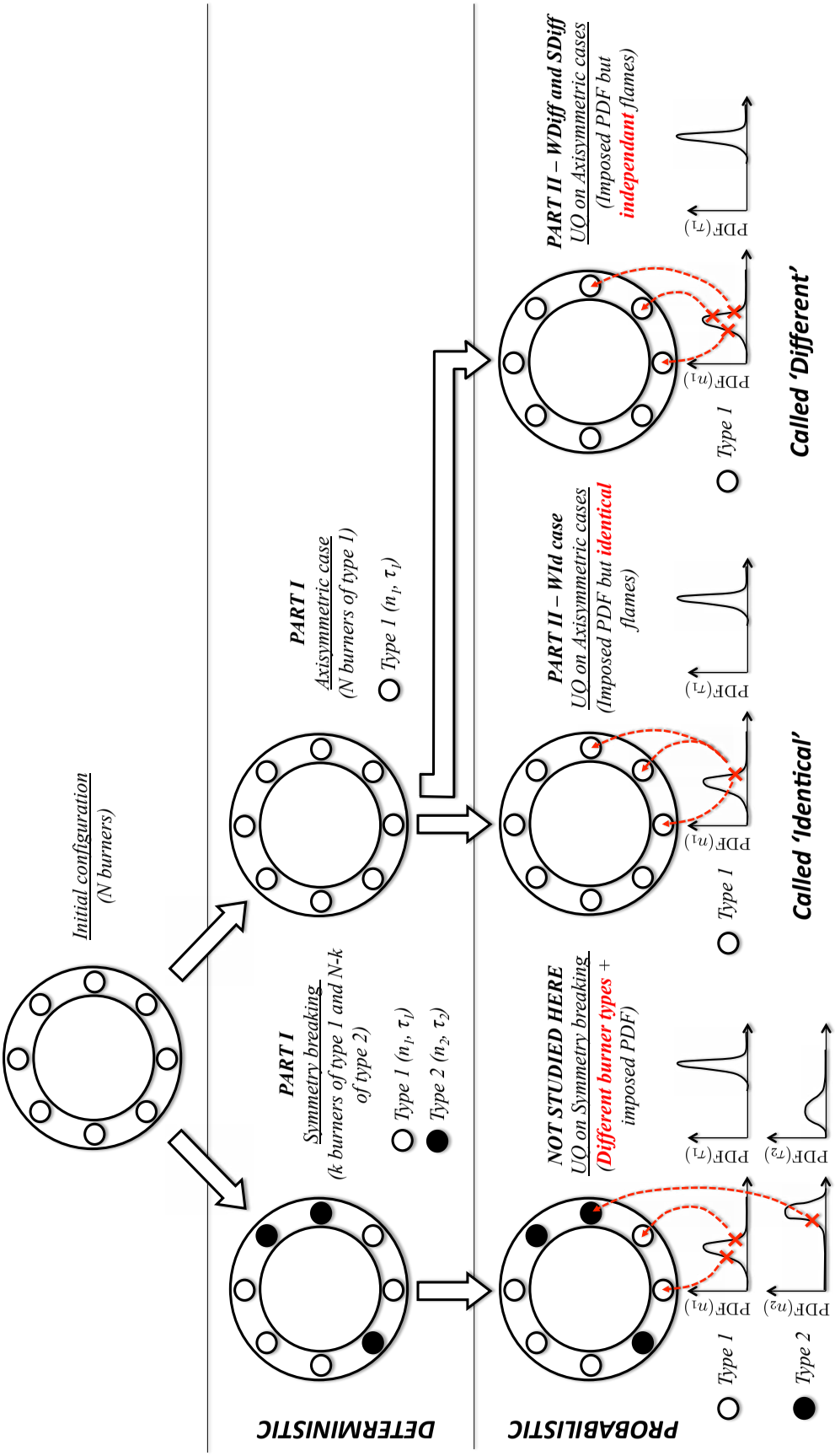

Figure 5.4: Deterministic (top) and probabilistic (bottom) models of annular combustors with identical or different flames. Symmetry breaking can be introduced on purpose with different burner types (left) or by uncertainties (*WDiff* and *SDiff*, right). The probabilistic case with identical flames (*WId*, middle) is studied for comparison but not fully investigated here.

Consequently, in a UQ context, 'identical' and 'different' flames have a particular meaning since the i^{th} flame of the system possesses two different types of properties:

1) The statistical properties, i.e. mean values ($\bar{n_i}$ and $\bar{\tau_i}$) and standard deviations (σ_{n_i} and σ_{τ_i}) of the FTF parameters.
2) The current or random properties (n_i^k and τ_i^k for the k^{th} sample).

The statistical properties are fixed by the chosen operating points (Section 5.2.2), do not change from one sample to another, and are always identical for all flames in this chapter. However, random properties change at each new sample k and can be 'identical' ($n_i^k = n_{j\neq i}^k$) or 'different' ($n_i^k \neq n_{j\neq i}^k$) for all flames, the latter meaning that the N flames are statistically independent, corresponding to the situation where engineers design combustion chambers with identical burners but manufacturing tolerances lead actually to different burners.

To perform a UQ analysis, data is required on the precision and distribution function with which input parameters are known. Mean values $\bar{n_i}$ and $\bar{\tau_i}$ are characterized by the chosen operating point (weakly or strongly coupled mode) defined in the previous Section (5.2.2). However, to date, no precise uncertainty quantification of the input flame parameters ($\sigma_{n_i}, \sigma_{\tau_i}$) is available. In this work, the numerical sensitivity analysis performed in Chapter 7 combined with experimental observations from EM2C and Cambridge lead to the following choice for the standard deviations: $\sigma_{n_i} = 10\%\bar{n_i}$ and $\sigma_{\tau_i} = 5\%\bar{\tau_i}$. In the absence of additional information about the distribution function of these parameters, uniform PDFs have been used in this work. This assumption has obviously an impact on the results but not on the robustness and feasibility of the UQ strategy proposed here. Finally, the two operating points (weakly and strongly) are investigated in the following with different (independent) flames, called *WDiff* and *SDiff* cases. For comparison, the weakly coupled case will be also investigated using identical flames, called *WId* case. Table 5.2 summarizes these three cases and their respective statistical properties.

Name	**Weakly/Strongly**	**Id./Diff.**	$\bar{n}$	$\bar{\tau}$	σ_n	σ_τ
WId	Weakly	Identical	0.5	0.635 ms	0.05	31.7 μs
WDiff	Weakly	Different	0.5	0.635 ms	0.05	31.7 μs
SDiff	Strongly	Different	1.75	0.735 ms	0.175	36.7 μs

Table 5.2: Summary of the three cases with identical or different flames investigated in this chapter and their respective statistical properties.

5.3.2 UQ approaches: Monte-Carlo and Active Subspace

This section briefly presents the classical Monte-Carlo method before focusing on the UQ strategy used in this PhD thesis. The question addressed in the following is to find a robust and fast method to compute the probability density function (PDF), or at least the first statistical moments (mean value, standard deviation etc.), of an output Y knowing the PDF of a number D of inputs $X_{i=1..D}$ chosen in the previous section: $X = (n_i, \tau_i)_{i=1..N}$

so that $D = 38$ for $N = 19$ burners. This problem is known as the forward uncertainty propagation (Chantrasmi & Iaccarino, 2012) problem where the output is viewed as the result of a "black box" which can be an experiment, a low-order model or a numerical solver characterized by an unknown function f:

$$Y = f(X_i) \quad \text{where PDFs of } X_i \text{ are known.} \tag{5.3}$$

where Y is the imaginary part of the complex frequency $Im(f)$, noted f_{Im} in this work and X_i's are the 38 independent parameters n_i and τ_i of the 19 burners. From the PDF of this growth rate, the probability of the mode to be unstable can be computed and is called the risk factor: 0% shows that the mode is perfectly stable, 100% that the mode is always unstable.

$$\text{Risk factor } (\%) = \frac{1}{100} \int_0^\infty \text{PDF}(f_{Im}) df_{Im} \tag{5.4}$$

To compute the PDF of the growth rate necessary to construct the risk factor, two UQ approaches are used in this thesis:

- **Monte-Carlo:** A well-known brute force method, called Monte-Carlo analysis, relies on repeated evaluations of the function f using a random sampling of the inputs X_i. M random values of X_i are chosen with respect to their known PDFs and the function f is evaluated M times to provide M output values f_{Im}. This method always converges but suffers from a slow convergence ($O\left(\frac{1}{\sqrt{M}}\right)$) which can become prohibitive if the function f is expensive to evaluate. Note that the convergence speed is independent of the dimension D. This method can be applied on the full input space only when using low-order models such as ATACAMAC. To apply this method using more expensive tools such as Helmholtz solvers, the size of the input space must be reduced: this is the main objective of this work using the active subspace approach.
- **Quasi-Monte-Carlo (not used in this PhD):** New methods based on Monte-Carlo analysis are constructed to improve the convergence speed by using low discrepancy sequences (e.g. the Sobol sequence) instead of random generators. It allows to reduce the convergence speed to $O\left(\frac{\ln(M)^D}{M}\right)$, where D is the input space dimension. This method is theoretically faster than a classic Monte-Carlo technique but only for low dimension D.
- **Active Subspace combined with low-order fitting:** To avoid expensive Monte Carlo methods, a UQ approach called "active subspace" (Constantine *et al.*, 2014) is used to reduce the dimension of the parameter space from 38 to just a few. This is a major breakthrough in our problem to break the dimensional curse since working with 38 dimensions is too expensive even for Helmholtz solvers: only low-order models like ATACAMAC can be applied directly on the full parameter space without the active subspace approach. It is also a necessary step prior to use efficient Quasi-Monte-Carlo techniques (not shown here). The active subspace method provides a solution around this issue. This method requires gradient evaluations to detect which directions in the parameter space lead to strong variations of

the growth rate. Other directions leading to flat response surface are not useful for describing the combustor stability and can be disregarded leading to a UQ analysis which can be performed on a much less variables.
The gradient of the growth rate $f_{Im}(p)$ with respect to the input parameters $p = \{n_i, \tau_i\}_{i=1..N}$ for the k^{th} sample, denoted $\nabla f_{Im}(p^k) = \nabla_p^k f_{Im}$, is thus computed by finite differences in this PhD. The uncentered covariance matrix $\mathcal{C}$ of the gradient vector can then be derived:

$$\mathcal{C} = \mathbf{E}[(\nabla_p^k f_{Im})(\nabla_p^k f_{Im})^T] \simeq \frac{1}{M}\sum_{k=1}^{M}(\nabla_p^k f_{Im})(\nabla_p^k f_{Im})^T \tag{5.5}$$

where $\mathbf{E}[.]$ is the expectation operator and M is the number of samples. Since this matrix is symmetric, positive and semidefinite, it admits a real eigenvalue decomposition:

$$\mathcal{C} = W\Lambda W^T, \quad \Lambda = \text{diag}(\lambda_1, ..., \lambda_m), \quad \lambda_1 \geq ... \geq \lambda_m \geq 0 \tag{5.6}$$

where W is the eigenvector corresponding to the coefficients of a linear combination of input parameters ($W^T p$) and Λ are the eigenvalues which quantify the effect of the active variable $W^T p$ on the growth rate response $f_{Im}(p)$: the higher λ_i is, the more significant the active variable $W_i^T p$ is on the average output response. Consequently only a few significant linear combinations of the input parameters are retained, reducing the dimension D from 38 to just a few.

These two approaches, Monte-Carlo and Active Subspace, are then combined in this thesis to provide an efficient method to compute growth rate PDFs and associated risk factors. The four steps of this methodology, the two-step validation and the reference case presented in this work are summarized below:

Active Subspace approach

- **Step SM1 -** A small (M_1 samples, typically from D to $10D$) Monte-Carlo analysis is performed on the full 38-dimensional space. Convergence tests show that $M_1 = 50$ is sufficient for $D = 38$ parameters.
- **Step SM2 -** For each sample k, gradients in all the $D = 38$ directions, $\nabla_p^k f_{Im}$ are computed using finite differences in this thesis. More efficient methods for gradient computations also exist, for example adjoint methods developed by the Cambridge group (Juniper *et al.*, 2015) requiring only $M_2 = M_1$ additional runs independently of the dimension D.
- **Step SM3 -** The D-by-D covariance matrix $\mathcal{C}$ (Eq. (5.5)) is now known and can be used as input of the active subspace approach (Eq. (5.6)) providing both the spectrum λ_j and the associated eigenvectors W_j^T.
- **Step SM4 -** Only a few significant eigenvalues $\lambda_{j=1..\delta}$ are retained where $\delta \ll D$. The associated eigenvectors $W_{j=1..\delta}^T$ are used as a new reduced input space of dimension δ.

Validation

- **Step SV1 -** A new small ($MV_1 = 10 - 100$ samples) Monte-Carlo analysis is performed on the reduced δ-dimensional active subspace to fit a low-order algebraic

model depending on linear or non-linear functions of the active variables. In this thesis, linear and quadratic models will be tested. Quasi-Monte-Carlo techniques can replace the classic Monte-Carlo method here since the dimension is low ($\delta \ll D$) but has not been tested in this work.

- **Step SV2 -** This algebraic model can be tested by comparing it with a full Monte-Carlo method ($MV_2 \simeq 100,000$) to evaluate the growth rate PDFs and associated risk factors. This task is not CPU demanding since algebraic models are efficiently evaluated compared to the initial "black box" function f while $10,000$ using a brute force method was out of reach.

Reference case

- **Ref. MC -** The Active subspace approach and the validation presented in this section are compared to UQ results (PDF of the growth rate and risk factor) considered as true values. This is achieved by a full Monte-Carlo method on the complete 38-dimensional space containing $M_{REF} = 10,000$ samples which is affordable using ATACAMAC for validation purposes only. Such a large evaluation of the 'black-box' function f cannot be obtained usually when using Helmholtz or LES solvers.

The associated cost of the UQ method proposed here relies mainly on the gradient evaluations. When adjoint methods or analytical gradients (if available) are used instead of the expensive finite differences, the cost due to the evaluation of the 'black-box' function f is of the order of $2 \times M_1 \simeq 100$. Moreover, the large number of simulations MV_2 are negligible since it corresponds to the evaluation of a simple algebraic model. Consequently, this methodology can be used for the risk factor predictions of complex gas turbines with Helmholtz solvers for which hundreds Monte-Carlo simulations in a reasonable time is feasible (Ndiaye *et al.*, 2015) while thousands or more is out of reach today.

5.3.3 Reference Monte-Carlo analysis on the $38D$ input space (Ref. MC case)

First a Monte Carlo analysis on the full parameter space is performed for the three cases presented in Tab. 5.2 to evaluate reference growth rate distributions and associated risk factors. Convergence tests prove that $M_{REF} = 10,000$ samples are sufficient to evaluate the risk factor as well as mean and standard deviation of the growth rate.

For both weakly *WId* and WDiff (Fig. 5.5, top and middle) and strongly *SDiff* cases (Fig. 5.5, bottom), the mean growth is negative (weakly: $-2.36\ s^{-1}$; strongly: $-3.53\ s^{-1}$): the mode would be stable if predicted by standard methods. However, uncertainties on flames input parameters $(n_i, \tau_i)_{i=1..N}$ lead to large standard deviations (weakly: $1.6\ s^{-1}$; strongly: $6.5\ s^{-1}$) so the mode can become unstable if uncertainties are taken into account. It is interesting to observe that reasonably small uncertainties on n's and τ's ($\sigma_n \simeq 0.1$ and $\sigma_\tau \simeq 30\ \mu s$) lead to a result for the strongly coupled case *SDiff* which is unacceptable for proper design of gas turbines: 40% probability that the mode will be stable against 60% that it will be unstable which corresponds to a useless result for the designers. This illustrates the challenge of thermo-acoustics prediction: they are very sensitive to small uncertainties in the input parameters.

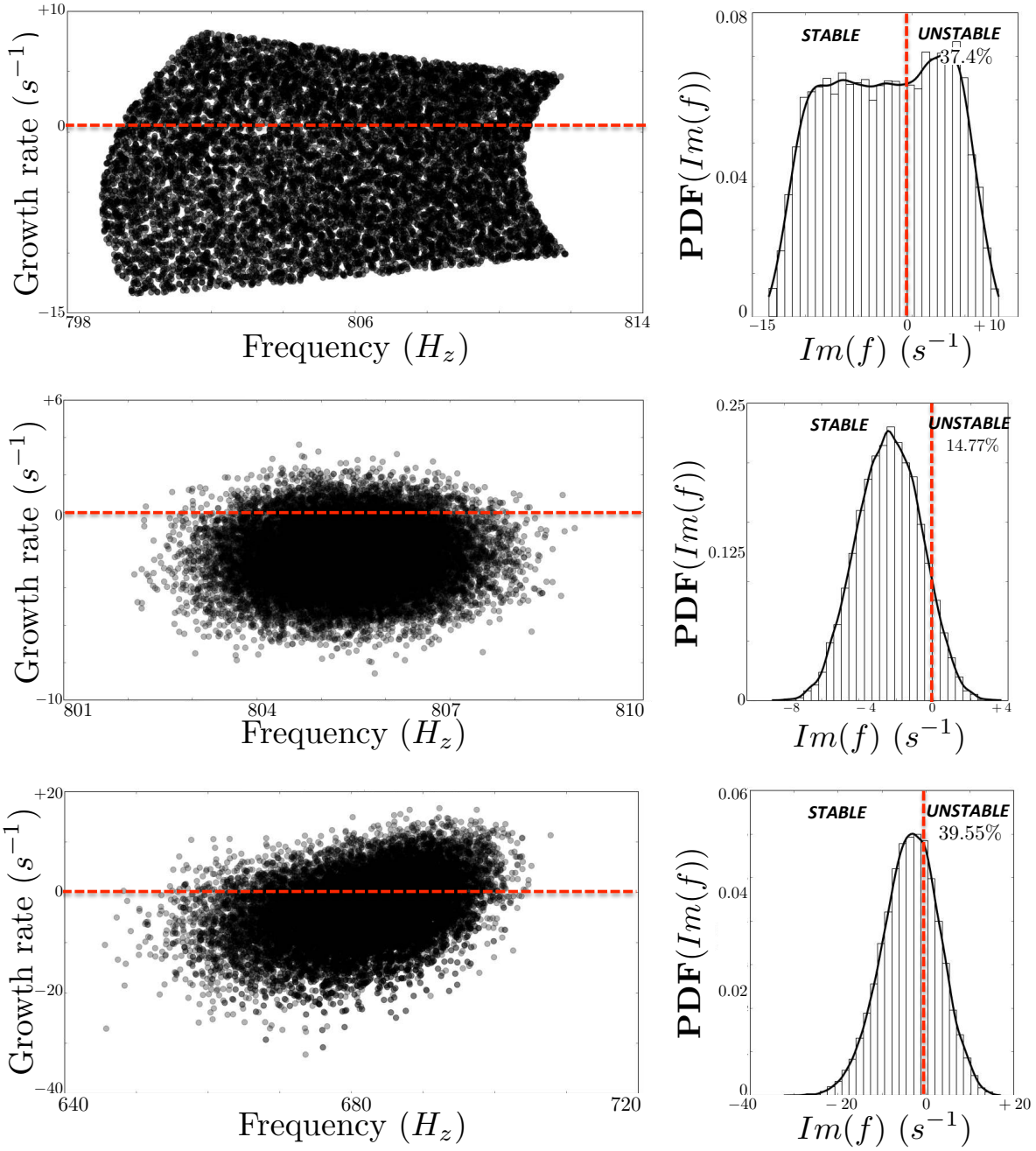

Figure 5.5: Monte-Carlo results (left) of the three cases *Wid* (top: all burners are identical, weak coupling), *WDiff* (middle: all burners are different, weak coupling) and *SDiff* (bottom: all burners are different, strong coupling) using $M = 10,000$ samples, where each black point corresponds to one ATACAMAC simulation. The PDFs (histogram and kernel density estimations) of the resulting growth rate are displayed (right) and the risk factor (Eq. (5.4)) is evaluated to 37.4% for the *WId* case, 14.8% for the *WDiff* case and 39.5% for the *SDiff* case.

This reference Monte-Carlo analysis (Figure 5.5, top and middle) also shows that an annular configuration with multiple identical or independent flames behaves statistically differently: the risk factor (Eq. (5.4)) of the weakly coupled case is 37.4% (Fig. 5.5, top) when flames are assumed identical but decreases to 14.8% (Fig. 5.5, middle) when they are assumed independent and shapes of the uncertain regions are different. This peculiar behavior results from the symmetry breaking effect on the mean flame characteristics. Indeed, at least for weakly coupled cases, the mean flame effect on the growth rate evaluated in the k^{th} sample can be expressed as:

$$Im(f^k) = -\frac{c^0}{4\pi L_c} N\Gamma^k \text{ for identical flames} \tag{5.7}$$

$$Im(f^k) = -\frac{c^0}{4\pi L_c} \sum_{i=1}^{N} \Gamma_i^k \text{ for independent flames} \tag{5.8}$$

where Γ_i^k is the coupling parameter of the i^{th} burner depending on the random flame parameters (n_i^k, τ_i^k). However, a new aspect arises in the current probabilistic approach compared to previous deterministic models elaborated in Chapters 2 and 3: when uncertainties are considered (i.e. the coupling parameter Γ_i has a known PDF called $\mathcal{P}_{\Gamma_i}$), mean flame effect described in Eqs. (5.7) and (5.8) lead to very different results[1]:

- **Identical flames:** When flames are considered identical, the PDF of the growth rate $f_{Im} = Im(f)$, called $\mathcal{P}_{f_{Im}}$, can be analytically derived from Eq. (5.7):

$$\mathcal{P}_{f_{Im}}(f_{Im}) = \frac{4\pi L_c}{Nc^0} \mathcal{P}_\Gamma \left(\frac{4\pi L_c f_{Im}}{Nc^0} \right) \tag{5.9}$$

  For example, if the input PDF $\mathcal{P}_\Gamma$ is uniform, then the output PDF is also uniform.
- **Independent flames:** However, when flames are independent, the PDF of the growth rate is much more complex[2]:

$$\mathcal{P}_{f_{Im}}(f_{Im}) = \frac{4\pi L_c}{c^0} \left[\mathcal{P}_{\Gamma_1} \star \mathcal{P}_{\Gamma_2} \star ... \star \mathcal{P}_{\Gamma_N} \right] \left(\frac{4\pi L_c f_{Im}}{c^0} \right) \tag{5.10}$$

where $\star$ designates the convolution product. For instance, if for all burners $\mathcal{P}_{\Gamma_i}$ is the uniform distribution on $[0, 1]$, the PDF of the output is not uniform, as for identical flames, but draws a much more complex shape known as the Irwin-Hall distribution which can be approximated by a gaussian function for a number of flames N sufficiently large, as observed in Monte-Carlo results presented here (Fig. 5.5, middle and bottom). This result proves that even for supposedly axisymmetric configurations, risk factors have to be evaluated by probabilistic methods with multiple independent flames to capture the correct growth rate response to uncertain input parameters.

[1]Consider the random variables X and Y and the linear relation: $Y = aX$, where $a \neq 0$. Then the PDF of Y, called f_Y is linked to the density function of X, called f_X, as follows: $f_Y(y) = \frac{1}{\|a\|} f_X(y/a)$.

[2]Consider the N independent random variables $X_{i=1..N}$ and the output $Y = \sum_{i=1}^{N} X_i$. Then the PDF of Y, called f_Y is linked to the density function of the X_i's, called f_{X_i}, as follows: $f_Y(y) = [f_{X_1} \star f_{X_2} \star ... \star f_{X_N}](y)$ where $\star$ is the convolution product.

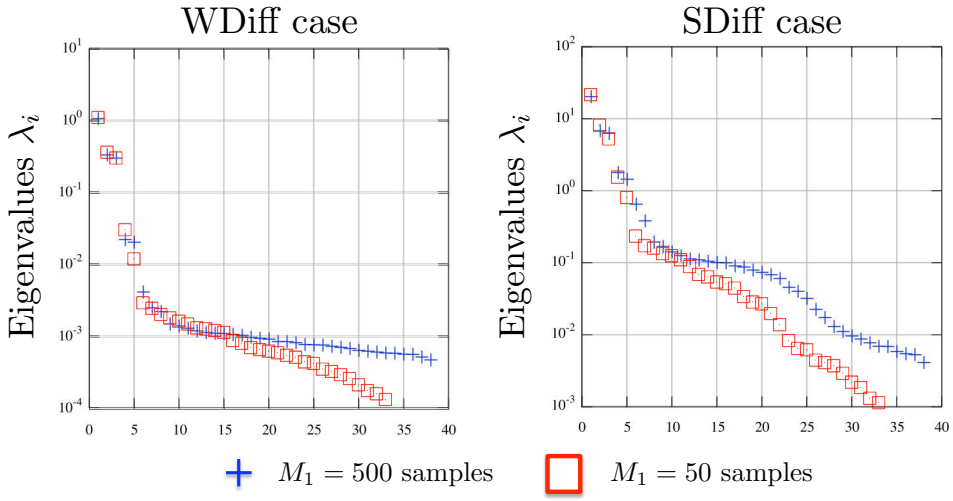

Figure 5.6: Eigenvalues Λ for the weakly *WDiff* (left) and strongly *SDiff* (right) coupled cases using $M_1 = 50$ samples (red square) or $M_1 = 500$ samples (blue cross).

5.3.4 Active subspace results (Steps SM - SM4)

Figure 5.6 shows the spectrum Λ obtained by the active subspace method for both the weakly *WDiff* and the strongly *SDiff* coupled cases. Two sample sizes $M_1 = 50$ (red square) and $M_1 = 500$ (blue cross) are used to show the eigenvalues convergence. First, the value of λ_1 associated to the mean variation of the growth rate in the strongest direction is a good indicator on how the annular configuration is sensitive to the input uncertainties: Fig. 5.6 reveals that the strongly coupled case is much more sensitive that the weakly coupled case by two orders of magnitude. Moreover, for the two cases, only the first five eigenvalues are relevant: only five parameters really control the results for the weakly and strongly coupled cases which suggests that the UQ problem can be reduced from a 38-dimensional to a 5-dimensional problem which is a significant result, especially for the *SDiff* case since no theoretical background is possible. The new inputs are the linear combinations $W^T p$ of the flame parameters $p = (n_i, \tau_i)_{i=1..N}$. It is interesting to note that coefficients associated to the FTF amplitude $n_{i=1..N}$ are almost null for the *WDiff* but not for the *SDiff* cases: weakly coupled modes are controlled only by the time-delays while both n_i and τ_i are necessary for strongly coupled cases. Coefficients associated to the time-delays are displayed in Fig. 5.7 for the three first eigenvectors of the weakly coupled case. It is interesting to see if these eigenvectors can be related to the physics of the problem.

The first active variable (AV1 in Fig. 5.7) converges to an equi-weighted linear combination associated with the mean flame transfer function over the $N = 19$ burners when enough samples are used. However, the two other eigenvectors (AV2 and AV3 in Fig. 5.7) have more complex behaviors which need to be unraveled: .

Previous chapters have shown that an annular configuration (with no plenum) is characterized by two parameters: (1) the coupling strength Σ_0 associated with the mean flame over the N burners and (2) a splitting strength $\mathcal{S}_0$ which involves two coefficients of

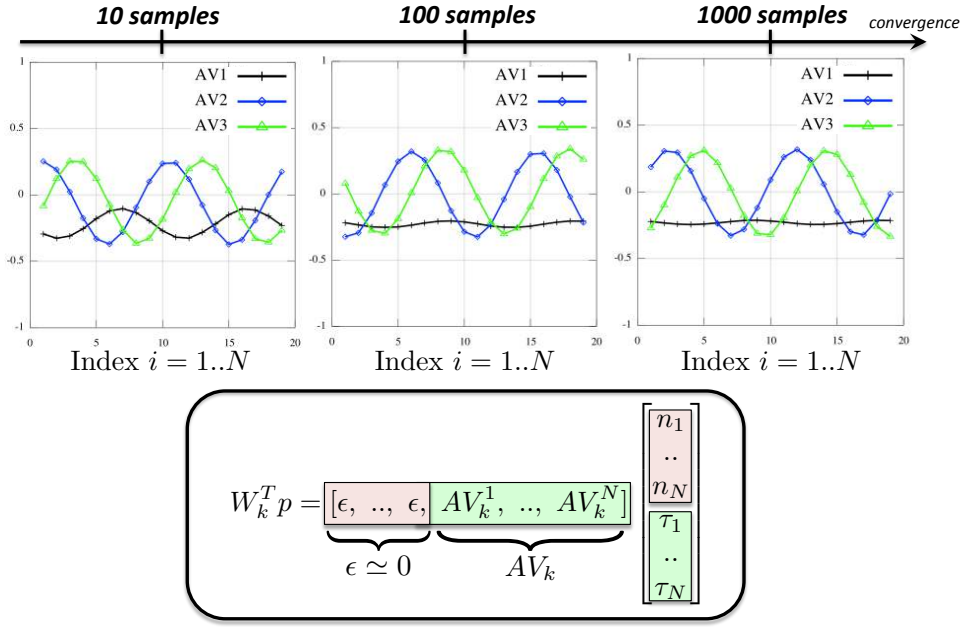

Figure 5.7: Three first eigenvectors $W_{k=1..3}$ coefficients of the *WDiff* case associated to the N uncertain time-delays $\tau_{I=1..N}$ called AV1, AV2 and AV3. For the weakly coupled case *WDiff*, coefficients of the eigenvectors associated to the N FTF amplitudes $n_{i=1..N}$ are almost zero (ϵ): they have no impact on the growth rate. The eigenvectors convergence is displayed for $M_1 = 10$, 100 and $1,000$ samples.

the Fourier transform $\widehat{\mathcal{F}}(\omega)$ of the collection of flame transfer functions $\{\mathcal{F}_i\}_{i=1..N}$: $\widehat{\mathcal{F}}(2p)$ and $\widehat{\mathcal{F}}(-2p)$, where p is the azimuthal mode order ($p = 1$ here). The two eigenvectors AV2 and AV3 displayed in Fig. 5.7 exhibit a periodic behavior of period 9 suggesting a direct link between the eigenvectors AV_2 and AV_3 and the coefficients $\widehat{\mathcal{F}}(\pm 2p)$. Note that the mean flame and therefore the eigenvector AV_1 is also linked to the 0^{th} coefficient of the Fourier transform $\widehat{\mathcal{F}}(0)$. These theoretical findings suggest that a change of variables could be used to ease the physical interpretation of active variables and Fig. 5.7 as well as to improve the accuracy of the eigen decomposition:

$$\{n_i,\ \tau_i\} \Rightarrow \{Re(\widehat{\mathcal{F}}(\omega^0)),\ Im(\widehat{\mathcal{F}}(\omega^0))\} \tag{5.11}$$

where $\mathcal{F} = [\mathcal{F}_1, ..., \mathcal{F}_N]^T$ is the array of FTF of all the N burners viewed as a periodic complex signal, $\mathcal{F}_i(\omega^0)$ is the FTF of the i^{th} flame depending on the parameter n_i, τ_i and the pulsation of the chamber in absence of burners $\omega^0 = \frac{\pi c^0}{L_c}$. Results for cases *WDiff* (left) and *SDiff* (right) are displayed in Figure 5.8. Associated active variables shown in Figure 5.9 demonstrate that the effect dominating the growth rate response corresponds to the coupling strength and splitting strength involving the 0^{th} and $\pm 2^{th}$ Fourier coefficients of the flame transfer function distribution (Figure 5.2), as suggested by the theoretical results of Chapter 2. Note that the splitting strength is a non-linear combination of the input parameters (n_i, τ_i) and is expressed as $\mathcal{S}_0 = \sqrt{\gamma(+2)\gamma(-2)}$. Since the Fourier coefficients $\gamma(k)$ are linear-combinations of the input parameters, the Active Subspace

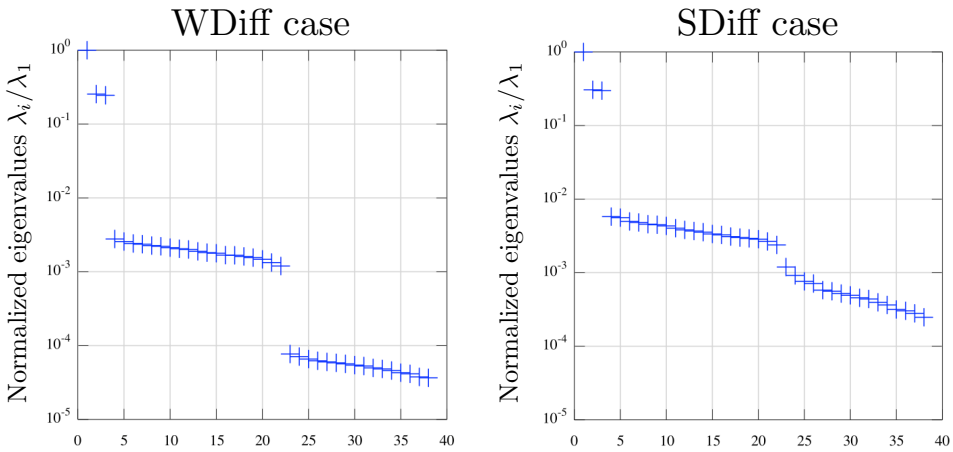

Figure 5.8: Normalized eigenvalues λ_i/λ_0 for the weakly (left) and strongly (right) coupled cases using 500 samples.

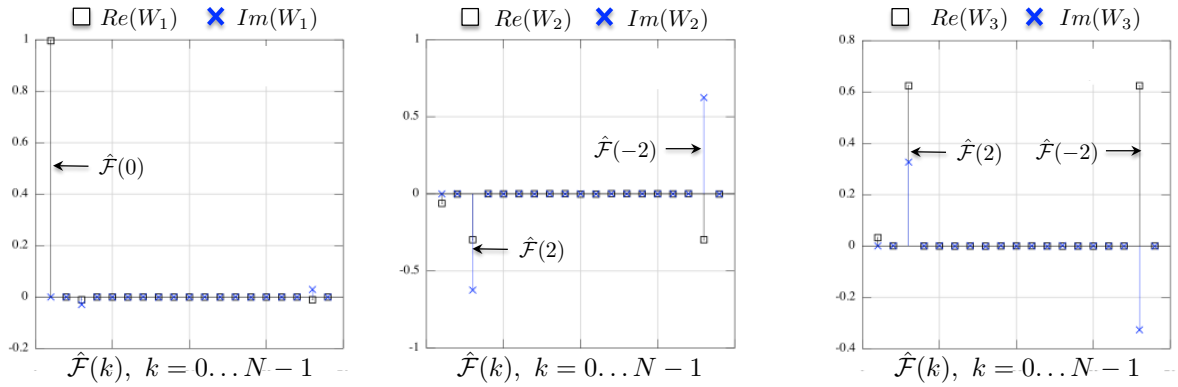

Figure 5.9: real (square) and imaginary (cross) parts of the three first active variables W_i obtained by the active subspace approach combined with a change of variable defined by Eq. (5.11) for the weakly coupled case with $1,000$ samples.

method is able to capture the two parameters $\gamma(2)$ and $\gamma(-2)$ but not $\mathcal{S}_0$ directly. Other coefficients only play a minor role especially for the weakly coupled regime. It is striking to see that the active subspace method actually recovers the parameters also exhibited in the weak coupling limit by the analytical derivation of ATACAMAC: the coupling and the splitting strength.

5.3.5 Growth rate PDF & risk factor estimation and validation (Steps SV1 - SV2)

The active subspace approach applied in Section 5.3.4 has provided successful results by reducing the 38-dimensional input space into a low-dimension space for both the weakly and the strongly coupled cases. The active variables involve physical quantities

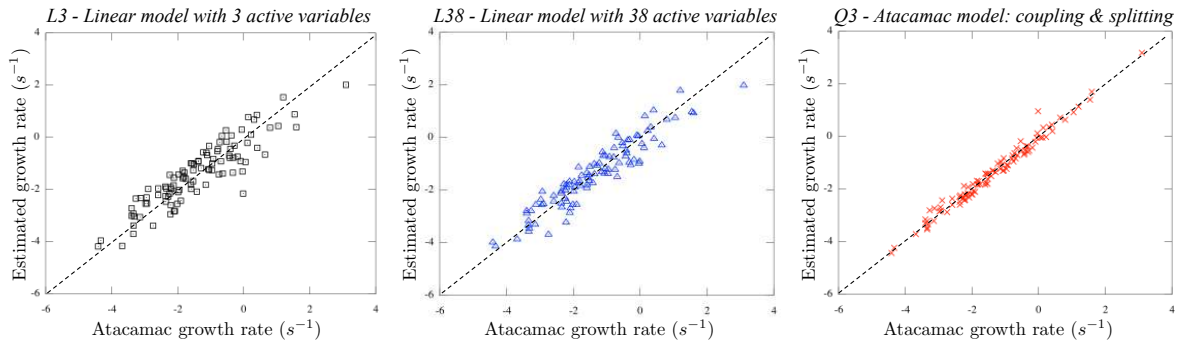

Figure 5.10: Atacamac growth rates (100 samples) for weakly (left) and strongly (right) regimes are compared with estimations obtained with linear (L3 and L38), quadratic (Q3) or analytical (AM) models on all (L38) or only the three dominant active variables (L3, Q3 and AM).

associated with the Fourier transform of the FTF or the $n-\tau$ parameters and therefore recover parameters exhibited analytically by ATACAMAC. Now the problem is reduced to a smaller one but the growth rate PDF and the risk factor are still unknown: this is the objective of the SV1 and SV2 steps (Section 5.3.2). These steps consist in estimating at low cost the risk factor of the first azimuthal mode: (SV1) a few samples (here $MV_1 = 100$ samples) are used to fit a low-order model and (SV2) a Monte-Carlo analysis is applied on this low-order model using a large number of simulations (MV_2 of the order of 10^4). Several Monte-Carlo simulations have been performed with different models to estimate the PDF of the growth rate and its associated risk factor:

- **L_{38}**: a linear model based on all 38 active variables $W^T_{k=1..38}p$:

$$\widetilde{f_{Im}}^{L38}(p) = \sum_{k=1}^{38} \alpha_k W_k^T p \tag{5.12}$$

- **L_3**: a linear model based on the three dominant active variables:

$$\widetilde{f_{Im}}^{L3}(p) = \alpha_1 W_1^T p + \alpha_2 W_2^T p + \alpha_3 W_3^T p \tag{5.13}$$

- **Q_3**: a quadratic model (with interactions) on the three dominant active variables:

$$\widetilde{f_{Im}}^{Q3}(p) = \sum_{k=1}^{3} \alpha_k W_k^T p + \sum_{k=1}^{3}\sum_{l=k}^{3} \alpha_{k,l} \left(W_k^T p \times W_l^T p\right) \tag{5.14}$$

- **AM**: a linear model based on the coupling and splitting strengths from the analytical work of Bauerheim *et al.* (2014*a*):

$$\widetilde{f_{Im}}^{AM}(p) = \alpha \left(W_1^T p + \sqrt{W_2^T p \times W_3^T p}\right) \tag{5.15}$$

These low-order models can be fitted with a small Monte-Carlo method: it provides an algebraic expression for the response surface which can be then used to compute the

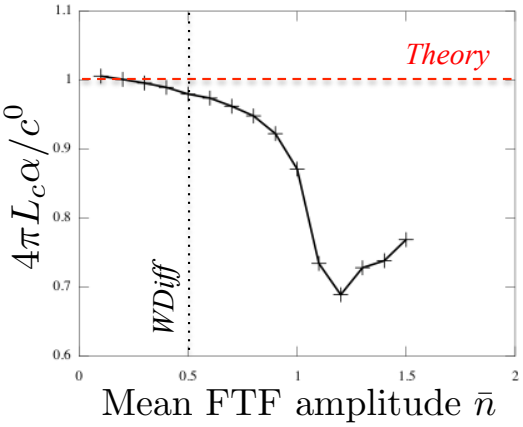

Figure 5.11: Results of a least square fitting on the parameter α of the AM low-order model for cases with various mean FTF amplitudes $\bar{n} = 0.1$ to 1.5.

growth rate PDF and the risk factor. For the weakly coupled case, the AM model can be obtained directly from the ATACAMAC analytical solutions. Therefore this is a case where the accuracy of the method can be checked. Indeed, the analytical growth rate is expressed as $f_{Im} = -\frac{c^0}{4\pi L_c}(\Sigma_0 \pm \mathcal{S}_0)$ for weakly coupled modes and is modeled in the AM model by $\widetilde{f_{Im}} = -\alpha\left(\hat{\mathcal{F}}(0) \pm \sqrt{\hat{\mathcal{F}}(-2) \times \hat{\mathcal{F}}(+2)}\right)$ (Eq. (5.15)). The parameter α, fitted by a least square method, can therefore be compared to its theoretical value, i.e. $c^0/4\pi L_c$. This exercise is performed not only for the *WDiff* case but also by varying the mean FTF amplitude $\bar{n}$ (with a fixed $\bar{\tau} = 0.625\ ms$). Figure 5.11 shows the ratio between the UQ vs. the theoretical value of α for $\bar{n} = 0.1$ to 1.5: it proves that UQ and theoretical results are in good agreement for low mean FTF amplitudes $\bar{n}$ (the error is below 10% for $\bar{n} < 1.0$).

Numerical results of the other fitting models (linear: L3 and L38 or quadratic: Q3) are displayed in Fig. 5.10 for the *WDiff* case using $M_5 = 100$ samples. The dashed lines in Fig. 5.10 correspond to an ideal perfect model where the estimated growth rate is equal to the ATACAMAC output. Figure 5.10 shows that both linear and quadratic models provide low discrepancies between the estimated (from the fitted low-order models) and the true (from ATACAMAC) growth rates. A similar fitting has been performed on the strongly coupled case *SDiff* and are compared to the weakly coupled case in Fig. 5.12. To assess the accuracy of these low-order models, Pearson's coefficients are provided in Tab. 5.3 and are evaluated by the formula:

$$R = \sqrt{\frac{\sum_{i=1}^{100}(\tilde{\omega}_i - \bar{\omega}_i)^2}{\sum_{i=1}^{100}(\omega_i - \bar{\omega}_i)^2}} \tag{5.16}$$

where ω_i and $\bar{\omega}_i$ are the reference and mean growth rate from ATACAMAC and $\tilde{\omega}_i$ is the estimated growth rate using different fitting models (Figure 5.12).

These results show that even if the weakly and strongly coupled regimes share the same active variables (Figure 5.9), their response surfaces (i.e. the model involving these

Models	Weakly	Strongly
L38	0.94	0.79
L3	0.91	0.67
Q3	0.99	0.86
AM	0.99	0.87

Table 5.3: Pearson's coefficients (Eq. 5.16) for weakly and strongly regimes using several fitting models.

Models	Weakly	Strongly
MC	**14.77**	**39.55**
L38	11.90	39.26
L3	11.54	34.86
Q3	14.90	41.65
AM	14.36	35.51

Table 5.4: Risk factors computed by the Monte Carlo (MC) and several fitting models (L38, L3, Q3 and AM).

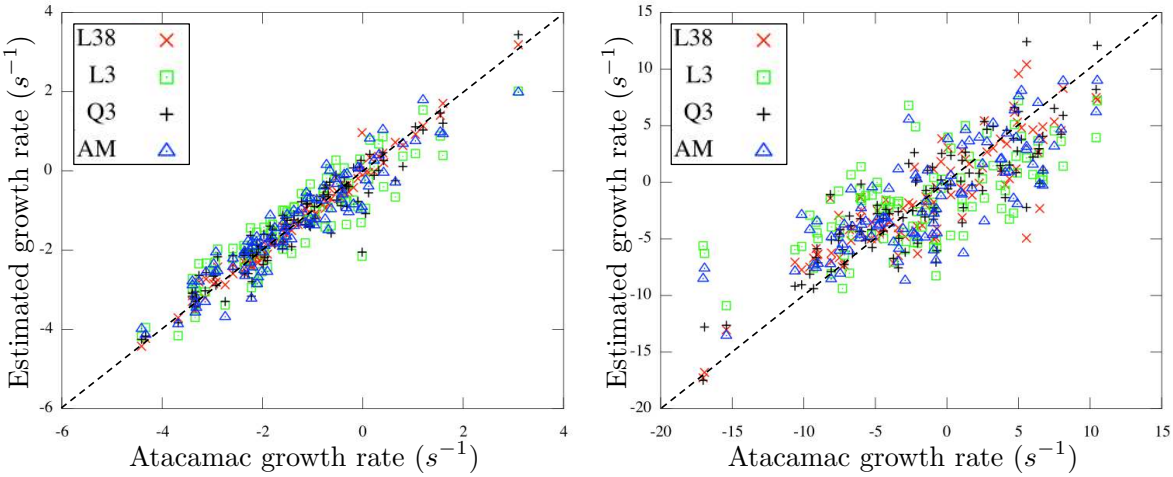

Figure 5.12: Atacamac growth rates (100 samples) for weakly (left) and strongly (right) regimes are compared with estimations obtained with linear (L3 and L38), quadratic (Q3) or analytical (AM) models on all (L38) or only the three dominant active variables (L3, Q3 and AM).

active variables) are clearly different. For the weakly coupled mode, a linear model with the three dominant active variables is sufficient to reproduce 90% of the growth rate variations while a quadratic model is required for the strongly coupled regime.

The step SV1 provides an algebraic expression for the response surface which can be then used to compute the growth rate PDF and its associated risk factor. If the PDFs of the δ new variables $W^T_{k=1..\delta}p$ are known, the PDF of the growth rate can be obtained analytically. However, this task is usually complex since the analytical expression of a linear combination of initial PDFs is not straightforward (see Eq. (5.10) for a similar problem). Consequently a numerical evaluation of the output PDF is usually required: this is the objective of the final step SV2. The low-order models (L38, 3, Q3 or AM) are algebraic and can be replayed efficiently at low cost, i.e. the cost to evaluate such algebraic models is negligible compared to the evaluation of the initial 'black-box' function f. Here $100,000$ samples of these models were computed to generate the PDF of the growth rate as well as the risk factor displayed in Tab. 5.4. A good agreement is found for both regimes. The two linear models produce higher error on the risk factor while the quadratic model is able to accurately evaluate the stability of the system: the relative risk factor error is 0.87% for the weakly coupled mode and 5% for the strongly coupled case when using this model. These results show the accuracy and efficiency of the UQ method proposed here.

5.4 Conclusion

For the first time, Uncertainty Quantification (UQ) has been applied on the thermo-acoustic stability of a simplified gas turbine to determine its risk factor defined as the probability of the first azimuthal chamber mode to be unstable. The realistic configuration considered here contains an annular plenum which connects 19 burners and an annular chamber which operates in two different regimes called weakly and strongly coupled regimes (Chapter 4). Each flame is modeled by two uncertain Crocco parameters (n, τ) leading to a large UQ problem involving 38 independent parameters. A UQ method is proposed to reduce the size of the problem and is compared with a classical Monte Carlo method using the quasi-analytical ATACAMAC tool to avoid expensive Helmholtz simulations. Results show that using 'identical' flames or 'different' flames lead to a different behavior of the combustor and strongly impacts the stability risk factor. In particular, when uncertainties are accounted for, symmetry breaking also modifies the mean flame effect and not only the splitting of the frequency. The present UQ method is able to predict the risk factor of the configuration with errors less that 1% for the weakly coupled case and 5% for the strongly coupled regime which demonstrates its accuracy and efficiency. This UQ methodology only requires a few simulations: (1) 50 simulations on the 38D parameter space used for the active subspace plus gradients evaluation and (2) 100 additional simulations on 5 parameters only to fit low-order models. The final $100,000$ evaluations of the low-order models have a negligible cost since they are purely algebraic. Consequently, this method could be applied to predict stability of complex gas turbines using a full 3D Helmholtz solver like AVSP since 150 Helmholtz simulations can be performed in a reasonable time as shown recently by Ndiaye *et al.* (2015).

Part II

High-fidelity simulations of azimuthal modes

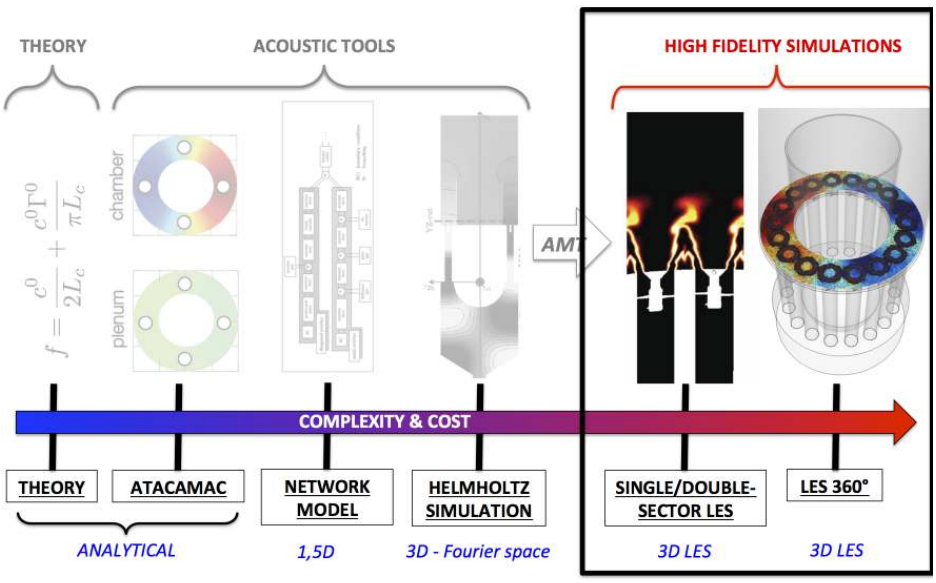

This part has lead to the following publications and communications:

1) M. Bauerheim, G. Staffelbach, N.A. Worth, J.R. Dawson, L. Gicquel and T. Poinsot, *'Sensitivity of LES-based harmonic flame response model for turbulent flames and impact on the stability of azimuthal modes' (2014)* **Proceedings of the 35th Combustion Institute** (in press, DOI 10.1016/j.proci.2014.07.021)
2) M. Bauerheim, L. Gicquel and T. Poinsot, *'Numerical investigation of azimuthal combustion instabilities in annular combustors' (2014)*, **CRCT, Centrale Paris, FRANCE**
3) M. Bauerheim, G. Staffelbach, N.A. Worth, J.R. Dawson, L. Gicquel and T. Poinsot, *'Numerical and experimental investigation of the establishment of azimuthal modes in an academic annular combustor'* **(in preparation)**

Chapter 6

Large Eddy Simulations and AVBP

This chapter gives a general introduction to Computational Fluid Dynamics and presents the concept and the governing equations for Large Eddy Simulations of turbulent reactive flows. It summarize models used in the AVBP code for reactive LES of combustors. The specific reduced kinetic schemes for methane and ethylene used and/or developed for the Cambridge experiment are presented. Transport coefficients used in the AVBP code have been validated. Finally, turbulent combustion modeling, a key feature of reacting flow computations, is briefly described.

(a) Claude Louis Navier (1785-1836).

(b) George Gabriel Stokes (1819-1903).

6.1 An introduction to Computational Fluid Dynamics

The aim of fluid mechanics is to study liquids and gases properties in various configurations, initially to predict its motion. The history of the equations governing the motion of a fluid started in 1757 when Leonhard Paul Euler published an important set of equations

to describe the motion of inviscid flows that are known as the Euler equations. Then in 1822 Claude-Louis Navier, a French engineer, introduced the notion of viscosity. Finally in 1845 George Gabriel Stokes wrote the final equations describing the motion of a viscous fluid (including the terms proposed by C.L. Navier). These nonlinear partial differential equations are now known as the 'Navier-Stokes equations'. They are used to study a wide range of situations: the design of aircraft and cars, the study of blood flows, the weather or ocean currents. Except in some very simple cases where analytical solutions exist, these nonlinear equations have to be solved numerically on computers: this field is called Computational Fluid Dynamics (CFD).

First, Section 6.1.1 presents the governing equations in fluid dynamics and then a short description of the methods to solve them is provided in Sec. 6.1.2.

6.1.1 The Navier-Stokes equations

The exact behavior of complex turbulent reacting flows is fully described by the following 'full' Navier-Stokes equations:

$$\frac{\partial \rho}{\partial t} + \frac{\partial}{\partial x_i}(\rho u_i) = 0 \quad \text{(Mass conservation)} \tag{6.1}$$

$$\frac{\partial \rho u_j}{\partial t} + \frac{\partial}{\partial x_j}(\rho u_i u_j) = -\frac{\partial}{\partial x_j}\left(P\delta_{ij} - \tau_{ij}\right) \quad \text{(Momentum conservation)} \tag{6.2}$$

$$\frac{\partial \rho E}{\partial t} + \frac{\partial}{\partial x_j}(\rho E u_j) = -\frac{\partial}{\partial x_j}[u_i(P\delta_{ij} - \tau_{ij}) + q_j] + \dot{\omega}_T \quad \text{(Energy conservation)} \tag{6.3}$$

$$\frac{\partial \rho Y_k}{\partial t} + \frac{\partial}{\partial x_j}(\rho Y_k u_j) = -\frac{\partial}{\partial x_j}(J_{j,k}) + \dot{\omega}_k \quad \text{(Specie } k \text{ conservation)} \tag{6.4}$$

where ρ is the mixture density, u_i is the i-component of the velocity, P is the static pressure, τ_{ij} is the viscous tensor, E is the energy, q_i is the i-component of the the energy flux, $\dot{\omega}_T$ is the heat release due to combustion, Y_k is the mass fraction of species k, $J_{i,k}$ is the i-component of the diffusive flux of species k and $\dot{\omega}_k$ is the reaction rate of species k.

Assuming a Newtonian fluid and the equality between the mechanical and dynamic pressure (Stokes assumption, null bulk viscosity) leads to:

$$\tau_{ij} = 2\mu S_{ij} + \mu_V S_{kk}\delta_{ij} = 2\mu\left(S_{ij} - \frac{1}{3}\delta_{ij}S_{kk}\right) \tag{6.5}$$

with μ the dynamic viscosity, μ_V is the volume (or second) viscosity and S_{ij} is the deformation tensor:

$$S_{ij} = \frac{1}{2}\left(\frac{\partial u_j}{\partial x_i} + \frac{\partial u_i}{\partial x_j}\right). \tag{6.6}$$

When combustion instabilities arise, viscosity mainly affects the acoustic damping and the sound speed field. From a linearization of the Navier-Stokes equations, Stokes (1845) expressed the sound speed and damping of acoustic waves due to tangential forces:

$$c = \sqrt{\gamma r \bar{T} - \frac{16\pi^2\mu^2}{9\lambda^2\bar{\rho}^2}} \quad \text{and} \quad \alpha = \frac{8\pi^2\mu}{3\lambda^2\bar{\rho}} \tag{6.7}$$

where c is the sound speed, α is the acoustic damping and λ is the acoustic wavelength. It appears that the damping (due to viscosity) and sound speed field can be approximated by $\alpha = 0$ and $c = \sqrt{\gamma r \bar{T}}$ since typical values of viscosity are 10^{-5}. Moreover, the damping increases as $1/\lambda^2 \sim \omega^2$ and therefore should be considered only at high frequencies and can be neglected for azimuthal modes which usually occur at low frequencies.

The reaction term is expressed as:

$$\dot{\omega}_T = -\sum_{k=1}^{N_s} \Delta h^0_{f,k} \dot{\omega}_k \tag{6.8}$$

where N_s is the number of species in the flow, $h^0_{f,k}$ is the mass enthalpy of formation of species k at $T = T_0$ and $\dot{\omega}_k$ is the reaction rate of species k. All details on $\dot{\omega}_k$ are given in Sec. 6.4. The computation of the exact formulation of the diffusive flux of species k, $J_{i,k}$, is a very difficult and costly task. A first-order approximation of this diffusive flux (approximation of Hirschfelder *et al.*, 1969) reads:

$$J_{i,k} = -\rho \left(D_k \frac{W_k}{\overline{W}} \frac{\partial X_k}{\partial x_i} - Y_k V_i^c \right),$$

where D_k is not a binary diffusion but an equivalent diffusion coefficient of species k in the rest of the mixture. In the AVBP code, a simpler formulation of these diffusion coefficients are used:

$$D_k = \frac{1 - Y_k}{\sum_{j \neq k} X_j / D_{jk}} \simeq \frac{\mu}{\rho S_{c,k}} \quad \text{where } S_{c,k} \text{ are constant parameters} \tag{6.9}$$

W_k is the molecular weight of species k and $\overline{W}$ is the mean molecular weight of the mixture. X_k is the mole fraction of species k and Y_k is the mass fraction of species k. V_i^c is a correction velocity to ensure global mass conservation:

$$V_i^c = \sum_{k=1}^{N_s} D_k \frac{W_k}{\overline{W}} \frac{\partial X_k}{\partial x_i} \tag{6.10}$$

This correction velocity impacts the heat flux term in multi-species flows: an additional term appears in the diffusive heat flux due to heat transport by species diffusion. The total heat flux vector then reads:

$$q_i = \underbrace{-\lambda_q \frac{\partial T}{\partial x_i}}_{\text{Heat conduction}} \underbrace{- \rho \sum_{k=1}^{N_s} \left(D_k \frac{W_k}{\overline{W}} \frac{\partial X_k}{\partial x_i} - Y_k V_i^c \right) h_{s,k}}_{\text{Heat flux through species diffusion}} \tag{6.11}$$

where λ_q is the heat conduction coefficient of the mixture.

6.1.2 Turbulence and simulation

Unfortunately, the exact resolution of Eqs. 6.1 - 6.4 using Computational Fluid Dynamics (CFD) for turbulent flows in complex geometries is and will remain a challenge for a long time. Indeed, turbulent flows are characterized by a wide range of length scales (eddies): from the integral scale (the largest) to the 'Kolmogorov' scales (the smallest). The size of the largest eddies l_t is typically of the order of the geometry considered. These structures contain most of the energy of the flow. The smallest eddies are the ones where the energy is dissipated. There is a 'cascade' of energy from the large scale to the smallest scales because large eddies interact with each other and breakdown into smaller eddies. The size of the Kolmogorov scale is noted η. Kolmogorov showed in 1941 (Kolmogorov, 1941) that the ratio between the integral length scale l_t and η is (see Fig. 6.2):

$$\frac{l_t}{\eta} = Re_t^{3/4} = \frac{\rho u' l_t}{\mu} \tag{6.12}$$

where Re_t is the turbulent Reynolds number based on a turbulent velocity u' and the integral length scale. The ratio l_t/η represents the number of points in each direction required to compute all the scales in the flow. Therefore, the total number of points N_{pt} needed to compute the flow in the three dimensions scales as:

$$N_{pt} \simeq \left(Re_t^{3/4}\right)^3 = Re_t^{9/4} \tag{6.13}$$

For example, lets imagine the number of points required to compute the flow in the Dawson's experiment computed in this PhD. thesis: the mean velocity at the bluff body exit is $U_{bb} = 18\ m/s$. Assuming that the turbulent velocity is five percent of this value leads to: $u' \simeq 0.05 \times U_{bb} = 0.9\ m/s$. The integral length scale can be approximated here by the chamber width which is 2.2 times the burner diameter (D) so that $2.2 \times D \simeq l_t \simeq 77\ mm$, the turbulent Reynolds number being therefore:

$$Re_t = \frac{\rho U_{bb} L_c}{\mu} = \frac{1.2 \times 0.9 \times 0.077}{1.8.10^{-5}} \simeq 4.6\ 10^3 \tag{6.14}$$

According to Eq. 6.13, the total number of grid points needed to compute this configuration is around $N_{pt} = 1.75\ 10^8$ which is not feasible considering current computer resources.

Therefore, three numerical approaches with different resolutions have been developed to describe flows using CFD:

- the Reynolds Averaged Navier-Stokes (RANS) computations have historically been the first possible approach thanks to their affordable computational costs. RANS techniques were developed to solve the mean values of all quantities. The balance equations for the averaged quantities are obtained by averaging the instantaneous balance of equations and require closure models for turbulence and combustion.

- The second level corresponds to Large Eddy Simulations (LES). The largest scale of the turbulence are explicitly calculated whereas the effects of smaller scales are modeled using subgrid closure rules. The balance of equations for LES are obtained by filtering the instantaneous balance of equations. unlike RANS, LES capture instantaneous motions and not only mean values.
- The third level of computations is Direct Numerical Simulations (DNS) where the full instantaneous Navier-Stokes equations are solved without any model for turbulent motions: all turbulence scales are explicitly determined. DNS would predict all time variations exactly like a high-resolution sensor in an experiment. This approach has changed the analysis of turbulent combustion but DNS requires a very important computational cost. Today, this approach is mainly used to study flows in academic configurations (low Reynolds number, very small configuration).

Figure 6.1 shows an example of the time evolution of local temperature predicted by RANS, LES or DNS for a stabilized flame. RANS capture only the mean value, LES capture the low frequency variations and DNS captures all time variations. These prop-

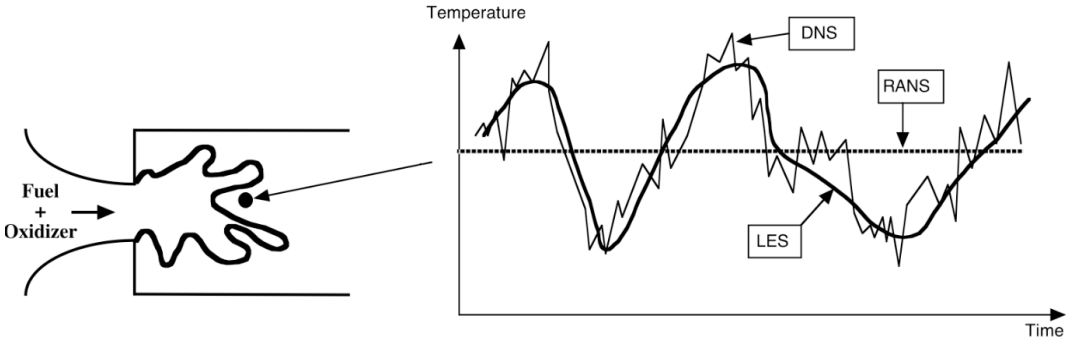

Figure 6.1: Time evolutions of local temperature computed with RANS, LES or DNS in a turbulent brush (Poinsot & Veynante, 2011).

erties can also be presented in terms of energy spectra as shown by Fig. 6.2. All spatial frequencies are resolved in DNS. In LES, the largest scales (up to a cut-off wave number k_c) are computed whereas the smallest are modeled. By construction, LES is expected to tend toward DNS when the cut-off length goes to zero (*ie.* the mesh is fine). In RANS, only mean flow fields are resolved: no turbulent motion is explicitly calculated.

6.2 The LES concept

Large Eddy Simulation is nowadays recognized as an intermediate approach in comparisons to classical RANS methodologies and expensive DNS. As previously discussed, in RANS, only mean fields are calculated (the derivation of the method consists in a temporal averaging of the Navier-Stokes equations Eqs. 6.1 - 6.4). It means than only a steady state can be expected. The unclosed terms (appearing during the derivation of the mean equations) are representative of the physics taking place over the entire range of

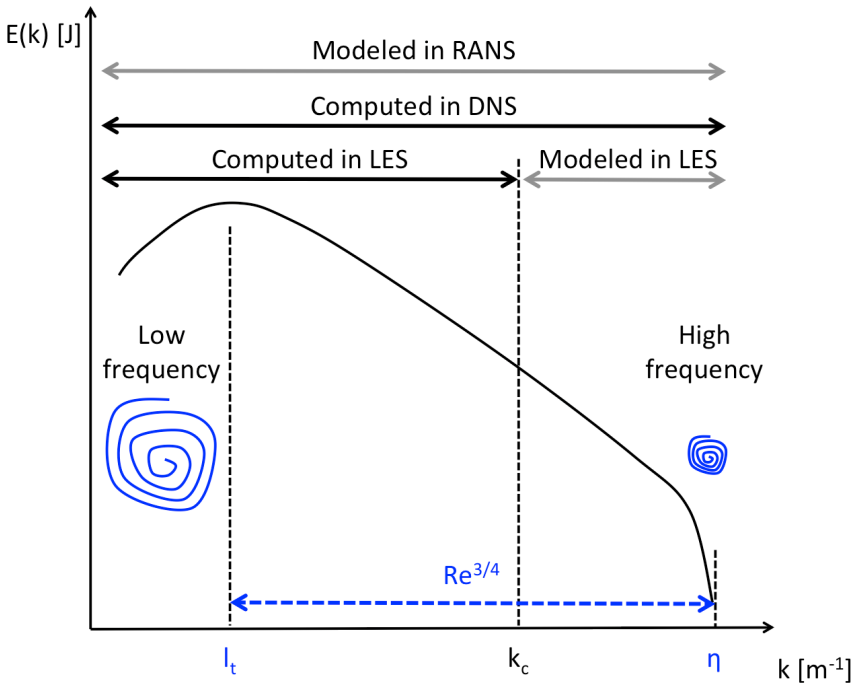

Figure 6.2: Log-log turbulence energy spectrum versus wave number. k_c is the cut-off wave number used in LES.

frequencies (see Fig. 6.2) and the closure models have an important prediction job to do. It explains the big impact of the model on the results. In LES, the operator is a spatially localized time independent filter of given size Δ. This 'spatial average' creates a separation between the large (greater than the filter size) and small (smaller than the filter size) scales. The unclosed terms are in LES representative of the physics associated with the small structures (with high frequencies) present in the flow. LES allows a dynamic representation of the large scale motions whose contributions are critical in complex geometries. The LES predictions of complex turbulent flows are henceforth closer to the physics since large scale phenomena such as large vortex shedding and acoustic waves are embedded in the set of governing equations.

For these reasons, LES has a clear potential in predicting turbulent flows encountered in industrial applications. All simulations performed in this thesis are LES, realized with the AVBP code developed at CERFACS and IFPEN on different grids to ensure grid dependency.

6.3 Multi-species flows

Combustion necessarily involves multi-species flows: at least one fuel (for example methane CH_4) and one oxidizer (for example O_2). In this section, the equation of state, the transport coefficients and the thermodynamical variables (enthalpy, energy and entropy) of such flows are presented.

6.3.1 The equation of state

In a flow composed of N_s species, the proportion of each species k can be described by its mass fraction Y_k or by its molar fraction X_k. Y_k (resp. X_k) is defined as the mass (resp. the mole number) of species k, m_k (resp. n_k) divided by the total mass m (resp. the total mole number n) in a given volume: $Y_k = m_k/m$ (reps. $X_k = n_k/n$). Necessarily, $\sum_k X_k = \sum_k Y_k = 1$.

The equation of state for an ideal gas mixture writes:

$$P = \rho r T \tag{6.15}$$

where r is the gas constant of the mixture dependent on time and space: $r = R/\overline{W}$ where $\overline{W}$ is the mean molecular weight of the mixture:

$$\frac{1}{\overline{W}} = \sum_{k=1}^{N} \frac{Y_k}{W_k} \tag{6.16}$$

The gas constant r and the heat capacities of the gas mixture depend on the local gas composition as:

$$r = \frac{R}{\overline{W}} = \sum_{k=1}^{N} \frac{Y_k}{W_k} R = \sum_{k=1}^{N} Y_k r_k \tag{6.17}$$

$$C_p = \sum_{k=1}^{N} Y_k C_{p,k} \quad \text{and} \quad C_v = \sum_{k=1}^{N} Y_k C_{v,k} \tag{6.18}$$

where $R = 8.3143$ J/mol.K is the universal gas constant. The adiabatic exponent for the mixture is given by $\gamma = C_p/C_v$. Thus, the gas constant, the heat capacities and the adiabatic exponent are no longer constant: they depend on the local gas composition as expressed by the local mass fractions $Y_k(x,t)$.

The temperature is deduced from the the sensible energy, using Eqs. 6.27 and 6.28.

6.3.2 Transport coefficients

In CFD codes for multi-species flows the molecular viscosity μ is often assumed to be independent of the gas composition. However, it depends on the temperature and a power-law or a Sutherland law provides a good estimation of this evolution:

$$\mu = \mu_0 \left(\frac{T}{T_0} \right)^b \quad \text{(Power law)} \quad \mu = c_1 \frac{T^{3/2}}{T + c_2} \frac{T_{ref} + c_2}{T_{ref}^{3/2}} \quad \text{(Sutherland law)} \tag{6.19}$$

with b typically ranging between 0.5 and 1.0 (e.g. $b = 0.76$ for air) or $c_1 = 1.71\ 10^{-5}$ kg/m.s and $c_2 = 110.4$ K for air $T_{ref} = 273$ K.

The heat conduction coefficient λ_q of the gas mixture can then be computed by introducing the molecular Prandtl number of the mixture as:

$$\lambda_q = \frac{\mu C_p}{Pr} \tag{6.20}$$

The Prandtl number Pr is supposed to be constant in time and space and is given in an input file in the AVBP code. For the molecular diffusion coefficients D_k the same approximation can be used in CFD codes. The Schmidt number of species k, Sc_k, is supposed to be constant (in space and time) so that the diffusion coefficient for each species is computed as:

$$D_k = \frac{\mu}{\rho S_{c,k}} \tag{6.21}$$

These thermal and species diffusions act together in a reacting flow. Therefore, an important dimensionless number is defined in combustion to characterize their respective strength: the Lewis number Le which compares the thermal heat diffusivity $D_{th} = \lambda/(\rho C_p)$ to the molecular diffusivity D_k:

$$Le_k = \frac{D_{th}}{D_k} \tag{6.22}$$

6.3.2.a Methane (CH_4) or ethylene (C_2H_4) / air flame transport coefficients

To determine the Schmidt number of species k, Sc_k, to impose in LES and the Prandtl number Pr, a reference flame with a complex transport is computed with Cantera. Cantera is an object-oriented, open source suite of software tools for reacting flow problems involving detailed chemical kinetics, thermodynamics and transport processes. For example, this software can compute one-dimensional laminar premixed flames with detailed chemistry and different transport model. The target fuels for the Cambridge experiment where methane and ethylene. Therefore, a methane/air and ethylene/air laminar flames have been computed with this tool using two different transport models: (1) a complex mixture model called "MIX" where the Schmidt number is not assumed to be constant and (2) the AVBP transport model implemented in Cantera called "AVBP" with constant Schmidt and Prandtl numbers. Typical variation of the Schmidt and Prandtl numbers in the MIX Cantera flame are displayed in Tab. 6.1. They confirm that indeed, $S_{c,k}$ and P_r numbers are almost constant. Their values in the burnt gas were used in AVBP ($S^b_{c,k}$ and P^b_r in Tab. 6.1). The impact of using constant Schmidt and Prandtl numbers can be measured by comparing MIX and AVBP results: adiabatic temperature (left) and laminar flame speed (right) results are displayed in Tab. 6.2 comparing the same ethylene/air flame at $\Phi = 0.85$ computed with these two models (and several kinetic schemes). The two quantities match very well ($T_{ad}^{MIX} = 2239K$, $T_{ad}^{AVBP} = 2245K$, $s_L^{MIX} = 0.557m/s$ and $s_L^{AVBP} = 0.531m/s$) which indicates that assuming constant Schmidt and Prandtl numbers is a valid approximation.

Species	$S^u_{c,k}$	$S^b_{c,k}$
C_2H_4	0.95	0.88
O_2	0.77	0.73
N_2	0.73	0.68
CO_2	0.99	0.94
CO	0.75	0.74
H_2O	0.69	0.54
Prandlt	$P^u_r = 0.713$	$P^b_r = 0.711$

Table 6.1: Schmidt and Prandlt numbers in the unburnt ($S^u_{c,k}$, P^u_r) and burnt ($S^b_{c,k}$, P^b_r) gas from an ethylene/air flame computed by Cantera. Burnt quantities are used in AVBP.

Data	**UCSD**	**MIX**	**AVBP**
s_L (m/s)	0.587	0.557	0.531
T_{ad} (K)	2233	2239	2245

Table 6.2: Adiabatic temperature and laminar flame speed are computed using Cantera ethylene/air flames with MIX and AVBP transport and a two-step mechanism. These results are compared to the detailed mechanism provided by UCSD.

6.3.3 Thermodynamical variables

Species energy and enthalpy are defined in reference to a given temperature T_0. Mass enthalpy of species k, h_k, is the sum of a reference enthalpy at $T = T_0$ and a sensible enthalpy $h_{s,k}$:

$$h_k = \underbrace{h_{s,k}}_{\text{sensible}} + \underbrace{\Delta h^0_{f,k}}_{\text{chemical}} \tag{6.23}$$

The internal energy of species k, $e_k = h_k - RT/W_k$, can also be split into a sensible and a chemical contribution $e_k = e_{s,k} + \Delta h^0_{f,k}$.

The standard reference state used in AVBP is $P_0 = 1$ bar and $T_0 = 0$ K. The sensible mass enthalpies ($h_{s,k}$) and entropies (s_k) for each species are tabulated for 51 values of the temperature (T_i with $i = 1...51$) ranging from 0K to 5000K with a step of 100 K. Therefore these variables can be evaluated by:

$$h_{s,k}(T_i) = \int_{T_0=0K}^{T_i} C_{p,k} dT = \frac{h^m_{s,k}(T_i) - h^m_{s,k}(T_0)}{W_k} \tag{6.24}$$

and:

$$s_k(T_i) = \frac{s^m_k(T_i) - s^m_k(T_0)}{W_k} \tag{6.25}$$

The superscript m corresponds to molar values. The tabulated values for $h_{s,k}(T_i)$ and $s_k(T_i)$ can be found in the JANAF tables (Stull & Prophet, 1971). With this assumption, the sensible energy for each species can be reconstructed using the following expression:

$$e_{s,k}(T_i) = \int_{T_0=0K}^{T_i} C_{v,k} dT = h_{s,k}(T_i) - r_k T_i \tag{6.26}$$

Note that the mass heat capacities at constant pressure $C_{p,k}$ and volume $C_{v,k}$ are supposed constant between T_i and $T_{i+1} = T_i + 100$. They respectively are defined as the slope of

the sensible enthalpy and the slope of the sensible energy ($C_{p,k} = \partial h_{s,k}/\partial T$ and $C_{v,k} = \partial e_{s,k}/\partial T$). The sensible energy henceforth varies continuously with the temperature and is obtained by using a linear interpolation:

$$e_{s,k}(T) = e_{s,k}(T_i) + (T - T_i)\frac{e_{s,k}(T_{i+1}) - e_{s,k}(T_i)}{T_{i+1} - T_i} \qquad \text{for T} \in [\mathrm{T_i}; \mathrm{T_{i+1}}] \tag{6.27}$$

The sensible energy and enthalpy of the mixture may then be expressed as:

$$\rho e_s = \sum_{k=1}^{N} \rho_k e_{s,k} = \rho \sum_{k=1}^{N} Y_k e_{s,k} \tag{6.28}$$

$$\rho h_s = \sum_{k=1}^{N} \rho_k h_{s,k} = \rho \sum_{k=1}^{N} Y_k h_{s,k} \tag{6.29}$$

6.4 Kinetics

The combustion process transforms cold reactants into hot products when a sufficiently high energy is available to activate the reactions. This process can be modeled by a global reaction where a budget between reactants and major products is written. For example, the global reaction of methane oxidation is:

$$CH_4 + 2O_2 \quad \longrightarrow \quad CO_2 + 2H_2O \tag{6.30}$$

Such a global reaction does not describe elementary reactions that occur during the combustion process. Combustion of reactants is in fact a set of reactions involving major and minor species. Generally, N_s species $\mathcal{M}_{kj}$ react through $j = 1, ..., M$ reactions, where N_s and M can be of the order of hundred or thousand:

$$\sum_{k=1}^{N} \nu'_{kj} \mathcal{M}_{kj} \rightleftharpoons \sum_{k=1}^{N} \nu''_{kj} \mathcal{M}_{kj}, \qquad j = 1, ..., M \tag{6.31}$$

The reaction rate of species k, $\dot{\omega}_k$, is the sum of rates $\dot{\omega}_{kj}$ produced by all M reactions:

$$\dot{\omega}_k = \sum_{j=1}^{M} \dot{\omega}_{kj} = W_k \sum_{j=1}^{M} \nu_{kj} \mathcal{Q}_j \tag{6.32}$$

where $\nu_{kj} = \nu''_{kj} - \nu'_{kj}$ and $\mathcal{Q}_j$ is the rate progress of reaction j. The total mass conservation gives:

$$\sum_{k=1}^{N} \dot{\omega}_k = 0 \tag{6.33}$$

The rate $\mathcal{Q}_j$ is written:

$$\mathcal{Q}_j = K_{f,j} \prod_{k=1}^{N} \left(\frac{\rho Y_k}{W_k} \right)^{\nu'_{kj}} - K_{r,j} \prod_{k=1}^{N} \left(\frac{\rho Y_k}{W_k} \right)^{\nu''_{kj}} \tag{6.34}$$

The $K_{f,j}$ and $K_{r,j}$ are the forward and reverse rates of reaction j:

$$K_{f,j} = A_{f,j} \exp\left(-\frac{E_{a,j}}{\mathcal{R}T} \right) \tag{6.35}$$

where $A_{f,j}$ and $E_{a,j}$ are the pre-exponential factor and the activation energy given in an input file. $K_{r,j}$ is deduced from the equilibrium assumption:

$$K_{r,j} = \frac{K_{f,j}}{K_{eq}} \tag{6.36}$$

where K_{eq} is the equilibrium constant defined by:

$$K_{eq} = \left(\frac{p_0}{\mathcal{R}T} \right)^{\sum_{k=1}^{N} \nu_{kj}} \exp\left(\frac{\Delta S_j^0}{\mathcal{R}} - \frac{\Delta H_j^0}{\mathcal{R}T} \right) \tag{6.37}$$

where $p_0 = 1$ bar. ΔH_j^0 and ΔS_j^0 are respectively the enthalpy (sensible + chemical) and the entropy changes for reaction j:

$$\Delta H_j^0 = h_j(T) - h_j(0) = \sum_{k=1}^{N} \nu_{kj} W_k (h_{s,k}(T) + \Delta h_{f,k}^0) \tag{6.38}$$

$$\Delta S_j^0 = \sum_{k=1}^{N} \nu_{kj} W_k s_k(T) \tag{6.39}$$

where $\Delta h_{f,k}^0$ is the mass enthalpy of formation of species k at temperature $T_0 = 0$ K and is given in an input file (molar value). Finally, the heat released by the combustion $\dot{\omega}_T$ in the initial enthalpy equation (Poinsot & Veynante, 2011) is calculated as:

$$\dot{\omega}_T = -\sum_{k=1}^{N} \dot{\omega}_k \Delta h_{f,k}^0 \tag{6.40}$$

6.4.1 Reduced schemes

In real flames, the combustion process involves many species and reactions as already mentioned. For example, the widely used GRI-MECH 3.0 mechanism describes the reaction of methane with air. It consists of 325 reactions that involve 53 species. These full schemes can be used only on very simple configurations (one-dimensional laminar flames for example). In an LES or DNS code, it is nor reasonable neither necessary to transport

such a large number of species (the code must solve one conservation equation for each specie). Moreover some of these reactions can be very fast and could limit the time step drastically. One possible solution consists in reducing the detailed chemistry. Reduced mechanisms are built to reproduce a minimum of flame features. In practice reduced schemes with two reactions are sufficient to reproduce the flame speed, the adiabatic flame temperature and the flame thickness for lean flames. Three criteria are usually sufficient to capture the important kinetic phenomena in most lean premixed turbulent flames.

1. For methane a standard one-step scheme is employed.

$$CH_4 + 2\ O_2 \longrightarrow CO_2 + 2\ H_2O \tag{6.41}$$

$$\tag{6.42}$$

2. For ethylene, a two-step mechanism has been developed:

$$C_2H_4 + 2\ O_2 \longrightarrow 2\ CO + 2\ H_2O \tag{6.43}$$

$$CO + \frac{1}{2}\ O_2 \longleftrightarrow CO_2 \tag{6.44}$$

Both schemes account for fuel oxidation through an irreversible reaction at a rate q_1 while a second reaction accounts for the equilibrium between CO and CO_2 with a rate q_2:

$$q_1 = A_1 \left(\frac{\rho Y_F}{W_F}\right)^{n_1^F} \left(\frac{\rho Y_{O_2}}{W_{0_2}}\right)^{n_1^{O_2}} \exp\left(\frac{E_{a,1}}{RT}\right) \tag{6.45}$$

$$q_2 = A_2 \left[\left(\frac{\rho Y_{CO}}{W_{CO}}\right)^{n_2^{CO}} \left(\frac{\rho Y_{O_2}}{W_{0_2}}\right)^{n_2^{O_2}} - \frac{1}{K_e}\left(\frac{\rho Y_{CO_2}}{W_{CO_2}}\right)^{n_2^{CO_2}}\right] \exp\left(\frac{E_{a2}}{RT}\right) \tag{6.46}$$

where K_e is the equilibrium constant for the CO/CO_2 equilibrium and R the perfect-gas constant. While the reduced scheme for methane has already been validated in AVBP (Franzelli *et al.*, 2013), the validation of the C2H4_BFER scheme for ethylene versus a detailed scheme proposed by UCSD is presented in Tab. 6.2 (the Cantera code is used to compare these two chemical schemes). For a one-dimensional planar flame at $P_0 = 101325$ Pa and $T_0 = 300$ K, the reduced scheme reproduces accurately the laminar flame speed s_L and burnt gases adiabatic temperature T_{ad}, for the target equivalence ratio $\Phi = 0.85$ used for the LES simulations of the Dawson's experiment.

6.5 Governing equations for non-reactive LES

As previously discussed, the LES concept consists in applying a spatially localized time independent filter of given size Δ on the Navier-Stokes equations. This filtering introduces a separation between the large (greater than the filter size) and small (smaller than the filter size) scales. This operation also exhibits unclosed terms which must be modeled. These equations and the closure models are presented in this section. It is a close transposition of the AVBP handbook [1].

[1] AVBP handbook: http://www.cerfacs.fr/~avbp/AVBP_V6.X/HANDBOOK/AVBP/HTML2/main.html

6.5.1 The filtering operation

A low-pass (in wavenumber) filter, G_Δ, is applied to the Navier-Stokes equations Eqs. 6.1 - 6.4. Mathematically, it consists of a convolution of any quantity, f, with the filter function G_Δ.

$$\bar{f}(x) = \int f(x')G_\Delta(x - x')dx' \tag{6.47}$$

The resulting filtered quantity, $\bar{f}$, represents the large-scale structures of the flow (*ie.* resolved in the LES) whereas all the structures of size smaller than the filter length, Δ, are contained in the residual field, $f' = f - \bar{f}$. Contrary to RANS averaging, the filtered value of a LES perturbation is not zero: $\overline{f'} \neq 0$ and the double filtered values are not equal to the filtered values in general: $\overline{\overline{f}} \neq \overline{f}$. For variable density ρ, a mass-weighted Favre filtering is introduced according to:

$$\bar{\rho}\widetilde{f}(x) = \int \rho f(x')G_\Delta(x - x')dx' = \overline{\rho f} \tag{6.48}$$

Filtering the instantaneous balance equations (Eqs. 6.1 - 6.4) leads to the following equations:

$$\frac{\partial \overline{\rho}}{\partial t} + \frac{\partial}{\partial x_i}(\overline{\rho}\widetilde{u}_i) = 0 \tag{6.49}$$

$$\frac{\partial \overline{\rho}\widetilde{u}_j}{\partial t} + \frac{\partial}{\partial x_j}(\overline{\rho}\widetilde{u}_i\widetilde{u}_j) = -\frac{\partial}{\partial x_j}(\overline{P}\delta_{ij} - \overline{\tau}_{ij} - \overline{\tau}^t_{ij}) \tag{6.50}$$

$$\frac{\partial \overline{\rho}\widetilde{E}}{\partial t} + \frac{\partial}{\partial x_j}(\overline{\rho}E\widetilde{u}_j) = -\frac{\partial}{\partial x_j}[\overline{u_i(P\delta_{ij} - \tau_{ij})} + \overline{q}_j + \overline{q}^t_j] + \overline{\dot{\omega}}_T + \overline{Q}_r \tag{6.51}$$

$$\frac{\partial \overline{\rho}\widetilde{Y_k}}{\partial t} + \frac{\partial}{\partial x_j}(\overline{\rho}\widetilde{Y_k}\widetilde{u}_j) = -\frac{\partial}{\partial x_j}[\overline{J}_{j,k} + \overline{J}^t_{j,k}] + \overline{\dot{\omega}}_k \tag{6.52}$$

where $\widetilde{u}_j$, $\widetilde{E}$ and $\widetilde{Y_k}$ denote the filtered velocity vector, total energy per unit mass and species mass fractions, respectively. A repeated index implies summation over this index (Einstein's rule of summation). Note also that the index k is reserved for referring to the k^{th} species and does not follow the summation rule.

Writing the vector of the filtered conservative variables as follows: $\overline{\mathbf{w}} = (\bar{\rho}\widetilde{u}, \bar{\rho}\widetilde{v}, \bar{\rho}\widetilde{w}, \bar{\rho}\widetilde{E}, \bar{\rho}\widetilde{Y_k})$, Eqs. 6.50 - 6.52, can be expressed as:

$$\frac{\partial \overline{\mathbf{w}}}{\partial t} + \nabla \cdot \overline{\mathbf{F}} = \bar{\mathbf{s}} \tag{6.53}$$

where $\bar{\mathbf{s}}$ is the filtered source term and $\overline{\mathbf{F}}$ is the flux tensor which can be divided in three parts:

$$\overline{\mathbf{F}} = \overline{\mathbf{F}}^I + \overline{\mathbf{F}}^V + \overline{\mathbf{F}}^t \tag{6.54}$$

where $\overline{\mathbf{F}}^I$ is the inviscid term, $\overline{\mathbf{F}}^V$ is the viscous term and $\overline{\mathbf{F}}^t$ is the turbulent subgrid-scale term.

6.5.1.a The inviscid term $\overline{\mathbf{F}}^I$

The three spatial components of the inviscid flux tensor are the same as in DNS but based on the filtered quantities:

$$\overline{\mathbf{F}}^I = \begin{pmatrix} \bar{\rho}\widetilde{u}_i\widetilde{u}_j + \overline{P}\delta_{ij} \\ \bar{\rho}\widetilde{E}\widetilde{u}_j + \overline{Pu_j}\delta_{ij} \\ \bar{\rho}_k\widetilde{u}_j \end{pmatrix} \tag{6.55}$$

6.5.1.b The viscous term $\overline{\mathbf{F}}^V$

The components of the viscous flux tensor take the form:

$$\overline{\mathbf{F}}^I = \begin{pmatrix} -\overline{\tau_{ij}} \\ -\left(\overline{u_i\tau_{ij}}\right) + \overline{q_j} \\ \overline{J_{j,k}} \end{pmatrix} \tag{6.56}$$

The filtered diffusion terms are:

- Laminar filtered stress tensor $\overline{\tau_{ij}}$ (for Newtonian fluids)

$$\overline{\tau_{ij}} = \overline{2\mu\left(S_{ij} - \frac{1}{3}\delta_{ij}S_{kk}\right)} \tag{6.57}$$

$$\text{approximation:} \quad \overline{\tau_{ij}} \simeq 2\bar{\mu}\left(\widetilde{S}_{ij} - \frac{1}{3}\delta_{ij}\widetilde{S}_{kk}\right) \tag{6.58}$$

$$\text{with:} \quad \widetilde{S}_{ij} = \frac{1}{2}\left(\frac{\partial\widetilde{u}_j}{\partial x_i} + \frac{\partial\widetilde{u}_i}{\partial x_j}\right) \tag{6.59}$$

$$\text{and:} \quad \bar{\mu} \simeq \mu(\widetilde{T}) \tag{6.60}$$

- Diffusive species flux vector $\overline{J_{i,k}}$

$$\overline{J_{i,k}} = \overline{-\rho\left(D_k\frac{W_k}{\overline{W}}\frac{\partial X_k}{\partial x_i} - Y_kV_i^c\right)} \tag{6.61}$$

$$\text{approximation:} \quad \overline{J_{i,k}} \simeq -\bar{\rho}\left(\overline{D}_k\frac{W_k}{\overline{W}}\frac{\partial\widetilde{X}_k}{\partial x_i} - \widetilde{Y}_k\widetilde{V}_i^c\right) \tag{6.62}$$

$$\text{with:} \quad \widetilde{V}_i^c = \sum_{k=1}^{N}\overline{D}_k\frac{W_k}{\overline{W}}\frac{\partial\widetilde{X}_k}{\partial x_i} \tag{6.63}$$

$$\text{and:} \quad \overline{D}_k \simeq \frac{\bar{\mu}}{\bar{\rho}Sc_k} \tag{6.64}$$

- Filtered heat flux $\overline{q_i}$

$$\overline{q_i} = -\overline{\lambda \frac{\partial T}{\partial x_i}} + \sum_{k=1}^{N} \overline{J_{i,k} h_{s,k}} \tag{6.65}$$

$$\text{approximation:} \quad \overline{q_i} \simeq -\bar{\lambda} \frac{\partial \widetilde{T}}{\partial x_i} + \sum_{k=1}^{N} \overline{J_{i,k}} \widetilde{h}_{s,k} \tag{6.66}$$

$$\text{with:} \quad \bar{\lambda} \simeq \frac{\bar{\mu} \overline{C}_p(\widetilde{T})}{Pr} \tag{6.67}$$

These forms assume that the spatial variations of molecular diffusion fluxes are negligible and can be modeled through simple gradient assumptions.

6.5.1.c The turbulent subgrid-scale term $\overline{\mathbf{F}}^t$

The components of the turbulent subgrid-scale flux take the form:

$$\overline{\mathbf{F}}^I = \begin{pmatrix} -\overline{\tau_{ij}}^t \\ \overline{q_j}^t \\ \overline{J_{j,k}}^t \end{pmatrix} \tag{6.68}$$

As highlighted above, filtering the transport equations leads to a closure problem evidenced by the so called "subgrid-scale" (SGS) turbulent fluxes. For the system to be solved numerically, closures need to be supplied. Details on the closures are:

- The Reynolds tensor $\overline{\tau_{ij}}^t$

$$\overline{\tau_{ij}}^t = -\bar{\rho} \left(\widetilde{u_i u_j} - \widetilde{u}_i \widetilde{u}_j \right) \tag{6.69}$$

$$\text{modeled as (Boussinesq, 1877}a\text{):} \quad \overline{\tau_{ij}}^t = 2\bar{\rho}\nu_t \left(\widetilde{S_{ij}} - \frac{1}{3}\delta_{ij}\widetilde{S_{kk}} \right) \tag{6.70}$$

$$\text{with:} \quad \widetilde{S}_{ij} = \frac{1}{2}\left(\frac{\partial \widetilde{u}_j}{\partial x_i} + \frac{\partial \widetilde{u}_i}{\partial x_j} \right) - \frac{1}{3}\frac{\partial \widetilde{u}_k}{\partial x_k}\delta_{ij} \tag{6.71}$$

In Eq. 6.70, $\overline{\tau_{ij}}^t$ is the SGS tensor, $\widetilde{S_{ij}}$ is the resolved rate tensor and ν_t is the SGS turbulent viscosity. The modeling of ν_t is explained in Sec. 6.5.2.

- The subgrid scale diffusive species flux vector $\overline{J_{j,k}}^t$

$$\overline{J_{i,k}}^t = -\bar{\rho} \left(\widetilde{u_i Y_k} - \widetilde{u}_i \widetilde{Y}_k \right) \tag{6.72}$$

$$\text{modeled as:} \quad \overline{J_{i,k}}^t = -\bar{\rho} \left(D_k^t \frac{W_k}{\overline{W}} \frac{\partial \widetilde{X}_k}{\partial x_i} - \widetilde{Y}_k \widetilde{V}_i^{c,t} \right) \tag{6.73}$$

$$\text{with:} \quad \widetilde{V}_i^{c,t} = \sum_{k=1}^{N} D_k^t \frac{W_k}{\overline{W}} \frac{\partial \widetilde{X}_k}{\partial x_i} \tag{6.74}$$

$$\text{and:} \quad D_k^t = \frac{\nu_t}{Sc_k^t} \tag{6.75}$$

The turbulent Schmidt number $Sc_k^t = 0.6$ is the same for all species. Note also that having one turbulent Schmidt number for all the species does not imply, $\widetilde{V}_i^{c,t} = 0$ because of the $W_k/\overline{W}$ term in Eq. 6.73.

- The subgrid scale heat flux vector $\overline{q_j}^t$

$$\overline{q_i}^t = -\bar{\rho}\left(\widetilde{u_i E} - \widetilde{u}_i \widetilde{E}\right) \tag{6.76}$$

$$\text{modeled as:} \quad \overline{q_i}^t = -\lambda_t \frac{\partial \widetilde{T}}{\partial x_i} + \sum_{k=1}^{N} \overline{J_{i,k}} \widetilde{h}_{s,k} \tag{6.77}$$

$$\text{with:} \quad \lambda_t = \frac{\mu_t \overline{C}_p}{Pr^t} \tag{6.78}$$

The turbulent Schmidt number is fixed at $Pr^t = 0.6$.

6.5.2 Models for the subgrid stress tensor

LES models for the subgrid stress tensor (see Eq. 6.70) are derived on the theoretical ground that the LES filter is spatially and temporally invariant. Variations in the filter size due to non-uniform meshes or moving meshes are not directly accounted for in the LES models. Change of cell topology is only accounted for through the use of the local cell volume, that is $\Delta = V_{cell}^{1/3}$.

The filtered compressible Navier-Stokes equations exhibit SGS tensors and vectors describing the interaction between the non-resolved and resolved motions. Generally, the influence of the SGS on the resolved motion is taken into account by a SGS model based on the introduction of a turbulent viscosity, ν_t (Boussinesq, 1877*b*). Such an approach assumes the effect of the SGS field on the resolved field to be purely dissipative. This hypothesis is essentially valid within the cascade theory of turbulence introduced by Kolmogorov (1941).

LES models for the subgrid stress tensor only differ through the estimation of ν_t. In this document, only the three models used during this PhD. thesis are presented: the Smagorinsky model, the WALE (Wall Adapting Local Eddy-viscosity), and the SIGMA model. For a better understanding of advantages and drawbacks of these different models, desirable properties required for a SGS viscosity model are given:

- **Prop A:** A positive quantity which involves only locally defined velocity gradients
- **Prop B:** A cubic behavior near walls
- **Prop C:** Be zero for any two-component or two-dimensional flows
- **Prop D:** Be zero for axisymmetric or isotropic expansion/contraction

While properties A and B are straightforward, properties C and D should be briefly discussed: 2D turbulence exist and has already been investigated experimentally and numerically. However, its nature is fundamentally different than the usual 3D turbulence because of the absence of vortex-stretching (if a vortex is stretched, matter is pulled towards the rotation axis of the vortex leading to a faster rotation because of the angular momentum conservation). Therefore, it is appropriate to consider **Prop C** to ensure that

the 3D SGS turbulence model phases out in two-dimensional cases. **Prop D** are related to axisymmetric case such as laminar round jet or spherical premixed flames (acting like acoustic monopole, one key acoustic generation which can lead to combustion instabilities) where turbulence effects should not be present.

- The Smagorinsky model

$$\nu_t = (C_S\Delta)^2\sqrt{2\widetilde{S}_{ij}\widetilde{S}_{ij}} \tag{6.79}$$

where Δ denotes the filter characteristic length (cube-root of the cell volume), C_S is the model constant set to 0.18 but can vary between 0.1 and 0.18 depending on the flow configuration. The Smagorinsky model (Smagorinsky, 1963) was developed in the sixties and heavily tested for multiple flow configurations. This closure has the particularity of supplying the right amount of dissipation of kinetic energy in homogeneous isotropic turbulent flows. Locality is however lost and only global quantities are maintained. It is known to be 'too dissipative and transitioning flows are not suited for its use (Sagaut, 2006). Moreover, this formulation is known for not vanishing in near-wall regions and therefore cannot be used when walls are treated as no-slip walls (as performed in this PhD. thesis).

- The WALE model

$$\nu_t = (C_w\Delta)^2\frac{\left(s^d_{ij}s^d_{ij}\right)^{3/2}}{\left(\widetilde{S}_{ij}\widetilde{S}_{ij}\right)^{5/2} + \left(s^d_{ij}s^d_{ij}\right)^{5/4}} \tag{6.80}$$

with:

$$s^d_{ij} = \frac{1}{2}\left(\widetilde{g}^2_{ij} + \widetilde{g}^2_{ji}\right) - \frac{1}{3}\widetilde{g}^2_{kk}\delta_{ij} \tag{6.81}$$

where Δ denotes the filter characteristic length (cube-root of the cell volume), $C_w = 0.4929$ is the model constant and $\tilde{g}_{ij}$ denotes the resolved velocity gradient. The WALE model (Ducros *et al.*, 1998) was developed for wall bounded flows in an attempt to recover the scaling laws of the wall. Similarly to the Smagorinsky model locality is lost and only global quantities are to be trusted.

- The SIGMA model

$$\mathcal{D}_s = \frac{\sigma_3(\sigma_1-\sigma_2)(\sigma_2-\sigma_3)}{\sigma_1^2} \quad \text{and} \quad \nu_t = (C_\sigma\Delta)^2\mathcal{D}_s \tag{6.82}$$

where C_σ is a constant: $C_\sigma = 1.35$.

The Smagorinsky and Wales SGS models have opposite behaviors: while the first one vanishes for pure rotation but not for pure shear, the other one (WALE) has the right near-wall behavior but not for pure rotation situations (**Prop C**). A new operator was

therefore constructed by Nicoud *et al.* (2011) based on singular values (σ_1, σ_2 and σ_3) of a tensor built using resolved velocity gradients ($G = g^t g$). Note that the singular values σ_i have the following near-wall behaviors:

$$\begin{cases} \sigma_1 = O(1) \\ \sigma_2 = O(y) \\ \sigma_3 = O(y^2) \end{cases} \tag{6.83}$$

where y is the normal coordinate to the wall surface and $O(y^p)$ denotes a term of the order of p, i.e. behaving like y^p when the distance to the solid boundary vanishes: $y \to 0$. It results that the SIGMA model behaves correctly near walls: $\nu_t = O(y^3)$.

6.5.3 Numerical schemes

To solve equations presented in Sec. 6.5.1, numerical schemes are needed. The AVBP solver is based on the finite volume method (Hirsch, 2007) with a cell-vertex discretization. Because they are less dissipative than non-centered schemes (up-wind or downwind), centered numerical schemes are implemented in AVBP. All numerical schemes developed in AVBP are presented in (Lamarque, 2007). The two numerical schemes used in this thesis are:

- The Lax-Wendroff (LW) scheme The LW scheme (Lax & Wendroff, 1960) is a finite volume centered scheme. This scheme uses an explicit time integration with a single Runge-Kutta step. Its accuracy in both space and time is of second order. The scheme is quite robust due to a stabilizing diffusive term. Furthermore, it is characterized by low computational cost and has been used during this PhD. thesis for initialization and ignition processor of the cold flow.

- The Two step Taylor-Galerkin 'C' scheme The TTGC scheme (Colin & Rudgyard, 2000) is a finite element centered scheme. Its accuracy in both space and time is of third order (4^{th} on regular grids (Moureau *et al.*, 2005)). It is characterized by very good properties regarding dissipation and dispersion making it well-suited for LES applications involving acoustics as combustion instabilities studied here. However, it is less robust than the LW scheme and is approximately 2.5 more expensive in terms of computational cost. This scheme is normally used after the flow has been stabilized using the *LW* scheme to accurately compute small vortices and acoustic waves.

6.5.4 Artificial viscosity

The numerical discretization methods in AVBP are spatially centered and prone to small-scale oscillations in the vicinity of steep solution variations. This is why it is common practice to add a so-called artificial viscosity (AV) term to the discrete equations, to control these spurious modes (also known as "wiggles"). These AV models are characterized by the "linear preserving" property which leaves unmodified a linear solution on

any type of element. The models are based on a combination of a "shock capturing" term (called 2^{nd} order AV) and a "background dissipation" term (called 4^{th} order AV). In AVBP, adding AV is done in two steps:

- first a sensor detects if AV is necessary, as a function of the flow characteristics,
- then a certain amount of 2^{nd} and 4^{th} AV is applied, depending on the sensor value and on user-defined parameters.

The 2^{nd} order AV acts just like a "classical" viscosity activated only in certain regions of the flow. It smoothes local gradients, and introduces artificial dissipation. The 4^{th} order AV is mainly used to control spurious high-frequency wiggles.

6.6 Combustion modeling

As described in Sec. 6.4, combustion is a process in which reactants are transformed into products. The domain where these transformations take place, called the flame front, is very small. Typically a flame thickness at atmospheric pressure for gasoline/air flames is around 0.1 to 0.5 mm. This raises a problem encountered for Large Eddy Simulation of reactive flows: the thickness δ_L^0 of a flame is generally smaller than the standard mesh size Δ used for LES. In order to resolve the flame front correctly, about 5 to 10 points are needed. This leads to very large grids, out of the capacity of the current calculators for large and complex industrial configurations.

Different models have been proposed to approximate the filtered species reaction rates $\overline{\dot{\omega}}_k$ (see Eq. 6.52) for turbulent premixed combustion using the LES approach. They may be separated into two main categories:

1. **Models assuming an infinitely thin reaction zone:** the turbulent premixed flame is modeled by fresh reactants and burnt products separated by an infinitely thin reaction zone. The local structure of the flame is assumed correspond to a laminar flame for which the inner structure is not affected by turbulence (flamelet assumption). The Bray-Moss-Libby (BML) models (Bray & Moss, 1977), the flame surface density models (Hawkes & Cant, 2000), and G-equation models (Moureau *et al.*, 2009) are some of the most common examples.
2. **Models describing the structure of the reaction zone thickness:** the turbulent premixed flame is characterized by a finite thin reaction zone that could interact with the turbulent flow and often behaves as a stretched laminar flame. Some examples are the Probability Density Function (PDF) models (Dopazo, 1994), the F-TACLES approach (the chemistry is tabulated as a function of a progress variable) developed by EM2C and the artificially Thickened Flame (TF) models (Colin *et al.*, 2000; Légier *et al.*, 2000).

Only the Thickened Flame model has been used in this thesis and therefore is described in more details in this document.

6.6.1 The Thickened Flame model for LES (TFLES)

An attractive solution to propagate a flame on a 'coarse' grid consists in artificially thickening this flame. This idea was first proposed by Butler & O'Rourke (1977). Figure 6.3 presents the concept of this approach. For sufficiently large values of the thickening factor F, the thickened flame front can be resolved explicitly on the grid nodes. Since the reaction rate is still expressed using Arrhenius law, various phenomena can be accounted for without requiring ad-hoc submodels (ignition, flame/wall interactions, heat losses at boundaries).

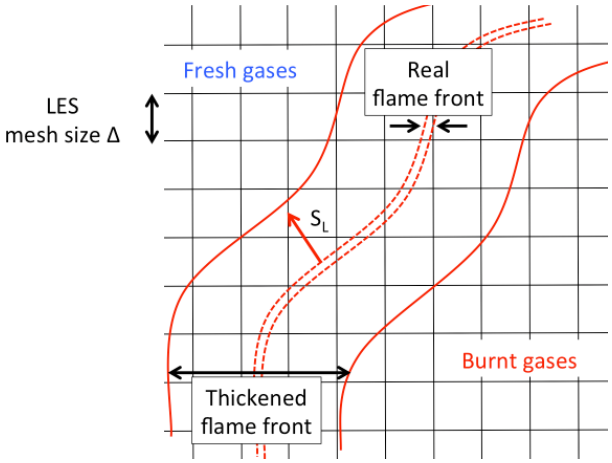

Figure 6.3: Thickened flame approach. The flame is artificially thickened but its flame speed is conserved.

Following simple theories of laminar premixed flames (Williams, 1985; Kuo, 2005), the flame speed s_L and the flame thickness δ_L^0 may be expressed as:

$$s_L \propto \sqrt{D_{th} B} \quad ; \quad \delta_L^0 \propto \frac{D_{th}}{s_L} = \sqrt{\frac{D_{th}}{B}} \tag{6.84}$$

where D_{th} is the thermal diffusivity and B the pre-exponential constant. If the thermal diffusivity is multiplied by a factor F while the pre-exponential constant is divided by F, the flame thickness δ_L^0 is multiplied by a factor F but the flame speed s_L is conserved: the flame propagates at the right speed on the computational domain.

When the flame is thickened by a factor F, the interaction between the flame and the turbulence is modified: the flame becomes less sensitive to turbulent motions and vortex may affect the reaction zone. This interaction is characterized by the Damköhler number D_a which compares turbulent τ_t to chemical τ_c time scales (for large values of D_a, turbulence is not able to affect the inner flame structure which remains close to a laminar flame wrinkled by turbulence motions):

$$D_a = \frac{\tau_t}{\tau_c} = \frac{l_t}{u'} \frac{s_L}{\delta_L^0} \tag{6.85}$$

It is straightforward to show that increasing the flame thickness by a factor F decreases the D_a number by the same factor F ($D_a^{thick} = D_a/F$). This point has been investigated using DNS by Angelberger *et al.* (1998) and Colin *et al.* (2000) (see Figure 6.4). To account for this unwanted effect, an efficiency function $\mathcal{E}_f$, corresponding to a subgrid scale wrinkling factor has been derived. This efficiency function depends on velocity (u'/s_L) and length scale ($\Delta/F\delta_L^0$) ratios.

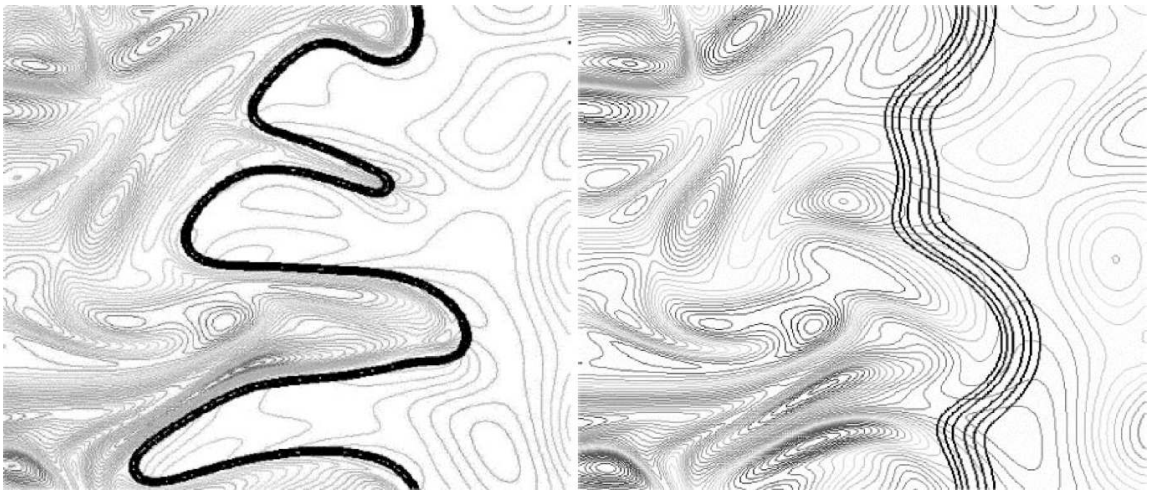

Figure 6.4: DNS of flame turbulence interactions. Reaction rate and vorticity fields are superimposed. Left: Reference flame ; Right: flame artificially thickened by a factor $F = 5$ (Poinsot & Veynante, 2011).

In practice, the thickened flame approach is implemented by changing the thermal diffusivity and the reaction rate according to:

$$\begin{array}{rccccc} \text{Diffusivity:} & D_{th} & \Rightarrow & FD_{th} & \Rightarrow & \mathcal{E}_f F D_{th} \\ \text{Pre-exponential constant:} & B & \Rightarrow & B/F & \Rightarrow & \mathcal{E}_f B/F \\ & & \text{thickening} & & \text{wrinkling} & \end{array}$$

According to Eq. 6.84, the flame speed s_L and the flame thickness δ_L^0 become respectively:

$$s_T = \mathcal{E}_f s_L \quad ; \quad \delta_T = F\delta_L^0 \tag{6.86}$$

In this thesis, two different efficiency functions $\mathcal{E}_f$ valid when equilibrium between the turbulent motions and the flame surface is reached, have been used and are briefly described:

- **Colin model:** Colin *et al.* (2000) have proposed an efficiency function $\mathcal{E}_{f,colin}$ which compares the flame wrinkling with and without thickening, called the wrinkling factor Ξ:

$$\Xi(\delta_l^0) = 1 + \alpha\Gamma\left(\frac{\delta_\Delta}{\delta_L^0}, \frac{u'_\Delta}{s_L^0}\right)\frac{u'_\Delta}{s_L^0} \tag{6.87}$$

where α is a constant and Γ is a function taking into account the subgrid strain rate depending on the fluctuating subgrid velocity u'_Δ and the filter size Δ.
The turbulent flame velocity is therefore obtained in the LES as a function of this efficiency function:

$$\frac{s_T}{s_L} = \frac{\Xi(F\delta_l^0)}{\Xi(\delta_l^0)} = \mathcal{E}_{f,colin} \tag{6.88}$$

Finally, this combustion model is closed by approximating the subgrid scale turbulent velocity u'_Δ with an operator based on the rotational of he velocity field to remove the dilatation part of the velocity and by estimating the constant α using HIT (Homogeneous Isotropic Turbulence) simulations (Angelberger *et al.*, 1998).

- **Charlette and Meneveau model:** Charlette *et al.* (2002) have proposed a power-law model for the wrinkling factor which extendes the Colin model proposed in Eq. 6.87:

$$\Xi(\delta_l^0) = \left(1 + \min\left[\max\left(\frac{\delta_\Delta}{\delta_l^0} - 1\right), \Gamma\left(\frac{\delta_\Delta}{\delta_L^0}, \frac{u'_\Delta}{s_L^0}, Re_\Delta\right)\frac{u'_\Delta}{s_L^0}\right]\right)^\beta \tag{6.89}$$

where the efficiency function Γ describes the ability of vortices to effectively wrinkle the flame front and is therefore related to the fractal dimension of the flame front, β is the model parameter and $Re_\Delta = \frac{u'_\Delta \delta_\Delta}{\nu}$ is the subgrid scale turbulent Reynolds number (ν being the fresh gas kinematic viscosity).

This TFLES model has been first developed for perfectly premixed combustion. But applying a uniform thickening in the whole domain accelerates diffusion in non reactive zones, where thickening is not necessary. In other words, the TF model can remain unchanged in the flame zone but must be adapted outside the flame region. So a dynamic thickening procedure (Légier *et al.*, 2000) (called D-TFLES) depending on the flame position and the local resolution has been developed and is therefore preferred.

The thickening factor F is not a constant any more but it goes to F_{max} in flame zones and decreases to unity in non reactive zones. This is obtained by writing:

$$F = F_{max}\mathcal{S} \tag{6.90}$$

with:

$$F_{max} = \frac{N_c}{\Delta}\delta_L^0 \tag{6.91}$$

N_c being the number of cells used to resolve the flame front (typically $N_c = 5$ guarantees a good behavior). $\mathcal{S}$ is a sensor depending on the local temperature and mass fractions:

$$\mathcal{S} = \tanh\left(\beta'\frac{\Omega}{\Omega_0}\right) \tag{6.92}$$

where β' is a constant equal to 500, Ω is a sensor function detecting the presence of a reaction front and Ω_0 corresponds to its maximum value. One possible method to construct Ω is to use the kinetic parameters of the fuel breakdown reaction:

$$\Omega = {Y_F}^{n_F}{Y_O}^{n_O}\exp\left(-\Gamma\frac{E_a}{RT}\right) \tag{6.93}$$

Ω_0 can be found running a 1D premixed non-thickened flame and measuring Ω_0 on it. Γ is used to start the thickening before the reaction, that is why $\Gamma < 1$ (usually $\Gamma = 0.5$).

Note that TFLES is not a "filtered" model: equations are first thickened so that LES filtering is not needed. In that sense, the "thickening" of species and temperature used in TFLES is not following the "filtering" operator used for density and velocity. Constructing thickened flames by rigorously filtering all equations is the path followed for example by the EM2C group in the FTACLES series of models (Fiorina *et al.*, 2010; Auzillon *et al.*, 2012). On the long term, FTACLES type models are promising methods but they were not tested here because this work focused on thermo-acoustics and not turbulent combustion.

The main advantages of the TFLES model are its simplicity and its performances for premixed and stratified flames. It has been used successfully in multiple configurations (Colin *et al.*, 2000; Légier *et al.*, 2002; Selle *et al.*, 2004*a*; Wolf *et al.*, 2010; Enaux *et al.*, 2011) and is also integrated now in commercial softwares such as Fluent or Charles (from Cascade Technologies). The effect of the combustion models on FTF results will be characterized by a sensitivity analysis developed in Chapter 7 by changing the mesh refinement (computations are performed on a coarse mesh using 5 millions cells and a fine mesh with 30 millions cells) and efficiency functions (Colin and Charlette efficiency functions).

6.7 Few words about the AVBP code

Historically, the AVBP code was started at CERFACS in January 1993 as an initiative of Michael Rudgyard and Thilo Schönfeld. The aim of this project was to build an efficient code handling unstructured grids of any cell type. Nowadays, AVBP is a parallel CFD code that solves the laminar and turbulent compressible reactive (or non-reactive) Navier-Stokes equations in two and three space dimensions[2]. It is also the baseline code of the ERC (European Research Council) advanced grant won by IMFT in 2013 on thermoacoustics (http://intecocis.inp-toulouse.fr).

The important development of the physical models done at CERFACS is completed by academics studies carried out at the IFP Energies Nouvelles, the EM2C lab of Ecole Centrale Paris (ECP) and the Institut de Mécanique des Fluides de Toulouse (IMFT). The ownership of AVBP is shared with IFP-Energies Nouvelles (IFP-EN), following an agreement of joint code development oriented towards piston engine applications. Important links with industry have been established with Safran Group (Snecma, Snecma DMS, Herakles, Turbomeca), Air Liquide, Gaz de France as well as with Alstom, Ansaldo, Honeywell and Siemens Power Generation.

[2]More details on AVBP here: http://www.cerfacs.fr/4-26334-The-AVBP-code.php.

Chapter 7

Sensitivity of FTF for turbulent swirled flames and impact on the stability of azimuthal modes

Contents

Part I has shown the first-order importance of FTF (Flame Transfer Function) on thermoacoustic codes results. We now address the problem of FTF prediction using LES. This chapter describes a preliminary numerical study of azimuthal unstable modes in the annular combustor of Cambridge before computing the full 360° *configuration. LES is used to compute a Flame Transfer Function (FTF) and a Helmholtz solver to predict the overall stability of the combustor. FTF quantifies the interaction between acoustics and the turbulent swirled flames. They must be known with precision because instabilities are very sensitive to small changes (see Chapter 5). The effects of azimuthal confinement (corresponding to the annular combustor equipped with* 12 *or* 18 *burners), thermal boundary conditions and fuel type (methane or ethylene) on FTFs are simulated here using LES of a single* 20 *degree (*$N = 18$*) or* 30 *degree (*$N = 12$*) sector. A double-sector LES is also computed to investigate flame / flame interactions. These LES-based FTFs are then used as inputs for a Helmholtz solver and results show that 1) subgrid-scale LES models lead to marginal effects on the Flame Transfer Function while 2) azimuthal confinement, thermal conditions and fuel type strongly affect the flame response to acoustics and therefore control the stability of the azimuthal mode. Computations reveal that the annular experiment performed with methane should be stable while ethylene should lead to azimuthal unstable modes as observed experimentally. From this sensitivity analysis, an operating point (ethylene, adiabatic,* $N = 18$ *burners) is extracted and will be computed using a full annular* 360° *configuration in the next chapter.*

7.1 Introduction

Studying experimentally an unsteady combustion is a daunting task and most experimentalists have to choose between providing very detailed space and time resolved measurements (velocity, species and temperature fields like for example in the Preccinsta burner (Franzelli *et al.*, 2013; Meier *et al.*, 2007)) or performing flame transfer function measurements. Therefore in practice, when FTFs measurements are available, almost no other experimental data is usually given to check the LES quality. Moreover, measuring any physical quantities in a self-excited combustor becomes an insuperable task since probes must cope with an extreme environment facing strong pressure oscillations. Here the Cambridge rig of Worth & Dawson (2013*b*) was used to compute FTF and predict mode stability. This rig belongs to the second category: information on thermo-acoustics is available but not much more so that the few experimental data available (no mean velocity profiles, FDF or FTF measurements etc.) raise the question of quality and accuracy of the full 360° LES which will be performed in the next chapter. Observations from Worth & Dawson (2013*b*,*a*) on the stability and frequencies of the experimental combustor in multiple conditions (fuels, wall materials, number of burners etc.) can be used to assess the validity of the LES and its underlying models (turbulence, combustion, chemistry etc.). Therefore, this chapter intends to first evaluate the robustness of the LES strategy to capture the flame/acoustic interaction and consequently to predict the

stability of the annular configuration by computing one or two sectors only.

Because of their extreme costs, computations of full 360° configurations are still out of reach today to study effects of number of burners N, mesh refinements, turbulence and combustion models as well as operating points on the predicted azimuthal mode. In this chapter, a reduced strategy is used: 1) A Flame Transfer Function (FTF, Crocco, 1951) or Flame Describing Functions (FDF, Noiray *et al.*, 2008) can be evaluated numerically to link the flame response to acoustics. To do so, only one sector with periodic and non-reflecting boundary conditions is computed using LES since capturing a self-excited azimuthal mode is not required (Giauque *et al.*, 2005; Kaess *et al.*, 2008) to obtain FTF or FDF. 2) The acoustic/flame model (FTF) is then introduced as a source term in a full annular acoustic solver, much cheaper than LES, to study the azimuthal acoustic mode in the complete 360° configuration. Although successful in determining the stability of real burners (Nicoud *et al.*, 2007) such coupled approaches are known to be sensitive to multiple parameters (Duchaine *et al.*, 2011). This last question is also addressed in this chapter by evaluating which parameters control the flame/acoustics interactions measured by the FTF models. Finally, this chapter addresses two crucial points:

1) Provide LES best practices and guidelines for turbulence models, combustion models and thermal boundary conditions to be followed when computing the whole 360° configuration of Cambridge.
2) Choose the operating point to be used to compute the full annular rig and verify its consistency with experimental observations performed by Worth & Dawson (2013*b*,*a*).

First, Section 7.2 describes the annular rig of Cambridge. In Section 7.3, the numerical strategy and the various cases used to evaluate the FTF (Section 10.2.2) and stability (Section 7.3.2) are defined. Results on mean and phase-averaged flow fields for unforced and forced cases are discussed and compared to experiment in Sections 7.4 and 7.5. Section 7.7 focuses on the FTF sensitivity to various LES sub models as well as key phenomena (azimuthal confinement, thermal conditions and fuel type) affecting the flow dynamics and flame shape as observed in previous sections. Finally, Section 7.8 gives the stability map of the 360° configuration. The impact of azimuthal confinement, thermal conditions and fuels on the stability is assessed: the annular rig is found to be stable when using methane while ethylene leads to azimuthal instabilities as observed in the annular experiment (Worth & Dawson, 2013*b*,*a*).

7.2 Target configuration: annular combustor of Cambridge (Worth & Dawson, 2013*b*)

The target experiment is the annular combustor of Cambridge studied by Worth & Dawson (2013*b*) (Fig. 7.1) The stainless steel rig can include $N = 12$, 15, or 18 equally spaced flames around a circumferential diameter of 170 mm which modifies the flame-flame interactions as shown in Fig. 7.2: for $N = 12$ burners, the distance between burners is large and flames are isolated but for $N = 18$ burners, the distance between burners is reduced leading to a strong flame merging between neighboring sectors. Note also that

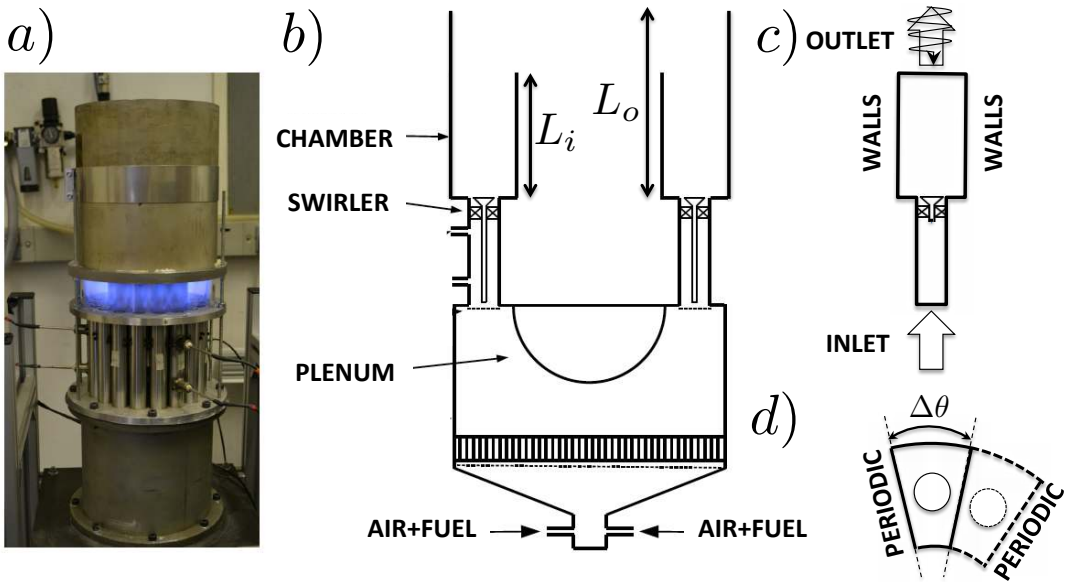

Figure 7.1: Photograph (a) and schematic (b) of the annular experiment with $L_i = 130\ mm$ and $L_o = 300\ mm$ complemented by a longitudinal (c) and a transverse (d) cut of the single (——) and double (- - -) sector computation domain.

isolated and merged flames react differently to heat-loss: the outer shear branch of the V-flame is weaker and even disappears for isolated flames, but no heat-loss effect is observed when flame merging occurs. Premixed reactants are supplied by a plenum which includes grids and flow straighteners for flow conditioning and acoustic damping. For all configurations, mass flow controllers are used to maintain a constant bulk velocity of $U = 18\ m.s^{-1}$ at the exit of each bluff body. This ensures that any change in the flame structure and dynamics is the result of azimuthal confinement (flame spacing). The rig is instrumented with microphones to characterize the instability modes and a high-speed intensified camera is used to measure the OH^* chemiluminescence of the whole annulus.

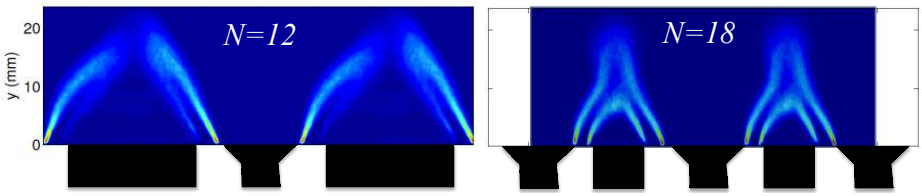

Figure 7.2: Flame visualization of two neighboring flames in the experiment for $N = 12$ burners (left) and $N = 18$ burners (right).

To find a set of conditions that give rise to self-excited azimuthal modes, the inner (L_i) and outer (L_o) lengths of the combustor walls, azimuthal confinement, and two fuel types (CH_4 and C_2H_4) were varied in the experiment (Worth & Dawson, 2013*b*,*a*): strong self-excited azimuthal modes at the frequency $f = 1800\ Hz$ (Fig. 7.3) only occurred for C_2H_4-air mixtures and when different inner and outer tube lengths $L_i = 130$ mm and $L_o = 300$ mm were used. Bourgouin *et al.* (2013) also found that L_i and L_o must

be different to excite azimuthal modes. The occurrence of self-excited azimuthal modes did not depend on azimuthal confinement but the limit-cycle amplitude and the flame structure did. Only longitudinal modes were observed for CH_4-air mixtures.

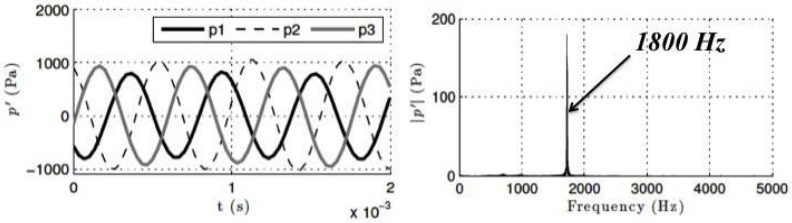

Figure 7.3: Acoustic pressure oscillations varying with time (left) and its Fourier transform (right) showing a strong instabilities at $f = 1800\ Hz$ corresponding to an azimuthal mode.

7.3 Numerical models

7.3.1 Large Eddy Simulations

Large Eddy Simulation (LES) of compressible flow (detailed in Chapter 6) is widely recognized as an accurate method (Poinsot & Veynante, 2011) to study combustion instabilities in complex configurations (Wolf *et al.*, 2012; Sengissen *et al.*, 2007; Fureby, 2010; Kuenne *et al.*, 2011) but the impact of subgrid scale models on LES results for instabilities is rarely discussed. As shown by the UQ study of Chapter 5, any uncertainty on FTF input data will have a strong effect on stability predictions. Quantifying uncertainties due to LES on FTF results is a mandatory step. This includes effects of the subgrid models, combustion models, chemistry and grid refinement on FTF outputs (n, τ). The effect of these numerical parameters will be compared to the effect of physical parameters such as the fuel, potential heat losses at walls or the number of sectors, hoping that the physical parameters introduce larger changes in n and τ than the numerical parameters do.

To study the impact of models on FTF computations, AVBP is used in this chapter to solve the filtered multi-species 3D Navier-Stokes equations with realistic thermochemistry on unstructured meshes (Schønfeld & Poinsot, 1999; Roux *et al.*, 2005). Numerics is based on a two-step Taylor-Galerkin finite element scheme of third-order in space and time (TTGC, Moureau *et al.*, 2005) to accurately propagate acoustic waves. Boundary conditions use the NSCBC approach (Poinsot *et al.*, 1992) and ensure non-reflecting conditions (Selle *et al.*, 2004*b*) as well as the proper introduction of acoustic waves in the LES domain for FTF computations. This computational domain corresponds to one single sector of the annular combustor of Cambridge equipped with $N = 18$ burners (Fig. 7.4). A swirler with 6 blades mounted with a bluff-body is installed at the burner/chamber junction (Fig. 7.5) to stabilize the flame.

Since the plenum contains dampers and grids, this cavity has been removed from the computational domain and therefore the inlet of the LES domain is located at the burner inlet, assuming that no aerodynamic perturbations from the plenum (e.g. vortex shedding due to the inflow jet impinging the plenum curbed walls) can affect the downstream

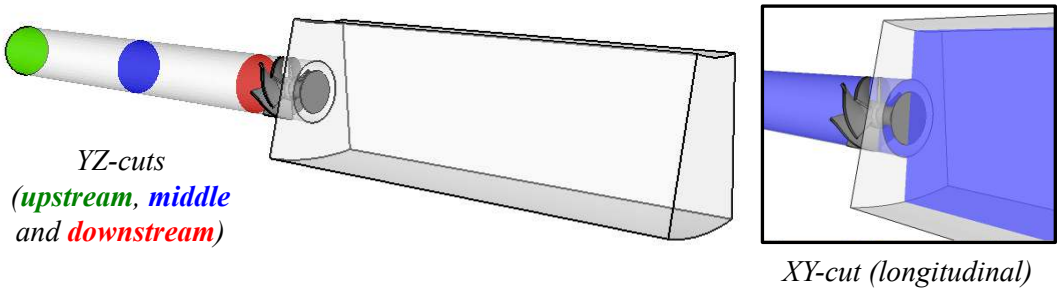

Figure 7.4: 3D view of the SHORT configuration (no plenum) corresponding to one sector of the annular combustor equipped with $N = 18$ burners. The upstream (green), middle (blue) and downstream (red) transverse YZ-cuts in the burner (left) and the longitudinal XY-cut (blue, right) are also displayed.

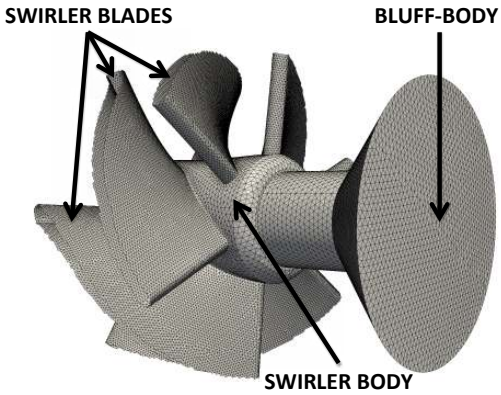

Figure 7.5: 3D view of the swirler and the associated surface mesh.

dynamics of the system. To validate this choice, two different non-reactive stabilized (i.e. no acoustic forcing) configurations with (called LONG) and without (called SHORT) plenum cavity have been computed by LES to analyze the effect of the plenum removal on the system dynamics. Especially, the velocity profile at the burner inlet is resolved in the LONG case while it is imposed in the SHORT case with a Poiseuille's profile: a comparison between the mean velocity profiles and spectra is required to ensure that no perturbation coming from the plenum can modify the mean flow topology (recirculation zones, jet opening at the swirler exit etc.) or excite the flame dynamics at 1800 Hz.

First, pressure (not shown here) and axial velocity signals in the burner and the chamber are analyzed in Fig. 7.6 and show that only the broadband noise, but not aerodynamics oscillations at specific frequencies, is affected by the plenum. Peaks observed in the pressure/velocity spectra come from aerodynamics perturbations generated by the swirlers. This validation is comforted by the mean (and RMS, not shown here) flow field in the chamber and at several longitudinal positions in the burners. This study highlights no particular differences between the LONG (top) and SHORT (bottom) cases (Fig. 7.7). This is due to the particular curved shape of the plenum/burner junction which reduces aerodynamics instabilities and lets acoustic waves leave the burners toward the plenum without reflections: experimental and numerical reflection coefficients at the plenum/burners junction are close to $R = 0.1$, i.e. the junction is almost non-reflecting.

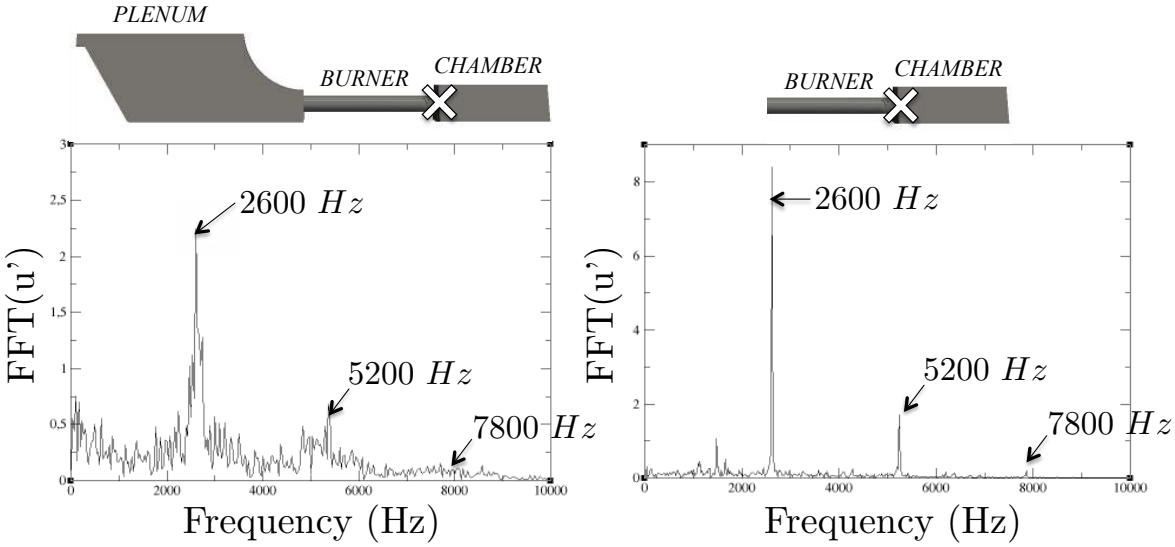

Figure 7.6: Fluctuation axial velocity u' spectra in the single sector configuration of the annular chamber for a stabilized non-reactive case with (LONG, left) and without (SHORT, right) plenum cavity. Only the broadband noise, but not the aerodynamics peaks, is affected by the plenum removal. The probe is located at the burner/chamber junction (white cross).

Moreover, aerodynamics noise and heterogeneities generated in the plenum are phased out in the long burners as observed in Fig. 7.7.

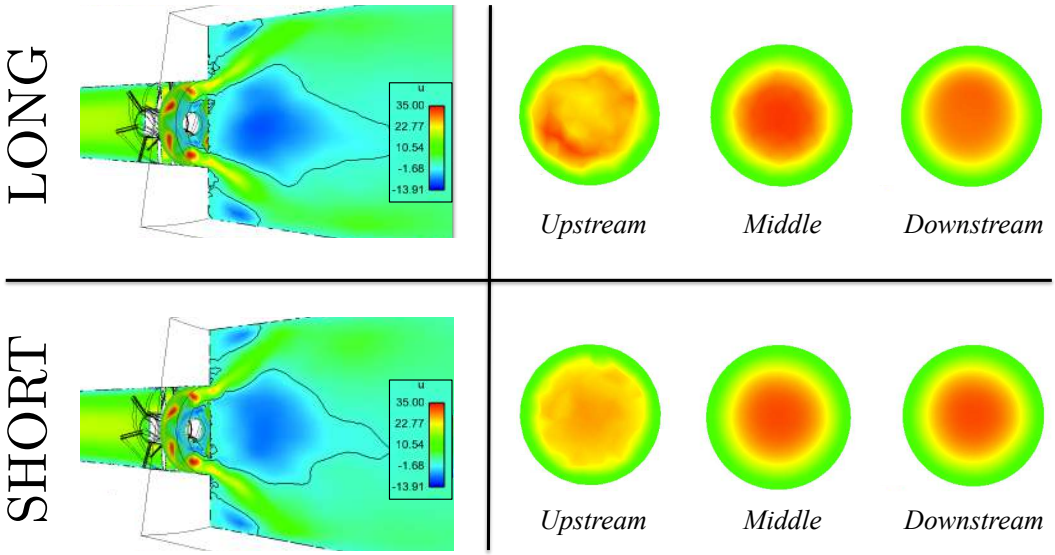

Figure 7.7: Mean axial flow field in the chamber (left) and at several positions in the burners described in Fig. 7.4 (right) for the LONG (top) and SHORT (bottom) configurations.

Finally, all computational domains computed in this thesis have no plenum but include the complete burner with an axial swirler composed of six blades mounted on a bluff-body (Figs. 7.5 and 7.8). Although FTF estimations can be obtained from an acoustically isolated single sector of a real configuration, flow confinement is known to play a role on

flame shape and stability. The effect of confinement and flame/flame interactions was tested here by comparing single and double sector LES (Fig. 7.1, d).

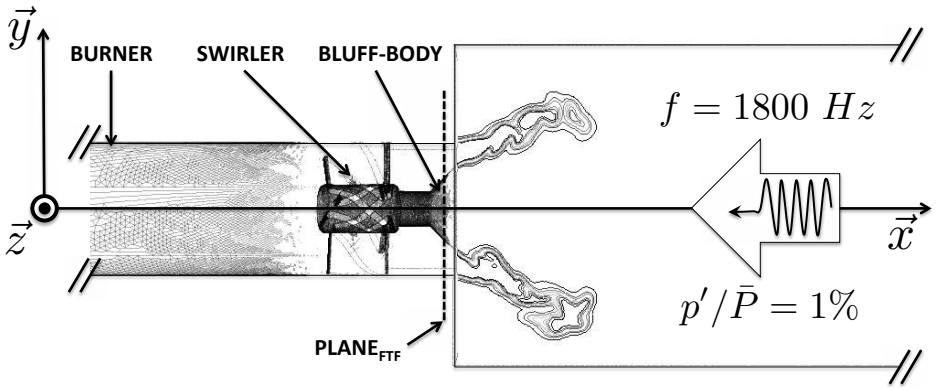

Figure 7.8: XY-cut of the single-sector configuration with iso-contours of heat release. Acoustic waves, needed for FTF evaluation in the LES, are introduced by pulsating the outlet pressure.

The sensitivity of FTF predictions to different sub-grid stress models is tested using the classical Dynamics Smagorinsky model (Smagorinsky, 1963) and both Wale (Nicoud & Ducros, 1999) and Sigma (Nicoud *et al.*, 2011) models (Section 6.5.2). Turbulent-flame interactions are addressed using the dynamic Thickened Flame (TF) approach with two different efficiency functions as a performance test: the Colin model (Colin *et al.*, 2000) and the Charlette-Meneveau model (Charlette *et al.*, 2002) described in Section 6.6.1. These combustion models are closed by approximating the subgrid scale turbulent velocity u'_Δ with an operator based on the rotational of the velocity field to remove the dilatation part of the velocity.

Since the overall number of injectors N also varies, different angles, $\Delta\theta = 30°$ or $20°$, are considered for the single-sector cases, corresponding respectively to the annular rig equipped with $N = 12$ or $N = 18$ burners (Fig. 7.1). All meshes are fully unstructured and contain 4.2 millions cells (for the case $\Delta\theta = 20°$) or 5.5 million cells (for $\Delta\theta = 30°$) per sector for the coarse cases while the refined case contains 31 million cells. This results in typical thickening factors of 3 to 5 in the flame zone to guarantee $5 - 10$ points in the flame. Cells lengths are typically $80\mu m$ near swirler walls and $150\mu m$ in the swirler passages.

Axial acoustic forcing is performed in the LES to compute FTFs since the main mechanism leading to azimuthal combustion instabilities is the modulation of the axial mass flow rate through the injectors. Transverse acoustic forcing by strong transverse velocity fluctuations (O'Connor & T.Lieuwen, 2012*c*; Lespinasse *et al.*, 2013) is not considered here since it occurs only for flames located at a pressure node which do not contribute to the stability of the system[1]. The forcing frequency corresponds to the azimuthal mode observed experimentally (Worth & Dawson, 2013*b*) ($f \simeq 1800\ Hz$) and is introduced in the LES by pulsating (with the NSCBC approach) the outlet ingoing acoustic wave of the

[1]The Rayleigh criterion is proportional to $\|\hat{p}\|\|\hat{q}\|$ thus flames at pressure nodes ($\|\hat{p}\| = 0$) lead to a null Rayleigh term and therefore do not contribute to the stability of the system.

sector (Figs. 7.1 and 7.8). No data on the forcing amplitude is reported since the experiment is self-excited ($p'/\bar{p} \simeq 1\%$): in the LES, various low amplitudes (from $p'/\bar{p} = 0.1\%$ to 1%) of the forcing wave have been tested and no impact on the FTF was observed. FTFs are constructed by recording the global heat release rate $\dot{Q}_i'(t)$ and the reference acoustic velocity $u'_{REF}(t)$ (Crocco, 1951). This velocity is obtained by averaging the axial fluctuating velocity over a plane ($\text{Plane}_{\text{FTF}}$ in Fig. 7.8).

Based on the experiments (Worth & Dawson, 2013*b*), a perfectly premixed air-fuel mixture (methane or ethylene) at equivalence ratio $\phi = 0.85$ is injected in the inlet (plenum/burner section). Worth & Dawson (2013*b*) mention that using ethylene (C_2H_4) leads to azimuthal instabilities while only longitudinal modes appear with methane (CH_4). These two fuels are investigated here with LES. Reaction rates are modeled with reduced kinetic schemes, which have been proved to accurately reproduce low frequency flame dynamics (Kedia *et al.*, 2011): 1 reaction, 4 species for CH_4 and 2 reactions, 6 species for C_2H_4. Adiabatic temperatures and laminar flame speeds have been compared to GRIMECH (Frenklach *et al.*, 1995) for methane and UCSD full schemes (UCSD, 2013) for ethylene (Lecocq *et al.*, 2013; Franzelli *et al.*, 2010; Goodwin, 2009).

Thermal effects also modify FTFs (Duchaine *et al.*, 2011; Tay-Wo-Chong & Polifke, 2012; Mejia *et al.*, 2014): here, adiabatic as well as heat-loss formulations were applied on the chamber walls. For the heat loss formulation, the heat flux imposed on a wall is locally expressed as $\Phi = (T - T_\infty)/R_w$ where the temperature T_∞ is set to 600 K and the thermal resistance is $R_w = 10^{-4}(Km^2)/W$. For these values, the chamber walls typically reach 1000 K.

For all computed cases (Table 7.1), as in the experiment, the mean axial velocity at the burner/chamber junction is conserved: 18 $m.s^{-1}$.

	CASE	COMB.	TURB.	N	MESH	THERM.	$\Delta\theta$	FUEL
	REF	Charlette	Wale	1	Coarse	Adiabatic	20	CH_4
Numerical	**COLIN**	***Colin***	Wale	1	Coarse	Adiabatic	20	CH_4
	SMAGO	Charlette	***Smago***	1	Coarse	Adiabatic	20	CH_4
	SIGMA	Charlette	***Sigma***	1	Coarse	Adiabatic	20	CH_4
	DOUBLE	Charlette	Wale	***2***	Coarse	Adiabatic	20	CH_4
	FINE	Charlette	Wale	1	***Fine***	Adiabatic	20	CH_4
Physical	**CH4-HL-20**	Charlette	Wale	1	Coarse	***Heat-loss***	20	CH_4
	C2H4-ADIA-20	Charlette	Wale	1	Coarse	Adiabatic	20	$\boldsymbol{C_2H_4}$
	CH4-ADIA-30	Charlette	Wale	1	Coarse	Adiabatic	***30***	CH_4
	CH4-HL-30	Charlette	Wale	1	Coarse	***Heat-loss***	***30***	CH_4
	C2H4-ADIA-30	Charlette	Wale	1	Coarse	Adiabatic	***30***	$\boldsymbol{C_2H_4}$

Table 7.1: LES simulations performed to investigate the FTF sensitivity to numerical and physical parameters.

7.3.2 Helmholtz simulations of the full annular combustor

In addition to evaluating uncertainties on input data such as (n, τ), it is also interesting to actually see what these changes lead to in terms of modes when they are injected in a Helmholtz solver. In the UQ study of Chapter 5, ATACAMAC was used to optimize speed but here we will favor precision and run a full 3D Helmholtz solver: the 3D acoustic solver called AVSP (Nicoud *et al.*, 2007) will be used to predict the effect of the FTF on the stability of the azimuthal mode observed experimentally at $f \simeq 1800\ Hz$. AVSP solves the eigenvalues problem issued from a discretization on unstructured meshes (with 3.6 millions cells) of the wave equation where the source term due to combustion is expressed using FTFs (Crocco, 1951). The local reaction term $\widehat{\dot{Q}_i'}$ is expressed for each burner i as:

$$\widehat{\dot{Q}_i'} = n_{u,i}\, e^{j\omega\tau_i}\, \widehat{u'}(\mathbf{x}_{ref,i}) \tag{7.1}$$

where $\widehat{u'}(\mathbf{x}_{ref,i})$ is the Fourier transform of the axial acoustic velocity component at the location $\mathbf{x}_{ref,i}$. The interaction index $n_{u,i}$ is constant for each sector i in the flame zone (Fig. 7.9) and its value is chosen to recover the global value of unsteady heat release (Nicoud *et al.*, 2007) computed by LES. It is set to zero outside of the flame zone.

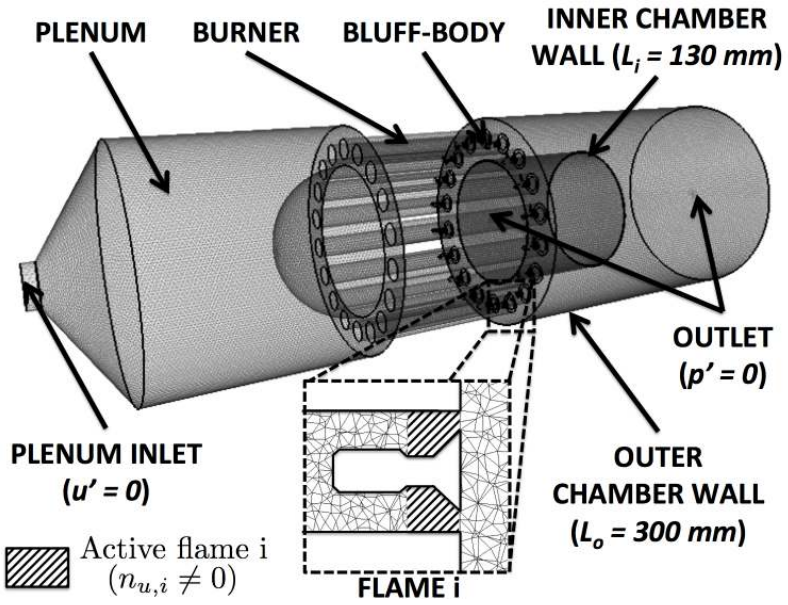

Figure 7.9: 3D view to the 360° acoustic domain with $N = 18$ burners and zoom on the i^{th} flame zone.

The acoustic domain computed with AVSP is the 360° configuration with $N = 12$ or 18 burners connected to the plenum (Fig. 7.9). Different lengths are used for the inner and outer chamber walls ($L_i = 130$ mm and $L_o = 300\ mm$) (Worth & Dawson, 2013*a*; Bourgouin *et al.*, 2013). Infinite impedances (corresponding to $u' = 0$) are applied on walls or plenum inlet and a pressure node ($p' = 0$) is applied at the outlet. Mean density and sound speed are extracted from LES simulations of the single-sector and replicated azimuthally for all sectors.

7.4 Unforced flow fields

A first indication of the effects of parameter changes on LES results is provided by unforced reactive LES predictions on a single-sector (or double sector in the DOUBLE case, Tab. 7.1) of the annular rig. Streamlines from the averaged flow fields are visualized by Line Integral Convolution (LIC, Cabral & Leedom, 1993) in Fig. 7.10 for the $\Delta\theta = 20°$ (right) and 30° (left) cases. They confirm that the distance between neighboring sectors deeply affects the aerodynamics, especially the central recirculation zone (CRZ in Fig. 7.10), and therefore the flame shape. More importantly, the neighboring azimuthal motions induced by the swirlers interact when burners are close to each other which modifies the jet-opening angle in the XZ-plane but not in the XY-plane: the axi-symmetry of the swirl motion is broken.

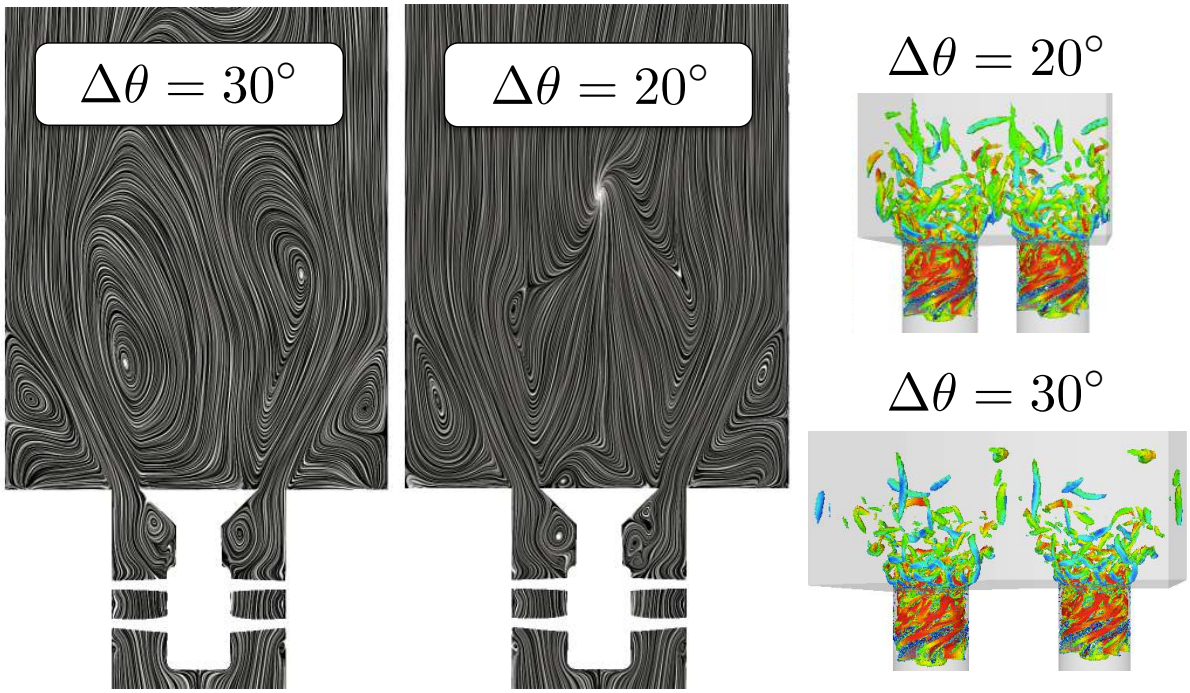

Figure 7.10: LES results: averaged streamlines visualized by Line Integral Convolution (LIC) (Cabral & Leedom, 1993) on the XY-plane (left) and the 3D Q-criterion (right) for the CH4-ADIA-30 ($\Delta\theta = 30°$) and REF ($\Delta\theta = 20°$) cases with no forcing.

On the contrary, taking heat losses into account or changing fuel only has a minor impact on aerodynamics. However, the flame anchoring point is slightly lifted (Fig. 7.11-a, middle) when heat losses are taken into account and the local heat release increases when methane is replaced by ethylene (Fig. 7.11-a, right).

The flame shapes obtained by LES (heat-release fields and iso-contours 20 mm downstream of the bluff-body, Fig. 7.11-b top) with $\Delta\theta = 20°$ and $\Delta\theta = 30°$ are compared to the experimental integrated chemiluminescence results provided by Worth & Dawson (2013*b*) (Fig. 7.11-b, bottom). LES and experiment are in good agreement: the inner flame wrinkling and the outer flame merging are observed in both LES and experiment

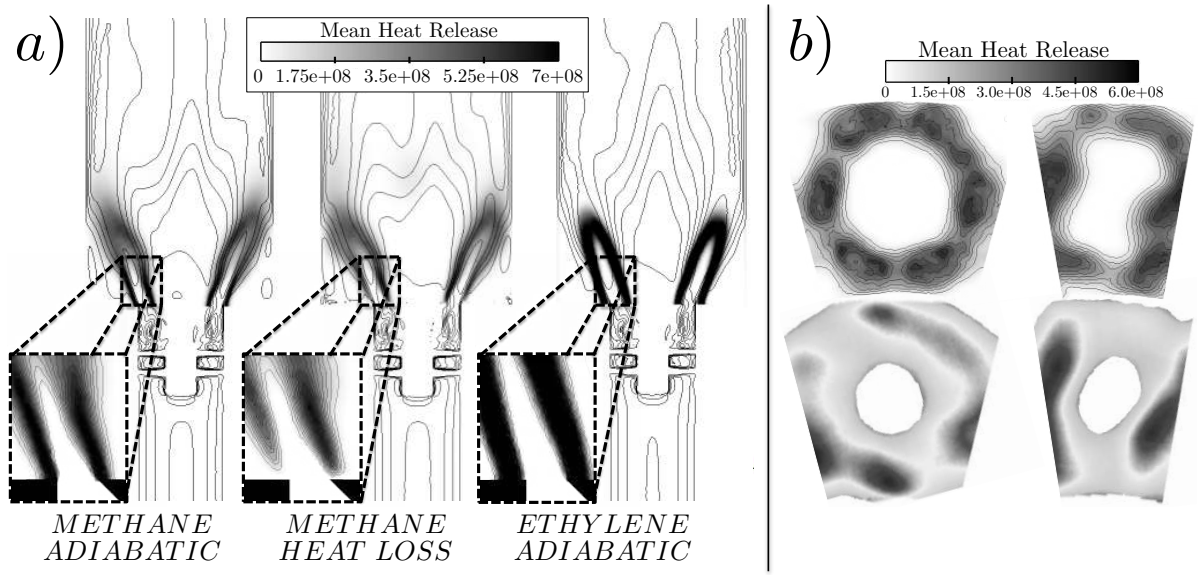

Figure 7.11: a) LES results: XY-cuts of the mean heat release with iso-contours of mean axial velocity for the REF case (left), CH4-HL-20 case (middle) and C2H4-ADIA-20 case (right). Zoom on heat release fields for each flame is provided to highlight the flame anchoring point. b) Comparison between LES heat-release 20 mm downstream of the bluff-body (top) and integrated OH^* measurements (experiment, Worth & Dawson, 2013*b*, bottom) for the case with $N = 12$ (left) and $N = 18$ (right) burners.

in the $\Delta\theta = 20°$ case. Burner/burner interactions clearly appear for $\Delta\theta = 20°$ where the flames are not axisymmetric.

7.5 Phase-averaged forced flow fields

The response of the forced flames at 1800 Hz can be first visualized by the averaged heat release rate at different phase angles of the pressure oscillation: 0° and 180° correspond to a zero acoustic pressure variation at the outflow while 90° and 270° correspond to the maximum and minimum pressure levels respectively. To focus on flame/flame interaction, the visualization domain differs from the single-sector computational domain (Fig. 7.12). As evidenced by Fig. 7.13, flame merging is the main consequence of external forcing for both cases. LES was used to compute the flame response at a frequency $f = 1800\ Hz$. Note that the forcing frequency is fixed and corresponds to the azimuthal frequency observed experimentally. Additional frequencies (1700 Hz and 1900 Hz), upstream/downstream forcing, as well as wave amplitudes (from 0.1% to 1% of the mean pressure) were also investigated and give similar results.

Figure 7.14 shows that the introduction of a model for heat losses strongly modifies the flame shape. Contrarily to adiabatic cases, the flame is lifted, has a weaker outer shear layer flame (Tay-Wo-Chong & Polifke, 2012) and its base oscillates near the injector tip as already evidenced for laminar premixed flames (Kedia *et al.*, 2011). The outer branch oscillates in the axial direction while the inner branch located nearby the bluff-body moves from left to right (—— in Fig. 7.14 displays the minimum and maximum flame

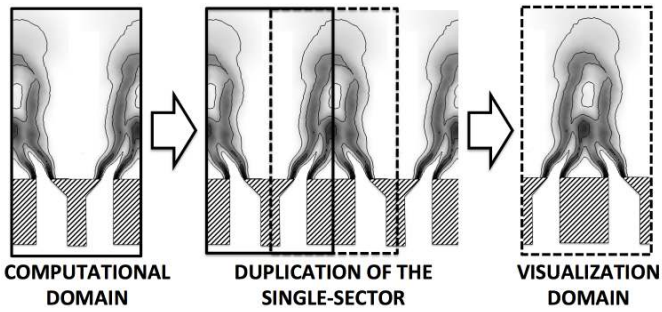

Figure 7.12: Computation domain (left) and visualization domain (right) used to study flame-flame interactions.

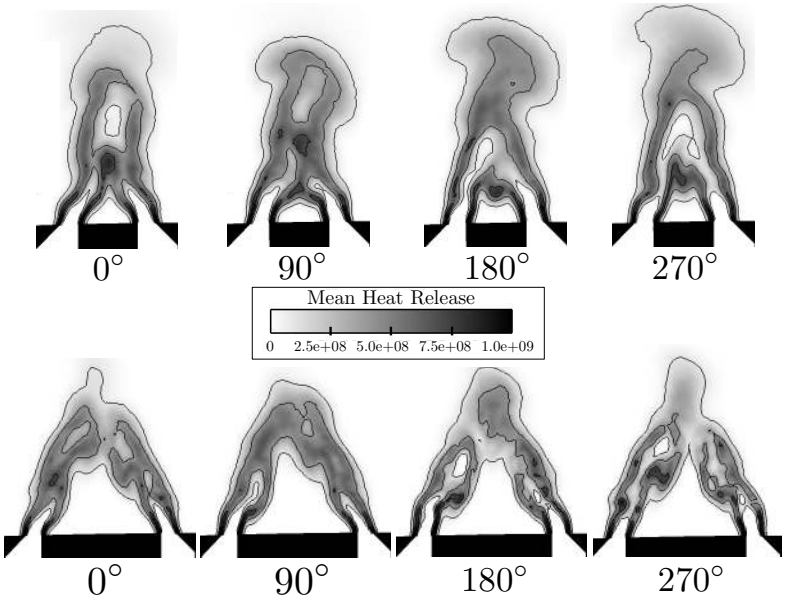

Figure 7.13: XZ-cuts of phase averaged heat release in two consecutive mid injector planes: REF case ($\Delta\theta = 20°$, top) and CH4-ADIA-30 case ($\Delta\theta = 30°$, bottom).

position over the acoustic period).

Replacing methane by ethylene (Tab. 7.1) impacts the flame dynamics (Fig. 7.15). For ethylene (runs C2H4-ADIA-20 and C2H4-ADIA-30), the laminar flame speed ($s^0_{l,\ C_2H_4} \simeq 0.56\ m/s$) and the heat release (as well as the adiabatic temperature $T^{ad}_{C_2H_4} \simeq 2232\ K$) are higher compared to methane ($s^0_{l,\ CH_4} \simeq 0.33\ m/s$ and $T^{ad}_{CH_4} \simeq 2070\ K$) leading to a shorter and more intense flame (Fig. 7.13 for methane and Fig. 7.15 for ethylene). Because of a smaller flame length, ethylene flame merging between neighboring injectors occurs only in the $\Delta\theta = 20°$ case and disappears for $\Delta\theta = 30°$ which is consistent with experimental observations (Worth & Dawson, 2013*b*) (while merging was only weaker for methane with $\Delta\theta = 30°$ compared to $\Delta\theta = 20°$). Note also that due to a higher laminar flame speed, the ethylene flame is less affected by the turbulence than the methane flame, as shown by the resolved wrinkling observed in Figs. 7.13 and 7.15.

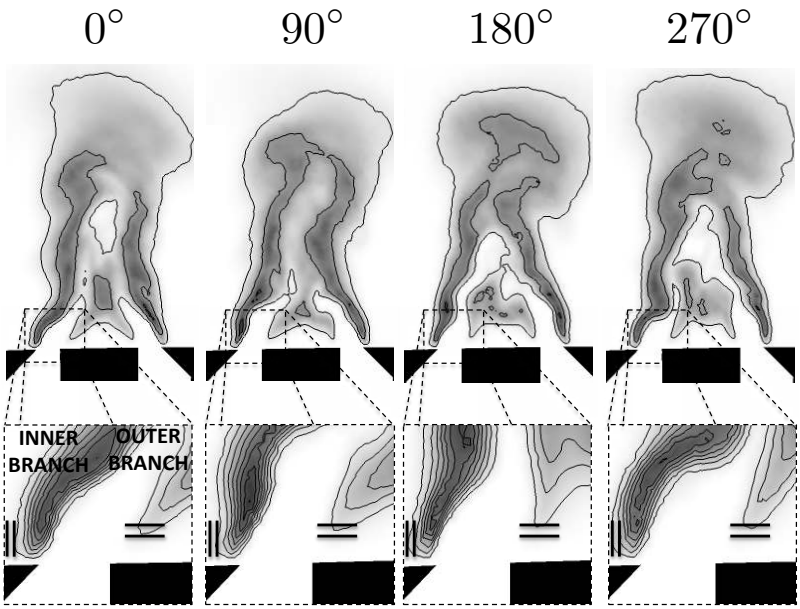

Figure 7.14: XZ-cuts of the phase averaged heat release (same color levels as in Fig. 7.13) for the CH4-HL-20 case (top) complemented by a zoom on the flame base oscillation (bottom). Lines: Minimum/maximum position of the inner and outer flame base.

7.6 Rayleigh criterion

Usually, simple interpretations are proposed to assess the stability of flames. For instance, it is well known that the time-delay of the Flame Transfer Function is crucial to predict combustion instabilities. However, its link with flame quantities is not straightforward. In particular, a direct correlation between the time-delay and the laminar flame speed may be too simple to understand underlying phenomena controlling the stability (heat loss, confinement or even turbulence effects), especially for turbulent non-adiabatic flames affected by flame merging. Therefore, a local criterion should be used to understand which phenomenon is driving the instability. Stability is analyzed here using the Rayleigh criterion to compare methane and ethylene cases. The Rayleigh criterion (R_S) over any surface S is computed from the complex fluctuating pressure ($\hat{p}$) and heat release ($\hat{q}$):

$$R_S = \frac{1}{S}\int_S \|\hat{p}\|\|\hat{q}\|\cos(\Phi_p - \Phi_q)dS \tag{7.2}$$

where $\|\hat{p}\|$ and $\|\hat{q}\|$ are the modulus of the pressure and heat release oscillations and Φ_p and Φ_q are their respective phases. The fluctuating quantities are obtained at the forcing frequency thanks to a Dynamic Mode Decomposition (DMD, Schmid, 2010) of 110 3D snapshots spaced by $\Delta t = 27\mu s$ (corresponding to five periods and a Nyquist cutoff frequency $f_n = 37\ kHz$). Figure 7.16 shows the Rayleigh criterion for the adiabatic methane (top) and ethylene (bottom) cases with $\Delta\theta = 20°$ over three different surfaces. These fields display regions where acoustic-flame interactions occur (grey zones correspond to regions where no flame-acoustic interaction takes place). The modulation of this interaction, from black (negative) to white (positive) is due to the phase between the fluctuating

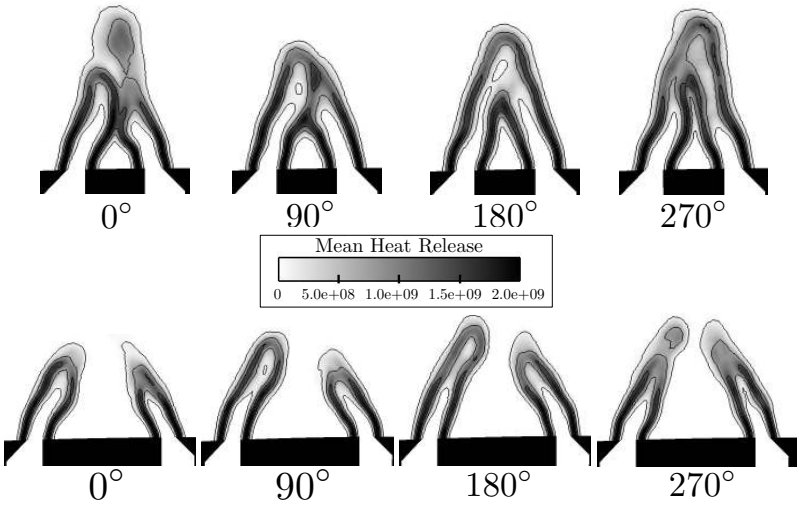

Figure 7.15: XZ-cuts of the phase averaging of the heat release in the C2H4-ADIA-20 case (top) and C2H4-ADIA-30 case (bottom).

pressure and heat release $[\phi_p - \phi_q](\vec{x})$. It clearly shows that even if the flame is compact with respect to the acoustic wavelength (i.e. $\phi_p(\vec{x})$ is almost constant), the local heat release phase $\phi_q(\vec{x})$ (or equivalently the local time-delay $\tau(\vec{x})$) varies strongly due to its convective nature. Consequently, a global criterion based on the volume-averaged time-delay τ is required and sufficient to compute the stability but local phase or time-delays quantities $\tau(\vec{x})$ are necessary to understand which phenomenon is driving the combustion instabilities.

In particular, the YZ-cut (right) highlights the swirler (with 6 blades) effect on stability with a 6^{th}-order azimuthal pattern while the XY and XZ-cuts display the flame-wall (left) and flame-flame (middle) interactions effect. The Rayleigh criterion expressed in Eq. (7.2) corresponds to a volume source (if positive) or sink (if negative) term for the acoustic energy: white zones in Fig. 7.16 promote combustion instabilities while black zones damp them. This local criterion can be integrated: (1) over the whole domain to obtain a global criterion as usually performed when computed a global time-delay or (2) over a small part of the domain to highlight its effect on combustion instabilities: in this work, the Rayleigh criterion is integrated over the XY-cut (left) to focus on flame-wall interaction and over the XZ-cut to focus on flame merging. Results are given in Tab. 7.2 for both methane (top) and ethylene (bottom) cases and show that:

- **Methane case (top):** Integrations of the Rayleigh criterion on both the XY and XZ-cuts of the methane case (top) are negative indicating that regions of flame merging and flame-wall interactions damp the acoustic mode at 1800 Hz.
- **Ethylene case (bottom):** The region of flame merging (along the XZ-cut) is also a sink term for the acoustic energy when using ethylene. However, due to a higher laminar flame speed, the ethylene flame is shorter than the methane flame. In particular, flames do not interact with side walls as observed in Fig. 7.16 (bottom left). The Rayleigh criterion integrated over this direction is positive: compared to the methane case where flame-wall interactions lead to a damping mechanism

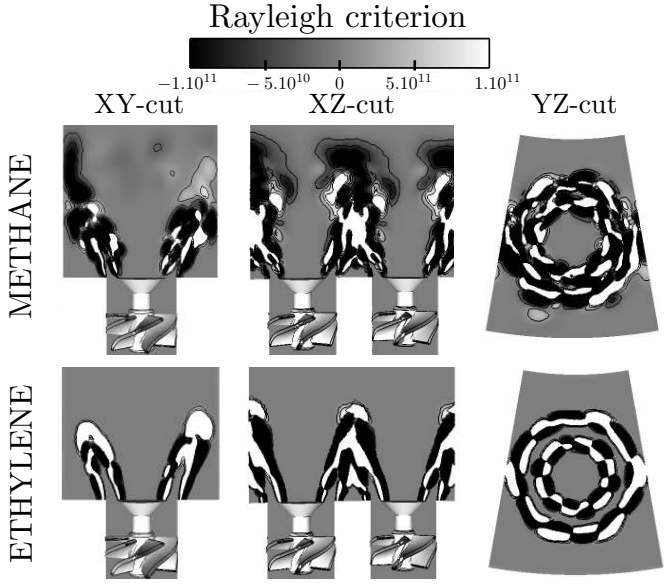

Figure 7.16: Rayleigh criterion constructed from DMD results at 1800 Hz (Eq. (7.2)) over three different surfaces for the adiabatic $\Delta\theta = 20°$ case with methane (top) and ethylene (bottom).

(negative criterion), here the shorter flames avoid flame-wall interaction and are associated to a driving mechanism (positive criterion).

This study shows that local time-delay and Rayleigh criteria are required to describe precisely the local damping or driving mechanisms. Here, the main difference observed between the methane and ethylene cases in both Fig. 7.16 and Tab. 7.2 is the presence or absence of flame-wall interactions along the XY-cut, the only direction in which the Rayleigh criterion goes from negative (damping, methane case) to positive (driving, ethylene case). It suggests that the driving mechanism leading to instabilities when using ethylene is the suppression of flame-wall interaction and not the flame merging. This analysis is in good agreement with experimental observations where changing the flame merging (by changing the azimuthal confinement $\Delta\theta$) had not significant impact on the azimuthal mode occurrence.

CASE	**XY-CUT**	**XZ-CUT**
Methane	$-3270\ W$	$-621\ W$
Ethylene	$+5315\ W$	$-1268\ W$

Table 7.2: Rayleigh criterion (Eq. (7.2)) for the adiabatic $\Delta\theta = 20°$ cases with methane and ethylene over two different surfaces: XY-cut where flame-wall interaction occurs and XZ-cut where flame merging is observed.

7.7 FTF sensitivity study

The sensitivity of FTFs to models (turbulence and combustion) as well as to numerical setups (single/double sectors and coarse/fine meshes) is first evaluated for adiabatic cases with methane and $\Delta\theta = 20°$ (REF, DOUBLE, COLIN, SIGMA and FINE cases in Tab. 7.1, Fig. 7.17). Hatched zones in Fig. 7.17 correspond to the minimum and maximum values of n and τ for these 5 cases. It is a rough indicator of the uncertainty on n and τ due to purely numerical or modeling parameters. Results depend only weakly on modeling parameters for amplitudes n and time-delays τ of the FTF (five first cases in Fig. 7.17): the amplitude n changes from 0.175 to 0.29 while τ varies between 0.29 ms and 0.34 ms.

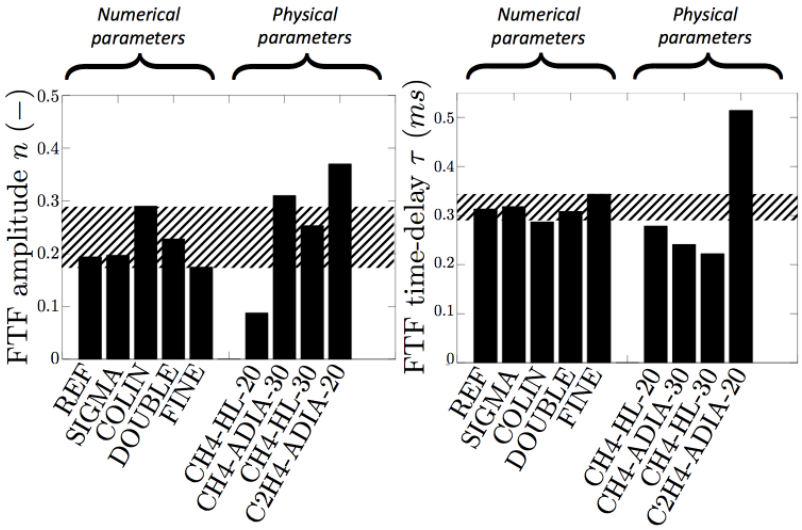

Figure 7.17: FTF amplitudes n and time-delays τ computed by LES for cases of Tab. 7.1.

Thermal, azimuthal confinement ($\Delta\theta = 20°$ or $30°$) and fuel effects were found to have strong impact on unforced (Section 7.4) and forced (Section 7.5) flames. For FTFs, the CH4-HL-20, CH4-ADIA-30, CH4-HL-30 and C2H4-ADIA-20 results (Fig. 7.17) confirm that confinement, thermal and fuel effects are significant compared to uncertainties coming from LES sub-models (hatched zones in Fig. 7.17):

- **Azimuthal confinement:** Using $\Delta\theta = 30°$ instead of 20° modifies the flow topology (Fig. 7.10) and affects flame merging (Fig. 7.13) which leads to a significant amplification of the acoustic/combustion interactions (the amplitude of the FTF n increases) and a shorter flame response (the time-delay τ decreases).
- **Thermal effect:** Including heat-losses modifies the flame shape and introduces flame base oscillations (Fig. 7.14) which are not present for adiabatic LES: both the FTF amplitude n and time-delay τ decrease. This behavior is consistent with other studies on longitudinal configurations (Tay-Wo-Chong & Polifke, 2012; Mejia *et al.*, 2014).
- **Fuel effect:** Methane and ethylene lead to completely different flame responses. The delay with C_2H_4 increases to 0.51 ms compared to about 0.3 ms for CH_4, everything else being equal. It is interesting to see that ethylene flame has a

longer time-delay even though it has a higher laminar flame speed. This shows that kinetics is not the only important factor here: flame-wall interactions, flame merging, heat losses or turbulent combustion effects are more important.

In conclusion, results of Fig. 7.17 allows to: (1) evaluate uncertainties due to numerical and physical parameters on n and τ to be used for UQ studies (Chapter 5) and (2) show that the effects of changes such as fuel or heat release are larger than the effects introduced by uncertainties on numerical parameters.

7.8 Effect of FTF uncertainties on stability of azimuthal modes

Variabilities in FTF numerical estimations have been clearly identified but their impact on the burner stability predictions is not yet evidenced. Helmholtz simulations are now performed using computed FTF to investigate the global stability of the 360° configuration (Fig. 7.9). Stability maps relying on the growth rate $Im(f)$ function of the time-delay τ (varying from 0 to $\tau_c^0 = 1/1800 \simeq 0.55\ ms$) are first computed for two baseline cases corresponding to the annular rig equipped with $N = 12$ burners ($\Delta\theta = 30°$) or 18 burners ($\Delta\theta = 20°$) and using $n = 0.25$ (estimation of an adiabatic case with methane, Fig. 7.17).

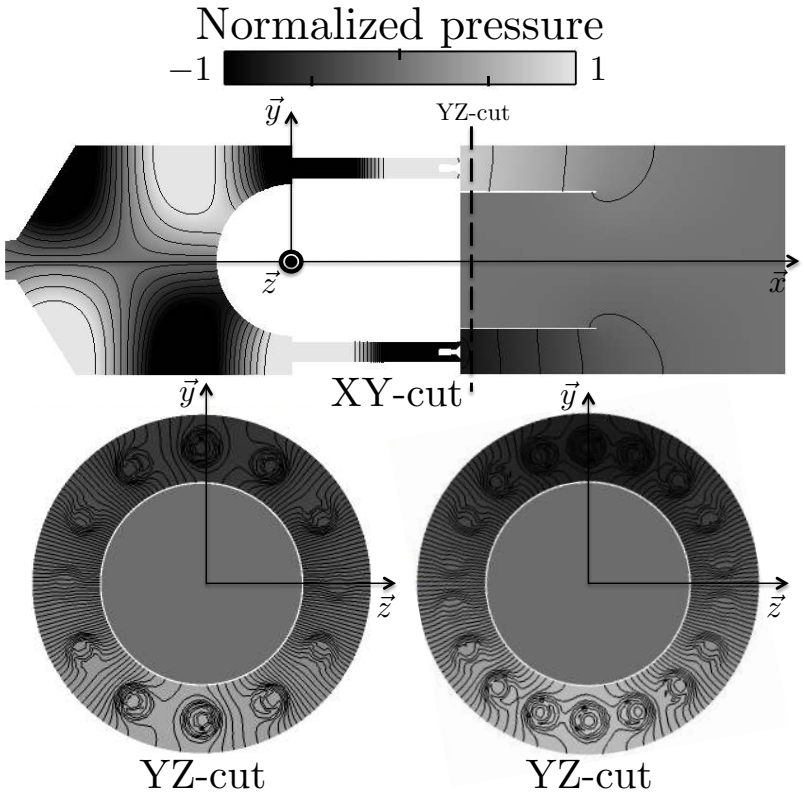

Figure 7.18: Mode structure (here $\|p'\|\cos(\phi)$) of the azimuthal mode at $f \simeq 1800$ Hz: XY-cut (top) and YZ-cuts (bottom) for both the $N = 12$ (left) and $N = 18$ (right) configurations.

The mode structure (*i.e.* $\|p'\|\cos(\phi)$ where $\phi = arg(p')$) of the azimuthal mode at $f \simeq 1800\ Hz$ obtained with AVSP (Fig. 7.18, top) involves both the annular plenum as well as the annular chamber. A longitudinal acoustic component is observed in the chamber because of pressure fluctuations are zero at the chamber outlet. YZ-cuts of the $N = 12$ and 18 burner cases (Fig. 7.9, bottom) underline the differences introduced in the acoustic mode due to the number of burners as well as to the FTF.

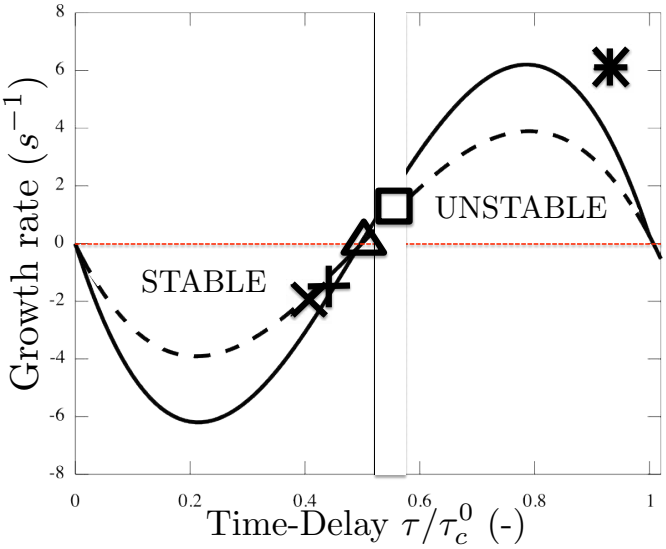

Figure 7.19: Stability maps of the $N = 12$ (---) and $N = 18$ (——) configurations obtained with the FTF amplitude $n = 0.25$ and a time-delay varying from 0 ms to $\tau_c^0 = 0.55$ ms. Growth rates of specific cases are also displayed: □: REF case, △: CH4-HL-20, +: CH4-ADIA-30, ×: CH4-HL-30 and ⋆: C2H4-ADIA-20. The hatched zone corresponds to the uncertainty on the time-delay due to LES sub models (Fig. 7.17)

Figure 7.19 shows the stability maps of the two baseline cases (--- : $N = 12$ and —— : $N = 18$ burner configurations) versus FTF time-delay τ, computed first with $n = 0.25$ (corresponding to an adiabatic case with methane). Results confirm that the azimuthal confinement modifies the acoustic domain leading to different growth rates, everything else being equal: using the same burner characteristics and FTF inputs, the 12 burner case generates lower flame/acoustic perturbations than the 18 burner case (Fig. 7.18 bottom).

Finally, the growth rate of the five distinct cases of interest are displayed on the stability map of Fig. 7.19 (□: REF case, △: CH4-HL-18, +: CH4-ADIA-12, ×: CH4-HL-12 and ⋆: C2H4-ADIA-18): thermal and fuel effects have a significant impact on the overall stability compared to uncertainties due to LES sub-models (hatched zone in Fig. 7.19). Results demonstrate the LES capability to predict FTF accurately and to provide useful results when FTFs are injected in Helmholtz codes: based on the FTFs of Fig. 7.17, the Helmholtz solver predicts correctly that almost all methane cases are stable and adding heat-losses stabilizes (in these cases) the annular rig. Using ethylene leads to a positive growth corresponding also to an unstable configuration. These results are consistent with experimental observations where methane leads only to longitudinal

instabilities while ethylene produces azimuthal instabilities (Worth & Dawson, 2013*b*).

7.9 Conclusion

This chapter describes a sensitivity analysis of the stability of a full annular academic configuration installed in Cambridge. It is based on forced compressible LES of a single (or double) sector computing FTFs which quantify the interaction between acoustics and the turbulent swirled flames. First, effects of different azimuthal confinements (corresponding to the annular chamber equipped with 12 or 18 burners), thermal boundary conditions (adiabatic or with heat losses) or fuels (methane or ethylene) have been investigated and compared to uncertainties on the FTF introduced by LES sub models. Phase-averaged heat release fields and FTF computations show that confinement, thermal and fuel effects are essential and affect the flame shape as well as their dynamics. The local Rayleigh criterion is obtained via a Dynamic Mode Decomposition highlighting which phenomenon is driving the instability: flame-flame (or flame merging) is not the key feature leading to instabilities, but flame-wall interaction does modify the FTF significantly. Then global FTFs computed by LES are used as inputs for an acoustic solver to evaluate the effect of FTF uncertainties on the stability of azimuthal modes in the 360° configuration. Results show that modeling issues inherent to LES models lead to marginal uncertainties on FTF while azimuthal confinement, thermal conditions and fuel type strongly affect the flame response to acoustics and control the stability of the azimuthal mode. In particular, Helmholtz computations show that the annular configuration performed with methane should be stable while ethylene should lead to unstable modes as observed in the real experiment. Thus, an operating point (ethylene, $N = 18$, adiabatic) is chosen to be computed on the full 360° configuration to obtain a self-excited azimuthal mode as discussed in the next chapter.

Chapter 8

LES of self-excited azimuthal modes in a full 360° configuration

Contents

This chapter focuses on the LES of the full 360° configuration of the experiment of Worth & Dawson (2013b). An operating point (ethylene, N=18 burners, adiabatic) is chosen according to the sensitivity analysis in Chapter 7. Here, a self-excited mode appears and is compared to experimental results provided by Cambridge. Experimental and numerical data have been post-processed during this PhD with the same post-processing methods to ensure a proper comparison. Results show that LES is able to capture a self-excited azimuthal mode at 1800 Hz as in the experiment. However, due to the long establishment of the mode and the extreme cost of 360° LES, only the growth phase is computed while the experiment is able to characterize the limit cycle reached after thousands periods. The numerical study of the establishment of the self-excited mode reveals that it is accompanied, as in the experiment, by longitudinal modes which are due to the start-up procedure and then decrease in time, while the self-excited azimuthal mode is emerging.

8.1 Introduction

Improvement of numerical techniques and the access to powerful supercomputer have allowed the first LES of a thermoacoustic mode of a full 360° industrial combustion chamber in 2010 (Wolf *et al.*, 2010). However, a comparison between 360° simulation and experiment as well as the study of how such a mode appears and grows until its limit cycle is still missing and is the topic of this chapter. While Chapter 7 focused on forced-modes using single or double sector LES with non-reflecting boundary conditions, this chapter targets the full annular rig with realistic inlet/outlet impedances. The annular configuration equipped with $N = 18$ burners, an annular chamber and a large atmosphere exhaust zone is computed by LES in Section 8.3. First, the experimental 360° mean flame shape measurement is compared to integrated heat-release pictures showing a very good agreement. In particular, flame merging already observed in Chapter 7 when $N = 18$ burners are distributed in the chamber leads to specific patterns on the 360° mean flame shape in both experiment and numerical results. A self-excited azimuthal mode appears in the LES at 1800 Hz as in the experiment but accompanied with a 500 Hz mode due to the start-up procedure. For a better comparison, both experimental and numerical data are analyzed with the same post-processing tool and show good agreement. The construction of the experimental spectrogram allows the analysis of the time-evolution of the longitudinal and azimuthal modes. Then the mode structure is characterized in Section 8.4.1 using both FFT (Fast-Fourier Transform) and DMD (Dynamic Mode Decomposition), the two different tools showing that the computed self-excited mode is globally standing. Section 8.4.2 presents a method called JAWA (Joint probability distribution for Azimuthal Waves Analysis) to study time-evolution and probability of azimuthal mode structures in LES. This tool shows that the azimuthal mode in the LES is highly perturbed although mainly standing during the growth phase. Experimental data are investigated using the same methodology showing that the azimuthal mode is mainly standing during the start-up phase before switching to a clockwise spinning mode in the

limit cycle. This analysis shows a good agreement between numerical and experimental data for the start-up phase. It proves that LES is a promising tool to investigate the growth, nature and dynamics of azimuthal modes, a necessary step to understand how they arise and how to control them.

8.2 Numerical setup

In this chapter, the full 360° configuration of the Cambridge experiment detailed in Chapter 7 is investigated. The computational domain includes $N = 18$ burners with an axial swirler composed of six blades mounted on a bluff-body (Fig. 8.1). Combustion takes place in the annular chamber with different wall lengths as in the experiment and a large atmosphere is added to impose properly the outlet impedance of the combustor. The mesh is fully unstructured and contain 110 millions cells, corresponding to a duplication of the "coarse" mesh used in the previous chapter which was proved to accurately predict FTFs. This results in typical thickening factors of 3 to 5 in the flame zone to guarantee $5 - 10$ points in the flame. Cells lengths are typically $150\mu m$ near swirler walls and $150\mu m - 300\mu m$ in the swirler passages.

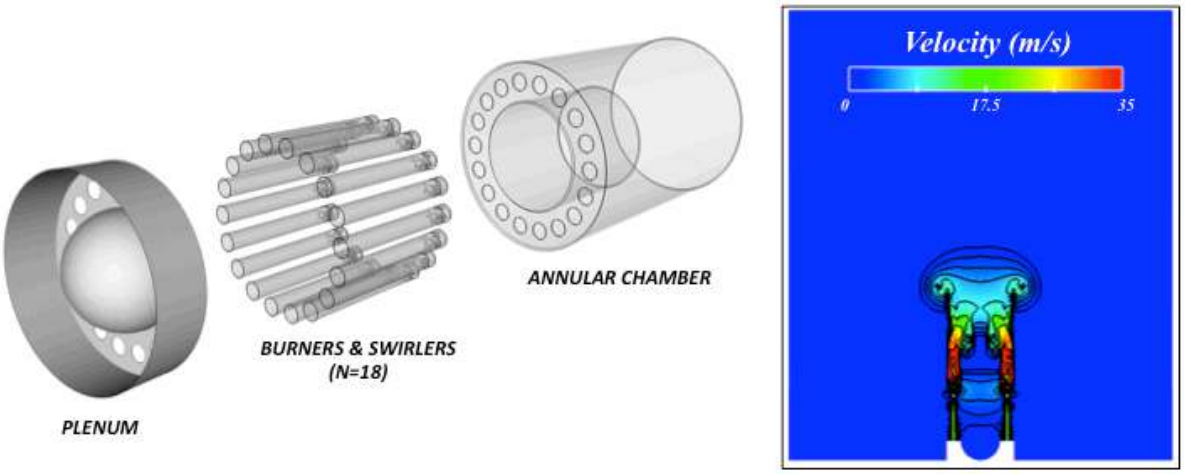

Figure 8.1: 360° LES configuration with the plenum exit, the $N = 18$ burners and the annular chamber with different wall lengths (left). The annular rig is displayed in the large atmosphere exhaust zone (right).

AVBP (Chapter 6) is used here to solve the filtered multi-species 3D Navier-Stokes equations with realistic thermochemistry on the configuration of Fig. 8.1. Based on the experiments (Worth & Dawson, 2013*b*) and the sensitivity analysis performed in Chapter 7, azimuthal modes are expected to be unstable only when using ethylene. Consequently, a perfectly premixed air-ethylene mixture at the equivalence ratio $\phi = 0.85$ is injected at the inlet (plenum/burner section). Reaction rates are modeled with a reduced kinetic scheme containing 2 steps and 6 species (Eq. (8.1)), which have been proved to accurately

reproduce low frequency flame dynamics (Kedia *et al.*, 2011):

$$\begin{cases} C_2H_4 + 2O_2 \Rightarrow 2CO_2 + 2H_2O \\ CO + \frac{1}{2}O_2 \Leftrightarrow CO_2 \end{cases} \tag{8.1}$$

Transport properties (constant Prandtl and Schmidt numbers) have been validated in Chapter 6 using Cantera and AVBP to compute DNS of 1D laminar ethylene/air flames. Numerics is based on a two-step Taylor-Galerkin finite element scheme of third-order in space and time (TTGC, Moureau *et al.*, 2005) to accurately propagate acoustic waves. Chapter 7 shows that, for this configuration, turbulent and combustion models yield minor uncertainties on the flame-acoustics interaction. For this study, the Wale (Nicoud & Ducros, 1999) model has been used and turbulent-flame interactions are addressed using the dynamic Thickened Flame (TF) approach with the efficiency function described by Charlette et al. (Charlette *et al.*, 2002). Boundary conditions use the NSCBC approach (Poinsot *et al.*, 1992). As in the previous section, the plenum cavity has been replaced by an equivalent reflection coefficient measured experimentally ($R \simeq 0.1$ corresponding almost to a non-reflecting condition) and adjusted using the relax coefficient of the NSCBC boundary condition (Selle *et al.*, 2004*b*). Adiabatic temperatures ($T_{ad} \approx 2230K$) and laminar flame speeds ($s_L^0 \approx 0.56\ ms^{-1}$) have been compared to the UCSD full scheme (UCSD, 2013) and show a good agreement. Thermal effects have been neglected (Chapter 7) and walls are treated as non-slip and adiabatic.

8.3 Growth of a self-excited azimuthal mode

8.3.1 Validation of the mean flame shape

Chapter 7 has proved that single sector LES was able to reproduce experimental behavior such as the flame length, the effect of fuel on the stability of azimuthal modes as well as flame merging between neighboring burners. Before analyzing acoustic modes present in the LES, an additional validation of the 360° computation is provided in Fig. 8.2. The flame merging mechanisms observed experimentally between neighboring burners yields a specific pattern on the experimental integrated OH^* measurements, where the rotating symmetry of the flame is broken which enhances combustion between burners (Fig. 8.2, left). The full 360° LES simulation has been post-processed by integrating the mean heat-release in the axial direction (Fig. 8.2, right) and shows a similar pattern. This proves that qualitative experimental results are well reproduced by the full 360° LES even though detailed velocity or species measurements would clearly be required to pursue this comparison.

8.3.2 A self-excited azimuthal mode at 1800 Hz

Self-excited pressure oscillations appear in the annular combustor in both LES and experiment (Worth & Dawson, 2013*b*,*a*) and can be compared. This chapter focuses on

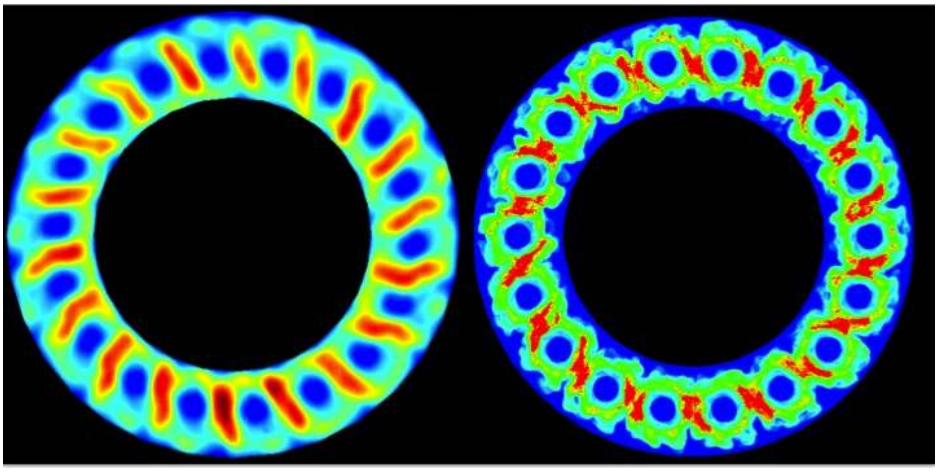

Figure 8.2: Comparison of the integrated mean OH^* in the experiment (left) and heat-release in the LES (right). Typical patterns due to the flame merging are observed both in experiment and simulation.

the start-up phase in which the azimuthal mode is growing. Note however that the experiment and LES are ignited differently:

- **Experiment:** First, the cold reactant flow rate is set to 18 m/s at the bluff body exit with $\Phi = 0.60$ and then is ignited giving a stable flames. The equivalence ratio is then switched to $\Phi = 0.85$ to obtain an unstable azimuthal mode.
- **LES:** A reacting stabilized single-sector simulation (with non-reflecting boundary conditions) is duplicated to obtain a 360° configuration and initial solution. Then a large atmosphere is brutally added to the configuration to impose a pressure node at the chamber outlet and trigger instabilities.

First, the experimental time-series and spectra of the fluctuating pressure (in the chamber) are displayed in Fig. 8.3 for three different signal durations $\Delta t = 800\ ms$ (top), 100 ms (middle) and 10 ms (bottom). The long signal (top) shows that a pure azimuthal limit cycle at 1800 Hz is established after hundred milliseconds. Zooming on the same pressure signal (middle and bottom images) reveals that the azimuthal growth phase is accompanied by longitudinal modes at 500 Hz, 1000 Hz and 1500 Hz which are decreasing in time. They are probably due to the experimental ignition procedure. It also suggests that LES, limited to short signals because of its cost, cannot easily predict the limit cycle of this configuration occurring after hundreds milliseconds. However LES can be used to investigate the growth phase which is the main topic of this chapter. A new methodology called AMT will be presented in Chapter 9 to study limit cycles using 360° LES.

Experimental time-series and spectra are compared to LES predictions in Fig. 8.4. Experimental data provided by Worth & Dawson (2013*b*) are sampled at 30 kHz giving $262,144$ samples over a duration of $10s$. On the other hand LES provides short pressure signals ($25ms$ long) sampled at 40 kHz and requiring a bandpass filtering around 1800 Hz. Consequently for a proper comparison between experiment and LES, the same filtering is applied on the experimental data provided in Fig. 8.3 with the same signal duration ($\Delta t = 25\ ms$ leading to $\Delta f = 40\ Hz$). The resulting filtered pressure signals and

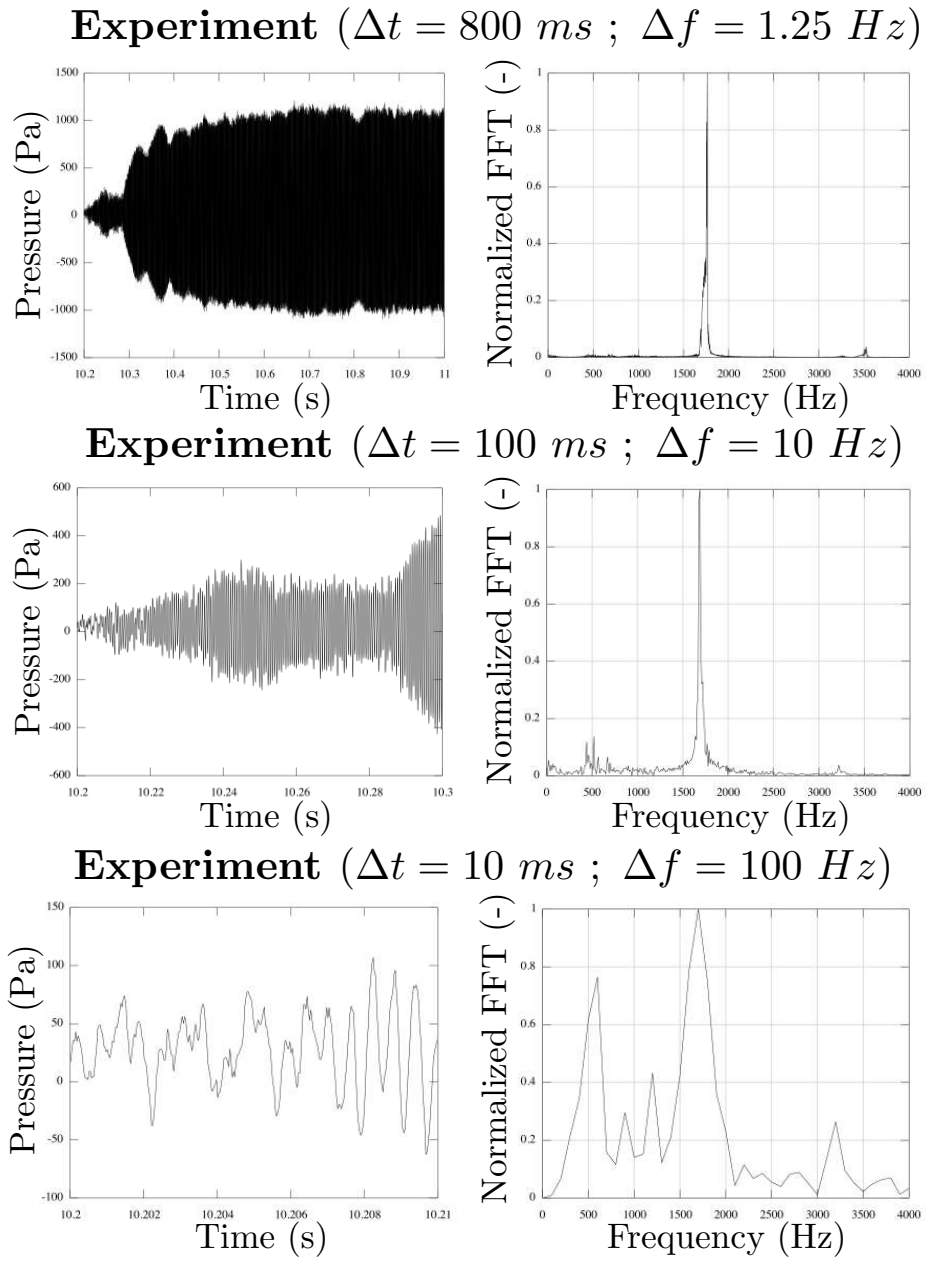

Figure 8.3: Time-series (left) and FFT (right) of experimental measurements provided by Worth & Dawson (2013*b*) from the start-up ($t = t_0$) to $t = t_0 + \Delta t$ where $\Delta t = 800\ ms$ (top), $100\ ms$ (middle) and $10\ ms$ (bottom) with the associated frequency resolution Δf.

spectra are shown in Fig. 8.4 showing that both experiment and LES are unstable. As observed previously, the unstable mode at $f = 1800\ Hz$ in the experiment is accompanied by a strong mode at $500\ Hz$ and a weaker harmonic at $3600\ Hz$. In the LES the mode at $f = 1800\ Hz$ is weaker compared to the other modes although its amplitude (a plateau at about $\pm 200\ Pa$) is larger than the experimental one ($\pm 100\ Pa$ at $t = t_0 + 25\ ms$). A similar plateau at $200\ Pa$ is observed in the experiment (Fig. 8.3, top and middle) but latter after the ignition procedure (from $t = t_0 + 40\ ms$ to $t = t_0 + 90\ ms$). This delay

can be due to the difference between the LES and experiment start-up procedures or by too low numerical acoustic dissipations (no volume viscosity, no heat losses, etc.).

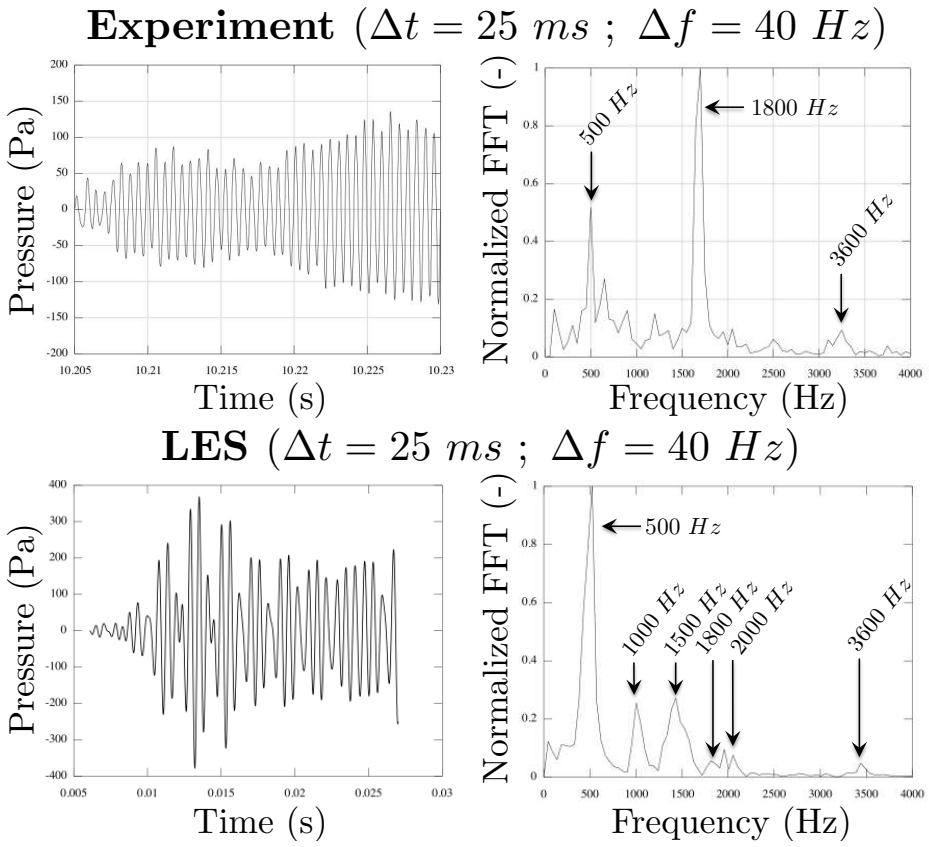

Figure 8.4: Filtered time-series around 1800 Hz (left) and FFT before the filtering (right) of pressure in the chamber from experimental measurements (top) and LES (bottom).

A summary of the time-evolution of the acoustic modes identified in Figs. 8.3 and 8.4 is given by the experimental spectrogram of Fig. 8.5 obtained using multiple FFTs with a resolution $\Delta f = 29\ Hz$ and $\Delta t = 8\ ms$. It shows the evolution of the three main modes observed in Fig. 8.3: the longitudinal mode at 500 Hz and the azimuthal mode at 1800 Hz and 3600 Hz. Dotted lines correspond to the LES and experiment start-up, the end of the transient phase (TP) and the end of the experiment respectively. The end of the LES is displayed by the dashed line, only $\Delta t = 25\ ms$ after the start-up showing that short LES cannot investigate the limit cycle in this case. It is also interesting to note that the 500 Hz and the 1800 Hz modes first appear, as in the LES (Fig. 8.4, bottom). The linear frequency drift observed on the azimuthal mode is due to the temperature increase induced by the combustion ignition. The longitudinal mode at 500 Hz is progressively phased-out while the azimuthal mode is growing. The second order azimuthal mode at 3600 Hz appears one second after the start-up either because (1) it requires a high temperature to exist or (2) because it is non-linearly triggered by the first order azimuthal mode at 1800 Hz or (3) because the combustion chamber is not a pure harmonic oscillator and therefore the 3600 Hz component is a non-linear harmonic

of the first azimuthal mode.

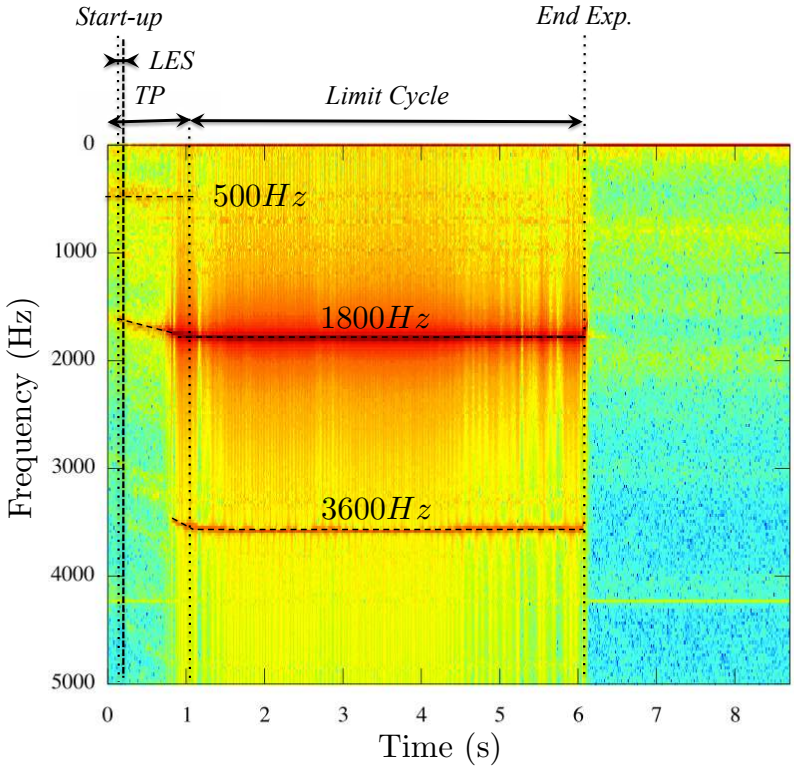

Figure 8.5: Experimental spectrogram obtained from multiple FFTs with a resolution $\Delta f = 29\ Hz$ and $\Delta t = 8\ ms$. It shows the evolution of the three main modes observed in Fig. 8.3: the longitudinal mode at 500 Hz and the azimuthal mode at 1800 Hz and 3600 Hz. Dotted lines correspond to the LES and experiment start-up, the end of the transient phase (TP) and the end of the experiment. The end of the LES is shown by the dashed line, only $\Delta t = 25\ ms$ after the start-up.

Finally, Fig. 8.6 shows several cuts of the instantaneous LES pressure field in the chamber at $\Delta t = 20\ ms$ after the start-up as well as iso-surface of heat release highlighting the flame merging between neighboring sectors. It shows the instantenous azimuthal structure of the acoustic mode observed at 1800 Hz and demonstrates that for the first time LES is able to capture azimuthal thermo-acoustic modes in an academic configuration with an open atmosphere, a complex boundary condition which requires the computation of a large atmosphere (Fig. 8.1, right). This 25ms-long LES has cost $1,500,000$ CPu hours on the GENCI supercomputer Turing with $8,196$ processors. Computing the full initialization phase ($1s$) would cost 60 millions CPu hours. Even though this is feasible today on Prace or Incite machine, an alternative solution to study limit cycles will be proposed in Chapter 9.

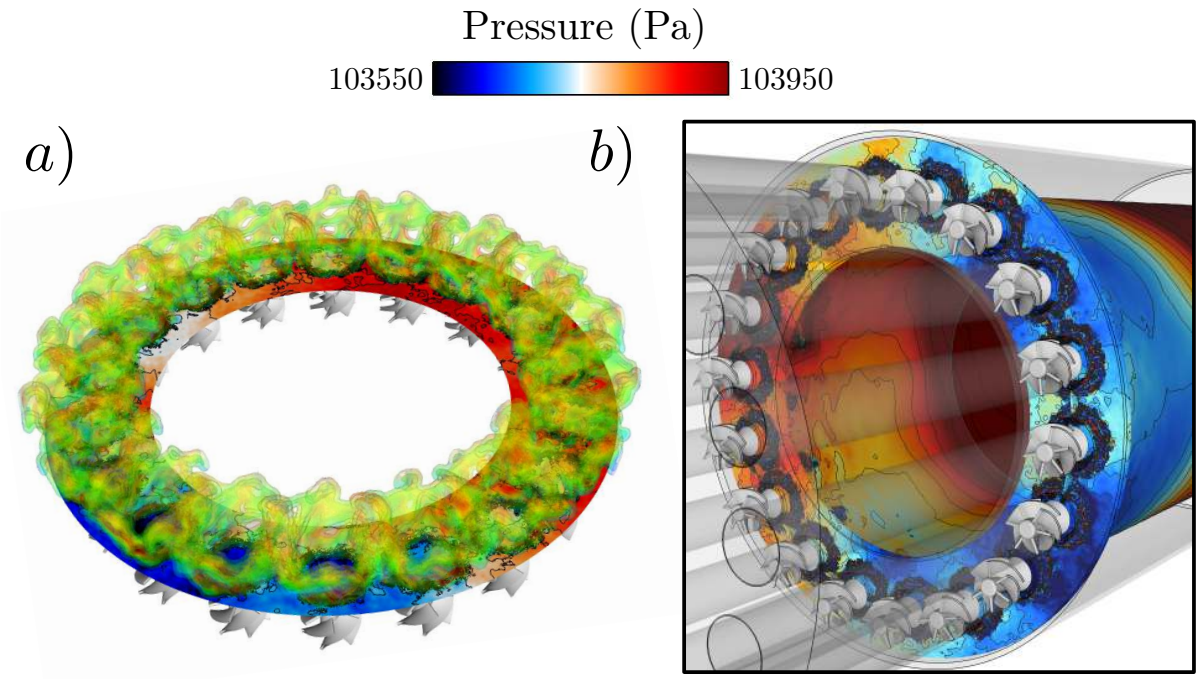

Figure 8.6: a) Transverse cut of the full 360° configuration highlighting the azimuthal pressure and iso-surfaces of heat release showing the flame merging between neighboring burners. b) Transverse and cylinder cuts showing the azimuthal and longitudinal components of the acoustic mode at $f = 1800\ Hz$.

8.4 Structure of the thermo-acoustic modes during the initial phase

8.4.1 Fluctuating pressure fields analysis

To investigate the inner structure and frequency associated to the azimuthal pressure fluctuations observed numerically and experimentally, post-processing tools are performed using Fast Fourier Transform (Fig 8.7, right) on each node of the computational domain and Dynamic Mode Decomposition (Fig 8.7, left) recently proposed by Schmid (2010). These tools provide the modulus $\|\hat{p}\|$ and the phase $\arg(\hat{p})$ of all modes which are then reconstructed:

$$p' = \|\hat{p}\| \cos(\arg(\hat{p}) \tag{8.2}$$

Here, the phase is constant ($\arg(\hat{p}) = 0$ or π, not shown here) which reveals that the mode is standing. As expected, the FFT suffers from a low frequency resolution ($\Delta f = \frac{1}{\Delta t} = 100\ Hz$) because of the limited computational time available: only $\Delta t = 10\ ms$ of simulation has been used here to concentrate on the plateau at $\pm 200\ Pa$. On the other hand DMD provides an accurate estimation of the frequency $f = 1800\ Hz$ as observed in the experiment (Fig. 8.3). Therefore, DMD has been also applied to the other modes present in LES as shown in the pressure signal analysis of Fig. 8.4: a longitudinal mode at 500 Hz and the second azimuthal mode combined with a half-wave longitudinal mode at 3600 Hz.

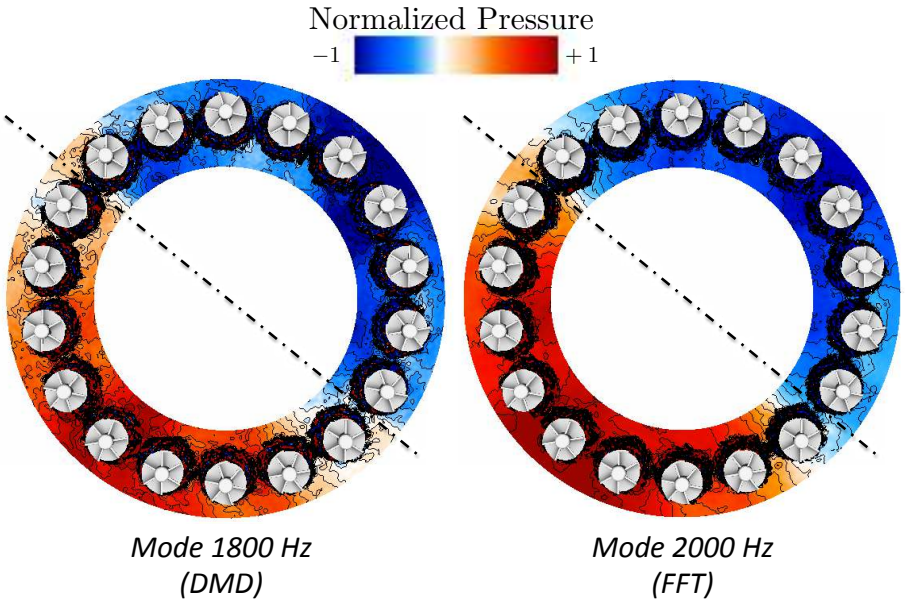

Figure 8.7: Comparison between the azimuthal mode obtained by the Dynamic Mode Decomposition (DMD, left) and Fast Fourier Transform (FFT, right) of the pressure field. the FFT suffers from a low frequency resolution due to the limited time of the LES.

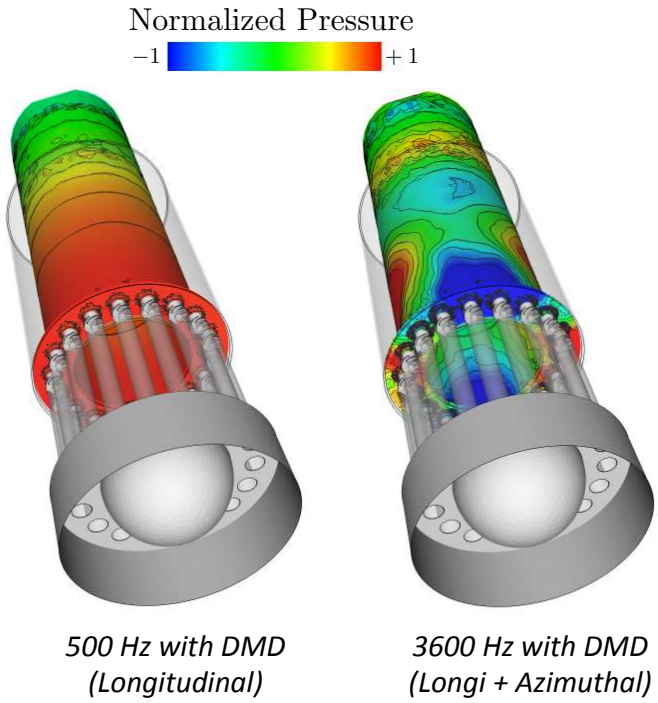

Figure 8.8: The two modes obtained by the Dynamics Mode Decomposition of the pressure field in the full annular LES: the longitudinal 500 Hz mode and the second azimuthal mode combined with a half-wave longitudinal mode at 3600 Hz.

8.4.2 Mode structure and dynamics

The previous section has shown mode structures obtained by FFT or DMD highlighting the global characteristics of the acoustic modes observed in the pressure signal analysis. An additional result of the FTF and DMD tools are the pressure phase which reveals the mode nature: here, the phase is constant ($\arg(\hat{p}) = 0$ or π, not shown here) which implies that the mode is standing. However, such diagnosis is not able to provide information on the mode dynamics and the evolution of its nature (standing, spinning or mixed) with time. Consequently, a five-step methodology is proposed here, called JAWA (Joint probability distribution for Azimuthal Waves Analysis), to analyze simultaneously both the dynamics and the structure evolution of the azimuthal modes:

- **Step 1:** The fluctuating pressure (p') and azimuthal velocity (u'_θ) are extracted from LES results at 4 different locations (Fig. 8.9). These fluctuations are then filtered around 1800 Hz to retain only the first azimuthal mode of the configuration.
- **Step 2:** The two propagating waves are constructed: $q^{\pm}(t) = p'(t) \pm \rho_0 c_0 u'_\theta(t) = A^{\pm}\cos(\omega t)$.
- **Step 3:** The envelopes of these two waves are obtained using the Hilbert transform[1] which gives their respective amplitude called A^+ and A^- (with a low frequency filtering to remove spurious oscillations).
- **Step 4:** The ratio of these amplitude waves A^+/A^-, or more conveniently the index $\alpha(t) = \frac{A^+ - A^-}{A^+ + A^-}$ proposed by EM2C group (Bourgouin, 2014) is computed.
- **Step 5:** Probability density function of $\alpha(t)$ can be computed. Moreover, a 3D shape of the Joint Probability Distribution (A^+, A^-) can be also extracted highlighting the evolution of both the growth and the nature of the acoustic mode. The joint probability distribution (JPD) is computed using a KDE technique (Kernel Density Estimation, detailed in Appendix G) to obtain highly resolved maps from short LES signals[2] of the mode structure in the plane (A^+, A^-).

The JAWA methodology is applied on the four probes P_1 to P_4 displayed in Fig. 8.9 (left) and provides the PDF of the spin ratio α (Bourgouin, 2014) (Fig. 8.9, right). Results show that, as obtained using the FFT and DMD tools, the mode is mainly standing (the mean spin ratio being $\mu_a = 0.03$) during the growth phase computed by LES. An Additional information is however provided compared to the previous tools. In particular, even if the mean state is standing, results show that the acoustic mode is not purely standing but mixed ($\|\alpha\| \simeq 0.5$ with $\sigma_a = 0.20$). However, no pure spinning azimuthal modes ($\|\alpha\| \simeq 1$) are observed.

The PDF of the spin ratio generated by the JAWA methodology is a useful information to analyze the azimuthal mode nature since it provides not only the mean state but its complete distribution (Fig. 8.9, right). In the LES, the azimuthal mode is mainly standing (the mean value of the spin ratio is μ_α) but with high perturbations (the standard

[1] Consider a signal $s(t)$ varying in time. The Hilbert transform of s is $\mathcal{H}(s) = \frac{1}{\pi t} \star s(t)$, where $\star$ designates the convolution product. The signal envelop is then defined as $\mathcal{E}_s(t) = \sqrt{s(t)^2 + \mathcal{H}(s)(t)^2}$.

[2] Unlike classical histograms, KDE provides a resolution which is independent of the number of samples. When the number of samples is limited, as in data extracted from short LES, this technique makes high resolved PDF or JPD possible. More detailed about KDE are given in Appendix G.

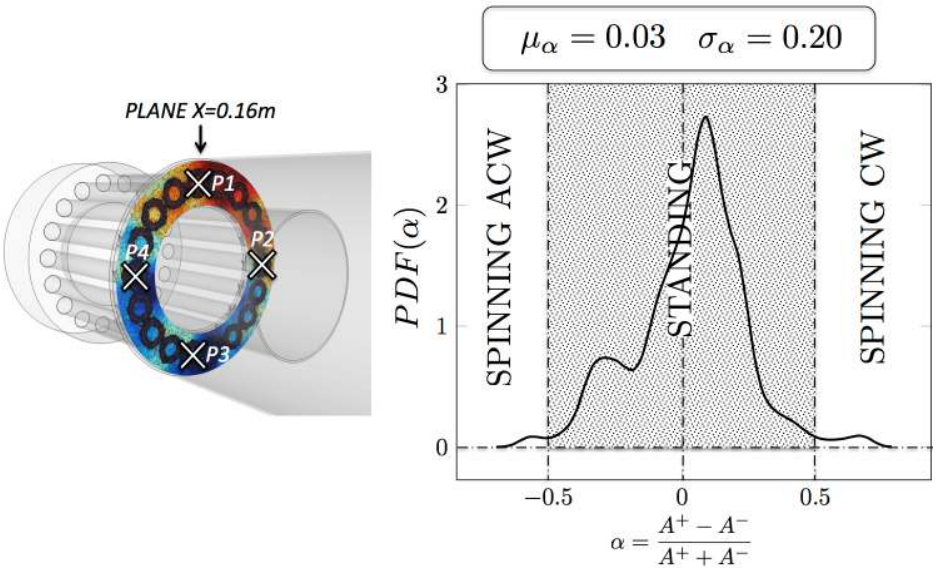

Figure 8.9: The four probes locations where acoustic pressure and velocity are extracted (left) and PDF estimation of the spin ratio α (Bourgouin, 2014) produced by JAWA. It shows that the azimuthal mode is mainly standing (mean value $\mu_\alpha = 0.03$) but with high perturbations (start deviation $\sigma_\alpha = 0.20$) and that no pure spinning modes occur during the growth phase computed by LES.

deviation is $\sigma_\alpha = 0.20$) as shown in Fig. 8.10 (right). The dynamic evolution of the mode structure with time is provided in Fig. 8.10 (left), the question to be answered being: how does the mode structure evolve during the transient phase ? The results show that the standing mode predicted by FFT and DMD tools is not steady but varies dynamically in time (Fig. 8.10, left). An additional information is obtained from the joint probability distribution (A^+, A^-). Indeed, the amplitude of the two waves A^+ and A^- are retained, while in the spin ratio only their respective strength is measured. Figure 8.10 (right) shows iso-contours of the Joint Probability Distribution computed by JAWA. This result indicates that the azimuthal mode is mainly standing during its growth phase but is also highly perturbed, from a standing to a mixed mode. No pure spinning modes occur in this case but the mode structure is slightly growing on the clockwise side (also observed in Fig. 8.9), suggesting that rotating modes might appear in the limit cycle as mentioned by Noiray *et al.* (2011) or can be due to a swirler effect (Worth & Dawson, 2013*b*).

The experimental data given in Fig. 8.3 are post-processed using the same JAWA methodology (the wave amplitudes are however extracted by a routine provided by Worth & Dawson (2013*b*)) to validate LES observations. Figure 8.11 shows the wave amplitudes A^+ (blue, $\times$), A^- (red, $+$) and $A^+ + A^-$ (black, $\square$) (left), the Joint Probability Function $[A^+, A^-]$ (middle) and the Probability Density Function of the normalized wave ratio $\alpha = \frac{A^+ - A^-}{A^+ + A^-}$ (right). These results are compared with numerical data displayed in Figs. 8.9 and 8.10.

Usually, experimentalists have access to long signals and focus on the limit cycle, disregarding the growth phase. This kind of treatment is displayed in 8.11 (top) for experimental data from the start-up ($t = t_0$) to $t = t_0 + \Delta t$ where $\Delta t = 800\ ms$, showing both the start-up phase and the limit cycle. Note that data are missing in the transient

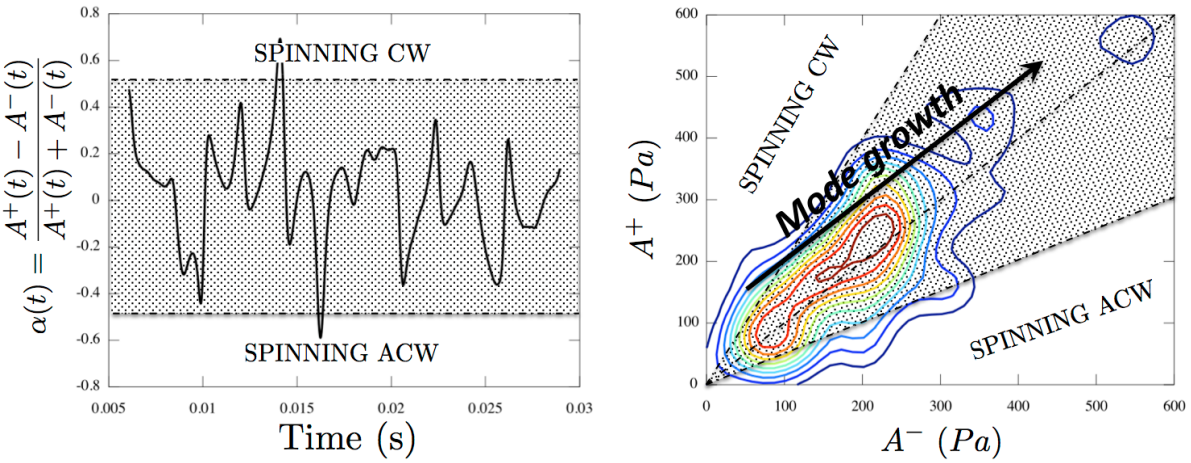

Figure 8.10: Time-evolution of $\alpha(t)$ (left) and isco-contours (right) of the joint probability distribution of (A^+, A^-) obtained by the JAWA methodology. Results show that the azimuthal mode, mainly standing during the growth phase, is also highly perturbed changing from standing to mixed. However, no pure spinning modes are found in this case.

phase (denoted NL-phase in Fig. 8.11) because of difficulties in the wave amplitudes extraction, probably due to the high non-linearities controlling this phase. The Joint Probability Function and Probability Density Function shows that the azimuthal mode nature fluctuates from a standing mode to a clockwise spinning mode, as already observed by Worth & Dawson (2013*b*,*a*) for this configuration. The mode nature during the linear growth phase is also displayed and is further studied in Fig. 8.11 (middle, $\Delta = 100\ ms$): this phase is mainly controlled by dynamic effects with large perturbations on the mode nature. Zooming on the start-up phase (the first $\Delta t = 20\ ms$), which corresponds to the LES computation, reveals that, as in the LES, the mode is initially standing (main peak around $\alpha = 0.03$ in LES and $\alpha = -0.03$ in the experiment) with a second small peak corresponding to an anti-clockwise spinning mode (peak around $\alpha = -0.3$ in the LES and -0.2 in the experiment) also appears. Compared to LES, the mode nature is less perturbed in the experiment with a standard deviation $\sigma(\alpha) = 0.06$ in the experimental start-up phase and $\sigma(\alpha) = 0.20$ in the LES, a point not fully understood yet. This behavior has been encountered in all the 10 independent experimental results provided by Worth & Dawson (2013*b*): the mode is always standing during the start-up phase and then becomes mostly spinning in the clockwise direction. These results shows that the growth, nature and dynamics of the azimuthal mode is globally well captured by LES. It proves that Large Eddy Simulation is a promising tool to investigate the growth of azimuthal modes, a necessary step to understand how these modes arise and how to control them.

8.5 Conclusion

This Chapter describes an LES of the full annular configuration of Cambridge. An operating point (ethylene, $N = 18$ burners, adiabatic) is chosen according to the sensitivity

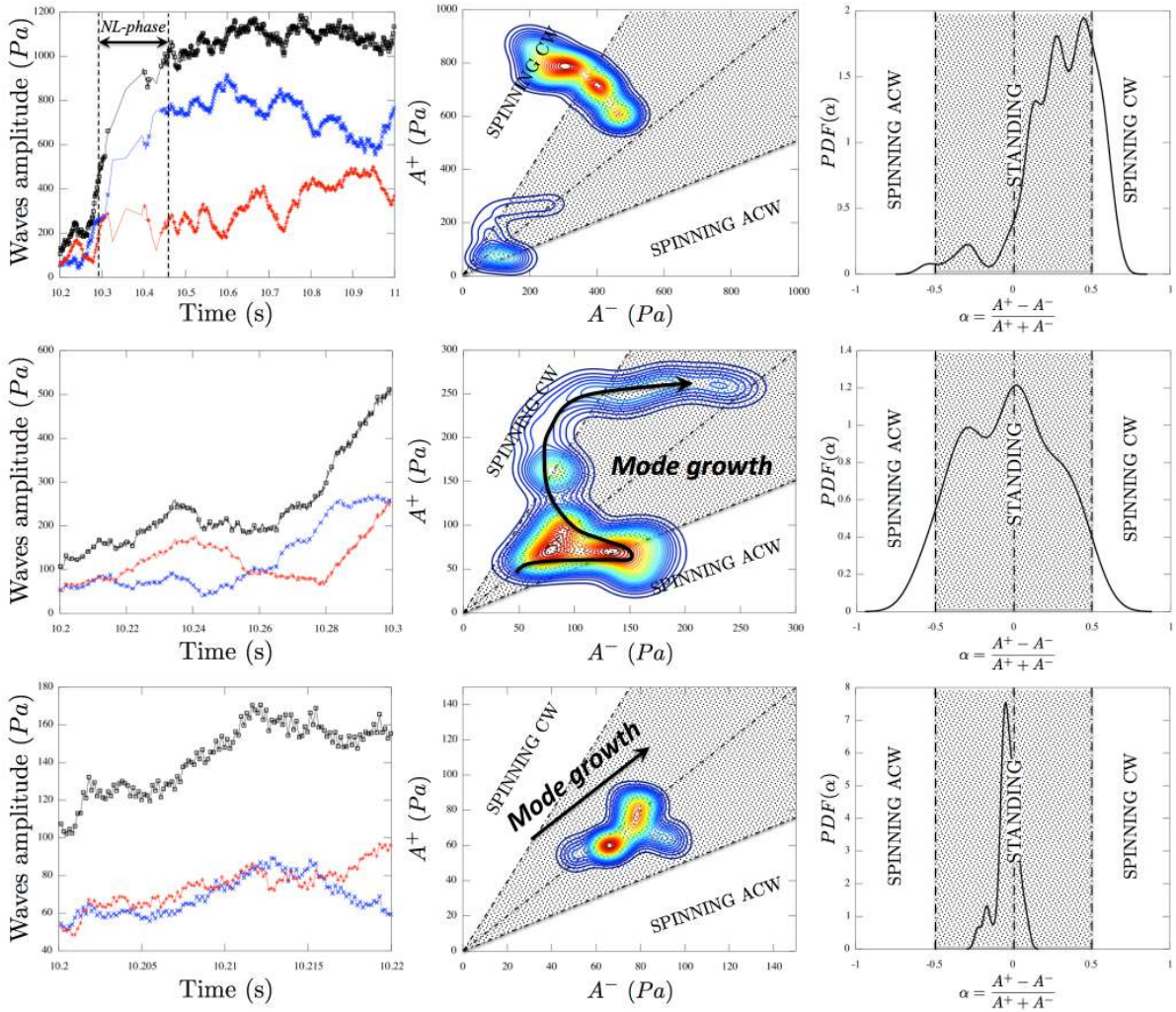

Figure 8.11: Mode structure analysis of experimental data provided by Worth & Dawson (2013*b*) for three different signal durations corresponding to Fig. 8.3: from the start-up ($t = t_0$) to $t = t_0 + \Delta t$ where $\Delta t = 800\ ms$ (top), $100\ ms$ (middle) and $20\ ms$ (bottom). The Jawa methodology is applied to obtained the waves amplitudes A^+ (blue, $\times$), A^- (red, $+$) and $A^+ + A^-$ (black, $\square$) (left), the Joint Probability Function (middle) and the PDF of the normalized waves ratio α (right).

analysis performed on previous forced-LES. First, mean azimuthal flame patterns obtained by integrating the LES heat release are compared to mean OH* measurements and show a good agreement. Then, the self-excited mode which appears in the LES is compared to experimental results provided by Cambridge. Experimental and numerical data have been post-processed with the same treatment to ensure a proper comparison. Results show that LES is able to capture a self-excited mode at 1800 Hz as in the experiment. However, due to the long establishment of the mode and the extreme cost of 360° LES, only the growth phase is computed while the experiment is able to fully capture the limit cycle. The study of the establishment of the self-excited mode reveals that it is accompanied, in both LES and experiment, by longitudinal modes which are due to the start-up procedure. Moreover, the azimuthal mode structure, which is predicted as

standing by classical tool (FFT, DMD), is in fact complex and highly perturbed. these numerical results are compared to experimental data post-processed with the same tool showing a good agreement for the start-up phase. Nevertheless, the complexity of the actual configuration and the limited data available by classic LES because of its cost make the study of symmetry breaking in such a complex configuration difficult. Consequently, a new methodology called AMT is proposed in the next chapter to investigated limit cycles and mode structure using LES at low cost.

Part III

Acoustic Mode Triggering: from low-order models to Large Eddy Simulations

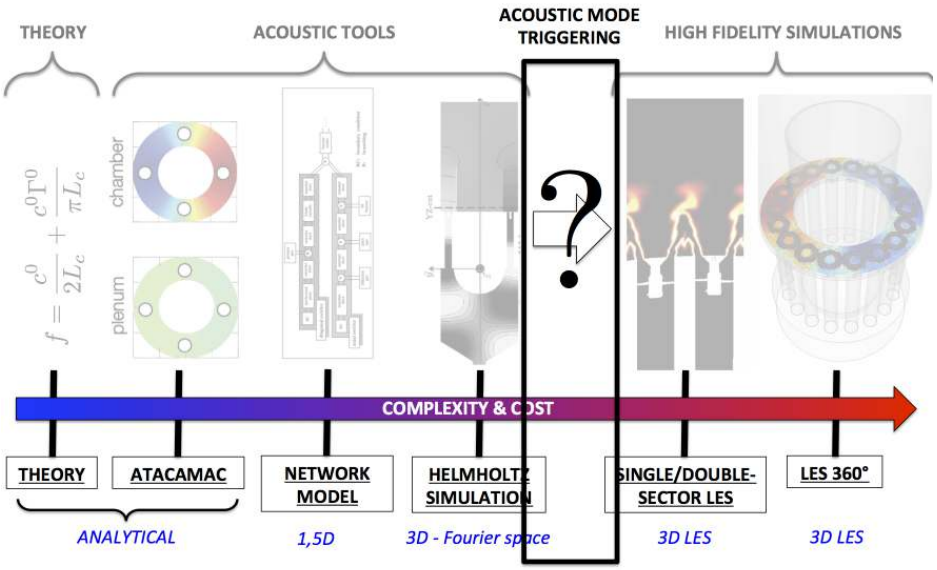

This part has lead to the following publication:

1) M. Bauerheim, F. Nicoud and T. Poinsot, *'Study of acoustic mode dynamics in simplified annular configurations using DNS and an Acoustic Mode Triggering (AMT) approach'* (**in preparation**)

Chapter 9

Study of acoustic mode dynamics using Acoustic Mode Triggering (AMT): validation on longitudinal configurations

Contents

The previous chapter has revealed that LES studies of thermo-acoustic modes in turbulent annular configurations are a complex task mainly because of the numerical short signals which can be obtained on present machines. Moreover, the limitations of linear methods to study instabilities in combustion systems are a usual controversial question: this chapter presents a method to verify the quality of linear predictions and theories for combustion instabilities presented in Part I of this thesis by using them as initial solutions of a LES or DNS solver. This approach (called AMT for Acoustic Mode Triggering) uses the results of a Helmholtz solver (at zero Mach number) or of theory (at zero or non-zero Mach number) as an initial condition of a LES to focus on this single mode growth. Such an approach provides the numerical estimation of the damping/growth rate of the injected mode and its limit cycle as well. In this chapter, the methodology is validated on longitudinal laminar configurations with various mean flows. An additional test case is presented where turbulence is injected to study its impact on the acoustic mode which is still an open topic today and is assumed to play a role in mode switching in certain theories (Noiray et al., 2011). Results show that AMT is able to reproduce non-linear behaviors such as acoustics at non-null Mach numbers. When turbulence is injected, non-linear interactions between the acoustic mode and the turbulence are observed leading to harmonics generation, which may explain why azimuthal modes may change nature in turbulent flames.

9.1 Introduction

The usual approaches to study combustion instabilities are (1) Large Eddy Simulations (High fidelity simulations, Fig. 9.1, right), (2) Helmholtz simulations assuming a zero Mach number flow (Pankiewitz & Sattelmayer, 2003; Nicoud *et al.*, 2007; Evesque & Polifke, 2002) (acoustic tools, Fig. 9.1, middle) and (3) theory on idealized configurations where only key phenomena are retained (Fig. 9.1, left). All these approaches have limitations:

- LES remains a very expensive approach as shown in Chapter 8. Moreover it usually features all modes appearing in a combustor and does not allow to isolate them unless specific treatments and advanced post-processing are introduced.
- Helmholtz solvers are much more efficient in terms of CPU time but since they assume a zero Mach number flow, they obviously miss convective effects. For most combustion chambers where the Mach number is small, convective mechanisms do not modify frequencies significantly but they do affect growth rates (Nicoud & Wieczorek, 2009; Dowling, 1995). Since growth rates control stability and are the most important output of such studies, the zero-Mach number hypothesis remains a major drawback and limitation.
- The flame response modeling used in Helmholtz solvers is usually approximate: Flame Transfer Function (FTF) approaches (Poinsot & Veynante, 2011; Paschereit *et al.*, 2002; Polifke *et al.*, 2001*b*) are the most common method and rely on multiple assumptions (linearity, flame response controlled only by the axial acoustic velocity

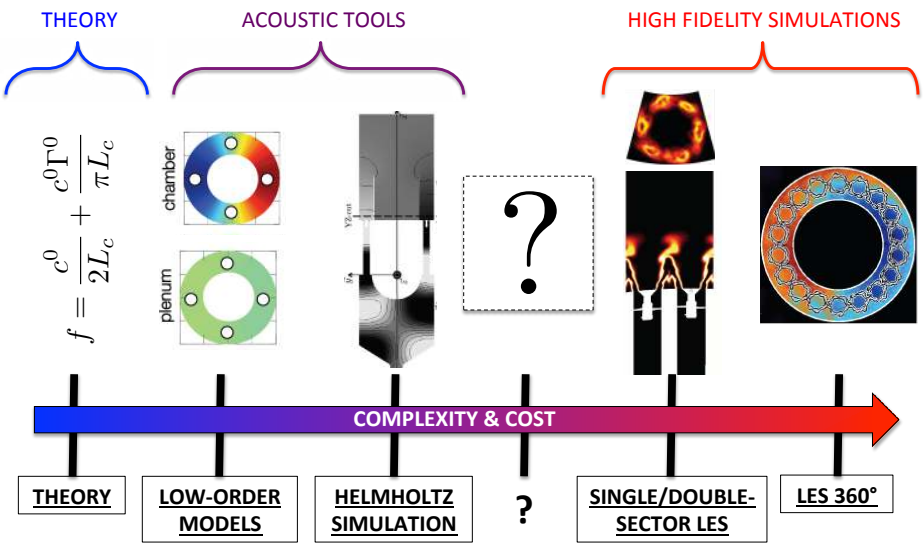

Figure 9.1: Tools developed to study acoustic and combustion instabilities: theory, low-order models, Helmholtz simulations and Large Eddy Simulations. A tool is missing between acoustic tools and high fidelity simulations.

fluctuations etc.).

- Theory allows to identify key phenomena involved in combustion instabilities but non-linear and mean flow effects as well as damping are still difficult to study analytically.

Usually LES and Helmholtz solvers are used separately although they already complement each other. LES information is indeed useful for the Helmholtz solver: for example, the Helmholtz solver requires a sound speed field and a model to take into account the unsteady combustion which can be obtained from a forced LES (Kaufmann *et al.*, 2002; Tay Wo Chong *et al.*, 2010; Kedia *et al.*, 2011; Duchaine & Poinsot, 2011). The main idea of the AMT (Acoustic Mode Triggering) methodology is to feed information in the other direction: from the Helmholtz solver to the LES code. This is done by using the Helmholtz eigenmodes to construct an initial solution fed to the LES solver. This is an approach which is similar to injecting Orr-Sommerfeld linear modes (Orr, 1907*a*,*b*) into CFD solvers to initialize these modes in a time-domain simulation and study hydrodynamic instabilities. The AMT approach has multiple advantages:

- The first advantage of AMT is its ability to use a single mode obtained by linear analysis (e.g. with a Helmholtz solver) and see in the LES how this mode grows and reaches a limit cycle (or not). This is a classical controversial issue in thermoacoustics where the usefulness of linear analysis is often questioned.
- AMT allows to relax the zero-Mach number assumption used in the Helmholtz solver: once a mode is identified in the Helmholtz solver, its exact growth rate can be determined by LES rapidly, taking into account all convective effects and damping phenomena.
- AMT provides an initial field which contains a single and well identified theoretically unstable mode which can be then analyzed in time and space more easily than for a

LES initialized randomly where multiple modes can grow and interact. Chapter 8 showed that the growth phase of a mode can be very long to capture with LES: being able to directly initiate an LES with the proper mode is an attractive path.

- AMT allows to control the initial mode structure: nature and pressure level. For annular configurations, a spinning, standing or mixed mode can be injected. Therefore effects of the mode structure on growth rate or limit cycles can be easily investigated.

The principle of AMT is described in Fig. 9.2: starting from a mean LES field (1), an acoustic tool (Helmholtz solver assuming zero Mach number or theory accounting for mean flow effects) identifies the unstable frequencies and the associated acoustic eigenmodes (2). One of these eigenmodes is reconstructed at a given time (3) and injected onto a three-dimensional initial condition for the LES (4). The LES solver then locks on this mode and predicts its time evolution accounting for all effects (non zero Mach number, realistic flame response and damping phenoma). An implicit assumption here is that the LES code will indeed adjust to the mode injected obtained using a Helmholtz solver, even though this mode does not include all effects that LES captures. As shown below, this seems to be the case in all the tests done here.

AMT is valid for any combustor but this Chapter focuses on its validation on simple longitudinal configurations while the next chapter emphasizes on annular combustors and symmetry breaking effects. These cases are studied with no combustion to highlight that non-linear flame behavior is not necessarily the only feature controlling the mode structures, as evidenced from experiments (Worth & Dawson, 2013*b*,*a*) and recent theories (Bauerheim *et al.*, 2014*e*).

This chapter describes the AMT (Acoustic Mode Triggering) approach in Section 9.2 where an acoustic mode computed by a Helmholtz solver or given by theory is imposed as an initial condition for LES, avoiding the computation of transient time required to reach limit cycles and allowing the numerical estimation of the damping/growth rate of the injected mode. AMT is evaluated on simple longitudinal configurations where multiple Mach numbers are tested. The injected mode is taken from: 1) a Helmholtz simulation assuming a zero-Mach number or 2) 1D theory accounting for an axial mean flow. Results show that at low-Mach number, both the Helmholtz and analytical solutions are properly injected into the LES domain. An additional test case is provided by adding turbulence to the baseline flow to investigate its impact on the acoustic mode. It shows that a non-linear interaction between acoustics and turbulence arises and triggers several modes. Mode structures of these generated modes are analyzed using FFT and DMD and compared to acoustic mode of the system: they correspond to harmonics of the injected mode that the interaction between acoustics and turbulence has triggered.

9.2 Acoustic Mode Triggering (AMT) methodology

Acoustic Mode Triggering (AMT, Fig. 9.2) methods use the output of an acoustic tool (Helmholtz solver or theory) as an initial condition for the LES solver (Fig. 9.2) which avoids computing the transient time required to reach the limit cycle and also allows to

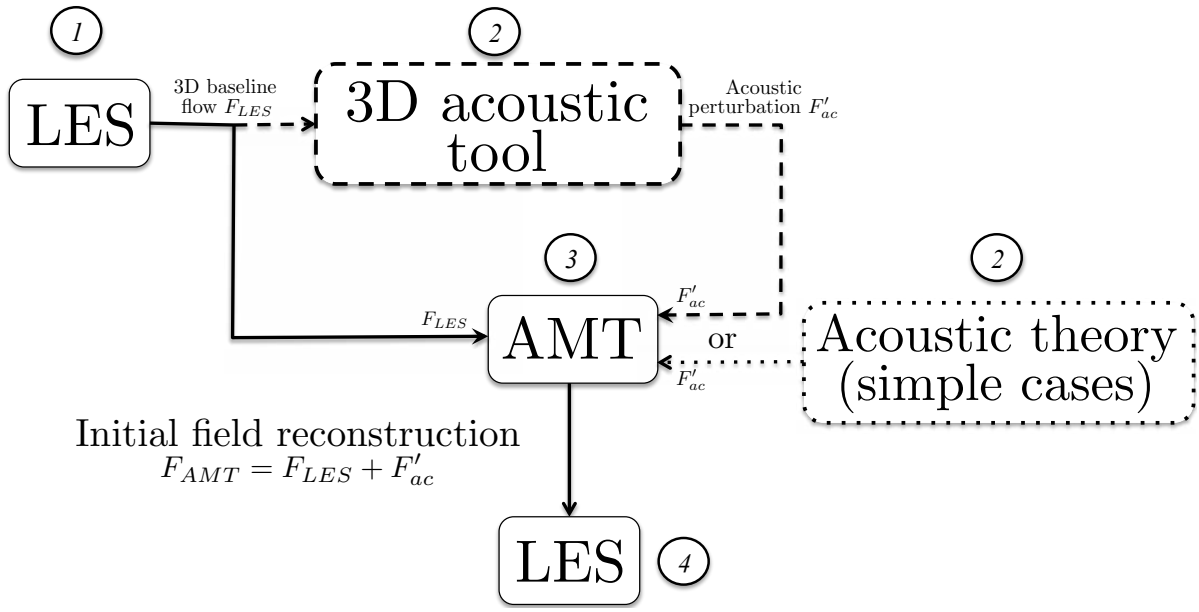

Figure 9.2: Principle of the AMT methodology: 1) An LES is performed and used as a baseline flow 2) A 3D acoustic solver (- - -) or theory (·····) provides the acoustic mode of the configuration 3) The acoustic mode is then added to the baseline flow into the LES domain 4) The limit cycle or the numerical estimation of the damping/growth rate of the injected mode are obtained using an LES at low cost. AMT can also be used with DNS.

focus on a single mode. This is done as follows.

First, acoustic quantities (subscript ac) are extracted from a Helmholtz simulation or theory. In longitudinal configurations only one acoustic component (subscript 1) is required while azimuthal modes investigated in the next chapter need to combine two different solutions (subscripts 1 and 2) to recover standing, spinning or mixed modes:

$$\begin{cases} P_{ac} = \alpha_1 \|\hat{P}_1\| \cos(\phi_{p,1}) + \alpha_2 \|\hat{P}_2\| \cos(\phi_{p,2}) \\ \overrightarrow{V_{ac}} = \alpha_1 \|\overrightarrow{\hat{V}_1}\| \cos(\phi_{v,1}) + \alpha_2 \|\overrightarrow{\hat{V}_2}\| \cos(\phi_{v,2}) \end{cases} \tag{9.1}$$

where $\|\hat{P}_i\|$ and $\|\overrightarrow{\hat{V}_i}\|$ are the pressure and velocity modulus while $\phi_{p,i}$ and $\phi_{v,i}$ are the pressure and velocity phases of the i^{th} component of the acoustic mode computed by the Helmholtz solver. Since this chapter focuses on longitudinal cases for validation, α_2 can be set to zero in the following.

The acoustic density and temperature are obtained using the isentropic relation and read:

$$\rho_{ac} = \frac{P_{ac}}{c^2_{LES}} = \frac{\alpha_1}{c^2_{LES}} \|\hat{P}_1\| \cos(\phi_{p,1}) + \frac{\alpha_2}{c^2_{LES}} \|\hat{P}_2\| \cos(\phi_{p,2}) \tag{9.2}$$

$$T_{ac} = \frac{P_{ac}}{\rho_{LES} C_p} = \frac{\alpha_1 \rho_{LES}}{C_p} \|\hat{P}_1\| \cos(\phi_{p,1}) + \frac{\alpha_2 \rho_{LES}}{C_p} \|\hat{P}_2\| \cos(\phi_{p,2}) \tag{9.3}$$

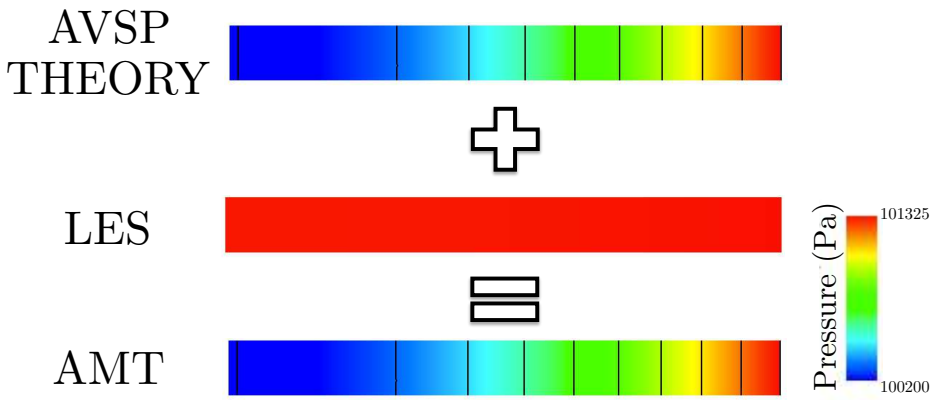

Figure 9.3: AMT methodology: a Helmholtz solution of a longitudinal 3D pipe (top) is combined with a 3D instantaneous LES solution (middle) as a new initial condition for the LES solver (bottom). Here the LES solution is trivial: homogeneous flow.

where c_{LES} and ρ_{LES} are the sound speed and density in the LES simulation around which acoustic linearization has been performed. Then acoustic quantities are added to the LES pressure, temperature, density and conservative velocity and species[1]:

$$\begin{cases} P_{AMT} = P_{LES} + P_{ac} \\ T_{AMT} = T_{LES} + T_{ac} \\ \rho_{AMT} = \rho_{LES} + \rho_{ac} \\ \rho\overrightarrow{V_{AMT}} = \rho\overrightarrow{V_{LES}} + \rho_{LES}\overrightarrow{V_{ac}} \\ \rho Y^k_{AMT} = \rho Y^k_{LES} + \frac{\rho_{ac}}{\rho_{LES}}\rho Y^k_{LES} = \frac{\rho_{AMT}}{\rho_{LES}} Y^k_{LES} \quad \text{for species} \quad k = 1 \text{ to } N_{sp} \end{cases} \tag{9.4}$$

The total energy is finally reconstructed from Eq. (9.4) and reads:

$$\rho E_{AMT} = \rho E_s + \frac{1}{2}\left(\rho u^2 + \rho v^2 + \rho w^2\right) \tag{9.5}$$

where the conservative sensible+chemical energy ρE_s and kinetic energy ρu^2, ρv^2 and ρw^2 are defined as follows:

$$\rho E_s = \int_{T_0}^{T_{AMT}} C_v dT - \frac{RT_0}{W} + \frac{1}{\rho_{AMT}} \sum_{k=1}^{N_{sp}} \Delta h^0_{f,k} \rho Y^k_{AMT} \tag{9.6}$$

$$\rho u^2 = \frac{1}{\rho_{AMT}} \left(\rho u_{AMT}\right)^2 \quad , \quad \rho v^2 = \frac{1}{\rho_{AMT}} \left(\rho v_{AMT}\right)^2 \quad , \quad \rho w^2 = \frac{1}{\rho_{AMT}} \left(\rho w_{AMT}\right)^2 \tag{9.7}$$

where T_0 is a reference temperature, C_v is the heat capacity at constant volume of the mixture, W is the mean molecular weight of the mixture, $R = 8.314\ J\text{mole}^{-1}K^{-1}$ is the perfect gas constant and $\Delta h^0_{f,k}$ is the formation enthalpy of species k. Hence, Eqs. (9.4) and (9.5) provide suitable conservative variables (ρ_{AMT}, $\rho\overrightarrow{V_{AMT}}$, ρY^k_{AMT} and ρE_{AMT}) close to 3D Navier-Stokes solutions to generate proper acoustic mode triggering without additional spurious perturbations.

[1]The conservative species are changed due to the acoustic perturbations acting on the density.

9.3 AMT validation on a longitudinal configuration

9.3.1 Objectives and longitudinal setup

First the AMT methodology is evaluated on a simple longitudinal configuration described in Fig. 9.4. This problem corresponds to a 3D pipe where zero velocity fluctuation is imposed at the inlet ($u' = 0$) and zero pressure fluctuation at the outlet ($p' = 0$). A mean homogeneous axial flow is added (Fig. 9.5), characterized by its axial Mach number M ($M = 0$, $M = 0.05$ and $M = 0.1$). Two different injected modes are tested:

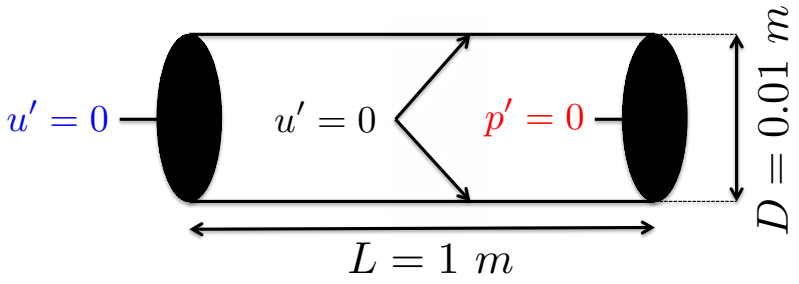

Figure 9.4: 3D longitudinal configuration.

- **from AVSP:** the acoustic mode is constructed from a Helmholtz simulation performed with the code AVSP, assuming a zero Mach number.
- **from analytical theory:** the acoustic mode is computed using a 1D theory taking into account the axial mean flow. Taking into account the boundary conditions $u' = 0$ at $x = 0$ and $p' = 0$ at $x = L$, the pressure and velocity fluctuations read at the initial time $t = 0$:

$$p'(x, t = 0) = P_0 \cos\left(\frac{\pi x}{2L}\right) \cos\left(\frac{\pi x M}{2L}\right) \tag{9.8}$$

$$u(x, t = 0) = \frac{P_0}{\rho_0 c_0} \sin\left(\frac{\pi x}{2L}\right) \sin\left(\frac{\pi x M}{2L}\right) \tag{9.9}$$

  which correspond to an acoustic mode satisfying $\hat{u}(x = 0) = 0$ and $\hat{p}(x = L) = 0$ with a frequency $Re(f) = \frac{c_0}{4L}(1 - M^2) \approx 86\ Hz$ and $Im(f) = 0$ (see H for details about longitudinal modes with a constant mean flow).

An additional test case is provided in Section 9.4 (Fig. 9.5 - d) to further study the impact of convective effects on the injected acoustic mode, in particular by adding turbulence naturally present in LES of complex industrial gas turbines.

9.3.2 AMT results on the laminar configuration

First the AMT methodology is applied to cases $M0$, $M0.05$ and $M0.1$ (Fig. 9.4) with the two mode injection types: i.e. the acoustic mode is obtained by a Helmholtz solver (AVSP) or by a 1D theory at non-null Mach number and is injected with an initial amplitude of 800 Pa (i.e. $p'/\bar{p}_0 < 1\%$ to satisfy the linear acoustic assumption). Figure 9.6

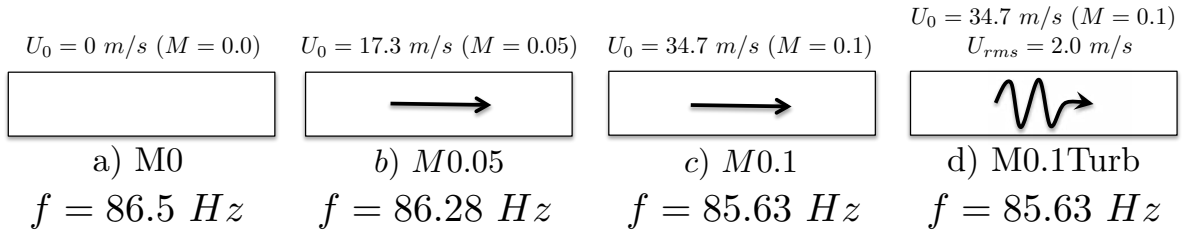

Figure 9.5: Longitudinal test cases: a) no mean flow, b) and c) mean flow with $M = 0.05$ and $M = 0.1$ and d) mean flow $M = 0.1$ with turbulent injection ($U_{rms} = 2\ m/s$). The theoretical frequency of each case is also indicated (expressions are given in Tab. H.1).

displays Fourier transforms of the pressure signal at the center point of the pipe ($x = 0.5\ m$). For low Mach numbers tested in this work ($M = 0$ and $M = 0.05$), the two injection types create initial modes which are close to the true solution: the LES exhibits only one mode. However for higher Mach numbers ($M = 0.1$), the solution at zero Mach number provided by AVSP is too far from the true solution and small spurious modes appear as shown in the spectrum (Fig. 9.6, right). For simple cases, this drawback can be avoided by injecting an acoustic mode closer to the Mach-dependent solution, for instance a 1D theory at non-zero Mach number (Eqs. (9.8) and (9.9)). In this case, the acoustic mode is correctly injected with no spurious mode (Fig. 9.6, `---`).

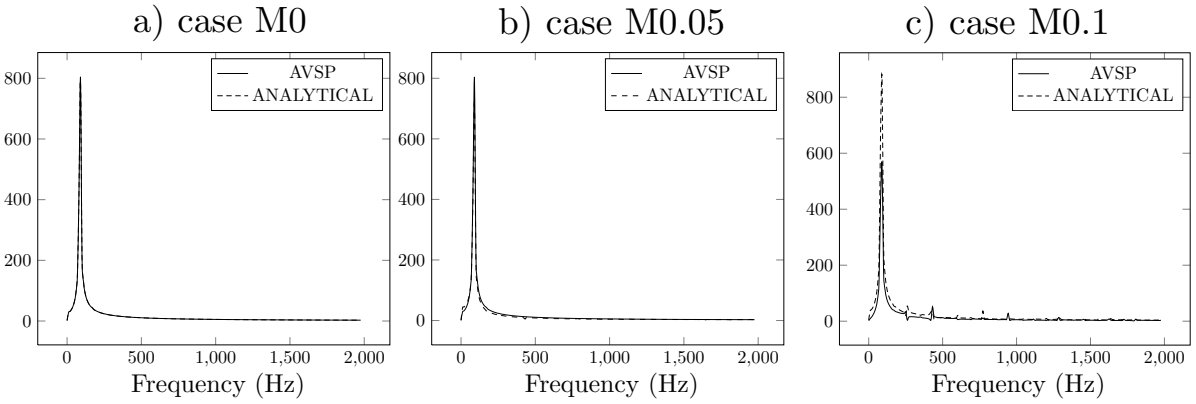

Figure 9.6: FFT of the pressure signal at the location $x = 0.5\ m$ for the three cases with $M = 0$ (left), $M = 0.1$ (middle) and $M = 0.2$ (right). Two different modes have been injected: —— : AVSP (solution at zero Mach number) and `---` : 1D theory taking into account the axial mean flow (Eqs. 9.8) and 9.9).

To further validate AMT results, frequencies and growth rates associated to each case are extracted. Dynamic Mode Decomposition (Schmid, 2010) is used here since FFT suffers from a low frequency resolution (here $\Delta f = 10\ Hz$ for the 100 ms-long pressure signals) compared to the subtle Mach effects on frequency (1 Hz at $M = 0.1$). Analytical expressions for frequency and growth rate at non-null Mach number are provided in Appendix H (Tab. H.1): the growth rate is null for all Mach numbers and the frequency depends on the square of the Mach number. Table 9.1 summarizes the comparison between the analytical and AMT frequencies and growth rates with the two different initialization: an acoustic mode computed by AVSP (null-Mach number assumption) or

by theory.

	Frequencies		
	$M = 0$	$M = 0.05$	$M = 0.1$
Theory	86.5 Hz	86.28 Hz	85.63 Hz
AMT-Theory	86.46 Hz	86.33 Hz	85.65 Hz
AMT-AVSP	86.46 Hz	86.25 Hz	85.65 Hz

	Growth rates		
	$M = 0$	$M = 0.05$	$M = 0.1$
Theory	$0\ s^{-1}$	$0\ s^{-1}$	$0\ s^{-1}$
AMT-Theory	$8.10^{-2}\ s^{-1}$	$-6.10^{-3}\ s^{-1}$	$-9.10^{-3}\ s^{-1}$
AMT-AVSP	$6.10^{-2}\ s^{-1}$	$-2.10^{-2}\ s^{-1}$	$-5.10^{-5}\ s^{-1}$

Table 9.1: Comparison of frequencies (top) and growth rates (bottom) obtained by theory (Appendix H) and AMT initialized by theory or AVSP, showing an absolute error of 10^{-2} on both frequencies and growth rates.

These three test cases prove the AMT capability to impose an acoustic mode as an initial condition for the LES solver. On simple longitudinal laminar configurations, AMT provides estimation of frequencies and growth rates with an absolute error of the order of 10^{-2} Hz. Thus, solutions provided by zero Mach-number codes like Helmholtz solvers are properly injected for low mean flows, i.e. $M < 0.1$, which corresponds to many applications encountered in modern gas turbines.

9.4 AMT validation on a turbulent configuration

In addition to the laminar cases investigated previously where an acoustic mode was added to a laminar flow (Fig. 9.5), a spatially decaying turbulent test case is studied in this section. Turbulence is naturally present in LES of complex industrial annular chambers. Up to now, sound propagation in a turbulent pipe was investigated either by forcing an acoustic wave at the inlet or by pulsating the solid boundaries (Comte *et al.*, 2006; Agarwal & Bull, 1989). AMT allows a third method which is to superimpose an acoustic cavity mode (here the first longitudinal mode at 86.5 Hz) on the baseline turbulent flow to investigate two reciprocal effects: (1) Turbulence can interact with the acoustic mode and trigger higher harmonics and (2) Acoustic can affect the turbulence production and consequently impact the energy turbulence spectrum. For this case (Fig. 9.7), the acoustic boundary conditions for the channel correspond to $u' = 0$ at the inlet and (imposed velocity) and $p' = 0$ at the outlet (imposed pressure).

In this chapter, a fine mesh is used containing 5.5 million cells (compared to 362,000 for the laminar case) which corresponds to a cell size $\Delta x = 1\ mm$ and ensure $\lambda_e \gg \Delta x$. Turbulence is injected at the duct inlet to study its interaction with the acoustic mode: a Passot-Pouquet spectrum (Passot & Pouquet, 1987) is injected via the inlet boundary

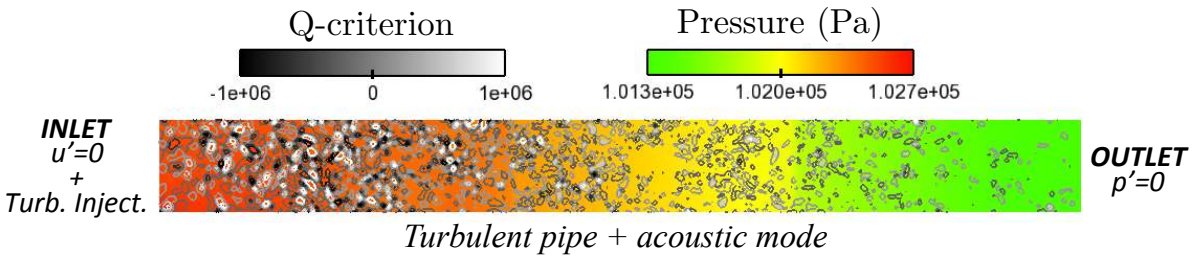

Figure 9.7: 3D Turbulent pipe with an acoustic mode injected by AMT. Boundary conditions are imposing a velocity node at the inlet ($u' = 0$) and a pressure node ($p' = 0$) at the outlet.

condition using the Kraichnan-Celik methodology (Smirnov *et al.*, 2001) and the NSCBC approach (Guezennec & Poinsot, 2009):

$$E(k) = 16\frac{U_p^2}{k_e}\left(\frac{k}{k_e}\right)^4 e^{-2\left(\frac{k}{k_e}\right)^2} \tag{9.10}$$

where E is the energy spectrum, k is the wavenumber, $k_e = 2\pi/\lambda_e$ is the most energetic wavenumber. The most energetic wavelength is $\lambda_e = D/3 \approx 0.03\ m$ and $U_p = U_{rms} \sim 2.0\ m/s$ is the turbulent velocity. For the Kraichnan-Celik methodology, $N = 1000$ modes are used and a cut-off length corresponding to twice the size of the largest cell edge on the inlet patch ($L_c = 2\max(\Delta x)$) is imposed to enforce the Shannon theorem.

Two-points correlation functions (longitudinal $f(r)$ and transverse $g(r)$ where r is the distance between two points) are extracted from the simulation[2] before AMT (i.e. no acoustic mode) and compared to the theory ($f_{th}(r)$ and $g_{th}(r)$) to check the turbulence injection:

$$\begin{aligned} f_{th}(r) &= e^{-\frac{1}{8}(k_e r)^2} \\ g_{th}(r) &= \left(1 - \frac{(k_e r)^2}{8}\right) e^{-\frac{1}{8}(k_e r)^2} \end{aligned} \tag{9.11}$$

Figure 9.8 shows that correlations functions in the LES (——) are close to theory (---). The oscillations for larger length scale are due to statistical convergence. The ratio of the longitudinal and transverse Taylor micro-scales $\lambda_f/\lambda_g \approx 1.409$ is in good agreement with the theoretical value $\lambda_f/\lambda_g = \sqrt{2} \approx 1.414$. Turbulence in the case M0.1Turb is visualized in Fig. 9.9 using the Q-criterion (blue: negative and red: positive): it illustrates the injected vortices decaying in the longitudinal direction.

After $t_0 = 100\ ms$ of simulation, an acoustic quarter-wave mode at 86.5 Hz is injected using AMT in the turbulent flow. Figure 9.10 shows the Fourier transform of the pressure signal at $x = 0.5\ m$ of the case $M01Turb$ compared to the laminar case (case $M0.1$, Fig. 9.5). Compared to the laminar case, two eigenmodes at 430 Hz and 770 Hz are triggered due to the interaction between acoustics and turbulent flow. Time-evolution of pressure (Fig. 9.10, right) reveals the initial acoustic mode ($t \approx t_0$) is only weakly

[2]Correlation functions are extracted using a probe at a location x which gives temporal velocity variations $\vec{u'}(t)$. Therefore, these correlation functions rely on the Taylor assumption: $\frac{\partial}{\partial t} \approx -u_0 \frac{\partial}{\partial r}$

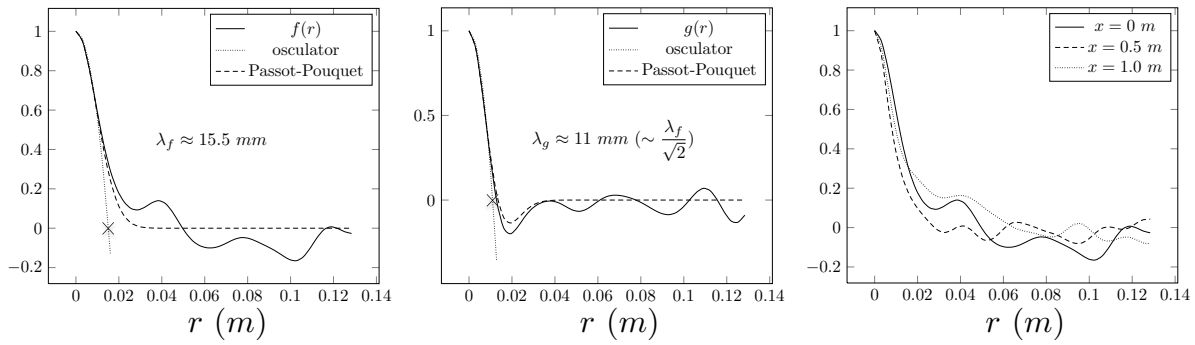

Figure 9.8: Longitudinal (left) and transverse (middle) correlations functions extracted from LES without AMT (i.e. no acoustic mode) at $x = 0m$ (inlet) and comparison with the Passot-Pouquet spectrum (Eq. 9.11, `---`). The intersection of the osculator parabola (⋯⋯) with the abscissa gives an estimation of the Taylor micro-scale λ_f and λ_g ($\times$). Correlation function at several longitudinal locations are also displayed (right).

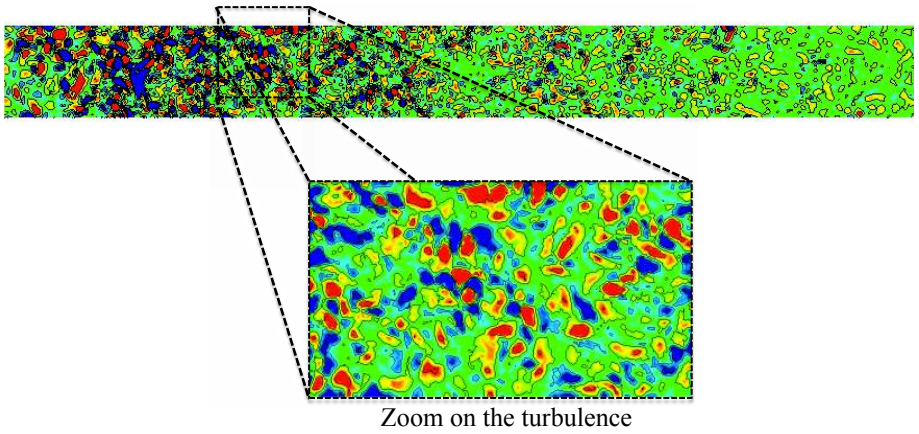

Figure 9.9: Longitudinal cut and zoom on turbulence displayed by Q-criterion in the case M0.1Turb with no acoustic mode.

affected by turbulence. However, after a few milliseconds ($t \gg t_0$), other modes with higher frequencies appear in the pressure signal which suggests that turbulent motion can trigger acoustic modes.

The triggered eigenmodes observed in the Fourier transform of pressure for the case $M0.1Turb$ are post-processed (Fig. 9.12, right) using both energy spectrum (Fig. 9.11) Fast Fourier Transform (FFT) and Dynamic Mode Decomposition (DMD). First, the energy spectra based on the axial velocity fluctuations u' are displayed for the case without mode injection (left) at three different locations: the inlet (—— , $x = 0\ m$), just after the inlet (`---` , $x = 0.2\ m$) and at the outlet (⋯⋯ , $x = 1\ m$). They show that turbulence is properly injected in the computational domain at the inlet. Turbulent vortices are then convected downstream. As expected, the energy level observed at $x = 0.2\ m$ is similar to the energy injected at the inlet because of the large turbulent Reynolds number ($Re_t = 15,000$ based on $L_{11} \simeq 0.4\lambda_e$ and $u_{rms} = U_p = 2\ m/s$). However, at the outlet ($x = 1\ m$), turbulent dissipation has decreased the energy level of one order of magnitude

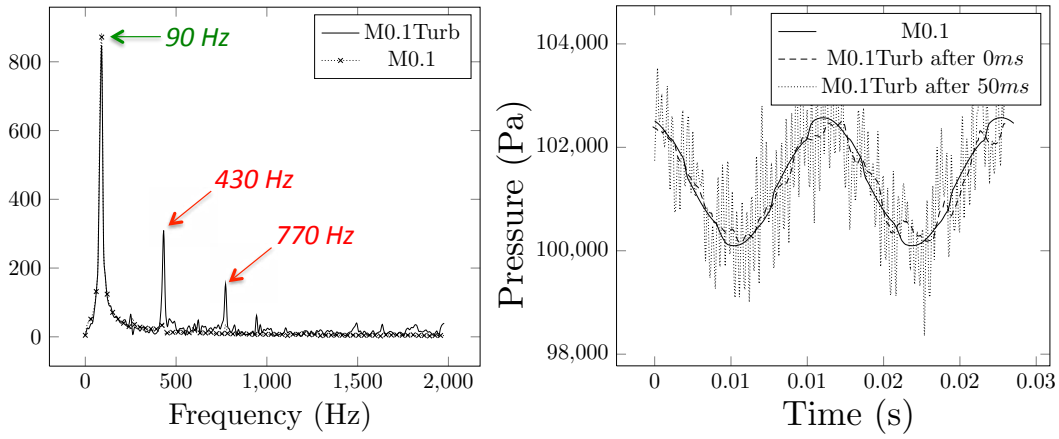

Figure 9.10: Fourier transform (left) and time-evolution (right) of the pressure signal at $x = 0.5m$ in the case $M0.1Turb$ compared to the laminar case $M0.1$. Initially turbulence weakly affects the acoustic mode (1- ▬▬ , just after AMT at $t - t_0 = 0ms$) but after a few milliseconds (2- ····· for $t - t_0 \approx 50\ ms$) turbulence triggers higher frequency modes.

as shown in Fig. 9.9. Then, the same post-processing tool is applied on the turbulent case with the injected acoustic mode at 86 Hz. It is interesting to notice that the inlet spectrum is not modified which is normal since the boundary condition $u'_{ac} = 0$ imposes no acoustic velocity fluctuations. It also suggests that no spurious oscillations are generated at the inlet. However, downstream of the inlet, the turbulence spectra are highly perturbed: (1) the acoustic mode at 90 Hz is observed (The FFT frequency resolution is $\Delta f = 10\ Hz$: the injected mode at 86 Hz is therefore captured at 90 Hz) and is maximal at the outlet because of the half-wave structure of the mode and (2) the classic turbulent dissipation at large frequencies is altered. These results reveal that the acoustic energy of the longitudinal mode at 86 Hz feeds the turbulence motion.

To further analyze these non-linear behavior, the pressure LES fields are also post-processed to identify modes triggered observed in Fig. 9.10. FFT and DMD results (9.12, right) are compared with the acoustic eigenmodes of the system computed by a Helmholtz solver (no mean flow and no turbulence): Fig. 9.12 (left) shows that modes observed at 86 Hz, 430 Hz and 770 Hz in Fig. 9.10 are acoustic eigenmodes of the configuration: a non-linear interaction between the longitudinal mode and the turbulence has triggered other eigenmodes of the system.

Even though this was not presented here, this example shows that AMT can be an efficient technique to study mechanisms through which turbulent fluctuations redistribute acoustic energy from one mode to others as suggested for example by Noiray *et al.* (2011) to explain mode switching in annular chambers.

9.5 Conclusion

Limitations of linear methods to study instabilities in combustion systems are a usual controversial question: this chapter presents a method to verify the quality of linear

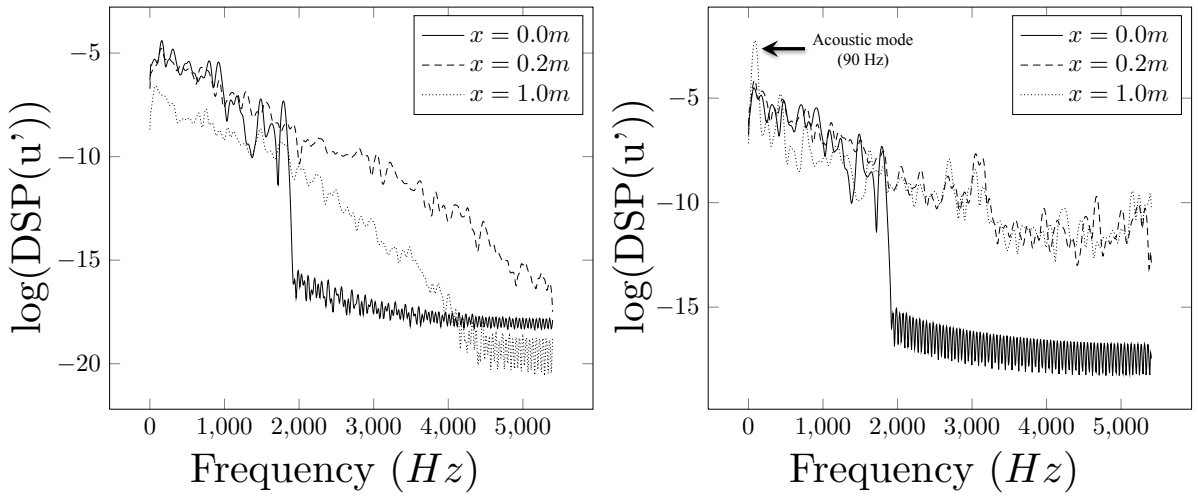

Figure 9.11: Energy spectrum on the axial velocity fluctuations u' for the turbulence case $M0.1TURB$ without (left) and with (right) an acoustic mode at 90 Hz injected by AMT. Probes are located at three locations: the inlet (——— , $x = 0$ m), just after the inlet (- - - , $x = 0.2$ m) and at the outlet (····· , $x = 1$ m).

predictions and theories for combustion instabilities presented in Part I of this thesis by using them as initial solutions of a LES or DNS solver which do not have the limitations due to the linear and low-Mach assumptions used in acoustic solvers. This approach (called AMT for Acoustic Mode Triggering) uses the results of a Helmholtz solver (at zero Mach number) or of theory (at zero or non-zero Mach number) as an initial condition of a LES to focus on this single mode growth. Such an approach provides the numerical estimation of the damping/growth rate of the injected mode and its limit cycle as well. In this chapter, the methodology is validated on longitudinal laminar configurations with various mean flows. An additional test case is presented where turbulence is injected to study its impact on the acoustic mode which is still an open topic today. Results show that AMT is able to reproduce non-linear behaviors such as acoustics at non-null Mach numbers. When turbulence is injected, non-linear interactions between the acoustic mode and the turbulence are observed and lead to harmonics generation.

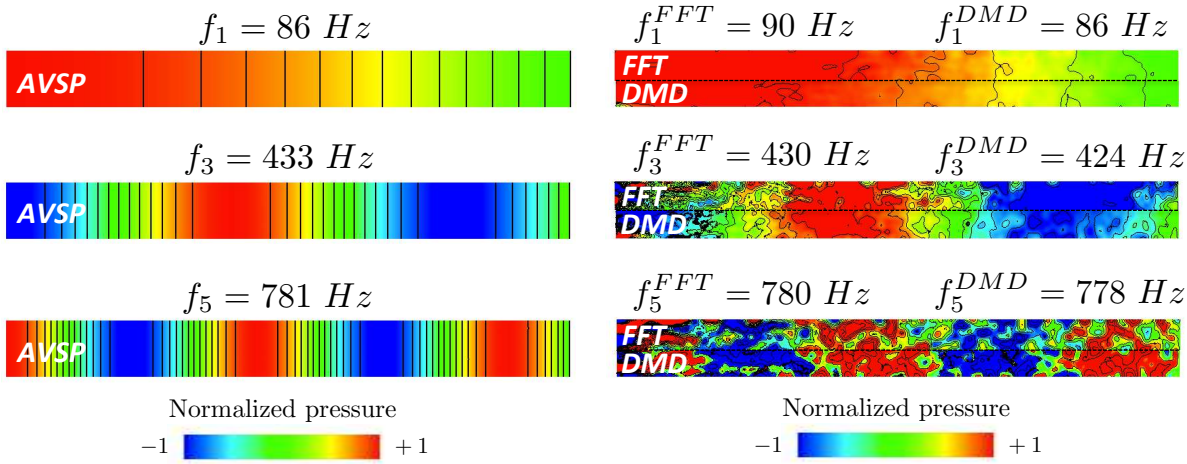

Figure 9.12: Eigenmodes obtained by the Helmholtz solver (left) and Fourier Transform (FFT) and Dynamics Mode Decomposition (DMD) of the $M0.1Turb$ case (right).

Chapter 10

Study of acoustic mode dynamics using Acoustic Mode Triggering (AMT): application to annular configurations

Contents

A new methodology combining acoustic simulations and LES, called AMT, was developed in the previous chapter and validated on laminar and turbulent longitudinal configurations. This tool is applied in this chapter on a simplified annular combustor to study effects of both FS and GS breaking. First, flow symmetry breaking is investigated by injecting an acoustic mode in an annular chamber with a mean azimuthal flow. As expected from theoretical results presented in Chapter 3, the initial mode is split into two distinct components leading to a warble phenomenon at low frequency. The mode structure of these two components is identified by a FFT as rotating, i.e. standing but rotating slowly at the mean flow velocity. Then GS breaking is studied by introducing Helmholtz dampers with various patterns distributed along the azimuthal direction. The dynamics of the resulting mode behavior is analyzed by changing the nature of the injected mode, from standing to spinning. It shows that breaking symmetry fixes the mode structure of the limit cycle for non-symmetric cases. However, for axisymmetric cases, the mode structure is determined by the initial state only. This application is a promising approach to study azimuthal modes in a time-domain with realistic damping mechanisms.

10.1 Introduction

The previous chapter described a new methodology called AMT to study acoustic modes in geometries with a mean flow and complex damping mechanisms. This tool was validated on laminar and turbulent longitudinal configurations. However, in modern gas turbines, thermo-acoustic modes often take the form of azimuthal modes and need to be investigated. The nature and stability of these modes have been the topic of numerous studies since the pioneering works of industrial companies like Siemens (Krebs *et al.*, 2002) or Alstom (Noiray *et al.*, 2011)but it is still an open topic today: high fidelity simulations applied to full annular configurations (Staffelbach *et al.*, 2009; Wolf *et al.*, 2012) (Fig. 9.1, right) show that azimuthal modes can randomly change in nature, evolving from spinning to standing structures at random instants. In parallel, new annular experiments developed at TU-Berlin (Moeck *et al.*, 2010; Gelbert *et al.*, 2012), Cambridge (Worth & Dawson, 2013*b*,*a*) and EM2C (Bourgouin *et al.*, 2013) prove that breaking symmetry by non-homogeneous power distribution of heating grids acting like flames (Moeck *et al.*, 2010), alternating co/counter-rotating swirlers (Worth & Dawson, 2013*b*,*a*) or distributing baffles along the annular chamber (Dawson & Worth, 2014), strongly affects the mode nature.

To complement LES and experiments, Noiray *et al.* (2011) have shown analytically on a simple annular chamber that non-linearities can also affect the limit cycle by fixing the nature of its two basic mode components. Ghirardo & Juniper (2013) have extended this model to take into account transverse velocity effects in the Flame Describing Function (Noiray *et al.*, 2008) describing the non-linear flame behavior. These non-linear theories rely on simple configurations where plenum, burners and mean flow have been removed. Yet, recent theories (Bauerheim *et al.*, 2014*a*,*e*) developed in Chapter 2 and 3

demonstrates that some linear effects cannot be ignored: breaking symmetry either by adding an azimuthal mean flow or by mixing burner types can also control the structure of the azimuthal components similarly to non-linear flame responses. However, all these theories fail to predict the ratio between these two components and new methodologies still need to be developed to study azimuthal modes.

10.2 AMT applied on a simple annular configuration

10.2.1 Objectives and annular setup

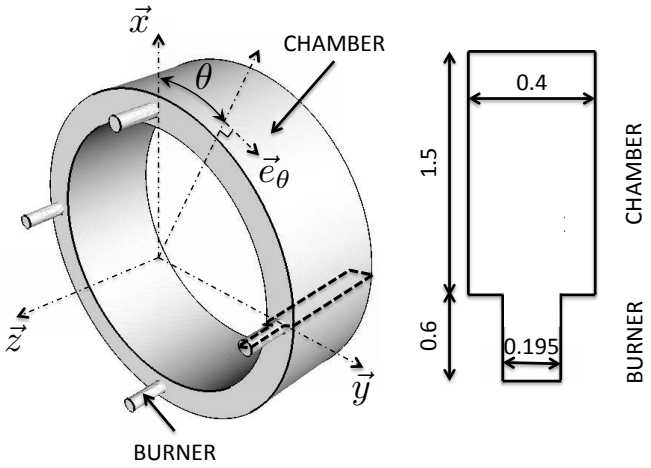

a) 3D view of the BC configuration b) Axial cut

Figure 10.1: 3D view (left) and axial cut (right) of the simplified configuration with $N = 4$ burners.

AMT is applied first on a simplified annular configuration where the rotating symmetry is broken either by FS or GS mechanism. Already studied analytically (Bauerheim *et al.*, 2014*e*) and experimentally (Moeck *et al.*, 2010; Worth & Dawson, 2013*b*,*a*), the nature and dynamics of azimuthal modes without combustion using LES can indicate that non-linearities on the flame behavior is not necessarily the only feature controlling the mode structure. The baseline configuration is a four-burner annular chamber (Fig. 10.1) without inlet, outlet or flame (no combustion, iso-thermal cases) since only geometry (Helmholtz resonators) and mean flow effects on injected azimuthal modes are investigated in this PhD:

1) **Flow Symmetry (FS) breaking:** AMT has been validated for small Mach numbers ($M < 0.1$) in Section 9.3 on longitudinal configurations and is now applied on a simple 360° case. To simplify the configuration, no inlet or outlet is introduced in the configuration. The mean azimuthal flow is therefore injected using the initial condition and walls are treated slip to minimize hydrodynamic perturbations and maintain a constant azimuthal Mach number M_θ during the simulation. Two different baseline flows are imposed as initial conditions:

a - *Quiescent flow:* The flow has no velocity ($\vec{V} = \vec{0}$) at atmospheric pressure ($P = 1013025\ Pa$) and the temperature corresponds to burnt gases ($T = 1800\ K$).

b - *Azimuthal mean flow:* An homogeneous azimuthal swirl motion (Eq. (10.1)) corresponding to $M_\theta = 0.1$ is introduced in the annular chamber to break its symmetry while no velocity is present in the surrogate burners (i.e. burners with no inlet and no flame).

$$\vec{V} = c^0 M_\theta \vec{e}_\theta = c^0 M_\theta \left(-\sin(\theta)\vec{e}_x + \cos(\theta)\vec{e}_y\right) \tag{10.1}$$

2) **Geometry Symmetry (GS) breaking:** Helmholtz resonators (Fig. 10.2) are introduced in the configuration with no mean flow to break symmetry and damp the injected azimuthal mode: both the dynamics (evolution of the nature of the azimuthal mode with time computed by the JAWA methodology presented in Chapter 8.4.2) and the damping rate α will be numerically measured. The dimensions V, L and A of the resonators are adjusted to damp the injected acoustic mode at $f^0 = 64\ Hz$:

$$f^0 = \frac{c^0}{2\pi}\sqrt{\frac{A}{VL^c}} \tag{10.2}$$

where $V = 0.125\ m^3$ is the volume of the resonator, $A = 0.00785\ m^2$ its surface and $L^c = L + \frac{8d}{3\pi} = 0.3\ m$ the corrected length depending on the diameter $d = \frac{\pi d^2}{4}$.

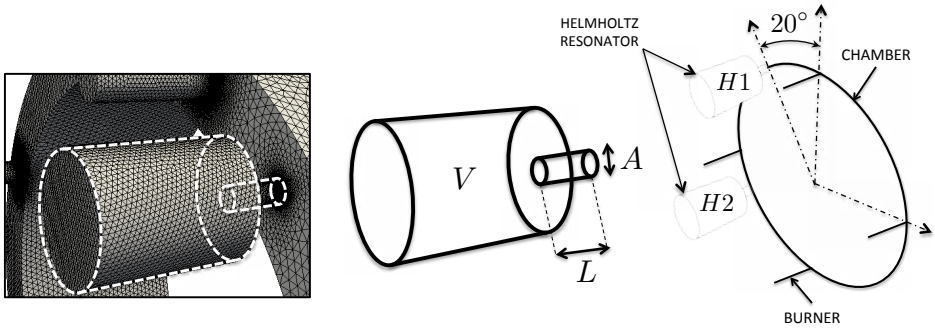

a) Mesh b) Sketch c) Localization

Figure 10.2: A) Mesh, b) sketch and c) localization of the two Helmholtz resonators introduced in the LES domain.

The different cases studied in this chapter are summarized in Fig. 10.3 and the AME methodology in Fig. 10.4. AMT requires both LES and Helmholtz simulations to be performed. The specificities of these two codes in the context of AMT applied on a annular combustor with FS and GS breaking are briefly presented in the following.

10.2.2 Large eddy simulations

Large Eddy Simulation (LES) of compressible flow is widely recognized as an accurate method (Poinsot & Veynante, 2011) to investigate acoustics in complex combustor configurations (Wolf *et al.*, 2012; Sengissen *et al.*, 2007; Fureby, 2010; Kuenne *et al.*, 2011).

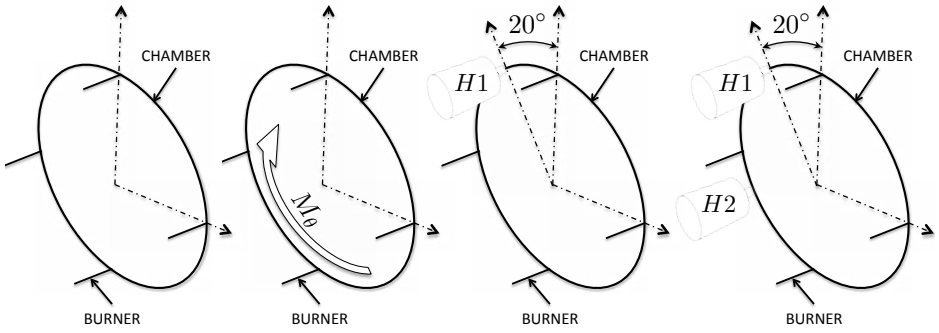

Figure 10.3: Four test cases studied: a) Quiescent flow without Helmholtz resonator, b) Swirl motion ($M_\theta = 0.1$) without Helmholtz resonator, c) Quiescent flow with one Helmholtz resonator and d) Quiescent flow with two Helmholtz resonators.

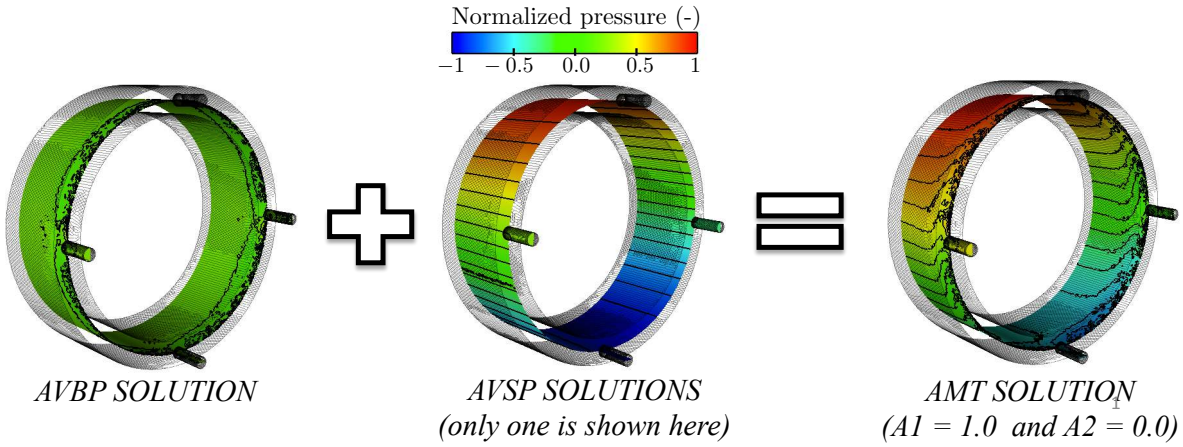

Figure 10.4: AMT methodology for annular combustors: a stable baseline flow is computed by LES (left). An acoustic solution is also computed using an Helmholtz solver (middle) and is combined with the LES baseline flow to provide a new initial solution for the LES solver (right).

To study the effect of Helmholtz resonators and mean flow on azimuthal modes dynamics, AVBP is employed again here, using a third-order spatial and temporal scheme (TTGC, Moureau *et al.*, 2005) to accurately propagate acoustic waves. Boundary conditions use the NSCBC approach (Poinsot *et al.*, 1992) to ensure reflecting/non-reflecting boundary conditions (Selle *et al.*, 2004*b*). The mean flow is introduced via the initial condition. For the case M0.1H0, a mean swirl motion (Eq. (10.1)) is imposed in the annular chamber and no velocity in the surrogate burners. The burner/chamber junctions are treated as no slip walls to avoid ill-posed problems at corners. Other walls are treated as slip walls to minimize pressure drops and to maintain the imposed mean flow as constant as possible. The swirl decay remains very small during the establishment of the acoustic cycle (typically the azimuthal mean velocity decreases by 5%). Prior to the application of the AMT methodology (Section 9.2), non-reflecting NSCBC boundary conditions (Poinsot *et al.*, 1992) are used to obtain a well established baseline flow and eliminate potential acoustic waves generated during this initialization phase. The 3D instantaneous LES

conservative variables (density ρ_{LES}, velocity $\rho\vec{V}_{LES}$ and total energy ρE_{LES}) are then extracted to be employed as a baseline flow for Helmholtz simulations (Section 10.2.3) and the application of AMT.

10.2.3 Helmholtz simulations

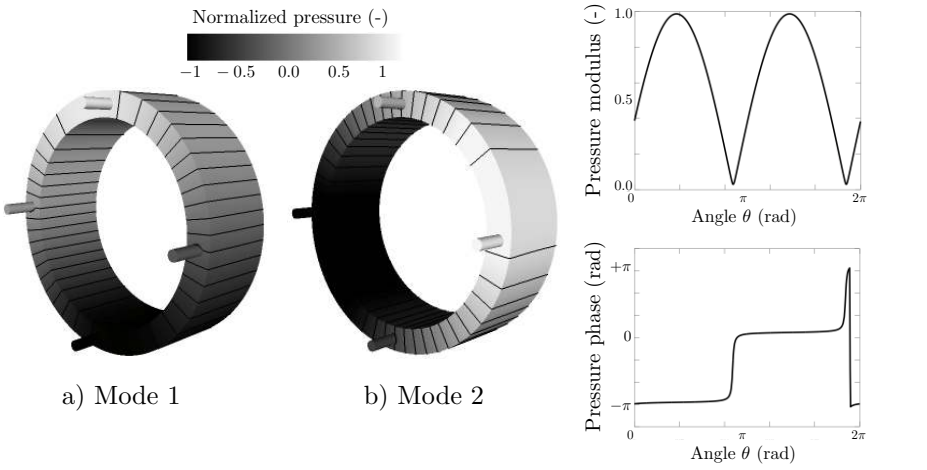

a) Mode 1 b) Mode 2

c) Pressure modulus and phase

Figure 10.5: a) and b) Normalized pressure $P_{ac} = \|\hat{P}\|\cos(\phi_p)$ fields and iso-contours for the two azimuthal modes obtained at 64 Hz reconstructed from the two outputs of the acoustic solver: c) $\|\hat{P}\|$ the pressure modulus and ϕ_p the pressure phase.

The full 3D acoustic solver called AVSP (Nicoud *et al.*, 2007) is used first to predict the azimuthal acoustic mode of the annular chamber. AVSP solves the eigenvalues problem issued from a discretization on unstructured meshes (with 1.9 millions cells) of the wave equation. Infinite impedances (corresponding to $\overrightarrow{V_{ac}} \cdot \vec{n} = 0$ where $\vec{n}$ is the wall normal) are applied on walls. Mean density and sound speed fields are extracted from the LES simulation and used as a baseline flow.

This study focuses on the first azimuthal modes of an annular chamber with four burners: as shown in Fig. 10.5, two standing modes at 64 Hz are predicted by the acoustic solver. This is a usual result at zero Mach number where the first azimuthal mode frequency is degenerate: the two modes can be combined to generate any mode structure (standing, spinning or mixed (Krebs *et al.*, 2002; Poinsot & Veynante, 2011; Evesque & Polifke, 2002)).

10.3 AMT results on the annular configuration

The AMT methodology described in Figs. 9.2 and 10.4 is then applied on the four symmetric and non-symmetric configurations presented in Fig. 10.3. The test matrix for annular configurations is summarized in Tab. 10.1. For each case, the injected acoustic mode is standing with an amplitude $\|\hat{p}\| \approx 500\ Pa$.

Cases	M_θ	Resonators	Symmetry
M0H0	0	0	Symmetric
M0.1H0	0.1	0	FS breaking
M0H1	0	1	GS breaking
M0H2	0	2	Symmetric

Table 10.1: Summary of the test cases performed on a simplified 360° annular configuration where symmetry is broken either by FS or GS mechanism by the introduction of a mean azimuthal flow or by Helmholtz resonators.

10.3.1 The symmetric case (M0H0)

First, the symmetric case without Helmholtz resonator and swirl motion is investigated (Fig. 10.3-a). A standing mode ($\alpha_1 = 500\ Pa$ and $\alpha_2 = 0\ Pa$ in Eq. (9.1)) is triggered using the AMT methodology. In this condition, the Helmholtz solver provides a solution which must match exactly the Navier-Stokes equation because the Mach number, as well as the pressure perturbation amplitude, are small. Figure 10.6 shows the result of 80 ms of the LES simulation: the amplitude remains constant, no damping is observed. The C-indicator (Wolf *et al.*, 2012; Worth & Dawson, 2013*b*) ($C(t) = \frac{1}{N}\sum_{k=1}^{N} p_k(\theta_k, t)e^{j\theta_k}$) computed from $N = 4$ equi-distributed pressure probes indicates that the mode remains standing (Appendix I). For this case, AMT performs exactly as expected.

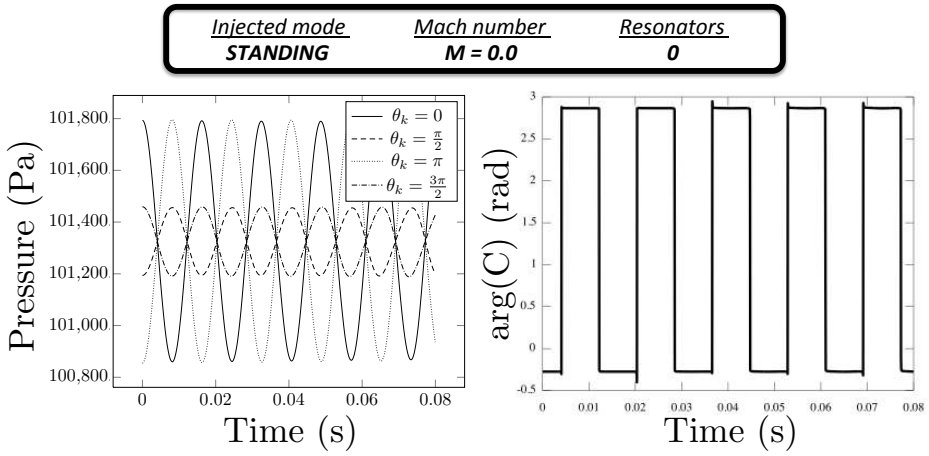

Figure 10.6: Pressure signal for the case $M0H0$ at four azimuthal locations (left) and phase of the C-indicator (right).

10.3.2 Flow symmetry breaking using a mean swirl motion (case M0.1H0)

A mean azimuthal flow is then introduced into the LES domain corresponding to $M_\theta = 0.1$ to break the axi-priodicity of the annular chamber. Recently, linear theory (Bauerheim *et al.*, 2014*e*) has shown that such a swirl motion can affect the azimuthal mode by

splitting its two components into two distinct spinning modes with different yet close frequencies f_1 and f_2 such that:

$$f_2 - f_1 = \Delta f = \frac{c^0 M_\theta}{L_c} = \frac{2}{T_c} = 12.7\ Hz \tag{10.3}$$

where $c^0 = 850\ ms^{-1}$ is the mean sound speed, $L_c = 6.7\ m$ is the half-perimeter of the annular chamber and T_c is the period of the mean flow rotation at the convective speed $u^0 = c^0 M_\theta$.

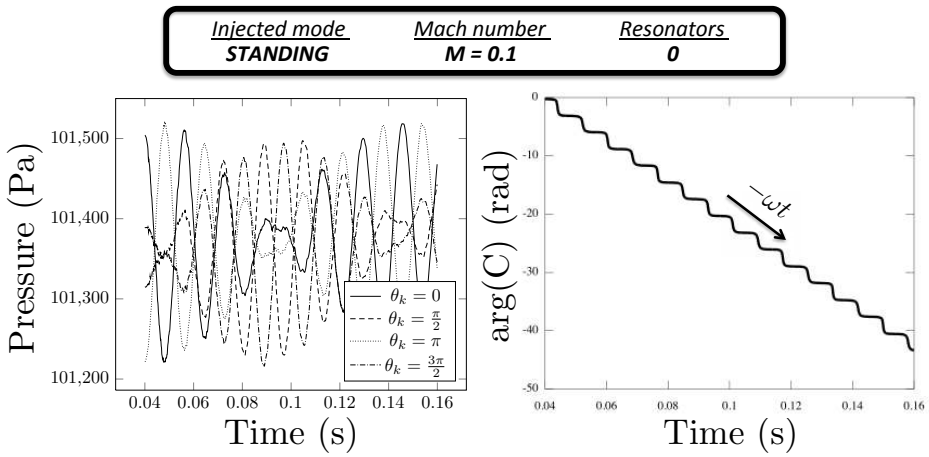

Figure 10.7: Pressure signal for the case $M0.1H0$ at four azimuthal locations (left) and phase of the C-indicator (right).

Pressure signals at different azimuthal locations θ_k (Fig. 10.7, left) show that the mode is neither standing nor spinning. The phase of the C-indicator (Fig. 10.7, right) indicates that the mode is rotating, i.e. the mode structure is standing but rotates slowly at the mean convected speed $u^0 = c^0 M_\theta$ as already observed in the full 360° LES of Wolf *et al.* (2012). This warble mode (i.e. a mode at very low frequency produced by two modes with different yet close frequencies) appears here on both the time-evolution and the Fourier analysis (Figs. 10.8 and 10.9). The measured warble frequency $f_w = \frac{1}{T_c} = \frac{\Delta f}{2} \approx 5\ Hz$ (where Δf is defined in Eq. (10.3)) leads to an estimated rotation velocity $\tilde{u^0} = 2L_c f_w \approx 67\ m/s$. This measured rotation velocity is smaller than the imposed azimuthal velocity $u^0 = 85\ m/s$ (Eq. (10.3)) due to the FTF resolution (providing f_w at $\pm 5\ Hz$) and the difficulty to maintain a constant azimuthal mean flow in the chamber.

FFT (Fig. 10.8) and DMD[1] (Fig. 10.9) of pressure signals can be compared to the symmetric case with a quiescent baseline flow: at zero Mach number ($M_\theta = 0$, left) the two components of the azimuthal modes are degenerate and share the same frequency $f = 62\ Hz$. Adding a mean swirl motion ($M_\theta = 0.1$, right) splits the azimuthal mode into two distinct components at $f^- = 55\ Hz$ and $f^+ = 65\ Hz$.

[1]The warble mode has been filtered out in the DMD post-processing to highlight the splitting between the two components at 56.6 Hz and 66.2 Hz.

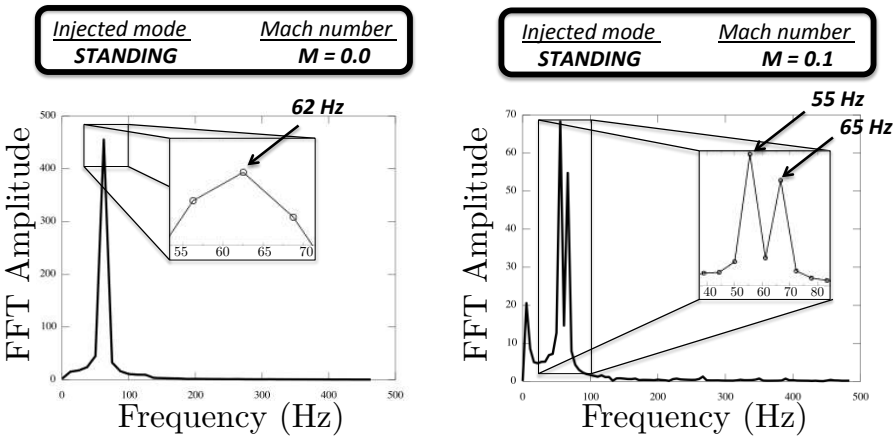

Figure 10.8: Highly resolved FTF ($\delta f = 5\ Hz$) of pressure for cases $M0H0$ (left) and $M0.1H0$ (right). At zero Mach number ($M_\theta = 0$) the two components are degenerate and share the same frequency $f = 62\ Hz$. With a mean swirl motion ($M_\theta = 0.1$), the azimuthal mode is split into two components at $f^- = 55\ Hz$ and $f^+ = 65\ Hz$ and a warble mode appears at $f_w = 10\ Hz$.

To analyze the mode structure of the two components, a Fourier Transform is performed on the whole pressure field for both the symmetric ($M0H0$) and non-symmetric ($M0.1H0$) cases. Only one component is found at $M_\theta = 0$ ($f = 62\ Hz$) while two components are obtained at 55 Hz and 65 Hz for $M_\theta = 0.1$. The associated pressure modulus and phase fields (Fig. 10.10) confirm that with no mean flow the mode is degenerate (the two components have the same frequency and structure) and remains standing (Fig. 10.10, left). The introduction of a bulk swirl however splits the mode into two spinning modes as predicted by linear analysis (Bauerheim *et al.*, 2014*e*): the co-rotating mode (Fig. 10.10, right) and a counter-rotating mode (Fig. 10.10, middle).

Indeed, adding two spinning modes with different frequencies $f^\pm = \frac{c^0(1\pm M_\theta)}{2L_c}$ but same amplitudes ($P_1 = P_2$) produces the rotating mode observed in this LES similarly to Staffelbach *et al.* (2009) and Wolf *et al.* (2012):

$$P = P_1 \cos\left(-\theta + 2\pi f^0 t + \frac{\pi c^0 M_\theta}{L_c} t\right) + P_2 \cos\left(\theta + 2\pi f^0 t - \frac{\pi c^0 M_\theta}{L_c} t\right) \quad (10.4)$$

$$= 2P_1 \cos(2\pi f^0 t)\cos(\theta - 2\pi t/T_c) \quad (10.5)$$

where $f^0 = \frac{c^0}{2L_c} \approx 62\ Hz$ is the frequency of the mode with no mean flow and $T_c = \frac{2L_c}{c^0 M_\theta} \approx 157\ ms$ is the period of rotation at the convective speed $c^0 M_\theta$ corresponding to a warble mode at the frequency $f_w = 1/T_c \approx 6\ Hz$.

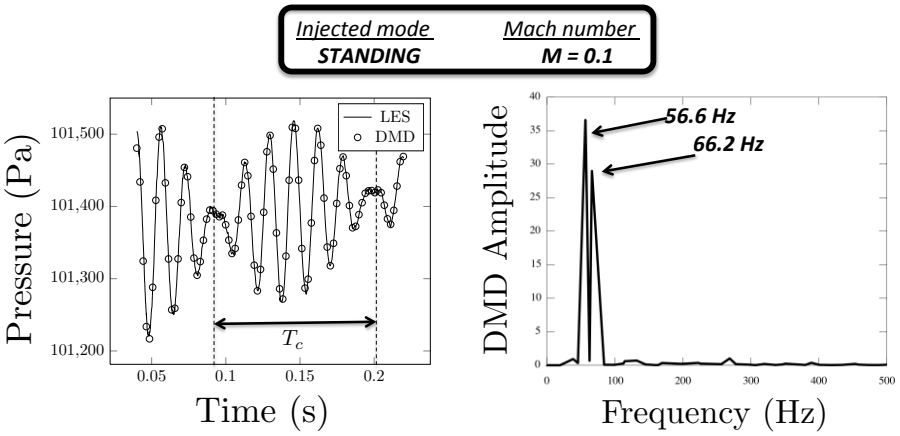

Figure 10.9: Time evolution of the pressure signal at $\theta_k = 0$ from LES and DMD reconstruction (left) and DMD spectrum (right) where low frequencies (below 20 Hz) have been filtered to highlight the two split components at 56.6 Hz and 66.2 Hz.

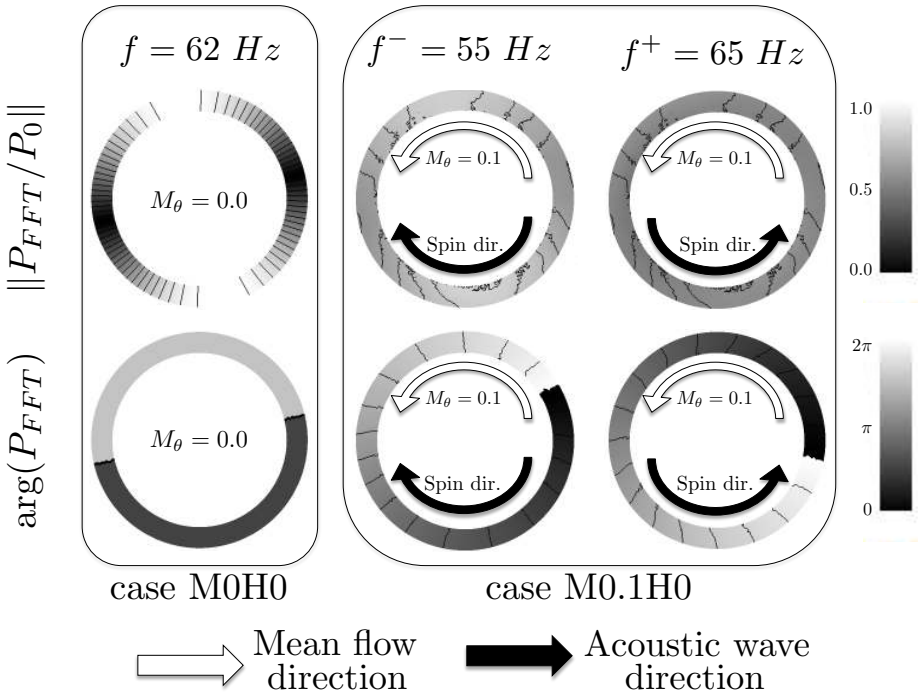

Figure 10.10: Modulus (top) and phase (bottom) of Fourier transform on pressure fields for the cases $M0H0$ (left) and $M0.1H0$ (middle and right). Mean swirl and acoustic wave directions are displayed to identify the contra-rotaing mode (middle) and the co-rotating mode (right).

10.3.3 Geometry Symmetry breaking using one Helmholtz resonator (case M0H1)

Stow & Dowling (2003) have shown that Helmholtz resonators can damp an azimuthal mode and suggest optimal locations of these damping devices. This can be tested using AMT. First, one Helmholtz resonator is introduced in the annular chamber to break symmetry (Figs. 10.2 and 10.3). Pressure signals at four probes (Fig. 10.11) located near the surrogate burners indicate that one mode is damped while the other is still present: the mode is split into two distinct components. The associated C-indicator shows that the azimuthal mode, initially standing at $t = 0\ ms$ (a- in Fig. 10.11), becomes spinning (b- in Fig. 10.11) until the limit cycle is reached at $t = 300\ ms$ (c- in Fig. 10.11), where the mode is standing again but imposing a pressure node at the Helmholtz resonator location.

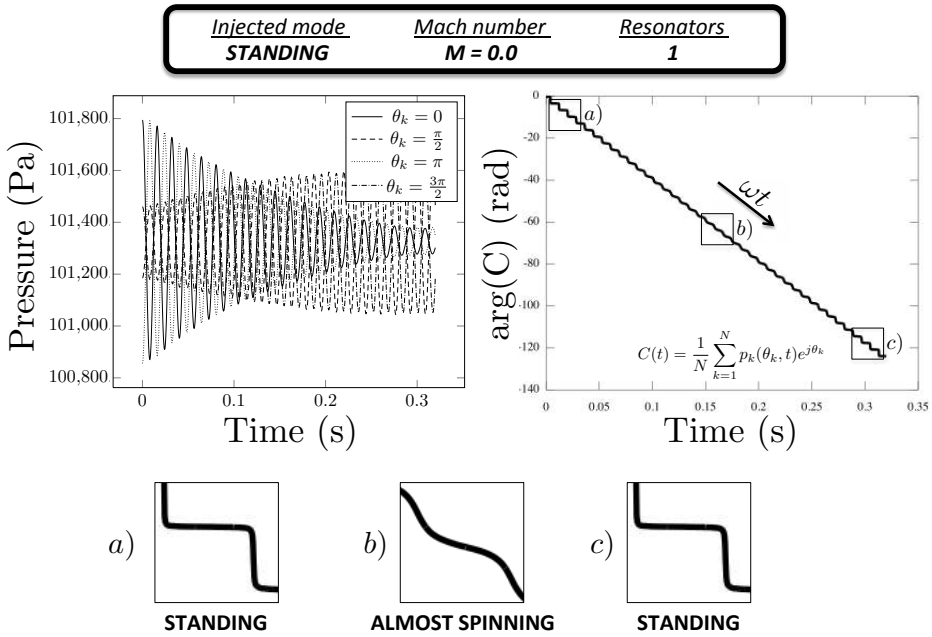

Figure 10.11: Pressure signals (left) and C-indicator (right) for the case $M0H1$: the azimuthal is split into two components with different growth rates. One is amplified while the other is damped. The nature of the mode is changing (bottom) from a) standing to b) almost spinning and finally c) standing.

To analyze these dynamic phases (standing - spinning - standing), a Sliding Fourier Transform (SFT) of the pressure field is performed. It focuses on three particular periods:

- From 0 ms to 50 ms (a- in Fig. 10.12): it corresponds to the injected standing mode.
- From 100 ms to 150 ms (b- in Fig. 10.12): a transient phase occurs where the nature changes, the azimuthal mode evolving from standing to spinning.
- From 270 ms to 320 ms (c- in Fig. 10.12): the limit cycle is reached and corresponds to a standing mode imposing a pressure node at the Helmholtz resonator location ($\times$ in Fig. 10.12).

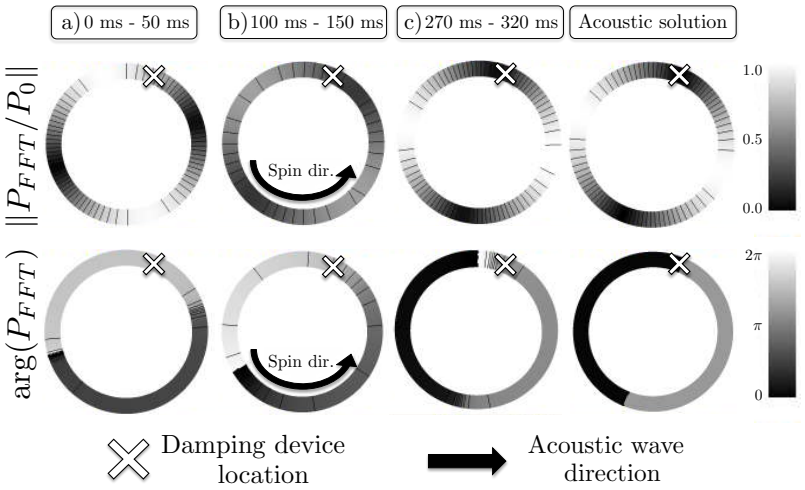

Figure 10.12: Sliding Fourier Transform (SFT) of the pressure field for the $M0H1$ case at three different time: a) initial standing mode (time from 0 ms to 50 ms), b) transient spinning mode (time from 100 ms to 150 ms) and c) final standing mode imposing a pressure node at the Helmholtz resonator location identified by $\times$ (time from 270 ms to 320 ms). In addition, the linear acoustic solution is displayed (right) showing a good agreement with the limit cycle (c).

In addition, the acoustic mode of the M0H1 case is also computed by a Helmholtz solver (Section 10.2.3). The mode (the damped component is not shown here) structure obtained (a standing mode imposing a pressure node at the Helmholtz resonator location) is in good agreement with the limit cycle observed in the LES (c- in Fig. 10.12) which demonstrates that linear analysis is able to predict structure of modes even in the limit cycle when no combustion occurs. As explained in (Bauerheim *et al.*, 2014*e*), the linear analysis provides here good estimations of mode structure because the mode nature is mainly controlled by the splitting due to the introduction of one damping device and not the non-linearities. These results show that breaking symmetry by introducing one Helmholtz resonator splits the azimuthal mode into two components which can have radically different behaviors and frequencies. This is the main specificity of azimuthal modes in non-symmetric annular combustors compared to simpler longitudinal modes with only one component or azimuthal modes in purely axisymmetric configurations where the two components are degenerate (i.e. with the same characteristics) (Bauerheim *et al.*, 2014*e*).

10.3.4 Symmetric case using two Helmholtz resonators (case M0H2)

As suggested by Stow & Dowling (2003), a second Helmholtz resonator has to be introduced to damp the two components of the azimuthal modes: the two damping devices are placed at 90° from each other (Fig. 10.3, d) to symmetrize the annular chamber and to efficiently damp the acoustic mode. Indeed, the theory developed for GS breaking in Chapter 2 proves that a splitting occurs if and only if $\gamma(\pm 2p) = 0$ where p is the azimuthal mode order (here $p = 1$) and γ is the Fourier transform of the asymmetry pat-

tern: $\gamma(k) = \sum_{i=0}^{N-1} \Gamma_i^0 e^{-j2ki\pi/N}$. For example, the previous case studied in Section 10.3.3 has introduced one Helmholtz resonator in the annular chamber with $N = 4$ sectors. If there is one resonator at the i^{th} junction between sectors, the coupling parameter is set to $\Gamma_i^0 = 1$ for the sake of simplicity here, while it is null ($\Gamma_i^0 = 0$) otherwise. Consequently, its asymmetry pattern is $s_1 = [1\ 0\ 0\ 0]$ and its Fourier transform $\gamma = \hat{s}_1 = [1\ 1\ 1\ 1]$: the splitting coefficients are $\gamma(\pm 2) = 1$ (corresponding to the third coefficient of $\hat{s}_1$ since Fourier coefficients are ranked from the 0^{th} to the $N - 1^{th}$) so that a splitting occurs, as shown in Fig. 10.11. However, introducing an other similar Helmholtz resonator at 90° modifies the asymmetry pattern (now $s_2 = [1\ 1\ 0\ 0]$) and its Fourier transform becomes $\hat{s}_2 = [2\ 1-j\ 0\ 1+j]$: the coefficients $\gamma(\pm 2)$ are now zero showing that the configuration is symmetric and that no splitting should occur. It is interesting to note that placing the second resonator at 180° instead of 90° would lead to $s_3 = [1\ 0\ 1\ 0]$ and $\hat{s}_3 = [2\ 0\ 2\ 0]$ indicating that the configuration is not symmetric ($\gamma(\pm) = 2$).

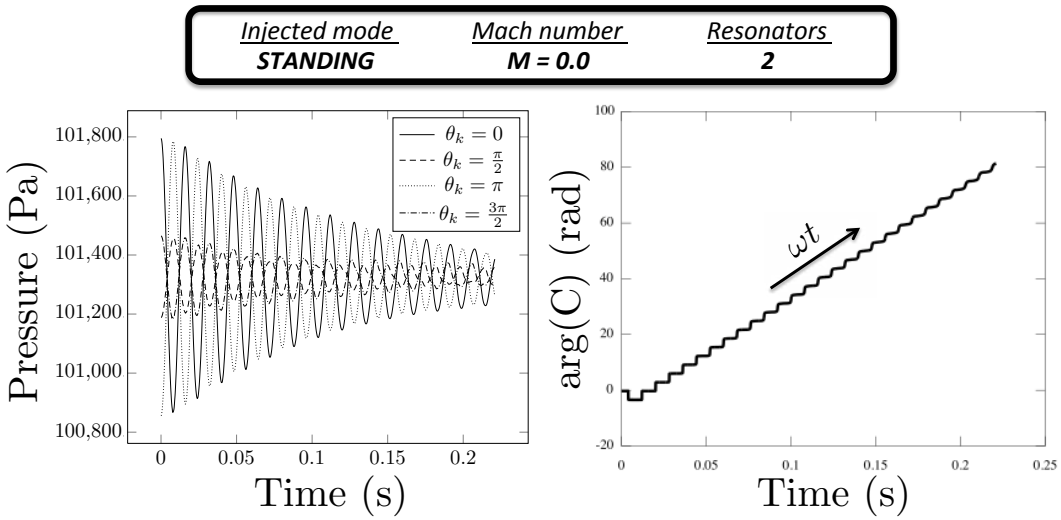

Figure 10.13: Pressure signals (left) and C-indicator (right) for the case $M0H2$: the two components of the azimuthal modes are damped with the same damping rate estimated at $\alpha = 1.0\ s^{-1}$.

Pressure signals at four probes (Fig. 10.13) located near the surrogate burners indicate that the two components are damped. The associated C-indicator shows that the azimuthal mode, initially standing at $t = 0\ ms$ becomes spinning in the clockwise direction. To numerically estimate the damping/growth rates of each component, a linear mode reconstruction is performed on the azimuthal mode. The generic form of the linear mode reconstruction is assumed to follow:

$$P_{rec} = \bar{P}_0 + \mathcal{A}e^{\alpha t}cos(2\pi ft + \phi_0) \tag{10.6}$$

where $\bar{P}_0 = 1.013\ 10^5\ Pa$ is the mean value of the pressure signal, $\mathcal{A}$ is the pressure amplitude, α is the growth or damping rate of the mode, f is the estimated frequency and ϕ_0 is a phase to match the initial pressure observed in the LES. Linear mode reconstruction using Eq. (10.6) is performed on the azimuthal mode (Fig. 10.14) using parameters described in Tab. 10.2. Both components are damped and have the same frequencies

(62.5 Hz) and growth rates ($\alpha \approx -7\ s^{-1}$): the mode is degenerate (i.e. the two components have the same characteristics) because the introduction of the second damping device has symmetrized the configuration. Note however that non-linear effects appear for low pressure amplitudes registered in the probe located at $\theta_k = \frac{\pi}{2}$ (and $\theta_k = \frac{3\pi}{2}$ not shown here) in Fig. 10.14.

Components	**Location**	$\mathcal{A}$	α	**f**	ϕ_0
Damped	$\theta_k = 0$	450 Pa	$-7\ s^{-1}$	62.5 Hz	0
Damped	$\theta_k = \frac{\pi}{2}$	125 Pa	$-7\ s^{-1}$	62.5 Hz	π

Table 10.2: Parameters used for the linear reconstruction with two Helmholtz resonators.

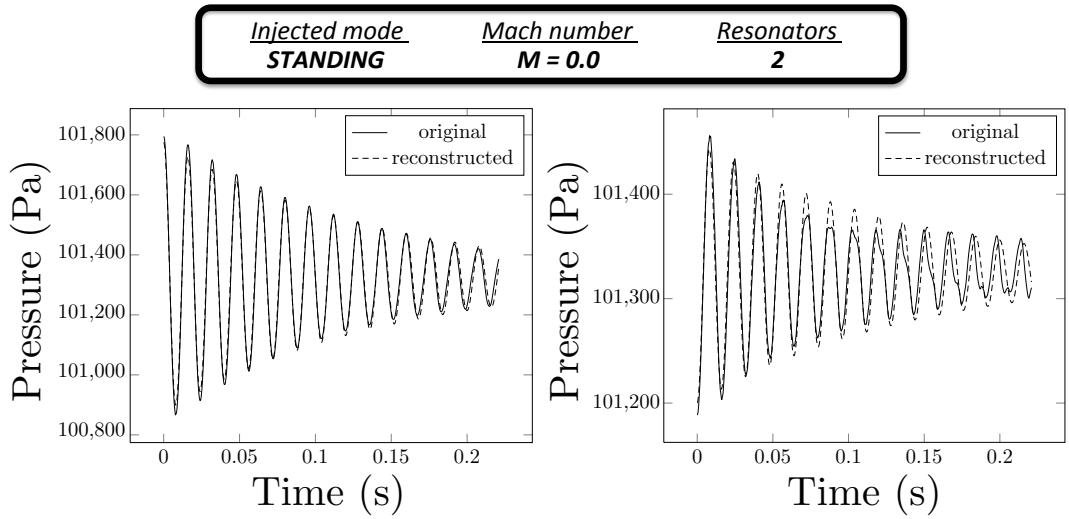

Figure 10.14: Pressure oscillations observed in the LES (——) for two probes located at $\theta_k = 0$ (left) and $\theta_k = \frac{\pi}{2}$ (right). Mode reconstruction with $\mathcal{A} \approx 450\ Pa$, $f \approx 62.5\ Hz$ and $\alpha \approx -7\ s^{-1}$ (- - - , left) and $\mathcal{A} \approx 125\ Pa$, $f \approx 62.5\ Hz$ and $\alpha \approx -7\ s^{-1}$ (····· , right).

10.4 Mode dynamics analysis: time-evolution of the azimuthal mode nature

Finally, the dynamics of azimuthal modes is unveiled for the three cases at null Mach number ($M0H0$, $M0H1$ and $M0H2$) by extracting the envelope $A^{\pm}(t)^2$ of the two components $q^{\pm} = \hat{p} \pm \rho_0 c_0 \hat{u}_\theta$ of each mode using the JAWA methodology (Section 8.4.2).

[2]The envelope extraction of the signal $q(t)$ is performed using the JAWA methodology using a filtered Hilbert transform: 1) the Hilbert transform $\mathcal{H}(q)$ is computed 2) the envelope defined by $A(t) = \sqrt{q^2 + \mathcal{H}(q)^2}$ is obtained and 3) a low-pass filtering of the envelope A(t) is performed to smooth out spurious oscillations.

Figure 10.15 shows the time evolution of the two envelopes $A^{\pm}$ for each case with iso-structure lines (i.e. constant ratio A^+/A^-, -·-·-) and iso-energy circles (i.e. constant acoustic energy[3] $E_{ac} = \frac{\hat{p}^2}{2\rho_0 c_0^2} + \frac{\rho_0}{2}\hat{u}^2$, ·····):

- **Case M0H0 :** (a) the injected mode is initially standing ($A^+ = A^-$) and remains the same because no damping, asymmetry or combustion are introduced (b).
- **Case M0H1 :** (a) the injected mode is initially standing leading to $A^+ = A^-$ but (b) because of the Helmholtz resonator, the mode rotates to impose a pressure node at the Helmholtz resonator location and cancel its effect (c): therefore the mode is finally standing ($A^+ = A^-$). Because of the damping device, acoustic energy has been dissipated leading to smaller final values of $A^{\pm}$. This result is consistent with the FFT analysis displayed in Fig. 10.12.
- **Case M0H2 :** (a) the injected mode is initially standing ($A^+ = A^-$) (b) damping devices dissipate the injected acoustic energy which leads to a decrease of the envelopes $A^{\pm}$. Compared to the previous case $M0H1$, the configuration is symmetric and only weakly affects the initial mode structure: the acoustic mode remains standing while it is dissipated by the two Helmholtz resonators. Nevertheless, the mode structure slightly drifts toward the clockwise spinning region at low amplitude as already shown by the C-indicator in Fig. 10.13

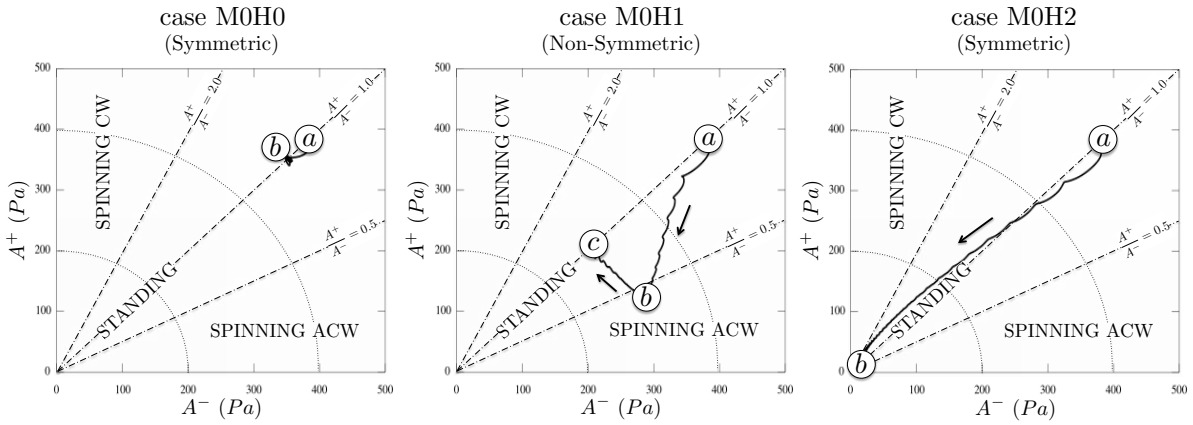

Figure 10.15: Time evolution of the two filtered envelopes of the waves $q^{\pm} = \hat{p} \pm \rho_0 c_0 \hat{u}_\theta$ in the cases at null Mach number $M0H0$ (left), $M0H1$ (middle) and $M0H2$ (right). -·-·- : Iso-structure lines $\frac{A^+}{A^-} = 0.5$, 1.0 and 2.0 ; ····· : Iso-energy circles. The initial injected modes are standing ($A^+ = A^-$).

Initializing similar cases to $M0H0$, $M0H1$ and $M0H2$ but with a clockwise (CW) spinning mode ($A^+/A^- = 4$) instead of a standing mode ($A^+/A^- = 1$) results in evolution shown in Fig. 10.16 where the time-evolution of mode dynamics for each case is:

- **Case M0H0 :** (a) the injected mode is initially spinning and remains the same (b) since no damping, asymmetry or combustion is introduced.

[3]Acoustic energy can be recast using the two waves $q^{\pm} = \hat{p} \pm \rho_0 c_0 \hat{u}$ as follow: $E_{ac} = \frac{\hat{p}^2}{2\rho_0 c_0^2} + \frac{\rho_0}{2}\hat{u}^2 = \frac{1}{4\rho_0 c_0^2}(q^{+2} + q^{-2})$. Therefore, iso-contours of acoustic energy in the diagram (q^+, q^-) or (A^+, A^-) are circles of radius $2c_0\sqrt{\rho_0 E_{ac}}$.

- **Case M0H1 :** (a) the injected mode is initially spinning ($A^+/A^- = 4$) but (c) because of the Helmholtz resonator the mode evolves and finally imposes a pressure node at the Helmholtz resonator location (after an overshoot (b)) to finish as standing ($A^+ = A^-$) . Because of the damping device, acoustic energy has been dissipated leading to smaller values of $A^{\pm}$.
- **Case M0H2 :** (a) the injected mode is initially spinning and (b) damping devices dissipate the injected acoustic energy which leads to a decrease of the envelopes $A^{\pm}$. Compared to the previous case $M0H1$, the configuration is symmetric and only weakly affects the initial mode structure: the acoustic mode remains spinning while it is dissipated by the Helmholtz resonators.

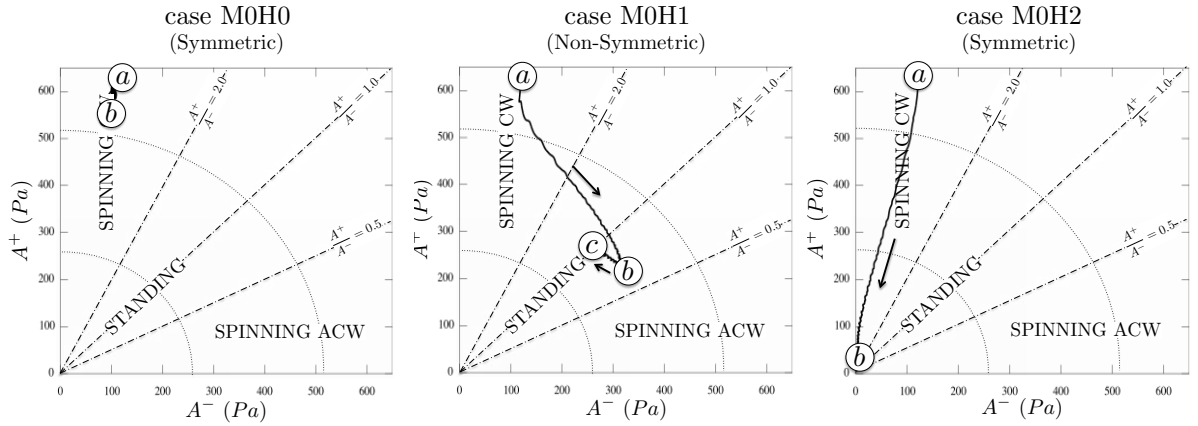

Figure 10.16: Time evolution of the two filtered envelopes of the waves $q^{\pm} = \hat{p} \pm \rho_0 c_0 \hat{u}_\theta$ in the cases at null Mach number $M0H0$ (left), $M0H1$ (middle) and $M0H2$ (right). -·-·- : Iso-structure lines $\frac{A^+}{A^-} = 0.5$, 1.0 and 2.0 ; ····· : Iso-energy circles. The initial injected modes are spinning in the clockwise direction ($A^+/A^- \sim +4$).

Figures 10.15 and 10.16 show that when the configuration is symmetric ($M0H0$ and $M0H2$), the initial ratio A^+/A^- remains constant. However, as soon as symmetry is broken ($M0H1$), the ratio A^+/A^- is not conserved and the final structure is fixed by the asymmetry of the system (here standing due to the Helmholtz resonator) as predicted by Bauerheim *et al.* (2014*e*). It proves that without combustion, the mode structure is fixed by the asymmetries of the system which can be due to an azimuthal mean flow, the introduction of one Helmholtz resonator or by mixing burners.

10.5 Conclusion

This paper presents a methodology called AMT (Acoustic Mode triggering) to study acoustic mode dynamics in annular configurations: an acoustic mode computed by a Helmholtz solver is properly introduced into the LES domain to avoid computing the transient period and study the limit cycles. In particular, this approach can provide a numerical estimation of the damping/growth rate of the injected mode. The AMT method is then applied on a simplified annular combustor with four surrogate burners

(no inlet and no combustion) to study two mechanisms controlling azimuthal modes by breaking the axi-periodicity of the annular chamber: 1) the introduction of one Helmholtz resonator and 2) the existence of a mean azimuthal flow. Results show that symmetry breaking, either by adding a Helmholtz resonator or with a swirl motion, splits the azimuthal mode into two components which can have different frequencies and growth rates. Because of this splitting, one Helmholtz resonator cannot damp completely the azimuthal mode: only one component is damped while the other remains present in the annular chamber. However, symmetrizing the configuration by adding a second Helmholtz resonator leads to a degenerate mode: the two components have the same frequencies and growth rates: both components are damped and the damping rate is numerically obtained via a linear mode reconstruction. Finally, the time-evolution of azimuthal mode dynamics is obtained by the JAWA methodology for the three cases at null Mach number showing both the asymmetry and damping devices effect on mode nature. This study proves that the dynamics of azimuthal modes can be investigated using LES combined with Helmholtz simulations. Results are in good agreement with recent linear theories which substantiates that non-linearities are not the only feature controlling the limit cycle.

Conclusion and Perspectives

The present PhD thesis deals with the fundamental aspects of symmetry breaking in azimuthal combustion instabilities and follows previous works performed at CERFACS on theory (Parmentier *et al.*, 2012) and LES (Wolf *et al.*, 2010, 2012) and at Cambridge and EM2C on the first annular experiments dedicated to azimuthal combustion instabilities (Worth & Dawson, 2013*b*,*a*; Dawson & Worth, 2014; Bourgouin *et al.*, 2013; Bourgouin, 2014). The objective was to propose and develop a novel approach and ideas on a major question encountered in the field of combustion instabilities: which key parameters control the stability and the nature of azimuthal modes ? Numerous studies have treated this problem experimentally (Krebs *et al.*, 2001; Moeck *et al.*, 2010; Worth & Dawson, 2013*b*; Bourgouin, 2014), numerically (Wolf *et al.*, 2010, 2012; Campa *et al.*, 2011) and theoretically (Parmentier *et al.*, 2012; Noiray *et al.*, 2011; Noiray & Schuermans, 2013; Ghirardo & Juniper, 2013) but usually emphasize on non-linear effects due to combustion. However, the recent experiment built at Cambridge has indicated that breaking the rotating symmetry, either by alternating different swirler types (Worth & Dawson, 2013*a*) or by introducing baffles distributed along the annular chamber (Dawson & Worth, 2014), can affect the mode nature. In addition Noiray & Schuermans (2013) also pointed out the possible effect of turbulence on the mode switching observed experimentally and on real gas turbines (Krebs *et al.*, 2001).

To investigate this new idea of symmetry breaking and unravel potential effects or even passive control techniques, the whole range of tools, from theory to full LES of the complete annular combustor, has been explored. Development of new theories (ATACAMAC, Parmentier *et al.*, 2012; Bauerheim *et al.*, 2014*d*,*a*,*e*,*c*) and tools (AMT, UQ, Bauerheim *et al.*, 2014*b*) are also required to cope with the extreme complexity of combustion instabilities in complex annular combustion chambers. Major results are summarized in the following.

Theoretical approaches

The preliminary work of Schuller *et al.* (2012) for longitudinal cases and Parmentier *et al.* (2012) for simple annular combustors was extended to more complex annular geometries to unravel coupling mechanisms between cavities. This analytical tool, called ATACAMAC provides the first fully analytical expression of the parameters controlling azimuthal modes in an annular chamber with identical or different burners, with or without mean flow.

ATACAMAC is a unique tool because it allows to study azimuthal modes directly on an analytical framework without any numerical method. For example, ATACAMAC, shows that bifurcations may occur where the annular plenum and chamber become strongly coupled which profoundly changes the stability of the whole system (Chapter 4). Validations against a full 3D acoustic tool demonstrate a good agreement between theory and acoustic simulations. Then, ATACAMAC is used to unveil key parameters on the stability of azimuthal modes. First, a generalization of the work of Parmentier *et al.* (2012) to a configuration with an arbitrary number of burners and allowing for asymmetry in the system shows that two parameters are controlling the mode in the low coupling factor limit (Chapter 2): (1) a coupling strength Σ_0 corresponding to the mean flame effect and (2) a splitting strength $\mathcal{S}_0$ associated to the symmetry breaking. Symmetry can be broken by distributing different burner types along the azimuthal direction, as done for a long time by Siemens using CBO devices on some of their burners (typically 20) and not on the others (typically 4). This type of asymmetry is called geometrical symmetry breaking (GS) and promotes standing modes. A second type of symmetry breaking, called flow symmetry (FS) breaking, is then investigated theoretically in Chapter 3 showing that a mean azimuthal Mach number can also split the azimuthal mode into two distinct components with a specific structure: this type of symmetry breaking promotes spinning modes. Finally, theory of symmetry breaking is applied on a more realistic combustion chamber containing 19 burners. The strongly coupled regime, where a full analytical solution is not known today, is investigated using a UQ methodology called Active Subspace (Chapter 5). This new method is able to reduce the size of the uncertain input space from 38 to juste a few key parameters and proves that symmetry breaking can be induced by uncertainties on the geometry or the flame models. It reveals that combustion instabilities are very sensitive to subtle changes in the chamber design. More importantly, it suggests that controlling azimuthal modes in real industrial gas turbines requires to control manufacturing margins.

This theoretical work and the ATACAMAC tool give promising results but still require future studies. More specifically:

- The strongly coupled regime is observed in many industrial applications (Campa *et al.*, 2011) but analytical studies fail to uncover this problem. More investigations, either by theory if possible or using numerical tools are needed to fully understand coupling mechanisms in axisymmetric configurations with multiple annular cavities
- Symmetry breaking in PBC configurations at high coupling factors need to be studied. Indeed, no benefit of breaking the rotating symmetry by mixing different burner types is demonstrated when coupling factors are small. However, at high coupling factors, symmetry breaking could potentially add degrees of freedom to control these modes and therefore require further investigations.
- The present ATACAMAC tool is limited to pure azimuthal modes, a limitation due to the outlet boundary condition. This limitation restrains the present work to the first azimuthal mode of industrial combustors with a chocked nozzle and fails to predict mixed modes in academic annular rig open to the atmosphere. Therefore, an extension of the quasi-one-dimensional ATACAMAC tool to a two-dimensional tool accounting for an arbitrary outlet impedance is an important path to follow.

In particular, the question of outlet impedance effects on the stability of the mode could be answered, which is still en open question today. This is one possible explanation of the difference between industrial gas turbines proned to azimuthal modes and academic configurations where azimuthal combustion instabilities are less frequent, longitudinal modes often dominating.

- For the first time UQ methodologies were applied on a thermo-acoustic problem. This path should be followed to treat more complex problems, for instance with a higher number of input parameters or by using more expensive tools such as Helmholtz solvers.
- Finally, more theories should focus on acoustic damping which is a key parameter controlling the stability of acoustic mode but only a few studies address this problem. This topic is currently investigated at CERFACS and should be continued.

Large Eddy Simulation of forced and self-excited azimuthal modes

Large Eddy Simulation is a promising tool to understand underlying phenomena leading to combustion instabilities since driving but also damping mechanisms are resolved. This PhD thesis has focused first on demonstrating the capability of such a tool to predict accurately the flame-acoustic interaction by computing Flame Transfer Functions of a single-sector of the Cambridge annular combustion chamber (Chapter 7). Results show that LES models do not affect the FTFs in this case and reveal key parameters controlling the azimuthal modes: the fuel type, the heat losses at walls and the azimuthal confinement. Combining these LES results with an Helmholtz solver computing acoustics in the full annular case demonstrates the accuracy of LES predictions, validated against experimental observations. Then, LES of the 360° configuration has been compared to experimental data provided by Cambridge (Worth & Dawson, 2013*b*,*a*; Dawson & Worth, 2014). Due to its extreme cost, only the growth phase is studied in this PhD and shows a good agreement with experimental observations. In particular, it reveals that the start-up procedure generates multiple modes in both the LES and in the experiment which complicates the understanding of key phenomena driving the instabilities and therefore methods to suppress them. Typically, the azimuthal mode grows together with a longitudinal mode, making the analysis complicated. A new post-processing methodology, called JAWA, is also developed to systematically analyze the mode nature and its dynamics even when short signals are provided. Only a few works on full LES of annular combustor have been conducted until now but this effort must be continued and complement experiments:

- A complete validation of a full annular LES against experiment is still missing due to the difficulty to represent experimental features in LES (for example here the annular plenum with sand, grids etc.). In that view, simulations and experiments in this field should be developed side-by-side and not separately.
- Even if mechanisms leading to combustion instabilities are well known in gaseous simple longitudinal premixed configurations, methodologies still lack for simulations with multiphase flows or multiple inputs - single output (MISO), sush as

complex industrial configurations with multipoint injection systems, effusive plates and complex swirlers where fuel and air are injected at different locations. Usually, these complex cases are treated by forcing one or only a few entries of the system which leads to an incomplete answer on combustion instabilities.

- A particular emphasis should be made on multiphase flows which are encountered in many industrial gas turbines. The first simulations of forced multiphase flow LES have been conducted in this PhD but not discussed in this thesis for confidentially purposes. These simulations have shown that numerous mechanisms due to liquid transport and the evaporation process lead to gaseous fuel oscillations and can impact the stability of the system. These multiphase mechanisms are less documented than pure gaseous ones and should be explored intensively using both LES and experiments. In particular, specific damping mechanisms are present in multiphase flows but are complex and not yet fully understood. An important research effort must be made in that direction.
- In general, damping mechanisms are needed for a complete framework on combustion instabilities. LES is a promising tool to build models for theories or low order models and acoustic tools. This path is currently followed at CERFACS and should be continued.

Acoustic Mode Triggering: a novel approach to study combustion instabilities

A novel methodology combining LES and Helmholtz simulations, called Acoustic Mode Triggering (AMT), is developed in this PhD thesis. It allows the study of acoustic modes in the time-domain at low cost. First, validation on simple laminar configurations have been conducted and show a very good accuracy (error is of the order of 10^{-2}) on the frequency and growth predictions at low Mach numbers (until $M = 0.1$). This tool is then applied on a longitudinal turbulent case. It offers a new method to study the cross-interaction between acoustics and turbulence. In particular, it proves that turbulence can trigger acoustic modes and that acoustic can affect back the turbulence by modifying its production and dissipation as observed on energy spectrum results. Finally, AMT is applied on simplified annular configurations to study the effects of both FS and GS breaking on azimuthal modes. Results are promising and show good agreement with the theoretical work developed in Part I of this thesis. Moreover, it allows the study of mode nature and its dynamics and reveal that: (1) Symmetry breaking affects the mode nature and (2) in axisymmetric configurations the nature is mainly impose by the initial state when no combustion occurs. This novel approach has shown interesting results and therefore needs to be applied on more complex configurations to investigate driving and damping mechanisms of combustion instabilities:

- Usually turbulence and acoustic interactions are investigated by forcing acoustic waves at the inlet or by pulsating walls. AMT provides here a third approach which deserves to be further exploited. In particular, the theoretical result of Noiray & Schuermans (2013) about turbulence affecting the azimuthal mode nature can be

investigated using AMT.

- The present work focused only on Helmholtz resonators. Other damping devices or mechanisms can be studied using AMT. In particular, baffles have been distributed along an academic chamber to analyze their impact on both stability and the nature of the unstable acoustic mode in a recent experimental work (Dawson & Worth, 2014). Moreover, mode conversion between acoustic waves into other forms like vorticity or entropy waves could be investigated using this approach. AMT appears as a potential efficient tool to build new damping models for low order and acoustic tools.
- In this PhD, AMT is applied only on configurations with no combustion. Flames should be introduced to investigate the effects and interactions between symmetry breaking and non-linear flame behavior in annular combustors and compare results to recent theories (Noiray *et al.*, 2011; Bauerheim *et al.*, 2014*e*,*a*).

Symmetry breaking in the aeroacoustic field

Symmetry breaking appears in a wide range of physical problems. A new perspective of this work is therefore the application of the theoretical background developed in Part I to other physical phenomena, especially in aeroacoustics. For instance, Fig. 10.17 (LES, left) shows the noise produced by a main landing gear (Giret *et al.*, 2013) which exhibits similar behaviors as ones observed in this thesis: coupling between the two cavities in the wheels (here in opposite phase) and GS symmetry breaking due to the vertical leg. AVSP simulations of the configuration with (Fig. 10.17, bottom right) and without (Fig. 10.17, top right) leg highlights both the coupling and the symmetry breaking effects on the mode structure and frequencies: similarly to Chapter 2, the symmetry breaking leads to a standing mode (constant phase, not shown here) and a frequency splitting $\Delta f \simeq 32\ Hz$ which may either destabilize the configuration, increase noise generation or lead to potential warble phenomena at low-frequencies. This recent observation requires further investigations, in particular using theory to complement numerical and experimental efforts.

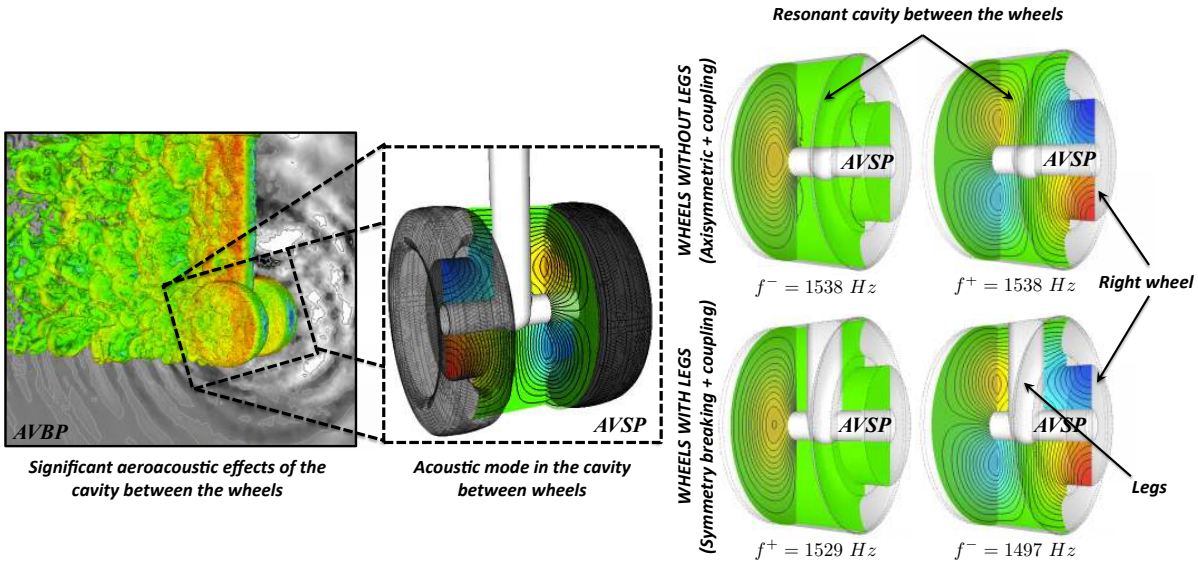

Figure 10.17: LES of an aircraft main landing gear (Lagoon project, left) and pressure fluctuations obtained by AVSP (middle) for the configuration with (right, bottom) and without (right, top) the vertical leg. Both coupling and symmetry breaking are observed and lead to a frequency splitting $\Delta f \simeq 32\ Hz$.

Publications

This work has lead to the following publications and conferences:

Ranked *A* papers

- M. Bauerheim, J-F. Parmentier, P. Salas, F. Nicoud and T. Poinsot *An analytical model for azimuthal thermo-acoustic modes in annular chamber fed by an annular plenum*, **Combustion and Flame**, 2014, 161, p. 1374-1389
- M. Bauerheim, F. Nicoud and T. Poinsot *Theoretical analysis of the mass balance equation through a flame at zero and non-zero Mach numbers*, **Combustion and Flame** (accepted, 2014, in press)
- M. Bauerheim, P. Salas, F. Nicoud and T. Poinsot *Symmetry breaking and control of azimuthal thermoacoustic modes in annular chambers*, **Journal of Fluid Mechanics** (accepted 2014, in press)
- M. Bauerheim, G. Staffelbach, N.A. Worth, J.R. Dawson, L. Gicquel and T. Poinsot *Sensitivity of LES-based flame transfer function for turbulent swirled flames and impact on the stability of azimuthal modes*, **35th International Symposium on Combustion** (accepted 2014, in press)
- M. Bauerheim, M. Cazalens and T. Poinsot *A theoretical study of mean azimuthal flow and asymmetry effects on thermoacoustic modes in annular combustors*, **35th International Symposium on Combustion** (accepted 2014, in press)

Conferences

- E. Courtine, L. Selle, F. Nicoud, W. Polifke, C. Silva, M. Bauerheim and T. Poinsot *Causality and intrinsic thermoacoustic instability modes*, **Proceedings of the Summer Program**, CTR Stanford 2014
- M. Bauerheim, A. Ndiaye, P. Constantine, G. Iaccarino, S. Moreau and F. Nicoud *Uncertainty Quantification of thermo-acoustic modes in annular combustors*, **Proceedings of the Summer Program**, CTR Stanford 2014
- M. Juniper, L. Magri, M. Bauerheim and F. Nicoud *Applications of adjoint methods in thermoacoustics*, **Proceedings of the Summer Program**, CTR Stanford 2014
- *A simple analytical model to study combustion instabilities in annular combustors*, **EuroMech colloquium 546 on acoustics** (Italy, May 2013)
- *Multiphase flow LES study of the fuel split effects on combustion instabilities in an ultra low-NOx annular combustor*, **ASME Turbo Expo 2015** (under review)
- *Uncertainty Quantification of thermoacoustic instabilities in a swirled stabilized combustor*, **ASME Turbo Expo 2015** (under review)
- *Numerical investigation of azimuthal combustion instabilities in annular combustors*, **CRCT Centrale Paris**, 2014
- *Development of ultra lean combustion systems for high OPR engines*, **3AF conference** 'Greener Aviation: Clean Sky breakthroughs and worldwide status' (Belgium, March 2014)

Appendix A

Analytical expression of the splitting strength

The general analytical expression of the splitting strength $\mathcal{S}_0$ is:

$$\mathcal{S}_0^2 = \sum_{i,k=1}^{N} \Gamma_i^0 \Gamma_k^0 \cos\left(\frac{4p\pi}{N}[k-i]\right) \tag{A.1}$$

Using $\cos(a-b) = \cos(a)\cos(b) + \sin(a)\sin(b)$ one may recast the splitting strength as:

$$\mathcal{S}_0^2 = \left[\sum_{i=1}^{N} \Gamma_i^0 \cos(4p\pi i/N)\right]^2 + \left[\sum_{i=1}^{N} \Gamma_i^0 \sin(4p\pi i/N)\right]^2$$

The above equation can be recast using the identity $a^2 + b^2 = (a+jb)(a-jb)$ where $j^2 = -1$:

$$\mathcal{S}_0^2 = \left[\sum_{i=1}^{N} \Gamma_i^0 e^{j4p\pi i/N}\right] \times \left[\sum_{i=1}^{N} \Gamma_i^0 e^{-j4p\pi i/N}\right] = \gamma(-2p) \times \gamma(2p) \tag{A.2}$$

where $\gamma(k)$ is the k^{th} Fourier coefficient of the asymmetry pattern Γ^0 defined as $\gamma(k) = \sum_{i=1}^{N} \Gamma_i^0 e^{-j2\pi ki/N}$.

Finally, the splitting strength is:

$$\mathcal{S}_0 = \sqrt{\gamma(2p) \times \gamma(-2p)} \tag{A.3}$$

The splitting strength obtained in the previous equation (A.3) gives some useful results:

- **1)** Noiray *et al.* (2011) obtained a similar result where the splitting strength is controlled only by $\gamma_{HR}(2p)$, the $2p^{th}$ Fourier coefficient of the heat-release distribution. Equation (A.3) is a generalization of such a result: the network model developed in this paper retains more geometry and flow features than the simple annular rig

considered in (Noiray *et al.*, 2011). In particular, it is shown here that the mode is controlled by the azimuthal distribution of the coupling parameter (which includes the active flame ($n-\tau$ model) but also the geometry characteristics, the upstream impedance Z of the burners as well as the difference between cold and burnt gases). It appears that all these features can effect the whole asymmetry of the system and therefore the stability and, consequently, cannot be neglected when studying combustion instabilities.

- **2)** If all coupling factors are the same (symmetric configuration), then the spectrum $\gamma(k)$ is null everywhere except for $k=0$ or $k=N$ (where $\gamma(0)=\gamma(N)=\Sigma^0=\sum_{i=1}^{N}\Gamma_i^0$ is the total coupling of the system) which leads to two types of azimuthal modes:
  a) If p is not $N/2$, N, $3N/2$ etc. then $\gamma(\pm 2p)=0$ and the splitting strength is null:

$$\mathcal{S}_0 = 0 \tag{A.4}$$

  These modes are characterized by no splitting: the two components of the azimuthal mode have the same frequencies and growth rates. They are called "degenerate doublets".
  b) However, if $p=N/2$, N, $3N/2$ etc. then $\gamma(\pm 2p)=\sum_{i=1}^{N}\Gamma_i^0=N\Gamma^0$ which gives:

$$\mathcal{S}_0 = N\Gamma^0 \tag{A.5}$$

  These modes are characterized by a strong splitting: the two components of the azimuthal mode have different frequencies and growth rates. They are called "non-degenerate singlets".
- **3)** If only two types of burner are introduced in the combustion chamber (i.e. coupling factors can only take the value Γ_1^0 or Γ_2^0 for $i\in[1,N]$), then for mode satisfying $p\neq N/2, N, ...$ the splitting strength $\mathcal{S}_0$ can be decomposed as:

$$\mathcal{S}_0 = \overbrace{2\mathcal{K}}^{\text{Imposed by the pattern}} \underbrace{\left(\Gamma_1^0-\Gamma_2^0\right)}_{\text{Imposed by the difference between burner types 1 and 2}} \tag{A.6}$$

where the reduced splitting strength $\mathcal{K}$ depends only on the asymmetry pattern and $(\Gamma_1^0-\Gamma_2^0)$ is fixed by the burner characteristics.

Proof:
The Fourier coefficient $\gamma(k)$ can be viewed as a polynomial of degree one with N indeterminates (or variables) Γ_i^0 and coefficients depending on the asymmetry pattern. When considering only two burner types (corresponding to coupling factors Γ_1^0 and Γ_2^0), $\gamma(k)$ reduces to a polynomial of only two variables. The previous point

(2) proves that for modes satisfying $p \neq N/2, N, ...$ the splitting strength and therefore $\gamma(\pm 2p)$ are null when $\Gamma_1^0 = \Gamma_2^0$. As $\Gamma_1^0 - \Gamma_2^0$ is a common root of $\gamma(\pm 2p)$ which are one-degree polynomials, they can be recast as:

$$\gamma(2p) = \alpha_{2p}(\Gamma_1^0 - \Gamma_2^0) \quad \text{and} \quad \gamma(-2p) = \alpha_{-2p}(\Gamma_1^0 - \Gamma_2^0) \tag{A.7}$$

where α_{2p} and α_{-2p} depend only on the asymmetry pattern. Consequently, using equation (A.3), the splitting strength reads:

$$\mathcal{S}_0 = \sqrt{\alpha_{2p}(\Gamma_1^0 - \Gamma_2^0) \times \alpha_{N-2p}(\Gamma_1^0 - \Gamma_2^0)} = \underbrace{\sqrt{\alpha_{2p}\alpha_{N-2p}}}_{2\mathcal{K}}(\Gamma_1^0 - \Gamma_2^0) \tag{A.8}$$

Appendix B

Summary of the analytical method providing the stability map of the p^{th} azimuthal mode

This Section summarizes the analytical method to provide the stability map of the p^{th} azimuthal mode of a chamber with N burners.

- **1)** Compute the coupling factors of each burner:

$$\Gamma_i^0 = -\frac{j}{2}\frac{S_i}{S_c}\frac{\mathbb{F}^0 C_{1-\alpha}^{k^0}[jS_\alpha^{k_u^0}Z + C_\alpha^{k_u^0}] + S_{1-\alpha}^{k^0}[jC_\alpha^{k_u^0}Z - S_\alpha^{k_u^0}]}{\mathbb{F}^0 S_{1-\alpha}^{k^0}[jC_\alpha^{k_u^0} - S_\alpha^{k_u^0}Z] + C_{1-\alpha}^{k^0}[C_\alpha^{k_u^0}Z + jS_\alpha^{k_u^0}]} \tag{B.1}$$

  where $\mathbb{F}^0 = \frac{c^0\rho^0}{c_u^0\rho_u^0}(1 + n_i e^{j\omega^0\tau_i})$, $C_x^y = cos(xyL_i)$, $S_x^y = sin(xyL_i)$, $k^0 = \omega^0/c^0$, $k_u^0 = \omega^0/c_u^0$, Z is the upstream impedance and $\omega^0 = \frac{p\pi c^0}{L_c}$.
- **2)** Compute the total "coupling strength" $\Sigma_0 = \sum_{i=1}^{N}\Gamma_i^0$.
- **3)** Compute the "splitting strength" $\mathcal{S}_0$:

$$\mathcal{S}_0 = \sqrt{\sum_{i,j=1}^{N}\Gamma_i^0\Gamma_j^0 cos\left(\frac{4p\pi}{N}(j-i)\right)} = \sqrt{\gamma(-2p)\gamma(2p)} \tag{B.2}$$

  where $\gamma(k)$ is the k^{th} Fourier coefficient of the asymmetry pattern.
- **4)** The p^{th} azimuthal mode is composed of two modes V^+ and V^- with the same order p but different wavenumber perturbations $\epsilon^\pm$ given by:

$$\epsilon^+ = -\frac{1}{2}(\Sigma_0 + \mathcal{S}_0) \quad \text{and} \quad \epsilon^- = -\frac{1}{2}(\Sigma_0 - \mathcal{S}_0) \tag{B.3}$$

- **5)** Then compute the complex frequency of the system from the definition of the wavenumber perturbation ($k^\pm L_c = \frac{2\pi f^\pm}{c^0}L_c = p\pi + \epsilon^\pm$) and equation (B.3):

$$f^\pm = \frac{pc^0}{2L_c} - \frac{c^0(\Sigma_0 \pm \mathcal{S}_0)}{4\pi L_c} \tag{B.4}$$

- **6)** Finally, the two components of the p^{th} azimuthal mode can have different frequencies ($f^+ \neq f^-$, non-degenerate singlets) if $\mathcal{S}_0 \neq 0$ or the same frequencies ($f^+ = f^-$, degenerate doublets) if $\mathcal{S}_0 = 0$. The growth rate of each mode is obtained from the imaginary part of the complex frequency obtained in equation (B.4):

$$\text{Growth rate}^{\pm} = Im(f^{\pm}) = -\frac{c^0}{4\pi L_c} Im\left(\Sigma_0 \pm \mathcal{S}_0\right) \tag{B.5}$$

Appendix C

Effect of non-linearities on symmetry breaking in annular combustors

This PhD. thesis focuses on the linear regime using $n-\tau$ or FTF models. This appendix however briefly describes a non-linear approach for ATACAMAC, similar to the one developed by Silva *et al.* (2013) to study its impact on symmetry breaking in annular gas turbines, recently observed by Ghirardo *et al.* (2015). This appendix tries to explain this non-linear behavior using the physical interpretation developed all along this PhD thesis and more specifically by relating non-linearities and the splitting strength coefficient.

For a set of FTF's (i.e. $(n_i, \tau_i)_{i=1..N}$), the ATACAMAC tool provides the corresponding frequency and growth rate of the azimuthal acoustic mode. As proposed by Silva *et al.* (2013), this linear analysis can be extended to non-linear regimes by introducing FDF's (i.e. $(n_i(\hat{u}_i), \tau_i(\hat{u}_i))_{i=1..N}$) firstly proposed by EM2C (Noiray *et al.*, 2008), which depend on the acoustic velocity level at the burner locations. Thus, the methodology follows four steps:

(1) A very small velocity perturbation $\hat{u}_i^0$ is imposed at the initial time $t = t^0$. At the initial time step, all burners have the same perturbation.
(2) The $FDF(\hat{u})$ is interpolated a the level $\hat{u}_i^0$, which provides a set $(n_i^0, \tau_i^0)_{i=1..N}$.
(3) ATACAMAC is used to predict the complex frequency ω associated to $(n_i^0, \tau_i^0)_{i=1..N}$.
(4) The frequency and growth rate are used to construct a new velocity perturbation $\hat{u}_i$ at the time $t = t^0 + \Delta t$:
(1 bis) The new velocity perturbation is used to interpolate the FDF's at the next step.

$$\hat{u}_i(t^0 + \Delta t) = \hat{u}_i(t^0) e^{-j\omega\Delta t} \tag{C.1}$$

To illustrate this methodology and non-linear behaviors of acoustic modes, a few examples are proposed here based on a PBC configuration (2 annular cavities) with $N = 4$ burners, similar to the one studied previously in this manuscript:

- **Example 1) Stable mode with standard FTF or FDF:** As shown in Fig. C.1, an arbitrary FDF and its associated FTF are chosen. The methodology proposed is performed focusing on the first azimuthal mode (the plenum mode at about 58 Hz). The velocity perturbation is rebuilt using Eq. (C.1) and is displayed in Fig. C.2. Since the mode is stable, no difference is observed between the FTF and

the FDF computations. It is worth noting that such a time-domain analysis using ATACAMAC is efficient to compute long time signals, information that cannot provide LES because of its extreme cost.

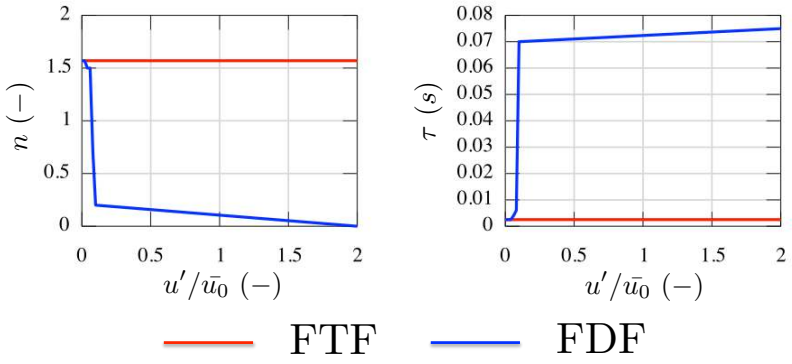

Figure C.1: FDF and its associated FTF choosen arbitrary here.

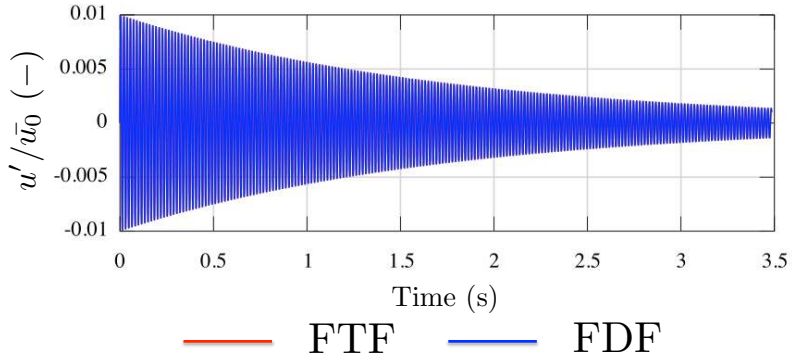

Figure C.2: Acoustic velocity perturbation of the first azimuthal mode varying in time at one burner location rebuilt using Eq. (C.1) for both FTF and FDF. Since the mode is stable, no difference between FTF and FDF is observed.

- **Example 2) Unstable mode with standard FTF or FDF:** The same FTF and FDF presented in Fig. C.1 are used but now ATACAMAC focuses on the second azimuthal mode (the chamber mode at about 90 Hz) of the configuration. Fig. C.3 shows that the mode is unstable. Compared to the FTF formulation, a limit cycle appears when using a FDF which proves, as suggested by Silva *et al.* (2013), that such an approach can incorporate non-linear behaviors into tools initially designed for the linear regime. First, for $t < 0.7s$, the amplitude and time-delay obtained by the FTF and FDF are similar and therefore both formulations leads to an unstable mode. Then, for t around $0.7s$ the FTF and FDF differ leading to different ATACAMAC predictions. In this case, the growth rate is lower when using a FDF than with a FTF, leading to a saturation effect. For $t > 0.7s$, the FTF still leads to an unstable mode while the FDF leads to a null growth rate estimation: the mode is non-linearly stable and the limit cycle appears.

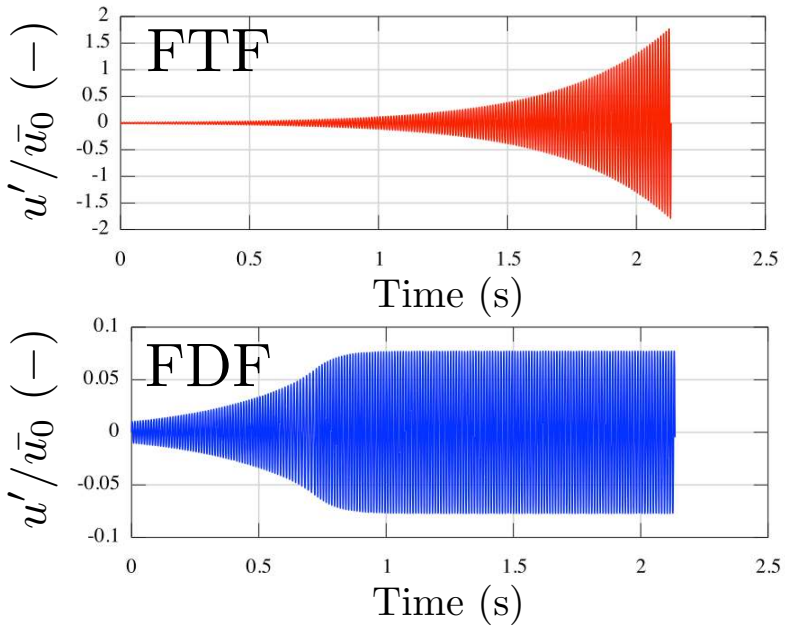

Figure C.3: Acoustic velocity perturbation of the second azimuthal mode varying in time at one burner location rebuilt using Eq. (C.1) for both FTF and FDF. The mode is found unstable and a limit cycle appears when using the FDF formulation.

- **Example 3) Mode switching and non-linear triggering:** Example 2 has shown that simple non-linear behaviors can be observed using the ATACAMAC tool (designed for the linear regime) accompanied with a FDF formulation. In this example, the same configuration is studied but with a different FDF (Fig. C.4) to highlight more complex non-linear phenomena such as mode switching and non-linear triggering. Figure C.5 displays the acoustic velocity perturbation varying in time at one burner location rebuilt using Eq. (C.1). At the initial time, the first azimuthal mode at 58 Hz is stable and the second azimuthal mode at 90 Hz is unstable. As soon as the acoustic velocity grows, the FDF is changing, leading to a case where the plenum and the chamber become strongly coupled (Bauerheim *et al.*, 2014*d*). Then, the non-linearities trigger the plenum mode which is now unstable. The acoustic perturbation growing, the plenum and chamber become again uncoupled. However, now, the chamber is stable while the plenum is unstable. Finally, the instability was triggered by the chamber mode at 90 Hz, but the limit cycle corresponds to the plenum mode at 58 Hz. Zooms on the mode switching (from chamber to plenum mode, bottom left) and on the limit cycle of the triggered plenum azimuthal mode (bottom right) are also given in Fig. C.5.

These few examples have examplified the ATACAMAC capability to retrieve some non-linear behaviors of azimuthal modes. The question asked now is "how non-linearities can affect azimuthal modes, and especially the symmetry breaking ?". Indeed, Ghirardo *et al.* (2015) have recently proven mathematically that non-linearities of the flame model can lead to a symmetry breaking. This idea is developed here using the ATACAMAC formulation, while Ghirardo *et al.* (2015) have used a full non-linear formulation, but on

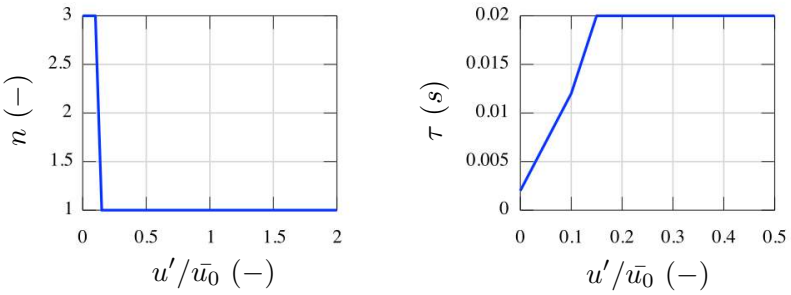

Figure C.4: FDF chosen for Example 3 to highlight mode switching and non-linear triggering.

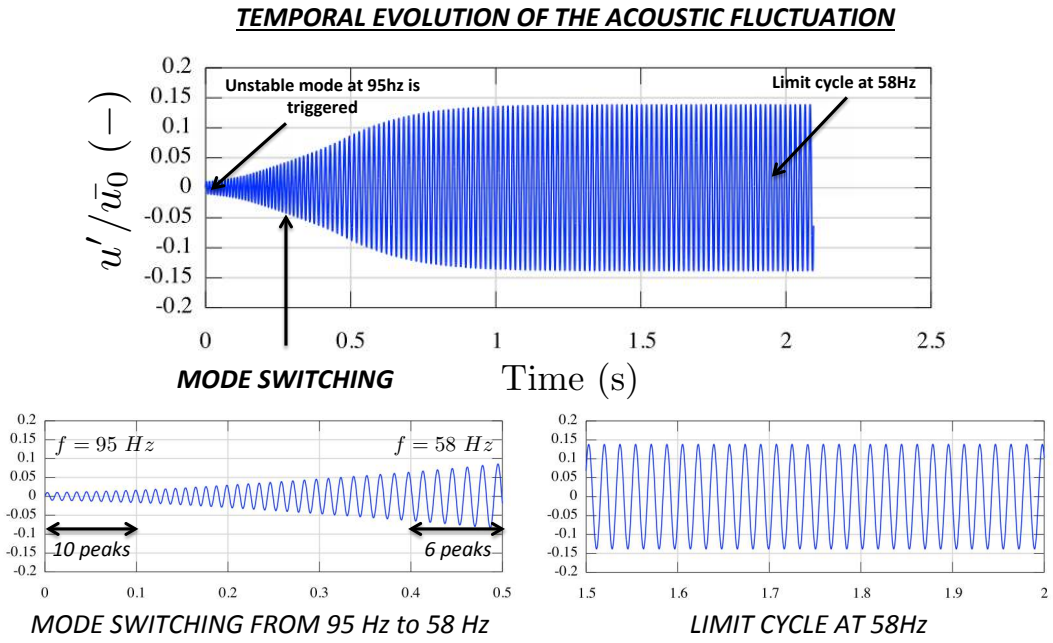

Figure C.5: Acoustic velocity perturbation of a strongly coupled mode (plenum/chamber) varying in time at one burner location rebuilt using Eq. (C.1). At the initial time the first azimuthal mode is stable while the second one is unstable. When the acoustic velocity grows, the FDF is changing leading to a mode switching (from a chamber to a plenum mode, bottom left). The final limit cycle corresponds to the plenum azimuthal mode initially stable (bottom right).

a simple annulus, as firstly proposed by Noiray *et al.* (2011) and extended by Ghirardo & Juniper (2013).

The idea proposed by Ghirardo *et al.* (2015) can be reformulated using the ATACAMAC formulation as follows: in a symmetric configuration, all flames are supposed identical, meaning that all flames have the same behavior characterized by their FTF or FDF. In other words, all flames have the same set $(n_i(\hat{u}_i,\omega),\tau_i(\hat{u}_i,\omega))$. In the FTF formulation, it implies that all flames have exactly the same (n,τ) and therefore the configuration is fully symmetric. However, in the non-linear regime, flames located at a velocity node and velocity anti-node will behave now differently: typically, flames at velocity nodes are characterized by $(n_i(\hat{u}_i,\omega),\tau_i(\hat{u}_i,\omega)) = (n_i(0,\omega),\tau_i(0,\omega)) = (n_{FTF},\tau_{FTF})$ while flames at velocity anti-nodes are described by $(n_i(\hat{u}_i,\omega),\tau_i(\hat{u}_i,\omega)) = (n_{FDF},\tau_{FDF}) \neq (n_{FTF},\tau_{FTF})$.

Consequently, as shown in Fig. C.6, the configuration is symmetric (left) but the solution is asymmetric (right). This asymmetry can be physically explained by the AT-ACAMAC formulation developed all along this PhD thesis: as displayed in Fig. C.6, the network model associated to the configuration with non-linear flames is not symmetric and the asymmetry pattern is directly linked to the azimuthal mode order p ($p = 1$ in Fig. C.6). Indeed, the FDF is usually, not a function of the velocity perturbation $\hat{u}$ itself, but rather a function of its module $\|\hat{u}\|$. For the case with $N = 4$ burners, it suggests that the two flames located at a velocity anti-node have the same $n - \tau$ parameters ($\circ$, subscript FDF) while the two other flames have different $n - \tau$ parameters ($\bullet$, subscript FTF because at a velocity node). Consequently, the asymmetry pattern is $\circ \bullet \circ \bullet$ which leads to a strong splitting strength (see Parmentier *et al.*, 2012; Bauerheim *et al.*, 2014*a*, for details about splitting effects with the asymmetry pattern $\circ \bullet \circ \bullet$): it shows that non-linearities can break the symmetry of the annular configuration. This GS breaking induces a splitting effect, which increases while the differences between $n_{FDF} - n_{FTF}$ and $\tau_{FDF} - \tau_{FTF}$ increase. More generally, an azimuthal mode of order p (i.e. $\hat{u} \sim \sin(p\theta)$) has a modulus, and therefore an asymmetry pattern due to non-linearities in the flame model, varying like $\|\hat{u}\| \sim \|\sin(p\theta)\|$ with a Fourier spectrum $\mathcal{F}[\|\hat{u}\|](k) = -\frac{2}{\pi(4k^2-1)}\delta(k - 2np)$ where $n \in \mathbb{Z}$[1]. Thus, since the splitting strength $\mathcal{S}_0$ is associated to the Fourier coefficient $\pm 2p^{th}$ of the asymmetry pattern, non-linearities can affect strongly the symmetry of the configuration leading to a non-null splitting effect increasing with the difference between the FTF (at velocity nodes) and the FDF (at velocity anti-nodes) but decreasing with the azimuthal mode order (since the Fourier coefficient varies like $\frac{1}{\pi(8p^2-1)}$).

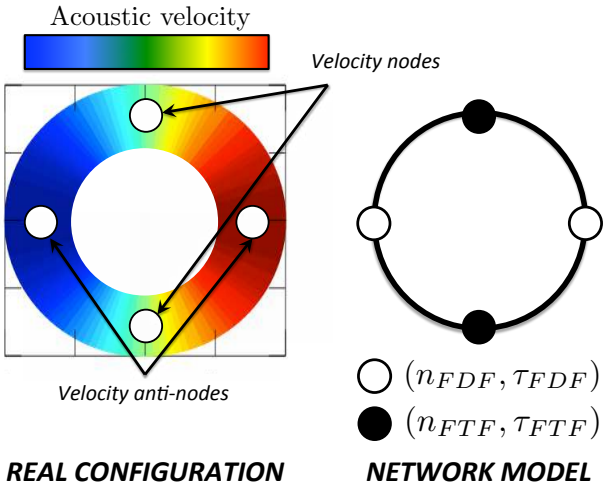

Figure C.6: First azimuthal mode in an annular cavity with $N = 4$ burners highlighting velocity nodes and anti-nodes (left) and its associated network model (right). Because of the FDF formulation, flames located at a velocity anti-nodes have different $n - \tau$ parameters than flames located at velocity nodes.

[1]One can prove that $\|sin(p\theta)\| = \frac{2}{\pi}\sum_{k\in\mathbb{Z}} \frac{sin^2(kp\theta)}{k^2-1/4} = -\frac{2}{\pi}\sum_{k\in\mathbb{Z}} \frac{1}{4k^2-1} e^{2jkp\theta}$ so that its spectrum is $-\frac{2}{\pi(4k^2-1)}\delta(k - 2np)$ where $n \in \mathbb{Z}$, thus with a strong $k = \pm 2p^{th}$ Fourier coefficient associated to the fact the $\|\hat{u}\|$ has a period two times small than $\hat{u}$

Appendix D

Analytical dispersion relation of a PBC configuration with a single burner ($N = 1$)

The analytical dispersion relation (Eq. (4.25)) is obtained for a general PBC configuration with N burners. To explain the ATACAMAC approach leading to the analytical eigenfrequencies of the system, the case of a single burner ($N = 1$) will be detailed[1].

Considering only one burner, the transfer matrix $M = R_1 T_1 - Id$ of the whole system is:

$$M = \begin{bmatrix} \cos(2k_u L_p) - 1 & -\sin(2k_u L_p) & \\ \sin(2k_u L_p) + 2\cos(2k_u L_p)\Gamma_1 & -2\sin(2k_u L_p)\Gamma_1 + \cos(2k_u L_p) - 1 & \dots \\ 0 & 0 & \\ 2\cos(k_u L_p)\Gamma_3 & -2\sin(2k_u L_p)\Gamma_3 & \end{bmatrix}$$
$$\begin{bmatrix} 0 & 0 \\ \dots \quad 2\cos(2kL_c)\Gamma_2 & -2\sin(2kL_c)\Gamma_2 \\ \cos(2kL_c) - 1 & -\sin(2kL_c) \\ \sin(2kL_c) + 2\cos(2kL_c)\Gamma_4 & -2\sin(2kL_c)\Gamma_4 + \cos(2kL_c) - 1 \end{bmatrix} \tag{D.1}$$

In the general case with N burners, a Taylor expansion of this matrix has to be performed as a first simplification. Here, the matrix is simple enough to compute analytically the determinant leading to the exact dispersion relation:

$$\begin{aligned} & (\Gamma_1\Gamma_4 - \Gamma_2\Gamma_3)\sin(2kL_c)\sin(2k_u L_p) \\ + \; & 2\Gamma_1[1 - \cos(2kL_c)]\sin(2k_u L_p) \\ + \; & 2\Gamma_4[1 - \cos(2k_u L_p)]\sin(2kL_c) \\ + \; & 4[1 - \cos(2kL_c)][1 - \cos(2k_u L_p)] = 0 \end{aligned} \tag{D.2}$$

The dispersion relation Eq. (D.2) is non-linear. The idea is to use a Taylor expansion at the second (or third) order and to solve it analytically. The expansion has to be done

[1]Since there is only one burner, the index i has been omitted to simplify notations (e.g Γ_1 instead of $\Gamma_{i=1,1}$)

around a FDCp (i.e. $kL_c = p\pi + \epsilon_c$) or FDPp (i.e. $k_u L_p = p\pi + \epsilon_p$) mode (see Section 4.3.3 for details). For instance, in the case of the WCC1 mode ($kL_c = \pi + \epsilon$ which implies $k_u L_p = \beta(\pi + \epsilon_c)$ where $\beta = \frac{c^0 L_p}{c_u^0 L_c}$), the dispersion relation Eq. (D.2) becomes:

$$[\cos(2\pi\beta) - 1][\epsilon_c \Gamma_4^0 + \epsilon_c^2 + o(\epsilon_c^2)] = 0 \tag{D.3}$$

where Γ_4^0 is the value of Γ_4 evaluated at $kL_c = p\pi$

Note that solutions of Eq. (D.3) being $\epsilon_c = -\Gamma_4^0$, it justifies that the term $\epsilon_c \Gamma_4^0$ is of the same order of magnitude than ϵ_c^2 and therefore has to be kept in the analytical dispersion relation Eq. D.2.

Analytical dispersion relations for $N > 1$ are more complex to derive but follow a similar procedure. When $N = 4$, the dispersion relation of Tab. (D.1) are obtained:

Type	Odd/Even	Second-order dispersion relation ($o(\epsilon^2)$)
WCC	Odd	$\sin(p\pi\beta)[\epsilon^2 + 4\epsilon\Gamma_4^0 + 4\Gamma_4^{0^2}] = 0$
	Even	$\sin(p\pi\beta/2)[\epsilon^2 + 4\epsilon\Gamma_4^0] = 0$
WCP	Odd	$\sin(p\pi/\beta)[\epsilon^2 + 4\epsilon\Gamma_1^0 + 4\Gamma_1^{0^2}] = 0$
	Even	$\sin(p\pi/(2\beta))[\epsilon^2 + 4\epsilon\Gamma_1^0] = 0$

Table D.1: Analytical expressions of wave number perturbation for WCCp and WCPp azimuthal modes

Appendix E

Stability criterion of weakly coupled modes for a four burners configuration ($N = 4$)

A mode is stable if the imaginary part of the wave number is negative. Table E.1 shows analytical expressions of the wave number perturbation ϵ for WCPp and WCCp modes[1]:

Type	Odd/Even	Wave number perturbation (ϵ)
WCC	Odd	$-2\Gamma_4^0 - H(\beta)\Gamma_2^0\Gamma_3^0$
	Even	$-2\Gamma_4^0 - G(\beta)\Gamma_2^0\Gamma_3^0$
WCP	Odd	$-2\Gamma_1^0 - H(1/\beta)\Gamma_2^0\Gamma_3^0$
	Even	$-2\Gamma_1^0 - G(1/\beta)\Gamma_2^0\Gamma_3^0$

Table E.1: Analytical expressions of wave number perturbation ϵ for WCCp and WCPp modes where $H(x) = 4\tan(p\pi x/2)$ and $G(x) = 4\frac{\sin(p\pi x/2)}{\cos(p\pi x/2)-(-1)^{p/2}}$ have real values.

Analytical stability criteria can be derived by calculating the sign of $Im(\Gamma_1^0)$, $Im(\Gamma_4^0)$ and $Im(\Gamma_2^0\Gamma_3^0)$ using the following definitions: $\mathbb{F}^*$ is the complex conjugate of the flame parameter $\mathbb{F} = \frac{\rho^0 c^0}{\rho_u^0 c_u^0}\left(1 + n.e^{j\omega^0\tau}\right)$, $\theta^0 = \omega^0(1-\alpha)L_i/c^0 \in \mathbb{R}$ and $\theta_u^0 = \omega^0\alpha L_i/c_u^0 \in \mathbb{R}$. The notation $\mathfrak{D}$ refers to $\mathfrak{D} = |\cos(\theta^0)\sin(\theta_u^0) + \mathbb{F}\sin(\theta^0)\cos(\theta_u^0)|^2$

With these notations, the sign of the imaginary part of these coupling parameters are:

$$Im(\Gamma_1^0) = \frac{S_i}{4S_p\mathfrak{D}}\sin(2\theta^0)Im(\mathbb{F}) \tag{E.1}$$

$$Im(\Gamma_4^0) = -\frac{S_i}{4S_c\mathfrak{D}}\sin(2\theta_u^0)Im(\mathbb{F}) \tag{E.2}$$

[1]Since all sectors are identical, the index i has been omitted to simplify notations (e.g Γ_1 instead of $\Gamma_{i,1}$)

Eqs. (E.1 - E.2) lead to simple analytical stability criteria for WCCp and WCPp modes:

$$\sin(2\pi\tau/\tau_c^0)\sin\left(2p\pi\frac{\alpha L_i c^0}{L_c c_u^0}\right) < 0 \quad \text{for WCCp modes} \tag{E.3}$$

$$\sin(2\pi\tau/\tau_p^0)\sin\left(2p\pi\frac{(1-\alpha) L_i c_u^0}{L_p c^0}\right) > 0 \quad \text{for WCPp modes} \tag{E.4}$$

Appendix F

Flame position effect on annular combustors stability

Similarly to longitudinal modes in the Rijke tube (Schuller *et al.*, 2012; Poinsot & Veynante, 2011; Kaess *et al.*, 2008), the flame position (defined by α) also controls the stability (Eq. (4.48)). In a quasi-isothermal Rijke tube, for common (small) values of the FTF time-delay τ, stability of the first longitudinal mode is obtained only when the flame is located in the upper half of the tubes (Heckl & Howe, 2007; Zhao, 2012), i.e. $\alpha > 1/2$, which can be extended for the p-th longitudinal mode:

$$\frac{2m+1}{2p} < \alpha < \frac{2(m+1)}{2p}, \ \forall m \in \mathbb{N} \quad \text{(Rijke tube)} \tag{F.1}$$

Eq. (4.48) highlights a similar behavior for azimuthal modes in a PBC configuration: for a WCCp mode with small values of the time-delay $\tau < \tau_c^0/2$, $\sin(2\pi\frac{\tau}{\tau_c^0})$ is positive and Eq. (4.48) leads to:

$$\frac{2m+1}{2p}\frac{L_c c_u^0}{L_i c^0} < \alpha < \frac{2(m+1)}{2p}\frac{L_c c_u^0}{L_i c^0}, \ \forall m \in \mathbb{N} \quad \text{(WCCp modes)} \tag{F.2}$$

Usually, the critical flame position $\alpha_{crit} = \frac{L_c c_u^0}{2pL_i c^0}$ is larger than unity because the half-perimeter of the annular cavity is much longer than the burner length ($L_c \gg L_i$). Since the range of the normalized flame position α is $[0-1]$, the flame position may affect the stability only for high-order modes (i.e. p large enough to get $\alpha_{crit} < 1$). For instance, in the case described in Table 4.1 with the corrected burner length $L_i \simeq 0.76\ m$, the critical flame positions α_{crit} and the stability ranges (Eq. (F.2)) are shown in Tab. F.1.

The change of stability with the flame position α for small time-delays predicted in Tab. F.1 has been validated using the numerical resolution of the dispersion relation (Eq. (4.25)) in Fig. F.1. The critical flame positions obtained in Tab. F.1 are well captured for all modes. A situation where the plenum/chamber interaction is not negligible is shown for the WCC1 mode with $\alpha = 0.3$ (i.e. the flame is close the pressure node imposed by the large annular plenum).

Mode order (p)	$p=1$	$p=3$	$p=5$	$p=7$
$\alpha_{crit} = \frac{L_c c_u^0}{2pL_i c^0}$	2.70	0.9	0.54	0.39
α satisfying Eq. (F.2)	none	[0.9 - 1]	$[0.54 - 1]$	$[0.39 - 0.78]$

Table F.1: Critical flame positions α_{crit} and flame positions satisfying Eq. (F.2) for WCCp odd-order modes of the case described in Table 4.1

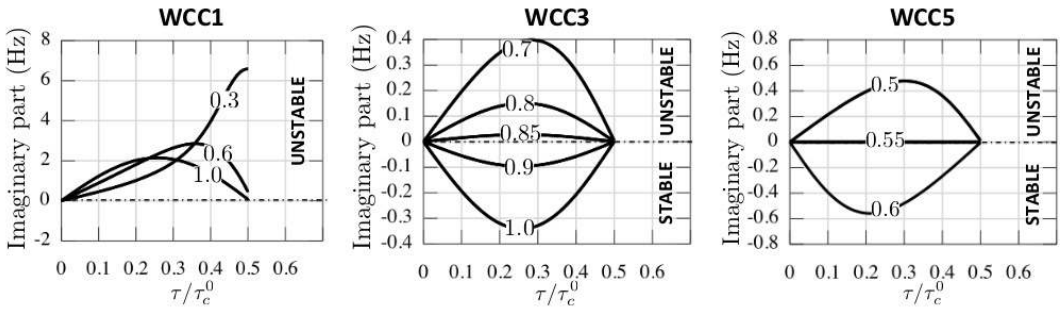

Figure F.1: Growth rate for several flame positions α of the WCC1 ($\alpha = 0.3,\ 0.6,\ 1.0$ - left), WCC3 ($\alpha = 0.5,\ 0.8,\ 0.85,\ 0.9,\ 1.0$ - middle) and WCC5 ($\alpha = 0.5,\ 0.55,\ 0.6$ - right) modes for small time delays ($\tau/\tau_c^0 < 1/2$) using the numerical resolution of the dispersion relation (Eq. (4.25)) with $n_i = 1.57$

Appendix G

Kernel Density Estimation (KDE)

Compared to experiment, Large Eddy Simulations (LES) usually provides high resolved but time-limited data or signals. This limitation complicates post-processing such as FFT or probability estimations, as the JAWA methodology proposed in Chapter 8. Indeed, a classic technique is, from a dataset α, to divide the range $[\min(\alpha) - \delta, \max(\alpha) + \delta]$ by N and create a histogram, where δ is defined by the user and corresponds to the anchor point of the histogram. However, as presented in Fig. G.1, such a simplistic method is highly sensitive to the used procedure (anchor point, number of point per bins etc.). Figure G.1 shows 50 random points whose PDF is estimated using histogram with two different anchor point (i.e. two different values for δ) leading to completely different estimated PDF. This drawback usually appears when the number of samples is limited. This problem can be tackled only by very low resolutions of the estimated PDF.

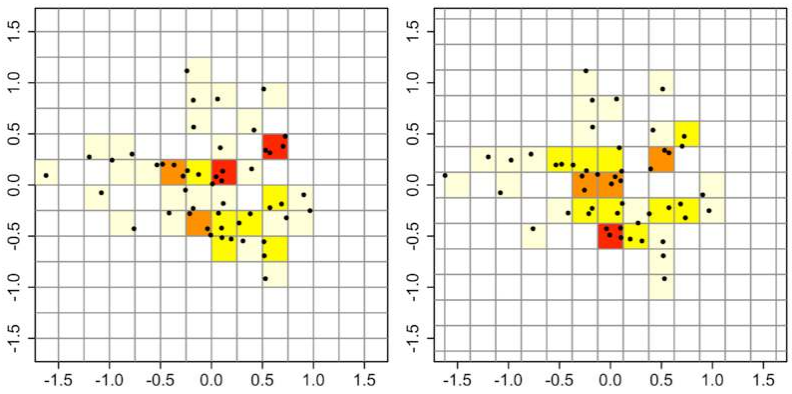

Figure G.1: Example (from internet) of the PDF estimation of 50 random values using histogram with two different anchor points: results (red for high PDF, white for null PDF) are completely different showing that such simplistic approaches are very sensitivity to the used procedure.

A solution is to use a technique known as Kernel Density Estimation (KDE) which provides accurate PDF estimations where the resolution is independent of the number of samples. Let's consider the dataset α with a true PDF called f_α. The estimation of this PDF is called f_h and is obtained by combining multiple local probability shapes, called

kernels, as shown in Fig. G.2 (left):

$$f_h(\alpha) = \frac{1}{n}\sum_{i=1}^{n} K_h(\alpha - \alpha_i) \quad \text{where} \quad K_h(\alpha - \alpha_i) = \frac{1}{h}K\left(\frac{\alpha - \alpha_i}{h}\right) \tag{G.1}$$

where K_h is called the smoothed kernel and h is the smoothing factor.

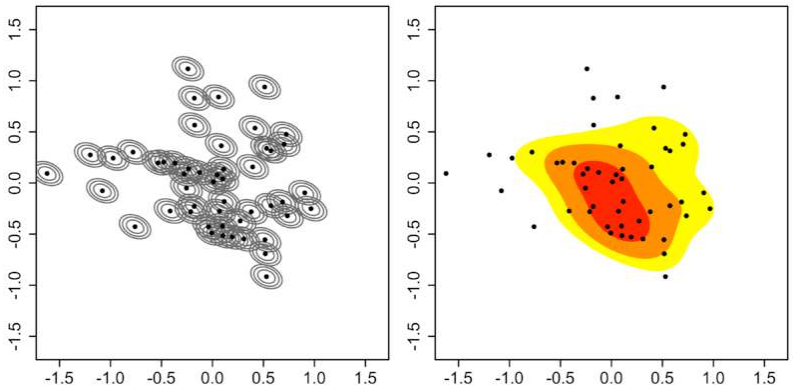

Figure G.2: Example (from internet) of the PDF estimation of 50 random values using KDE (right). Local probability functions, here smoothed gaussian functions, are centered at each sample location (left).

Usually, the kernel is chosen as a gaussian (normal) distribution since it provides simple theoretical results. The kernel is smoothed by a factor h which has to be chosen by the user. Nevertheless, this parameter can be evaluated analytically from an optimization of the error between f_α and f_h, leading to an optimal value:

$$h_{opt} = \left(\frac{\mathcal{R}(K)}{n\mathcal{M}(K)^2\mathcal{R}(f''_\alpha)}\right)^{1/5} \tag{G.2}$$

where $\mathcal{R}(g) = \int g(x)^2 dx$ and $\mathcal{M}(g) = \int x^2 g(x)$.

Obviously, the optimal smoothing factor cannot be rigorously obtained since the true PDF f_α is not known. An iterative procedure can be constructed by assuming that $f''_\alpha \simeq f''_h$. In this PhD thesis, a full analytical formula is used to approximate this parameter:

$$h_{opt} = \left(\frac{4 \times med(\|\alpha - med(\alpha)\|)}{3 \times 0.6745 \times n}\right)^{1/5} \tag{G.3}$$

An example is given in Fig. G.3 showing the PDF estimation of the centered wave ratio $\alpha = \frac{A^+ - A^-}{A^+ + A^-}$, extracted from a short LES (Chapter 8), using histogram (top left) and KDE with several smoothing factor h, from $0.25h_{opt}$ to $4h_{opt}$ where h_{opt} is obtained from Eq. (G.3). It shows that the histogram is under resolved, while KDE with $h < h_{opt}$ are noisy and $h > h_{opt}$ are over smoothed. KDE with h_{opt} provides the best PDF estimation possible. Note that the smoothing parameter h_{opt} is defined using only the sample data α and not the grid resolution on which the PDF will be estimated (corresponding to the

number of bins for a classic histogram). Therefore, increasing the resolution of the PDF does not change the procedure and the PDF results since h_{opt} is unchanged (only data can modify its value, which is what an accurate well-posed procedure intends to do). Note that this KDE procedure can be improved by choosing a local, instead of a global as presented here, smoothing factor but this topic is still an open question today.

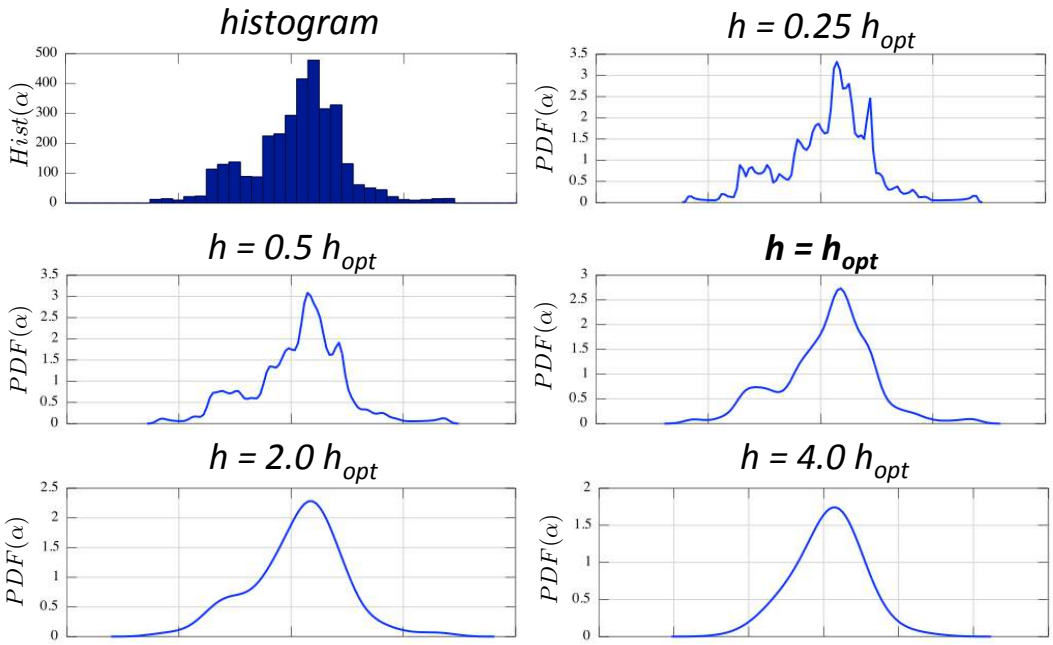

Figure G.3: Example of the PDF estimation of the centered wave ratio $\alpha = \frac{A^+ - A^-}{A^+ + A^-}$, extracted from a short LES (Chapter 8), using histogram (top left) and KDE with several smoothing factors h, from $0.25h_{opt}$ to $4h_{opt}$, where h_{opt} is obtained from Eq. (G.3)

Appendix H

Acoustic flux and growth rate of a longitudinal acoustic mode with a non-null mean flow

The case with a mean axial flow described in Fig. 9.4 is investigated here with different boundary conditions:

- **Case UP:** the inlet boundary condition is set to $\hat{u}(x=0)=0$ while the outlet is $\hat{p}(x=L)=0$.
- **Case MP:** the inlet boundary condition is now set to $\hat{m}(x=0)=\rho_0\hat{u}(x=0)+\frac{M}{c_0}\hat{p}(x=0)=0$ while the pressure outlet is still enforced: $\hat{p}(x=L)=0$.
- **Case UJ:** the inlet boundary condition is set to $\hat{u}(x=0)=0$ but now the outlet condition is an imposed enthalpy: $\rho_0\hat{J}(x=L)=\hat{p}(x=L)+\rho_0 c_0 M\hat{u}(x=L)=0$.

For these three cases, the pressure and velocity expressions are:

$$\hat{p}(x)=Ae^{jk^+x}+Be^{-jk^-x} \tag{H.1}$$

$$\rho_0 c_0\hat{u}(x)=Ae^{jk^+x}-Be^{-jk^-x} \tag{H.2}$$

where A and B are constants, x is the axial coordinate, $j^2=-1$ and $k^{\pm}=\frac{\omega}{c_0(1\pm M)}$.

Using the pressure and velocity expressions and applying boundary conditions for each case, a dispersion relation is obtained. The argument of the dispersion relation gives the frequency while its modulus gives the growth rate. Results are summarized in Tab. H.1:

Case	Frequency $Re(f)$	Growth rate $Im(f)$	$Im(f)$ (low Mach)
UP	$\frac{(2p+1)c_0}{4L}(1-M^2)$	0	0
MP		$-\frac{c_0(1-M^2)}{4\pi L}\ln\left(\frac{1+M}{1-M}\right)$	$\sim-\frac{c_0 M}{2\pi L}$
UJ		$+\frac{c_0(1-M^2)}{4\pi L}\ln\left(\frac{1+M}{1-M}\right)$	$\sim+\frac{c_0 M}{2\pi L}$

Table H.1: Analytical frequency and growth rate for the three cases UP, MP and UJ.

Table H.1 shows that non-zero Mach numbers can lead either to neutral, damped or amplified mode. Moreover the real frequency is only weakly affected by the mean

flow ($\propto M^2$) while the growth rate is significantly changed ($\propto M$). At non-null Mach numbers, the acoustic flux $\hat{F}$ is (Myers, 1986):

$$\hat{F}(x) = (\hat{u} + \frac{u_0}{\rho_0 c_0^2}\hat{p})(\hat{p} + \rho_0 u_0 \hat{u}) = \hat{m}\hat{J} \tag{H.3}$$

Consequently, acoustic fluxes at the inlet and outlet boundaries as well as the total acoustic flux $\hat{F}_{tot} = \hat{F}(x=0) - \hat{F}(x=L)$ for the three cases read:

Case	$\hat{F}(x=0)$	$\hat{F}(x=L)$	$\hat{F}_{tot}$
UP	$\frac{M}{\rho_0 c_0}\hat{p}^2(x=0) = \frac{4MA^2}{\rho c_0}$	$\rho_0 c_0 M \hat{u}^2(x=L) = \frac{4MA^2}{\rho c_0}$	0
MP	0	$\rho_0 c_0 M \hat{u}^2(x=L) > 0$	$-\rho_0 c_0 M \hat{u}^2(x=L) < 0$
UJ	$\frac{M}{\rho_0 c_0}\hat{p}^2(x=0) > 0$	0	$\frac{M}{\rho_0 c_0}\hat{p}^2(x=0) > 0$

Table H.2: Analytical frequency and growth rate for the three cases UP, MP and UJ.

Table H.2 is consistent with growth rates obtained in Tab. H.1 since the acoustic energy conservation for an isentropic flow reads (Myers, 1986):

$$\frac{\partial \hat{E}}{\partial t} = \hat{F}_{tot} \tag{H.4}$$

where the acoustic energy is $\hat{E} = \frac{\hat{p}^2}{2\rho_0 c_0^2} + \frac{1}{2}\rho_0 \hat{u}^2 + \frac{u_0}{c_0^2}\hat{p}\hat{u}$. Note that in the case UJ, the inlet boundary condition acts like an active device (positive acoustic flux $\hat{F}(x=0) = \frac{M}{\rho_0 c_0}\hat{p}^2(x=0) > 0$, Tab. H.2) and therefore a fixed velocity inlet is not a physical boundary condition.

Appendix I

C-indicator with N equi-distributed pressure probes

In this paper, the C-indicator $C(t) = \frac{1}{N}\sum_{k=1}^{N} p_k(\theta_k, t)e^{j\theta_k}$ proposed by Schuermans et al. and already used in (Wolf *et al.*, 2012; Worth & Dawson, 2013*b*) is applied to highlight the nature of the azimuthal modes observed in LES. This section intends to derive the analytical expression of the C-indicator according to the mode nature: standing or spinning.

- **Standing mode:** Assuming a standing mode at the frequency f, the pressure at the probe k reads:

$$P_k(t) = P_0 \cos(2\pi f t)\cos(\theta_k) \tag{I.1}$$

Using $\cos(\theta_k) = \frac{1}{2}\left(e^{j\theta_k} + e^{-j\theta_k}\right)$, the C-indicator reduces to:

$$C(t) = \frac{P_0}{2N}\cos(2\pi f t)\sum_{k=1}^{N}\left(e^{2j\theta_k}+1\right) = \frac{P_0}{2}\cos(2\pi f t) + \frac{P_0}{2N}\cos(2\pi f t)\sum_{k=1}^{N} e^{2j\theta_k} \tag{I.2}$$

If $N \neq 1$ or 2 (i.e. more than two probes are used), the term $\sum_{k=1}^{N} e^{2j\theta_k}$ is null leading to the C-indicator:

$$C(t) = \frac{1}{2}P_0\cos(2\pi f t) \quad \text{with the phase} \quad \arg(C(t)) = 0 \text{ or } \pi \tag{I.3}$$

- **Spinning mode:** Assuming a spinning mode at the frequency f, the pressure at the probe k reads:

$$P_k(t) = P_0\cos(2\pi f t \pm \theta_k) \tag{I.4}$$

where wave $(-)$ rotates in the clockwise direction and the wave $(+)$ in the anti-clockwise direction.
Using $\cos(2\pi f t \pm \theta_k) = \frac{1}{2}\left(e^{j2\pi f t \pm j\theta_k} + e^{-j2\pi f t \mp j\theta_k}\right)$, the C-indicator reduces to:

$$C(t) = \frac{P_0}{2}e^{\mp j2\pi f t} + \frac{P_0}{2N}e^{\pm j2\pi f t}\sum_{k=1}^{N} e^{\mp 2j\theta_k} \tag{I.5}$$

If $N \neq 1$ or 2 (i.e. more than two probes are used), the term $\sum_{k=1}^{N} e^{\mp 2j\theta_k}$ is null leading to the C-indicator:

$$C(t) = \frac{P_0}{2} e^{\mp j2\pi ft} \quad \text{with the phase} \quad \arg(C(t)) = \mp 2\pi ft = \mp \omega t \tag{I.6}$$

where ω is the angular frequency and $+$ (resp. $-$) characterizes the clockwise (resp. anti-clockwise) spinning wave.

Consequently, the phase of the C-indicator provides the nature of the azimuthal modes considering two assumptions: 1) Pressure probes are equip-distributed and 2) more than two probes are used to identified the mode. Table I.1 summarizes these results:

Nature	$\mathbf{2C(t)/P_0}$	$\arg(\mathbf{C(t)})$
Standing	$\cos(2\pi ft)$	0 or π
Spinning (clockwise)	$e^{+j2\pi ft}$	$+\omega t$
Spinning (anti-clockwise)	$e^{-j2\pi ft}$	$-\omega t$

Table I.1: analytical expressionsof the C-indicator and its phase according to the mode nature.

Bibliography

Acharya, V. & Lieuwen, T. 2013 Dynamics of axisymmetric premixed, swirling flames subjected to helical disturbances. *AIAA 51th Aerosp. Sci. Meet., AIAA Pap. 2013-1179* . (Cited on page 25.)

Agarwal, N.K. & Bull, M.K. 1989 Acoustic wave propagation in a pipe with fully developed turbulent flow. *J. Sound Vib.* **132** (2), 275–298. (Cited on page 211.)

Angelberger, C., Veynante, D., Egolfopoulos, F. & Poinsot, T. 1998 Large eddy simulations of combustion instabilities in premixed flames. *Proc. of the Summer Program* pp. 61–82. (Cited on pages 161 and 162.)

Auzillon, P., Gicquel, O., Darabiha, N., Veynante, D. & Fiorina, B. 2012 A filtered tabulated chemistry model for les of stratified flames. *Combust. Flame* **159** (8), 2704–2717. (Cited on page 163.)

Barman, A., Barman, S., Kimura, T., Fukuma, Y. & Otani, Y. 2010 Gyration mode splitting in magnetostatically coupled magnetic vortices in an array. *J. Phys. D: Appl. Phys.* **43**, 422001. (Cited on pages 15 and 16.)

Bauerheim, M., Cazalens, M. & Poinsot, T. 2014*a* A theoretical study of mean azimuthal flow and asymmetry effects on thermo-acoustic modes in annular combustors. *Proc. Combust. Inst. (accepted, in press)* **35**. (Cited on pages 17, 26, 27, 56, 120, 135, 218, 235, 239, and 253.)

Bauerheim, M., Ndiaye, A., Constantine, P., Iaccarino, G., Moreau, S. & Nicoud, F. 2014*b* Uncertainty quantification of thermo-acoustic instabilities in annular combustors. *Proc. of the Summer Program (in press)* . (Cited on pages 26 and 235.)

Bauerheim, M., Nicoud, F. & Poinsot, T. 2014*c* Theoretical analysis of the mass balance equation through a flame at zero and non-zero mach numbers. *Combust. Flame (in press)* . (Cited on pages 29 and 235.)

Bauerheim, M., Parmentier, J.F., Salas, P., Nicoud, F. & Poinsot, T. 2014*d* An analytical model for azimuthal thermoacoustic modes in an annular chamber fed by an annular plenum. *Combustion and Flame* **161**, 1374–1389. (Cited on pages 15, 26, 27, 32, 44, 46, 47, 51, 55, 69, 74, 76, 77, 78, 84, 118, 121, 235, and 251.)

Bauerheim, M., Salas, P., Nicoud, F. & Poinsot, T. 2014*e* Symmetry breaking of azimuthal thermoacoustic modes in annular cavities: a theoretical study. *J. Fluid Mech. (in press)* . (Cited on pages 17, 26, 27, 206, 218, 219, 223, 225, 228, 232, 235, and 239.)

Berenbrink, P. & Hoffmann, S. 2001 Suppression of dynamic combustion instabilities by passive and active means. *ASME Paper 2001-GT-42* . (Cited on pages 32, 43, 54, 62, and 63.)

Blimbaum, J., Zanchetta, M., Akin, T., Acharya, V., J.O'Connor, Noble, D.R. & Lieuwen, T. 2012 Transverse to longitudinal acoustic coupling processes in annular combustion chambers. *International journal of spray and combustion dynamics* **4** (4), 275–298. (Cited on pages 46 and 75.)

Blumenthal, R.S., Subramanian, P., Sujith, R. & Polifke, W. 2013 Novel perspectives on the dynamics of premixed flames. *Combust. Flame* **160** (7), 1215–1224. (Cited on page 25.)

Borisnika, S.V. 2006 Symmetry, degeneracy and optical confinement of modes in coupled microdisk resonators and photonic crystal cavities. *IEEE J. Sel. Topics Quantum Electron* **12** (6), 1175–1182. (Cited on page 15.)

Bourgouin, J-F. 2014 Dynamique de flamme dans les foyeres annulaires comportant des injecteurs multiples. PhD thesis, Ecole Centrale de Paris (EM2C). (Cited on pages 23, 195, 196, and 235.)

Bourgouin, J-F., Durox, D., Moeck, J.P., Schuller, T. & Candel, S. 2013 Self-sustained instabilities in an annular combustor coupled by azimuthal and longitudinal acoustic modes. *ASME Paper 2013-GT-95010* . (Cited on pages 23, 32, 35, 72, 84, 89, 120, 168, 174, 218, and 235.)

Bourgouin, J-F., Durox, D., Moeck, J.P., Schuller, T. & Candel, S. 2014 Characterization and modeling of a spinning thermoacoustic instability in an annular combustor equipped with multiple matrix injectors. *ASME Paper 2014-GT-25067* . (Cited on page 114.)

Boussinesq, J. 1877*a* Essai sur la théorie des eaux courantes. *26ème édn. Acad. Sci. Paris* . (Cited on page 155.)

Boussinesq, J. 1877*b* Théorie de l'écoulement tourbillant. *Mém. Présentés par Divers Savants. Acad. Sci. Inst. Fr.* **23**, 46–50. (Cited on page 156.)

Branley, N. & Jones, W. P. 2001 Large eddy simulation of a turbulent non-premixed flame. *Combust. Flame* **127**, 1914–1934. (Cited on page 28.)

Bray, K. N. C. & Moss, J. B. 1977 A closure model for the turbulent premixed flame with sequential chemistry. *Combust. Flame* **30**, 125–131. (Cited on page 159.)

Brear, M.J., Nicoud, F., Talei, M., Giauque, A. & Hawkes, E.R. 2012 Disturbance energy transport and sound production in gaseous combustion. *J. Fluid Mech.* **707**, 53–73. (Cited on page 24.)

Brown, R. S., Blackner, A., M. Willoughby, P. G. & Dunlap, R. 1986 Coupling between acoustic velocity oscillations and solid propellant combustion. *Tech. Rep.*. United Technologies Chemical Systems, San Jose, CA. (Cited on page 19.)

Busse, F.H. 1984 Oscillations of a rotating liquid drop. *J. Fluid Mech.* **142**, 1–8. (Cited on page 17.)

Butler, T. D. & O'Rourke, P. J. 1977 A numerical method for two-dimensional unsteady reacting flows. *Proc. Combust. Inst.* **16** (1), 1503 – 1515. (Cited on page 160.)

Cabral, B. & Leedom, L.C. 1993 Imaging vector fields using line integral convolution. *Proceedings of the 20th annular conference on computer graphics and interactive techniques* pp. 263–270. (Cited on page 175.)

Campa, G. & Camporeale, S.M. 2014 Influence of nonlinear effects on the limit cycle in a combustion chamber equipped with helmholtz resonators. *ASME Paper 2014-GT-25228* . (Cited on page 88.)

Campa, G., Camporeale, S.M., Guaus, A., Favier, J., Bargiacchi, M., Bottaro, A., Cosatto, E. & Mori, G. 2011 A quantitative comparison between a low order model and a 3d fem code for the study of thermoacoustic combustion instabilities. *ASME Paper 2011-GT-45969* . (Cited on pages 27, 87, 88, 89, 93, 120, 235, and 236.)

Candel, S. 1992 Combustion instabilities coupled by pressure waves and their active control. *Proc. Combust. Inst.* **24**, 1277–1296. (Cited on pages 19 and 21.)

Candel, S. 2002 Combustion dynamics and control:. *Proc. of the Combustion Institute* **29**, 1–28. (Cited on pages 18, 19, and 23.)

Candel, S., Durox, D., Schuller, T., Bourgouin, J-F. & Moeck, J.P. 2014 Dynamics of swirling flames. *Annu. Rev. fluid Mech.* **46**, 147–173. (Cited on page 25.)

Chantrasmi, T., Constantine, P., Etemadi, N., Iaccarino, G. & Wang, Q. 2006 Uncertainty quantification in simple linear and non-linear problems. *Annual Research Briefs of CTR* . (Cited on page 118.)

Chantrasmi, T. & Iaccarino, G. 2012 Forward and backward uncertainty propagation for discontinuous system response using the padé-legendre method. *International Journal of Uncertainty Quantification* **2** (2), 125–143. (Cited on page 127.)

Charlette, F., Veynante, D. & Meneveau, C. 2002 A power-law wrinkling model for LES of premixed turbulent combustion: Part I - non-dynamic formulation and initial tests. *Combust. Flame* **131**, 159–180. (Cited on pages 162, 172, and 188.)

Chu, B. T. 1965 On the energy transfer to small disturbances in fluid flow (part i). *Acta Mechanica* pp. 215–234. (Cited on page 24.)

Clanet, C., Searby, G. & Clavin, P. 1999 Primary acoustic instability of flames propagating in tubes: cases of spray and premixed gas combustion. *J. Fluid Mech.* **385** (157-197). (Cited on page 25.)

Clavin, P. & Joulin, G. 1983 Premixed flames in large scale and high intensity turbulent flow. *J. Physique Lettres* **44**, L1–L12. (Cited on page 23.)

Clavin, P. & Siggia, E. D. 1991 Turbulent premixed flames and sound generation. *Combust. Sci. Tech.* **78**, 147–155. (Cited on page 19.)

Colin, O., Ducros, F., Veynante, D. & Poinsot, T. 1999 A thickened flame model for large eddy simulations of turbulent premixed combustion. *Tech. Rep.* HEP/123-qed. CERFACS. (Cited on page 28.)

Colin, O., Ducros, F., Veynante, D. & Poinsot, T. 2000 A thickened flame model for large eddy simulations of turbulent premixed combustion. *Phys. Fluids* **12** (7), 1843–1863. (Cited on pages 159, 161, 163, and 172.)

Colin, O. & Rudgyard, M. 2000 Development of high-order taylor-galerkin schemes for unsteady calculations. *J. Comput. Phys.* **162** (2), 338–371. (Cited on page 158.)

Comte, P., Haberkorn, M., Bouchet, G., Pagneaux, V. & Auregan, Y. 2006 *Large-Eddy Simulation of acoustic propagation in a turbulent channel flow*, pp. 521–528. Direct and Large Eddy Simulation VI. (Cited on page 211.)

Constantine, P. G., Dow, E. & Wang, Qiqi 2014 Active subspace methods in theory and pratice: applications to kriging surfaces. *SIAM Journal on Scientific Computing* **36** (4), 1500–1524. (Cited on pages 120 and 127.)

Creighton, J. A. 1982 Splitting of degenerate vibrational modes due to symmetry perturbations in tetrahedral m4 and octahedral m6 clusters. *Inorganic Chemistry* **21** (1), 1–4. (Cited on page 15.)

Crighton, D. G., Dowling, A. P., Williams, J. E. Ffowcs, Heckl, M. & Leppington, F. 1992 *Modern methods in analytical acoustics*. New-York: Springer Verlag. (Cited on page 21.)

Crocco, L. 1951 Aspects of combustion instability in liquid propellant rocket motors. Part I. *J. American Rocket Society* **21**, 163–178. (Cited on pages 47, 54, 94, 102, 167, 173, and 174.)

Crocco, L. 1952 Aspects of combustion instability in liquid propellant rocket motors. part II. *J. American Rocket Society* **22**, 7–16. (Cited on page 119.)

Crocco, L. 1969 Research on combustion instability in liquid propellant rockets. *Proc. Combust. Inst.* **12**, 85–99. (Cited on page 25.)

Culick, F. E. C. 1987 Combustion instabilities in liquid-fueled propulsion systems- an overview. *AGARD 72B PEP meeting* . (Cited on page 18.)

Culick, F. E. C. & Kuentzmann, P. 2006 *Unsteady Motions in Combustion Chambers for Propulsion Systems*. NATO Research and Technology Organization. (Cited on pages 18 and 33.)

Cummings, D.L. & Blackburn, D.A. 1991 Oscillations of magnetically levitated aspherical droplets. *J. Fluid Mech.* **224**, 395–416. (Cited on page 17.)

Cuquel, A., Durox, D. & Schuller, T. 2011 Theoretical and experimental determination of the flame transfer function of confined premixed conical flames. *Proceedings of the seventh Mediterranean Combustion Symposium* . (Cited on page 25.)

Davey, A. & Salwen, H. 1994 On the stability in an elliptic pipe which is nearly circular. *J. Fluid Mech.* **281**, 357–369. (Cited on page 17.)

Davies, P. O. A. L. 1988 Practical flow duct acoustics. *J. Sound Vib.* **124** (1), 91–115. (Cited on page 46.)

Dawson, J.R. & Worth, N.A. 2014 The effect of baffles on self-excited azimuthal modes in an annular combustor. *Proc. Combust. Inst. (in press)* . (Cited on pages 34, 218, 235, 237, and 239.)

Domingo, P., Vervisch, L. & Bray, K. 2002 Partially premixed flamelets in LES of non premixed turbulent combustion. *Combust. Theory and Modelling* **6** (529-551). (Cited on page 28.)

Dopazo, C. 1994 Recent developments in pdf methods. In *Turbulent Reacting Flows* (ed. P. A. Libby & F. A. Williams), pp. 375 – 474. London: Academic. (Cited on page 159.)

Dowling, A & Stow, R. S. 2003 Acoustic analysis of gas turbine combustors. *AIAA* **19**, 751–764. (Cited on page 19.)

Dowling, A. P. 1995 The calculation of thermoacoustic oscillations. *J. Sound Vib.* **180** (4), 557–581. (Cited on pages 19, 26, 46, 75, and 204.)

Dowling, A. P. 1997 Nonlinear self-excited oscillations of a ducted flame. *J. Fluid Mech.* **346**, 271–290. (Cited on page 19.)

Duchaine, F. & Poinsot, T. 2011 Sensitivity of flame transfer functions of laminar flames. *Proc. of the Summer Program* pp. 250–258. (Cited on page 205.)

Duchaine, F., Selle, L. & Poinsot, T. 2011 Sensitivity analysis of transfer functions of laminar flames. *Combust. Flame* **158** (12), 2384–2394. (Cited on pages 29, 120, 167, and 173.)

Ducros, F., Nicoud, F. & Poinsot, T. 1998 Wall-adapating local eddy-viscosity models for simulations in complex geometries. *ICFD* pp. 293–300. (Cited on page 157.)

Duran, I. & Moreau, S. 2013 Solution of the quasi-one-dimensional linearized euler equations using flow invariants and the magnus expansion. *J. Fluid Mech.* **723**, 190–231. (Cited on page 26.)

Enaux, B., Granet, V., Vermorel, O., Lacour, C., Pera, C., Angelberger, C. & Poinsot, T. 2011 Les and experimental study of cycle-to-cycle variations in a spark ignition engine. *Proc. Combust. Inst.* **33**, 3115–3122. (Cited on page 163.)

Evesque, S. & Polifke, W. 2002 Low-order acoustic modelling for annular combustors: Validation and inclusion of modal coupling. *ASME Paper 2002-GT-30064* . (Cited on pages 19, 26, 27, 32, 204, and 222.)

Evesque, S., Polifke, W. & Pankiewitz, C. 2003 Spinning and azimuthally standing acoustic modes in annular combustors. *AIAA Paper 2003-3182* . (Cited on pages 21, 32, and 87.)

Feng, Z.C. & Sethna, P.R. 1989 Symmetry-breaking bifurcation in resonant surface waves. *J. Fluid Mech.* **199**, 495–518. (Cited on pages 15 and 16.)

Fiorina, B., Vicquelin, R., Auzillon, P., Darabiha, N. & Veynante, D. 2010 A filtered tabulated chemistry model for les of premixed combustion. *Combust. Flame* **157** (3), 465–475. (Cited on page 163.)

Forkel, H. & Janicka, J. 2000 Large-eddy simulation of a turbulent hydrogen diffusion flame. *Flow, Turb. and Combustion* **65** (2), 163–175. (Cited on page 28.)

Franzelli, B., Riber, E. & Cuenot, B. 2013 Impact of the chemical description on a large eddy simulation of a lean partially premixed swirled flame. *Combustion, spray and flow dynamics for aerospace propulsion* **341** (1-2), 247–256. (Cited on pages 152 and 166.)

Franzelli, B., Riber, E., Sanjosé, M. & Poinsot, T. 2010 A two-step chemical scheme for Large-Eddy Simulation of kerosene-air flames. *Combust. Flame* **157** (7), 1364–1373. (Cited on page 173.)

Frenklach, M., Wang, H., Goldenberg, M., Smith, G. P., Golden, D. M., Bowman, C. T., Hanson, R. K., Gardiner, W. C. & Lissianki, V. 1995 GRI-mech: an optimized detailed chemical reaction mechanism for methane combustion. *Tech. Rep.* GRI-Report GRI-95/0058. Gas Research Institute. (Cited on page 173.)

Fureby, C. 2010 LES of a multi-burner annular gas turbine combustor. *Flow, Turb. and Combustion* **84**, 543–564. (Cited on pages 169 and 220.)

Gelbert, G., Moeck, J.P., Paschereit, C.O. & King, R. 2012 Feedback control of unstable thermoacoustic modes in an annular rijke tube. *Control Engineering Practice* **20**, 770–782. (Cited on pages 33, 44, and 218.)

Ghirardo, G. & Juniper, M. 2013 Azimuthal instabilities in annular combustors: standing and spinning modes. *Proceedings of the Royal Society A* (2013-0232). (Cited on pages 72, 84, 87, 89, 218, 235, and 252.)

Ghirardo, G., Juniper, M.P. & Moeck, J.P. 2015 Stability criteria for standing and spinning waves in annular combustors. *Turbo Expo GT2015-43127* . (Cited on pages 25, 43, 249, 251, and 252.)

Giauque, A., Selle, L., Poinsot, T., Buechner, H., Kaufmann, P. & Krebs, W. 2005 System identification of a large-scale swirled partially premixed combustor using LES and measurements. *J. Turb.* **6** (21), 1–20. (Cited on page 167.)

Giret, J-C., Sengissens, A., Moreau, S. & Jouhaud, J-C. 2013 Prediction of lagoon landing-gear noise using an unstructured les solver. *19th AIAA/CEAS Aeronautics conference* . (Cited on page 240.)

Goodwin, D.G. 2009 Cantera code site (http://code.google.com/p/cantera/). (Cited on page 173.)

Guckenheimer, J. & Mahalov, A. 1992 Instability induced by symmetry reduction. *Physical Review Letter* **68**, 2257. (Cited on page 17.)

Guezennec, N. & Poinsot, T. 2009 Acoustically nonreflecting and reflecting boundary conditions for vorticity injection in compressible solvers. *AIAA Journal* **47**, 1709–1722. (Cited on page 212.)

Guslienko, K.Y., A.N.Slavin, Tiberkevich, V. & Kim, S.K. 2008 Dynamic origin of azimuthal modes splitting in vortex-state magnetic dots. *Physical Review Letter* **24**, 247203. (Cited on pages 15 and 16.)

Harrje, D. J. & Reardon, F. H. 1972 Liquid propellant rocket instability. *Tech. Rep.* Report SP-194. NASA. (Cited on page 18.)

Hawkes, E. R. & Cant, S. R. 2000 A flame surface density approach to large eddy simulation of premixed turbulent combustion. *Proc. Combust. Inst.* **28**, 51–58. (Cited on page 159.)

Heckl, M.A. & Howe, M.S. 2007 Stability analysis of the rijke tube with a green's function approach. *Journal of Sound and Vibration* **305**, 672–688. (Cited on page 259.)

Hirsch, C. 2007 Finite volume method and conservative discretization with an introduction to finite element method. In *Numerical Computation of internal & external flows: Fundamentals of Computational Fluid Dynamics, second edition*, chap. 5, pp. 203–248. New York: John Wiley & Sons. (Cited on page 158.)

Hirschfelder, J. O., Curtiss, C. F. & Bird, R. B. 1969 *Molecular theory of gases and liquids*. New York: John Wiley & Sons. (Cited on page 143.)

Hoffmann, F., Woltersdorf, G., Perzlmaier, K., Slavin, A.N., Tiberkevich, V.S., Bischof, A., Weiss, D. & Back, C.H. 2007 Mode degeneracy due to vortex core removal in magnetic disks. *Physical Review B* **76**, 014416. (Cited on pages 15 and 16.)

Howe, M. S. 1979 On the theory of unsteady high reynolds number flow through a circular aperture. *Proc. R. Soc. Lond. A , Mathematical and Physical Sciences* **366** (1725), 205–223. (Cited on page 26.)

Howe, M. S. 1997 Influence of wall thickness on Rayleigh conductivity and flow-induced aperture tones. *J. Fluids Struct.* **11** (4), 351–366. (Cited on page 26.)

J. Kopitz, E. Brocker, W. Polifke 2005 Characteristics-based filter for identification of planar acoustic waves in numerical simulation of turbulent compressible flow. *12th International Congress on Sound and Vibration* . (Cited on page 28.)

Janicka, J. & Sadiki, A. 2004 Large eddy simulation for turbulent combustion. *Proc. Combust. Inst.* **30**, 537–547. (Cited on page 28.)

Jiménez, C., Quinard, J., Grana-Otero, J., Schmidt, H. & Searby, G. 2012 Unsteady response of hydrogen and methane flames to pressure waves. *Combust. Flame* **159**, 1894–1908. (Cited on page 25.)

Jones, W. P. & Whitelaw, J. H. 1982 Calculation methods for reacting turbulent flows: a review. *Combust. Flame* **48**, 1–26. (Cited on page 28.)

Juniper, M.P., Magri, L., Bauerheim, M. & Nicoud, F. 2015 Applications of adjoint methods in thermoacoustics. *Proc. of the Summer Program* . (Cited on page 128.)

Kaess, R., Polifke, W., Poinsot, T., Noiray, N., Durox, D., Schuller, T. & Candel, S. 2008 Cfd-based mapping of the thermo-acoustic stability of a laminar premix burner. *Proc. of the Summer Program* pp. 289–302. (Cited on pages 167 and 259.)

Kammerer, M., Weigand, M., Curcic, M., Sproll, M., Vansteenkiste, A., Waeyenberge, B. Van, Stoll, H., Woltersdorf, G., Back, C.H. & Schuetz, G. 2011 Magnetic vortex core reversal by excitation of spin waves. *Nature communication* **2**, 279. (Cited on pages 15 and 16.)

Kaufmann, A., Nicoud, F. & Poinsot, T. 2002 Flow forcing techniques for numerical simulation of combustion instabilities. *Combust. Flame* **131**, 371–385. (Cited on page 205.)

Kedia, K.S., Altay, H.M. & Ghoniem, A.F. 2011 Impact of flame-wall interaction on premixed flame dynamics and transfer function characteristics. *Proc. Combust. Inst.* **33**, 1113–1120. (Cited on pages 173, 176, 188, and 205.)

Kippenberg, T.J. 2010 Microresonators: particle sizing by mode splitting. *Nature Photonics* **4**, 9–10. (Cited on page 16.)

Kolmogorov, A. N. 1941 The local structure of turbulence in incompressible viscous fluid for very large reynolds numbers. *C. R. Acad. Sci. , USSR* **30**, 301. (Cited on pages 27, 144, and 156.)

Kopitz, J., Huber, A., Sattelmayer, T. & Polifke, W. 2005 Thermoacoustic stability analysis of an annular combustion chamber with acoustic low order modeling and validation against experiment. *ASME Paper 2005-GT-68797* . (Cited on pages 19, 23, 25, and 32.)

Kosovichev, A.G. 1999 Inversion methods in helioseismology and solar tomography. *Journal of computational and applied mathematics* **109**, 1–39. (Cited on page 16.)

Krebs, W., Flohr, P., Prade, B. & Hoffmann, S. 2002 Thermoacoustic stability chart for high intense gas turbine combustion systems. *Combust. Sci. Tech.* **174**, 99–128. (Cited on pages 15, 21, 26, 32, 72, 87, 218, and 222.)

Krebs, W., Walz, G., Flohr, P. & Hoffmann, S. 2001 Modal analysis of annular combustors: effect of burner impedance. *ASME Paper 2001-GT-42* . (Cited on pages 76 and 235.)

Krstic, M., Krupadanam, A. & Jacobson, C.; 1999 Self-tuning control of a nonlinear model of combustion instabilities. *Control Systems Technology* **7**. (Cited on page 20.)

Krüger, U., Hüren, J., Hoffmann, S., Krebs, W. & Bohn, D. 1999 Prediction of thermoacoustic instabilities with focus on the dynamics flame behavior for the 3a-series gas turbines of siemes kwu. *ASME Turbo Expo 99-GT-111* . (Cited on page 26.)

Krüger, U., Hüren, J., Hoffmann, S., Krebs, W., Flohr, P. & Bohn, D. 2000 Prediction and measurement of thermoacoustic improvements in gas turbines with annular combustion systems. *J. Eng. for Gas Turbines and Power* **123** (3), 557–566. (Cited on pages 26, 33, 43, 54, 62, and 63.)

Kuenne, G., Ketelheun, A. & Janicka, J. 2011 LES modeling of premixed combustion using a thickened flame approach coupled with fgm tabulated chemistry. *Combust. Flame* **158** (9), 1750 – 1767. (Cited on pages 169 and 220.)

Kumar, A. & Krousgrill, C.M. 2012 Mode-splitting and quasi-degeneracies in circular plate vibration problems: The example of free vibrations of the stator of a travelling wave ultrasonic motor. *J. Sound Vib.* **331** (26), 5788–5802. (Cited on page 15.)

Kuo, K.K. 2005 *Principles of combustion*. Hoboken, New Jersey: John Wiley & Sons, Inc. (Cited on page 160.)

Lamarque, N. 2007 Schémas numériques et conditions limites pour la simulation aux grandes échelles de la combustion diphasique dans les foyers d'hélicoptère. Phd thesis, INP Toulouse. (Cited on page 158.)

Lavely, E.M. 1983 Theoretical investigations in helioseismology. PhD thesis, Columbia University. (Cited on pages 15 and 16.)

Lax, P. D. & Wendroff, B. 1960 Systems of conservation laws. *Commun. Pure Appl. Math.* **13**, 217–237. (Cited on page 158.)

Lecocq, G., Hernandez-Vera, T., Poitou, D., Riber, E. & Couenot, B. 2013 Soot prediction by large-eddy simulation of complex geometry combustion chambers. *Comptes rendus de l'Académie des Sciences - Mécanique* **341** (1-2), 230–237. (Cited on page 173.)

Lee, D. S. & Anderson, T. J. 1999 Measurements of fuel/air-acoustic coupling in lean premixed combustion systems. *AIAA paper 99-0450* . (Cited on page 19.)

Lee, J. G. & Santavicca, D.A. 2003 Experimental diagnostics for the study of combustion instabilities in lean premixed combustors. *Journal of Propulsion and Power* **19**, 735–750. (Cited on page 19.)

Légier, J.-Ph., Poinsot, T. & Veynante, D. 2000 Dynamically thickened flame LES model for premixed and non-premixed turbulent combustion. *Proc. of the Summer Program* pp. 157–168. (Cited on pages 159 and 162.)

Légier, J.-Ph., Varoquié, B., Lacas, F., Poinsot, T. & Veynante, D. 2002 Large eddy simulation of a non-premixed turbulent burner using a dynamically thickened flame model. In *IUTAM Symposium on Turbulent Mixing and Combustion*, pp. 315 – 326. Kluwer Academic Publishers. (Cited on page 163.)

Lepers, J., Krebs, W., Prade, B., Flohr, P., Pollarolo, G. & Ferrante, A. 2005 Investigation of thermoacoustic stability limits of an annular gas turbine combustor test-rig with and without helmholtz resonators. *ASME Turbo Expo GT2005-68246* . (Cited on page 26.)

Lespinasse, F., Baillot, F. & Boushaki, T. 2013 Response of v-flames placed in an hf transverse acoustic field from a velocity to pressure antinode. *Comptes rendus de l'Académie des Sciences - Mécanique* **341**, 110–120. (Cited on pages 21 and 172.)

Levich, E. & Tsinober, A. 1983 On the role of helicity structures in three-dimensional turbulent flow. *Phys. Lett. A* **93** (6), 293–297. (Cited on page 17.)

Lieuwen, T. 2001 Theoretical investigation of unsteady flow interactions with a premixed planar flame. *J. Fluid Mech.* **435**, 289–303. (Cited on page 25.)

Lieuwen, T. & Neumeier, Y. 2002 Nonlinear pressure-heat release transfer function measurements in a premixed combustor. *Proc. Combust. Inst.* **29**, 99–105. (Cited on page 20.)

Lieuwen, T. & Yang, V. 2005 *Combustion Instabilities in Gas Turbine Engines. Operational Experience, Fundamental Mechanisms and Modeling*, , vol. 210. Progress in Astronautics and Aeronautics, AIAA. (Cited on pages 18, 21, and 87.)

Lieuwen, T. & Zinn, B. T. 1998 The role of equivalence ratio oscillations in driving combustion instabilities in low nox gas turbines. *Proc. Combust. Inst.* **27**, 1809–1816. (Cited on page 20.)

Lin, J. & Parker, R.G. 2000*a* Mesh stiffness variation instabilities in two-stage gear systems. *Journal of Vibration and Acoustics* **124**, 68–76. (Cited on page 15.)

Lin, J. & Parker, R.G. 2000*b* Structured vibration characteristics of planetary gears with unequally spaced planets. *J. Sound Vib.* **235** (5), 921–928. (Cited on page 15.)

Lumley, J. 1967 The structure of inhomogeneous turbulent flows. *Atmospheric Turbulent and Radio Wave Propagation* pp. 166–178. (Cited on page 28.)

Lynch, E.D. 2011 High fidelity modeling program approach. *ALREST, Technical meeting* . (Cited on pages 18 and 19.)

Marble, F. E. & Candel, S. 1977 Acoustic disturbances from gas nonuniformities convected through a nozzle. *J. Sound Vib.* **55**, 225–243. (Cited on pages 26 and 44.)

Mazzei, A., Gotzinger, S., de S. Menezes, L., Zumofen, G., Benson, O. & Sandoghdar, V. 2007 Controlled coupling of counterpropagating whispering-gallery modes by a single rayleigh scatterer: a classical problim in a quantum optical light. *Physical Review Letter* **99**, 173603. (Cited on page 16.)

McIntosh, A.C. 1993 The linearized response of the mass burning rate of a premixed flame to rapid pressure changes. *Combust. Sci. Tech.* **91**, 329–346. (Cited on page 25.)

McManus, K., Poinsot, T. & Candel, S. 1993 A review of active control of combustion instabilities. *Prog. Energy Comb. Sci.* **19**, 1–29. (Cited on page 19.)

Meier, W., Weigand, P., Duan, X.R. & Giezendanner-Thoben, R. 2007 Detailed characterization of the dynamics of thermoacoustic pulsations in a lean premixed swirl flame. *Combust. Flame* **150** (1-2), 2–26. (Cited on page 166.)

Mejia, D., Selle, L., Bazile, R. & Poinsot, T. 2014 Wall-temperature effects on flame response to acoustic oscillations. *Proc. Combust. Inst. (in press)* . (Cited on pages 26, 29, 173, and 181.)

Mendez, S. & Eldredge, J. 2009 Acoustic modeling of perforated plates with bias flow for large-eddy simulations. *J. Comput. Phys.* **228** (13), 4757–4772. (Cited on page 26.)

Moeck, J.P., Bourgouin, J-F., Durox, D., Schuller, T. & Candel, S. 2012 Non-linear interaction between a precessing vortex core and acoustic oscillations in a turbulent swirl flame. *Combust. Flame* **159**, 2650–2668. (Cited on page 25.)

Moeck, J.P., Paul, M. & Paschereit, C. 2010 Thermoacoustic instabilities in an annular flat rijke tube. *ASME Paper 2010-GT-23577* . (Cited on pages 26, 33, 44, 89, 218, 219, and 235.)

Moin, P. 2002 Advances in large eddy simulation methodology for complex flows. *Int. J. Heat Fluid Flow* **23** (5), 710–720. (Cited on page 28.)

Motheau, E., Nicoud, F. & Poinsot, T. 2012 Using boundary conditions to account for mean flow effects in a zero mach number acoustic solver. *ASME Paper 2012-GT-68852* . (Cited on pages 26 and 75.)

Moureau, V., Fiorina, B. & Pitsch, H. 2009 A level set formulation for premixed combustion LES considering the turbulent flame structure. *Combust. Flame* **156** (4), 801–812. (Cited on page 159.)

Moureau, V., Lartigue, G., Sommerer, Y., Angelberger, C., Colin, O. & Poinsot, T. 2005 Numerical methods for unsteady compressible multi-component reacting flows on fixed and moving grids. *J. Comput. Phys.* **202** (2), 710–736. (Cited on pages 158, 169, 188, and 221.)

Myers, M.K. 1986 An exact energy corollary for homentropic flow. *J. Sound Vib.* **109**, 277–284. (Cited on page 266.)

Ndiaye, A., Bauerheim, M., Moreau, S. & Nicoud, F. 2015 Uncertainty quantification of thermo-acoustic instabilities in a swirled stabilized combustor. *ASME Turbo Expo (accepted)* . (Cited on pages 129 and 138.)

Nicoud, F., Baya-Toda, H., Cabrit, O., Bose, S. & Lee, J. 2011 Using singular values to build a subgrid-scale model for large eddy simulations. *Physics of fluids* **23** (085106), 1–12. (Cited on pages 158 and 172.)

Nicoud, F., Benoit, L., Sensiau, C. & Poinsot, T. 2007 Acoustic modes in combustors with complex impedances and multidimensional active flames. *AIAA Journal* **45**, 426–441. (Cited on pages 27, 43, 52, 54, 55, 80, 102, 103, 119, 167, 174, 204, and 222.)

Nicoud, F. & Ducros, F. 1999 Subgrid-scale stress modelling based on the square of the velocity gradient. *Flow, Turb. and Combustion* **62** (3), 183–200. (Cited on pages 27, 172, and 188.)

Nicoud, F. & Poinsot, T. 2005 Thermoacoustic instabilities: should the rayleigh criterion be extended to include entropy changes ? *Combust. Flame* **142**, 153–159. (Cited on pages 24 and 105.)

Nicoud, F. & Wieczorek, K. 2009 About the zero mach number assumption in the calculation of thermoacoustic instabilitie. *Int. J. Spray and Combustion Dynamic* **1**, 67–112. (Cited on pages 26 and 204.)

Noiray, N., Bothien, M. & Schuermans, B. 2011 Analytical and numerical analysis of staging concepts in annular gas turbines. *Combustion Theory and Modelling* **15** (5), 585–606. (Cited on pages 15, 17, 22, 31, 33, 44, 52, 57, 72, 80, 81, 82, 84, 87, 89, 120, 196, 204, 214, 218, 235, 239, 243, 244, and 252.)

Noiray, N., Durox, D., Schuller, T. & Candel, S. 2008 A unified framework for nonlinear combustion instability analysis based on the flame describing function. *J. Fluid Mech.* **615**, 139–167. (Cited on pages 25, 26, 167, 218, and 249.)

Noiray, N. & Schuermans, B. 2013 On the dynamic nature of azimuthal thermoacoustic modes in annular gas turbine combustion chambers. *Proceedings of the Royal Society A* **469** (2151), 1471–2946. (Cited on pages 31, 32, 72, 235, and 238.)

O'Connor, J. & T.Lieuwen 2012*a* Further characterization of the disturbance field in a transversely excited swirl-stabilized flame. *Journal of Engineering for Gas Turbines and Power* **134** (011501-9). (Cited on page 91.)

O'Connor, J. & T.Lieuwen 2012*b* Influence of transverse acoustic modal structure on the forced response of a swirling nozzle flow. *ASME Paper 2012-GT-70053* . (Cited on pages 21 and 46.)

O'Connor, J. & T.Lieuwen 2012*c* Recirculation zone dynamics of a transversely excited swirl flow and flame. *Physics of fluids* **24** (075107). (Cited on pages 17, 21, 32, 46, 75, 91, and 172.)

Oefelein, J. C. & Yang, V. 1993 Comprehensive review of liquid-propellant combustion instabilities in f-1 engines. *J. Prop. Power* **9** (5), 657–677. (Cited on page 32.)

Orr, W. McFadden 1907*a* The stability or instability of the steady motions of a perfect liquid and of a viscous liquid. part i: A perfect liquid. *Proceedings of the Royal Irish Academy* **27**, 9–68. (Cited on page 205.)

Orr, W. McFadden 1907*b* The stability or instability of the steady motions of a perfect liquid and of a viscous liquid. part ii: A viscous liquid. *Proceedings of the Royal Irish Academy* **27**, 69–138. (Cited on page 205.)

Palies, P. 2010 Dynamique et instabilités de combustion de flammes swirlées. Phd thesis, Ecole Centrale Paris. (Cited on pages 25, 47, and 76.)

Palies, P, Durox, D, Schuller, T & Candel, S 2011 Experimental study on the effect of swirler geometry and swirl number on flame describing functions. *Combustion Science and Technology* **183** (7), 704–717. (Cited on page 25.)

Pang, L., Tetz, K.A. & Fainman, Y. 2007 Observation of the splitting of degenerate surface plasmon polariton modes in a two-dmiensional metallic nanohole array. *Applied Physics Letters* **90** (11), 111103. (Cited on page 15.)

Pankiewitz, C. & Sattelmayer, T. 2003 Time domain simulation of combustion instabilities in annular combustors. *ASME Journal of Engineering for Gas Turbines and Power* **125** (3), 677–685. (Cited on pages 27, 32, 87, 120, and 204.)

Parmentier, J.F., Salas, P., Wolf, P., Staffelbach, G., Nicoud, F. & Poinsot, T. 2012 A simple analytical model to study and control azimuthal instabilities in annular combustion chamber. *Combustion and Flame* **159**, 2374–2387. (Cited on pages 15, 17, 26, 31, 32, 36, 42, 43, 44, 45, 47, 52, 74, 76, 77, 79, 88, 89, 99, 100, 115, 120, 235, 236, and 253.)

Paschereit, C. O., Polifke, W., Schuermans, B. & Mattson, O. 2002 Measurement of transfer matrices and source terms of premixed flames. *J. Eng. Gas Turb. and Power* **124**, 239–247. (Cited on page 204.)

Passot, T. & Pouquet, A. 1987 Numerical simulation of compressible homogeneous flows in the turbulent regime. *J. Fluid Mech.* **181**, 441–466. (Cited on page 211.)

Perrin, R. & Charnley, T. 1973 Group theory and the bell. *J. Sound Vib.* **31** (4), 411–418. (Cited on pages 15, 32, 33, 57, 58, and 68.)

Pierce, A. D. 1981 *Acoustics: an introduction to its physical principles and applications*. New York: McGraw Hill. (Cited on pages 55 and 103.)

Piomelli, U., Moin, P. & Ferziger, J. H. 1988 Model consistency in large eddy simulation of turbulent channel flows. *Phys. Fluids* **31** (7), 1884–1891. (Cited on page 28.)

Pitsch, H. 2006 Large eddy simulation of turbulent combustion. *Ann. Rev. Fluid Mech.* **38**, 453–482. (Cited on page 28.)

Poinsot, T. 1987 Analyse des instabilités de combustion de foyers turbulents prémélangés. Thèse d'etat, Université d'Orsay. (Cited on page 29.)

Poinsot, T., Echekki, T. & Mungal, M. G. 1992 A study of the laminar flame tip and implications for premixed turbulent combustion. *Combust. Sci. Tech.* **81** (1-3), 45–73. (Cited on pages 29, 169, 188, and 221.)

Poinsot, T., Trouvé, A., Veynante, D., Candel, S. & Esposito, E. 1987 Vortex driven acoustically coupled combustion instabilities. *J. Fluid Mech.* **177**, 265–292. (Cited on pages 19 and 25.)

Poinsot, T. & Veynante, D. 2005 *Theoretical and Numerical Combustion*. R.T. Edwards, 2nd edition. (Cited on pages 21, 23, 26, and 119.)

Poinsot, T. & Veynante, D. 2011 *Theoretical and Numerical Combustion*. Third Edition (www.cerfacs.fr/elearning). (Cited on pages 18, 28, 46, 54, 93, 94, 105, 145, 151, 161, 169, 204, 220, 222, and 259.)

Polifke, W. 1990 Aspects of helicity in turbulent flows. PhD thesis, City university of New York. (Cited on page 17.)

Polifke, W., Paschereit, C. & Doebbeling, K. 2001*a* Constructive and destructive interference of acoustic and entropy waves in a premixed combustor with a choked exit. *Int. J. Acoust. Vib.* **6**, 135–146. (Cited on page 26.)

Polifke, W., Poncet, A., Paschereit, C. O. & Doebbeling, K. 2001*b* Reconstruction of acoustic transfer matrices by instationnary computational fluid dynamics. *J. Sound Vib.* **245** (3), 483–510. (Cited on pages 119 and 204.)

Rayleigh, L. 1894 *The Theory of Sound*. Mac Millan (reprinted by Dover, New York, 1945). (Cited on pages 20 and 24.)

Riber, E., García., M., Moureau, V., Pitsch, H., Simonin, O. & Poinsot, T. 2006 Evaluation of numerical strategies for LES of two-phase reacting flows. *Proc. of the Summer Program* pp. 197–211. (Cited on page 28.)

Roache, P.J. 1997 Quantification of uncertainty in computational fluid dynamics. *Annu. Rev. fluid Mech.* **29**, 123–160. (Cited on page 118.)

Roux, A., Gicquel, L. Y. M., Sommerer, Y. & Poinsot, T. J. 2007 Large eddy simulation of mean and oscillating flow in a side-dump ramjet combustor. *Combust. Flame* **152** (1-2), 154–176. (Cited on page 28.)

Roux, S., Lartigue, G., Poinsot, T., Meier, U. & Bérat, C. 2005 Studies of mean and unsteady flow in a swirled combustor using experiments, acoustic analysis and large eddy simulations. *Combust. Flame* **141**, 40–54. (Cited on page 169.)

Sagaut, P. 2006 *Large eddy simulation for incompressible flows*. Springer-Verlag, 3rd Edition. (Cited on page 157.)

Saito, M., Hoshikawa, M. & Sato, M. 1996 Enhancement of evaporation/combustion rate coefficient of a single fuel droplet by acoustic oscillation. *Fuel* **75** (6), 669–674. (Cited on page 25.)

Sattelmayer, T. 2003 Influence of the combustor aerodynamics on combustion instabilities from equivalence ratio fluctuations. *J. Eng. Gas Turb. and Power* **125** (1), 11–19. (Cited on page 20.)

Schmid, P.J. 2010 Dynamic mode decomposition of numerical and experimental data. *J. Fluid Mech.* **656**, 5–28. (Cited on pages 178, 193, and 210.)

Schmitt, P., Poinsot, T., Schuermans, B. & Geigle, K. P. 2007 Large-eddy simulation and experimental study of heat transfer, nitric oxide emissions and combustion instability in a swirled turbulent high-pressure burner. *J. Fluid Mech.* **570**, 17–46. (Cited on page 28.)

Schønfeld, T. & Poinsot, T. 1999 Influence of boundary conditions in LES of premixed combustion instabilities. In *Annual Research Briefs* , pp. 73–84. Center for Turbulence Research, NASA Ames/Stanford Univ. (Cited on page 169.)

Schuermans, B., Paschereit, C. & Monkewitz, P. 2006 Non-linear combustion instabilities in annular gas-turbine combustors. *AIAA paper 2006-0549* . (Cited on pages 21, 22, 33, 72, and 87.)

Schuller, T., Durox, D. & Candel, S. 2003 A unified model for the prediction of laminar flame transfer functions: comparisons between conical and v-flames dynamics. *Combust. Flame* **134**, 21–34. (Cited on page 25.)

Schuller, T., Durox, D., Palies, P. & Candel, S. 2012 Acoustic decoupling of longitudinal modes in generic combustion systems. *Combustion and Flame* **159**, 1921–1931. (Cited on pages 26, 47, 76, 88, 100, 105, 115, 235, and 259.)

Searby, ed. 2008 *Le bruit de combustion*, 11e Ecole de Combustion. (Cited on page 19.)

Selle, L., Benoit, L., Poinsot, T., Nicoud, F. & Krebs, W. 2006 Joint use of compressible large-eddy simulation and Helmholtz solvers for the analysis of rotating modes in an industrial swirled burner. *Combust. Flame* **145** (1-2), 194–205. (Cited on pages 27, 43, and 54.)

Selle, L., Lartigue, G., Poinsot, T., Koch, R., Schildmacher, K.-U., Krebs, W., Prade, B., Kaufmann, P. & Veynante, D. 2004*a* Compressible large-eddy simulation of turbulent combustion in complex geometry on unstructured meshes. *Combust. Flame* **137** (4), 489–505. (Cited on page 163.)

Selle, L., Nicoud, F. & Poinsot, T. 2004*b* The actual impedance of non-reflecting boundary conditions: implications for the computation of resonators. *AIAA Journal* **42** (5), 958–964. (Cited on pages 26, 169, 188, and 221.)

Sengissen, A., Giauque, A., Staffelbach, G., Porta, M., Krebs, W., Kaufmann, P. & Poinsot, T. 2007 Large eddy simulation of piloting effects on turbulent swirling flames. *Proc. Combust. Inst.* **31**, 1729–1736. (Cited on pages 169 and 220.)

Sensiau, C. 2008 Simulations numériques des instabilités thermoacoustiques dans les chambres de combustion aéronautiques - th/cfd/08/127. PhD thesis, Université de Montpellier II, - Institut de Mathématiques et de Modélisation de Montpellier, France. (Cited on page 22.)

Sensiau, C., Nicoud, F. & Poinsot, T. 2009 A tool to study azimuthal and spinning modes in annular combustors. *Int. Journal Aeroacoustics* **8** (1), 57–68. (Cited on pages 22, 32, 33, 43, 54, 55, 57, 58, 69, and 72.)

Silva, C.F., Nicoud, F., Schuller, T., Durox, D. & Candel, S. 2013 Combining a helmholtz solver with the flame describing function to assess combustion instability

in a premixed swirled combustor. *Combustion and Flame* **160**, 1743–1754. (Cited on pages 27, 43, 54, 55, 249, and 250.)

Silva, F., Guillemain, Ph., Kergomard, J., Mallaroni, B. & Norris, A.N. 2009 Approximation formulae for the acoustic radiation impedance of a cylindrical pipe. *Journal of Sound and Vibration* **322**, 255–263. (Cited on pages 55 and 103.)

Simonelli, F. & Gollub, J.P. 1989 Surface wave mode interactions: effects of symmetry and degeneracy. *J. Fluid Mech.* **199**, 471–494. (Cited on pages 15, 16, and 17.)

Smagorinsky, J. 1963 General circulation experiments with the primitive equations: 1. the basic experiment. *Mon. Weather Rev.* **91**, 99–164. (Cited on pages 27, 157, and 172.)

Smirnov, A., Shi, S. & Celik, I. 2001 Random flow generation technique for large eddy simulations and particle-dynamics modeling. *Trans. ASME. J. Fluids Eng.* **123**, 359–371. (Cited on page 212.)

Smith, R., Anderson, W. & Merkle, C.L. 2010 Computational studies of the effects of oxidizer injector length on combustion instability. *AIAA 2010-6564* . (Cited on page 20.)

Smith, R., Xia, G., Anderson, W. & Merkle, C.L. 2012 Computational studies of the effects of oxidizer injector length on combustion instability. *Combustion Theory and Modelling* **16** (2), 2012. (Cited on page 20.)

Staffelbach, G., Gicquel, L.Y.M., Boudier, G. & Poinsot, T. 2009 Large eddy simulation of self-excited azimuthal modes in annular combustors. *Proc. Combust. Inst.* **32**, 2909–2916. (Cited on pages 19, 28, 32, 55, 72, 89, 90, 91, 218, and 225.)

Stow, S. & Dowling, A.P. 2004 Low-order modelling of thermoacoustic limit cycles. *ASME Paper 2004-GT-54245* . (Cited on pages 26 and 89.)

Stow, S. R. & Dowling, A. P. 2001 Thermoacoustic oscillations in an annular combustor. *ASME Paper 2001-GT-0037* . (Cited on pages 26, 32, and 75.)

Stow, S. R. & Dowling, A. P. 2003 Modelling of circumferential modal coupling due to helmholtz resonators. *ASME Paper 2003-GT-38168* . (Cited on pages 32, 75, 227, and 228.)

Strahle, W. 1985 A more modern theory of combustion noise. In *Recent Advances in the Aerospace Sciences*, pp. 103–114. New York: Plenum Press. (Cited on page 19.)

Strahle, W. C. 1972 Some results in combustion generated noise. *J. Sound Vib.* **23** (1), 113–125. (Cited on page 19.)

Stull, D. R. & Prophet, H. 1971 JANAF thermochemical tables, 2nd Edition. *Tech. Rep.* NSRDS-NBS 37. US National Bureau of Standards. (Cited on page 149.)

Tay Wo Chong, L., Kaess, R., Komarek, T., Foller, S. & Polifke, W. 2010 Identification of flame transfer functions using les of turbulent reacting flows. In *High Performance Computing in Science and Engineering, Garching/Munich 2009*, pp. 255–266. Springer Berlin Heidelberg. (Cited on page 205.)

Tay-Wo-Chong, L. & Polifke, W. 2012 Les-based study of the influence of thermal boundary condition and combustor confinement on premix flame transfer functions. *ASME Paper 2012-GT-68796* . (Cited on pages 29, 173, 176, and 181.)

Tran, N., Ducruix, S. & Schuller, T. 2009 Damping combustion instabilities with perforates at the premixer inlet of a swirled burner. *Proc. Combust. Inst.* **32** (2), 2917–2924. (Cited on page 26.)

Tripathy, S.C., Jain, K. & Bhatnagar, A. 2000 Helioseismic solar cycle changes and splitting coefficients. *J. Astrophys. Astr.* **21**, 349–352. (Cited on page 16.)

UCSD 2013 "chemical-kinetic mechanisms for combustion applications", san diego mechanism web page, ucsd. (Cited on pages 173 and 188.)

Venkataraman, K. K., Preston, L. H., W., Simons D., Lee, B.J., Lee, J.G. & Santavicca, D. 1999 Mechanism of combustion instability in a lean premixed dump combustor. *Journal of Propulsion and Power* **15**, 909–918. (Cited on page 19.)

Williams, F. A. 1985 *Combustion Theory*. Menlo Park, CA: Benjamin Cummings. (Cited on pages 23 and 160.)

Wolf, P., Staffelbach, G., Balakrishnan, R., Roux, A. & Poinsot, T. 2010 Azimuthal instabilities in annular combustion chambers. *Proc. of the Summer Program* pp. 259–269. (Cited on pages 19, 28, 163, 186, and 235.)

Wolf, P., Staffelbach, G., Gicquel, L.Y.M., Muller, J.D & T., Poinsot 2012 Acoustic and large eddy simulation studies of azimuthal modes in annular combustion chambers. *Combustion and Flame* **159**, 3398–3413. (Cited on pages 28, 32, 72, 87, 120, 169, 218, 220, 223, 224, 225, 235, and 267.)

Wolf, P., Staffelbach, G., Roux, A., Gicquel, L., Poinsot, T. & Moureau, V. 2009 Massively parallel LES of azimuthal thermo-acoustic instabilities in annular gas turbines. *C. R. Acad. Sci. Mécanique* **337** (6-7), 385–394. (Cited on pages 19, 21, 28, and 44.)

Worth, N.A. & Dawson, J.R. 2013*a* Modal dynamics of self-excited azimuthal instabilities in an annular combustion chamber. *Combustion and Flame* **160** (11), 2476–2489. (Cited on pages 22, 23, 28, 32, 33, 35, 36, 44, 73, 91, 166, 167, 168, 174, 188, 197, 206, 218, 219, 235, and 237.)

Worth, N.A. & Dawson, J.R. 2013*b* Self-excited cricumferential instabilities in a model annular gas turbine combustor: global flame dynamics. *Proceedings of the Combustion Institute* **34**, 3127–3134. (Cited on pages 5, 12, 22, 23, 28, 32, 33, 34, 36, 44,

69, 72, 73, 84, 89, 91, 120, 165, 166, 167, 168, 172, 173, 175, 176, 177, 184, 186, 187, 188, 189, 190, 196, 197, 198, 206, 218, 219, 223, 235, 237, and 267.)

Yang & Anderson 1995 Liquid rocket engine combustion instability, progress in astronautics and aeronautics. *AIAA* **169**. (Cited on page 18.)

You, D. & Moin, P. 2007*a* A dynamic global-coefficient subgrid-scale eddy-viscosity model for large-eddy simulation in complex geometries. *Phys. Fluids* **19** (6), 065110. (Cited on page 27.)

You, D. & Moin, P. 2007*b* A dynamic global-coefficient subgrid-scale model for large-eddy simulation of turbulent scalar transport in complex geometries. In *Annual Research Briefs* , pp. 169–182. Center for Turbulence Research, NASA Ames/Stanford Univ. (Cited on page 27.)

Zhao, Dan 2012 Transient growth of flow disturbances in triggering a rijke tube combustion instability. *Combustion and Flame* **159** (6), 2126–2137. (Cited on page 259.)

Résumé court

Une large gamme de problèmes physiques, des petites molécules aux étoiles géantes, contiennent des symétries de rotation et sont sujets à des oscillations azimutales ou transverses. Quand cette symétrie est rompue, le système peut devenir instable. Dans cette thèse, les brisures de symétries sont étudiées dans les chambres de combustion annulaires, sujettes à des instabilités thermo-acoustiques azimutales. En premier lieu, deux types de brisures sont obtenues analytiquement : la première en répartissant des bruleurs différents le long de la chambre et la seconde provoquée par le champ moyen lui-même. Ces ruptures de symétries entraînent une séparation des fréquences, fixe la structure du mode et peut déstabiliser le système. De plus, une approche Quantification d'Incertitudes (UQ) permet d'évaluer l'effet de la rupture de symétries provoquée par les incertitudes sur la description ou le comportement des flammes. Pour compléter cette théorie, des Simulations aux Grandes Echelles (SGE) sont réalisées sur un mono-secteur ainsi que sur une configuration complète 360° de l'expérience annulaire de Cambridge. Les résultats numériques sont comparés aux données expérimentales et montrent un bon accord. En particulier, un mode instable à 1800 Hz croît dans les deux cas. Cependant, la SGE, limitée par son coût important, ne permet pas l'étude du cycle limite s'établissant après plusieurs centaines de millisecondes. Pour palier à ce problème, une nouvelle approche, appelée AMT, est développée : les résultats d'une théorie ou d'un solveur acoustique sont injectés dans une simulation SGE. Cette approche permet d'étudier les brisures de symétries, la nature et la dynamique des modes acoustiques, ainsi que d'évaluer l'amortissement dans des configurations réalistes.

Short abstract

A large range of physical problems, from molecules to giant stars, contains rotating symmetry and can exhibit azimuthal waves or vibrations. When this symmetry is broken, the system can become unstable with chaotic behaviors. Symmetry breaking is investigated in annular combustors prone to azimuthal thermo-acoustic instabilities. First, theories reveal that two types of symmetry breaking exist : due to different burner types distributed allong the chamber or due to the flow itself . It leads to frequency splitting, fixes the mode structure and can destabilize the configuration. A UQ analysis is also performed to quantify the symmetry breaking effect due to uncertainties of flame descriptions or behaviors. To complete theory, Large Eddy Simulations are performed on a single-sector as well as on a complete 360° configuration of the annular experiment of Cambridge. Numerical results are compared to experimental data showing a good agreement. In particular, an unstable azimtuthal mode at 1800 Hz grows in both LES and experiment. However, LES cannot investigate the limit cycle because of its extreme cost. To tackle this problem, a new methodology is developed, called AMT, where theory or Helmholtz solver predictions are injected into LES or DNS. This method allows to study symmetry breaking, mode nature and dynamics as well as evaluating damping in realistic annular configurations.